UNIVERSIDAD COMPLUTENSE DE MADRID
FACULTAD DE CIENCIAS FÍSICAS

TESIS DOCTORAL

Exotic quantum matter generated from Floquet engineering

Materia cuántica exótica generada con ingeniería de Floquet

MEMORIA PARA OPTAR AL GRADO DE DOCTOR

PRESENTADA POR

Gregor Pieplow

Directores

Fernando Sols
Charles E. Creffield

Madrid

Universidad Complutense de Madrid

Facultad de Ciencias Físicas
Departamento de Física de Materiales

Tesis doctoral

Exotic quantum matter generated from Floquet engineering

Materia cuántica exótica generada con ingeniería de Floquet

Gregor Pieplow

Dirigida por:
Fernando Sols
Charles E. Creffield

Madrid 2019

UNIVERSIDAD
COMPLUTENSE
MADRID

DECLARACIÓN DE AUTORÍA Y ORIGINALIDAD DE LA TESIS PRESENTADA PARA OBTENER EL TÍTULO DE DOCTOR

D. **Gregor Pieplow**,
estudiante en el Programa de Doctorado **D9AD - Doctorado en Física**,
de la Facultad de **Ciencias Físicas** de la Universidad Complutense de Madrid, como autor de la tesis presentada para la obtención del título de Doctor y titulada:
"Exotic quantum matter generated from Floquet engineering"
"Materia cuántica exótica generada con ingeniería de Floquet"
y dirigida por: Charles E. Creffield y Fernando Sols

DECLARO QUE:

La tesis es una obra original que no infringe los derechos de propiedad intelectual ni los derechos de propiedad industrial u otros, de acuerdo con el ordenamiento jurídico vigente, en particular, la Ley de Propiedad Intelectual (R.D. legislativo 1/1996, de 12 de abril, por el que se aprueba el texto refundido de la Ley de Propiedad Intelectual, modificado por la Ley 2/2019, de 1 de marzo, regularizando, aclarando y armonizando las disposiciones legales vigentes sobre la materia), en particular, las disposiciones referidas al derecho de cita.

Del mismo modo, asumo frente a la Universidad cualquier responsabilidad que pudiera derivarse de la autoría o falta de originalidad del contenido de la tesis presentada de conformidad con el ordenamiento jurídico vigente.

En Madrid, a 10 de Julio de 2019

Fdo.: 

For Summer, my partner and the season.

Acknowledgements

I am profoundly grateful to my thesis advisors, Fernando Sols and Charles E. Creffield, for their patience and advice. Without our regular discussions, their continuous support and very helpful input, this work would not have been possible. I would also like to thank my host Nathan Goldman at the Université libre de Bruxelles, who inspired the work on magnetic monopoles. The scientific exchange and the hospitality of his group was greatly appreciated. Furthermore, Wolfgang Ketterle and Anthony J. Leggett also provided guidance in brief exchanges. It is of immeasurable value to have the fortune to exchange ideas with such clear-sighted and thoughtful minds. I am forever thankful for the love and support of my partner Summer A. Banks. She is not only responsible for a thorough proofreading of this thesis but she is also the architect and engineer guaranteeing the structural integrity of my sanity throughout my time in Madrid. I am, of course, also thankful for the emotional support of my family in Hamburg, Berlin and Peckatel and my in- laws in Ridgecrest, California. The friendship of my colleagues Alicia Prados and Belén Cortés-Llanos was also instrumental to the process of working on this thesis. I have them to thank for most of my Spanish, as well as for the assistance and help they provided during my first years at the Complutense. I greatly appreciate the company of my fellow office mates Manuel Alonso Orts, María Taeño González, Jaime José Dolado, David Gonzáles Gonzáles, Francisco Carreño Puertas, Marina García Carrión and Antonio Vázquez López. Our office has been on a steady climb to grandeur and its furnishings have peaked with the addition of a fridge. I have also thoroughly enjoyed the company of my fellow colleagues in the material science department. Javier Bartolome Vilchez, Belén Sotillo Buzarra, Beatriz Martnez Pabon, Alvaro Díaz, Víctor García, Felix del Prado Hurtado, Fernando Glvez Alonso and Marta Saiz Bretín provided the necessary distractions which turned the nourishing loaf of bread that is a PhD, into a series of gratifying slices, complete with wholesome and sustaining spreads. I would also like to thank Konstancja Satalecka and Jürgen Schiefele, who contributed significantly to smoothing out my move to and first weeks in Madrid. A special mention goes to Marc A. Valdez. We had some very productive and fruitful exchanges during his brief stay in our group. Finally, I would like to thank my friends back home in Germany and all over the world. They tolerated a continuous feed of pictures of sunny Madrid and Iberian pork products without banishing me to the shadowy corners of their phones.

Summary

Exotic quantum matter generated from Floquet engineering

This thesis investigates three time periodic quantum mechanical systems, all of which are of particular interest for research related to ultracold atoms in optical lattices.

In the first system (Chapter 2), a synthetic uniform magnetic field is created through the shaking of a two dimensional square optical lattice [1]. In this way an effective magnetic field can be felt by ultra cold atoms trapped in the lattice. Simple continuous shaking, however, produces non-uniform effective masses (tunneling amplitudes) which lead to non-uniform flux configurations. This is addressed both analytically and numerically in this work. In addition, the limitations of continuous shaking schemes are discussed and several non-continuous shaking protocols are analyzed and compared. At the end of this investigation, the shaking schemes that yield a uniform effective mass and magnetic flux are identified.

The second system (Chapter 3) under investigation in this work centers on the effect of a rapidly oscillating magnetic charge of a magnetic monopole. Floquet theory is used to derive a high-frequency limit of an electric charge coupled to such a Floquet magnetic monopole. A non-relativistic solution to the Schrödinger equation of this effective system is presented. This solution is then compared to a charge confined to a sphere and coupled to a static magnetic monopole.

The third system (Chapters 4 and 5) under investigation is a one-dimensional Bose-Hubbard chain, whose tunneling amplitude is varied periodically (kinetic driving) with a zero time average. We reported on this work in Refs. [2] and [3]. The system is investigated for both periodic and hard wall boundary conditions. With the help of Floquet theory, a time-independent effective Hamiltonian is calculated, in which nearest-neighbor single particle hopping is suppressed. The effective Hamiltonian consists of correlated hoppings and non-local interaction processes. For a critical value of the driving parameter, the system shows evidence of a Mott to superfluid transition. The superfluid consists of two fragmented condensates with opposite non-zero momenta.

For large values of the driving parameter, the system shows similarities to Richardson-Gaudin models. This connection provides key insights into the problem of interacting bosons. A particular type of pairing interaction in momentum space explains the formation of the macroscopic superposition of bosons in non-zero and opposite momentum eigenstates. These interactions also give rise to a peculiar depletion cloud (reduction cloud) that is shared by both branches of the cat. The branches are identified precisely through symmetry considerations and studied with regard to several quality measures. In the ring (periodic boundary conditions), the system is sensitive to variations of the effective flux but only in such a way that the macroscopic superposition is preserved. The cat

structure stays intact in the presence of a harmonic confinement, with a single impurity in the ring and a disorder potential, as long as it does not cause localization. The shared reduction cloud provides additional protection against premature decay due to particle losses. These and other considerations discussed in this work highlight a remarkable intrinsic protection against collapse.

Materia cuántica exótica generada con ingeniería de Floquet

En la presente tesis doctoral se muestran los resultados obtenidos en la investigación de tres sistemas cuánticos periódicos en el tiempo, todos ellos de gran interés dentro de la investigación relacionada con átomos ultrafríos en redes ópticas.

En el primer sistema (Capitulo 1), un campo magnético uniforme es creado de manera artificial a partir del sacudido periódico de una red óptica bidimensional cuadrada [1]. De este modo, los átomos ultra fríos atrapados en dicha red pueden experimentar un campo magnético efectivo. Una perturbación simple y continua produce, sin embargo, masas efectivas no uniformes (amplitudes de tuneleo) que dan lugar a configuraciones de flujo no uniforme. Ambos puntos son abordados de manera analítica y numérica. Además de ello, las limitaciones de una perturbación continua son discutidas y varios protocolos de perturbación discontinua son analizados y comparados. Finalmente, los protocolos de perturbación que producen una masa efectiva y un flujo magnético uniformes son identificados.

El segundo tema (Capitulo 3) investigado en esta tesis está centrado en el efecto de una carga magnética asociada a un monopolo magnético y que oscila rápidamente. La teoría de Floquet es empleada para derivar el límite de alta frecuencia de una carga eléctrica acoplada a dicho monopolo magnético tipo Floquet. Se presenta una solución no relativista de la ecuación de Schrödinger para este sistema efectivo. Dicha solución se compara con una carga confinada a una esfera y acoplada a un monopolo magnético estático.

El tercer sistema (Capitulos 4 y 5) investigado es una cadena Bose-Hubbard unidimensional cuya amplitud de tunelización es mudulado periódicamente (de forma "cinética") con un promedio temporal nulo. Este trabajo está recogido en las referencias [2] y [3]. Este sistema es investigado aplicando condiciones de frontera tanto periódicas como de paredes duras. Con la ayuda de la teoría de Floquet, se calcula el Hamiloniano efectivo e independiente del tiempo en el que el tuneleo de partículas individuales entre primeros vecinos es suprimida. El Hamiltoniano efectivo consiste en saltos correlacionados y procesos de interacción no locales. Para un valor crítico del parámetro de control, el sistema muestra evidencias de una transición entre un estado Mott y un superfluido. El superfluido consiste en dos condensados fragmentados con momentos opuestos no nulos. Para valores grandes del parámetro impulsor, el sistema se asemeja a modelos de Richardson-Gaudin. Esta similitud proporciona información clave sobre la interacción entre bosones. Un tipo particular de interacción por pares en el espacio de momento explica la superposición macroscópica de bosones en estados con momento no nulo y opuesto. Estas interacciones también dan lugar a una peculiar nube de vaciamiento (nube de reducción) que es compartida por ambas ramas del estado de gato. Las ramas son identificadas con precisión a través de consideraciones de simetría y estudiadas con respecto a varias medidas de calidad. En el anillo (condiciones de frontera periódicas), el sistema es sensible a las

variaciones del flujo efectivo, pero de tal manera que la superposición macroscópica se conserva. La estructura del estado de gato permanece intacta en presencia de un confinamiento armónico, con una única impureza en el anillo y un potencial desordenado, siempre que éste no produzca localización. La nube de reducción compartida proporciona protección adicional contra el deterioro prematuro debido a la pérdida de partículas. Estas y otras consideraciones discutidas en este trabajo resaltan una notable protección intrínseca contra el colapso.

Contents

Introduction

Over the past century our understanding of the interactions of light with matter has advanced steadily. The expertise required to apply this understanding to the cooling and trapping of atoms with lasers has also increased in parallel. This culminated in the observation [4, 5] of Bose-Einstein condensates [6], which had been predicted by Satyendranath Bose and Albert Einstein 70 years earlier. The Bose-Einstein condensates commonly encountered in laboratories form out of a cloud of ultracold atoms at temperatures very close to the absolute zero of $-273.15°\mathrm{C}$.

The condensate consists of many atoms sharing the same state, which is one of the consequences of Bose-Einstein statistics. This form of quantum coherence, which involves a macroscopic number of atoms, is what makes condensates such a remarkable resource. Indeed, they can consist of so many atoms and occupy a large enough amount of space that their fluorescence is visible to the naked eye.

Ever since Bose-Einstein condensates were created in the laboratory, the field has made huge strides. A recent example of the use of Bose Einstein condensates for precision measurements involves atom gravimeters [7–10], which measure local accelerations due to gravity and have even been proposed as a means for detecting gravitational waves [11].

These applications prove that ultracold atom systems are no longer just a quantum mechanical curiosity but also represent a building block for an ever expanding quantum mechanical tool box. This thesis addresses both aspects: it investigates curious aspects of ultracold atom systems and expands the tool box by investigating the effects of various time dependent systems.

The ability to trap ultracold atoms with light not only makes them attractive for quantum sensing, but also allows experimenters to design artificial crystals. This is commonly accomplished with interfering lasers that create a stable pattern of low and high intensity regions of light. This optical lattice is a potential landscape that can then be filled with ultracold atoms [12]. Crystals created in this manner offer a remarkable level of control and tuneability. They can be one, two, three or even higher dimensional, if internal states are used in addition to spatial dimensions [13]. In two dimensions, triangular, square, hexagonal, kagome and ring geometries [14–16] have all been produced in experiments. An excellent review of ultracold atoms in optical crystals can be found in [17]. Although these experimental techniques can also be used for fermions, this thesis focuses on bosons.

The lasers not only control the lattice geometry, but also the depth of the potential wells, which has a direct impact on the tunneling dynamics of the confined atoms. In combination with the control over the interaction strength via Feshbach resonances [18], numerous possibilities emerge for the simulation of many-body systems with ultracold atoms in optical lattices [17, 19].

A very prominent example is the implementation of the Hubbard model [20]. It is

an approximation that describes electrons and their motion in a solid, and it can be adapted for bosons to describe their motion in an optical lattice. With these advances, experimental implementation of the Bose-Hubbard model [21] became possible. It is highly interesting that the Bose-Hubbard model has a quantum phase transition, from a Mott-insulator to a superfluid [22], which was observed in [23]. This and many other experiments proved that ultracold atoms can indeed be used to simulate condensed matter systems and investigate their properties in this manner. In the spirit of Feynman's idea of quantum simulation [24], this spurred a flurry of proposals and experiments dedicated to the exploration of the vast new landscape that has opened up with these experimental techniques.

Optical lattices do not have to be static. They can be made explicitly time dependent by accelerating them uniformly [25], shaking them or superposing a moving lattice [1]. The time periodic manipulations in particular suggest the use of Floquet theory, which provides an elegant treatment of time periodic systems. Classically Floquet theory helps analyze the stability of system. In a quantum mechanical setting, it explains how time periodically driven optical lattices can be used to engineer topological bands [1].

The previous paragraphs provided a broad overview of the context of this thesis. This work is devoted to exploring the possibilities of time periodic manipulations of zero-, one- and two-dimensional systems. The main goals for this research are twofold: quantum simulation and the exploration of potentially new and interesting effects related to periodically driven systems. The particularly interesting applications for ultra cold atoms in driven optical lattices are discussed in detail in the chapters summarized below.

Chapter 1 is devoted to an introduction of Floquet theory and provides a solid foundation for the rest of the thesis. It details some of the historical developments in the treatment of time periodic systems, as well as the concepts that connect classical and quantum mechanical systems. The quantum mechanical implementation of Floquet theory is of particular relevance for this work, so care has been taken to introduce its modern implementation in the context of many-body systems. The stage for the next chapter is set with a treatment of Floquet engineering. The chapter then concludes with a brief discussion of heating in Floquet systems.

Chapter 2 is a review of our work in Ref. [1], where the shaking of a square optical lattice was proposed for the creation of a synthetic uniform magnetic field with a uniform effective mass. The quantum simulation aspect is at its most evident in this part of the work. Various transformations related to the derivation of an effective Hamiltonian are discussed and interpreted. The minimal requirements of shaking protocols are investigated and, in particular, we address the question of whether or not continuous shaking schemes can generate uniform synthetic magnetic fields. This chapter concludes with an analysis and comparison of various shaking schemes.

Chapter 3 stays within the theme of magnetic fields, dealing with the implications of a magnetic monopole with a rapidly switching magnetic charge. This system is an interesting combination of a periodic time variation and a curious hypothetical particle: the magnetic monopole. The effects of such a particle on an electric charge are investigated, with a focus on the limit of large frequencies of the charge oscillations. A charge is coupled to such monopoles, and its Hilbert space is constructed for both a charge that can move freely in three dimensions and a charge that is confined to a sphere.

Chapter 4 also addresses an unusual system, and truly centers on exploring new quan-

tum phases of matter. This chapter is based on our work in Ref. [2], which presents a one dimensional Bose-Hubbard model whose kinetic energy depends periodically on time. An effective description of the oscillation of the kinetic energy in the limit of large frequencies is developed. Its properties are studied for a ring lattice and a hard-wall box. This effective model features many local and non-local interactions and hoppings, and no longer possesses single-particle nearest-neighbor hoppings. An intriguing Mott to superfluid transition also takes place. In the superfluid phase, the ground state is comprised of a fragmented condensate which is condensed at two nonzero momenta. The fragmented condensate is best described by a Schrödinger cat-like superposition of two condensates, which is the central topic of the following chapter.

Chapter 5 continues the investigation of the kinetically driven Bose-Hubbard chain, and develops a microscopic picture to explain the unusual fragmented condensate. This chapter draws on work presented in Ref. [3], where the main focus lies on the characterization of the Schrödinger cat-like ground state. The cat state is characterized for both the ring lattice as well as the hard-wall box. A new type of depletion cloud is introduced (which is labeled reduction cloud) and various measures of cat quality are discussed.

The ground states are investigated with regard to their intrinsic quality as a cat state, the feasibility of their preparation, and their resistance to collapse. The picture that emerges is that of a boson system whose ground doublet is formed by two cat-like states. Their most remarkable property is their resilience to collapse.

The final chapter contains the conclusion and outlook, and in the appendix the numerical methods that were used are explained.

Chapter 1

Floquet Theory

Floquet theory is the theory of ordinary linear differential equations that have time periodic coefficients. In physics ordinary linear differential equations play an important role in the modeling of systems. Often they are useful first-order approximations that help explain aspects of an initially nonlinear description. One of the best known examples of such a system is the parametric oscillator whose natural frequency changes periodically in time. This could be the *O Botafumeiro* (a giant censer [26]) which is kept swinging by periodically changing the length of its suspension rope, or a child on a swing, periodically extending its legs and thereby lowering and raising its center of mass. The crucial difference between a parametric and a forced oscillator is that energy is not directly put into the system, such as a parent pushing the child on the swing, or the wind forcing the deck of a bridge into oscillations [1]. As far as modeling goes, these forces appear as inhomogeneous terms in a differential equation, and not necessarily as a time-dependent coefficient. Floquet theory provides an elegant means of studying the motion and stability of a system. A historically important example of this is Hill's treatment of the lunar motion around the earth in a gravitational potential, which is time periodic due to the presence of the sun [28]. In honor of this work, Hill's equation

$$\ddot{y} + f(t)y = 0 \ , \tag{1.1}$$

where $f(t+T) = f(t)$, was named after him [29]. In the following introduction to Floquet theory, two special cases of Hill's equation are presented and the process of analyzing their stability explained.

These examples from classical mechanics provide a way to familiarize oneself with the historical context of Floquet theory and to recognize how relevant it still is for quantum many-body physics. The development of laser cooling enabled the manipulation of large ensembles of quantum matter [30–32] and played a major role in achieving Bose-Einstein condensation [4, 5]. Advancements in experimenters' ability to sculpt their trapping potentials spatially and temporally in so-called optical lattices made it possible to study condensed matter systems with a hitherto unprecedented level of control. From the first preparation of a Bose Einstein condensate to quantum gas microscopes [33, 34] that allow

[1] Although the Tacoma Narrows bridge structural failure is often cited in physics textbooks as an example of forced resonance, the actual mechanism that led to its demise was the runaway self-excitation of a torsional degree of freedom [27]. This catastrophe of self excitation is fundamentally different from that caused by a forced resonance.

single site resolution of atoms in an optical lattice, the field has come a long way. The formalism I will present here is more suited to these quantum many-body problems even though many of the examples work on a single-particle level as well.

In the spirit of the second quantum revolution [35], Floquet theory appears under the banner of Floquet engineering [36]. It is often geared towards the simulation of condensed matter Hamiltonians. The idea of quantum simulators was popularized by Feynman [24] with the goal of emulating quantum systems that are either very difficult or impossible to create in a laboratory. Some examples for proposed quantum simulators are trapped ions [37], superconducting circuits [38] and simulators based on photons [39]. More important for this thesis are simulators based on ultracold atoms [17, 40]. A rapidly growing branch of theory and experimental works is focused on the generation of artificial gauge potentials, allowing for the study of electrons in a lattice under the influence of a magnetic field [41], topological quantum matter [42] or even more elusive gauge theories [43, 44]. I will expand on this in Chapter 2.

Simulation is, however, not the only use of Floquet engineering. It also promises the generation of entirely new quantum phases of condensed matter, and the study of their properties. In this thesis I will present examples of both: simulation (Chapter 2) and the generation of an interesting quantum phase (Chapter 4 and 5).

This chapter is organized as follows: First a more formal mathematical introduction to Floquet theory is provided in Section 1.1. The treatment mostly cites results, and features more detailed derivations that help underline important concepts. Throughout the chapter formal theory will be supplemented with examples to illustrate its practical uses.

This is followed (Section 1.2) by an application of Floquet theory to time periodic quantum systems. This application builds a bridge between its formal introduction and the more specialized manifestation in quantum mechanics, providing a connection between concepts relevant to both classical and quantum mechanical systems. For example, the monodromy matrix, an important quantity introduced in classical systems, will be shown to be equivalent to the time evolution operator after one period of modulation in quantum mechanics. Additionally, an overview of the important concept of the effective Hamiltonian and its construction is given. Finally, Section 1.3 provides examples of Floquet engineering of various condensed matter Hamiltonians, and the chapter is concluded with some remarks on heating (section1.4).

1.1 Introduction to Floquet theory

In this section a general introduction to Floquet theory is given. Most of the results are presented without rigorous proofs. Those can be found in the excellent book on ordinary differential equations (ODE) by Gerald Teschl [45], whose treatment has been instrumental in constructing this section. As mentioned earlier, the Floquet theorem comes up in the analysis of linear first order differential equations with time-periodic coefficients. Quite generally this can be written as

$$\dot{\mathbf{y}} = A(t)\mathbf{y} \ , \quad A(t+T) = A(t) \ , \tag{1.2}$$

where $A(t)$ is the periodic (with period T) coefficient matrix of the system. Before stating the most general form of the Floquet theorem, it is useful to introduce the principal matrix

solution of a linear ODE. For each initial condition $\mathbf{y}(t_0) = \mathbf{y}_0$ the general solution of Eq. (1.2) can be expanded according to

$$\mathbf{y}(t) = \sum_{n=1}^{N} \mathbf{u}_n(t, t_0) y_{0,n} \tag{1.3}$$

where the $y_{0,n}$ are the components of $\mathbf{y}_0$. The $\mathbf{u}_n(t, t_0)$ are the solutions of (1.2) with the associated initial conditions $\mathbf{y}_0^n = \mathbf{e}_n = (0, \cdots, 1_n, \cdots, 0)$, i.e. the canonical base vectors. One can thus define the matrix $U(t, t_0) \equiv \{\mathbf{u}_1(t, t_0), \mathbf{u}_2(t, t_0), \cdots, \mathbf{u}_N(t, t_0)\}$ whose columns are made of the $\mathbf{u}_n(t, t_0)$. The matrix $U(t, t_0)$ is called the principal matrix solution. It solves the matrix valued equivalent of Eq. (1.2)

$$\dot{U}(t, t_0) = A(t)U(t, t_0) \tag{1.4}$$

with the initial value $U(t_0, t_0) = \mathbb{1}$. An important property of the principal matrix solution is

$$U(t, t_1)U(t_1, t_0) = U(t, t_0) \ , \quad U(t_1, t_0)U(t_0, t_1) = \mathbb{1} \tag{1.5}$$

The Floquet theorem [46] can now be stated as follows: A principal matrix solution to Eq. (1.4) must have the form

$$U(t, t_0) = P(t, t_0)e^{Q_0(t-t_0)} \ , \tag{1.6}$$

with

$$P(t + T, t_0) = P(t, t_0) \ , \quad P(t_0, t_0) = \mathbb{1} \ . \tag{1.7}$$

where $Q_0 = Q(t_0)$ is a constant matrix and $P(t, t_0)$ is a time periodic matrix with the same period as $A(t)$. Moreover, it can be shown that $U(t + T, t_0 + T) = U(t, t_0)$. The Floquet theorem is essentially the analog of Bloch's theorem [47] for time periodic systems. A proof of Floquet's theorem can be found in Ref. [45]. In more mathematical contexts, the eigenvalues λ_n of Q_0 are called characteristic exponents and the eigenvalues γ_n of $M(t_0) = \exp(Q_0 T)$ are called Floquet (or characteristic) multipliers. Later in section 1.2 the eigenvalues λ_n are identified as quasienergies of a time-dependent Hamiltonian. The reason for this will become clear when when quantum mechanical systems are addressed. An important and very useful quantity is the monodromy matrix

$$M(t_0) \equiv U(t_0 + T, t_0) = e^{Q_0 T} \tag{1.8}$$

which is the principal matrix solution evaluated after one period. One of its many useful features is the independence of its eigenvalues γ_n of the initial time t_0. This is because $M(t_0')$ and $M(t_0)$ are similar matrices:

$$\begin{aligned} M(t_0') &= U(t_0' + T, t_0)U(t_0, t_0') \\ &= U(t_0' + T, t_0 + T)U(t_0 + T, t_0)U(t_0, t_0') \\ &= U(t_0, t_0')^{-1} M(t_0) U(t_0, t_0') \end{aligned} \tag{1.9}$$

Another intuitive argument for its importance is that it generates the stroboscopic evolution of the system:

$$U(t + nT, t_0) = P(t, t_0)e^{Q_0(nT+t-t_0)} = U(t, t_0)M(t_0)^n \ . \tag{1.10}$$

If there were any cases when $Re(\lambda_n) > 0$ ($|\gamma_n| > 1$) then $M(t_0)^n$ would cause exponential growth (for finite systems $P(t, t_0)$ is bounded) and hence system Eq. (1.4) would be unstable. Quite generally, the stability of the system can be inferred from the monodromy matrix.

As an example, the stability of the Meissner equation is analyzed

$$\ddot{y} + \{\alpha + \delta\,\mathrm{sgn}[\cos(\omega \mathrm{t})]\}\mathrm{y} = 0\ , \tag{1.11}$$

where sgn is the sign function and $y(t) \in \mathbb{R}$. The Meissner equation - a special case of Hill's equation (1.1) - has the advantage of being amenable to explicit integration. Thus it is possible to calculate the monodromy matrix and infer the regions of stability of Meissner's equation (1.11). If $\delta < \alpha$ one can interpret (1.11) as a harmonic oscillator with a spring that periodically and abruptly changes its stiffness with frequency ω. One can use the standard trick $\dot{y} = v$ to write (1.11) as

$$\begin{pmatrix} \dot{y} \\ \dot{v} \end{pmatrix} = \begin{pmatrix} 0 & 1 \\ -\alpha - \delta\,\mathrm{sgn}[\cos(\omega \mathrm{t})] & 0 \end{pmatrix} \begin{pmatrix} y \\ v \end{pmatrix}\ . \tag{1.12}$$

A general solution to (1.12) in the first half of the period is

$$\begin{pmatrix} y \\ v \end{pmatrix} = V_-(t) \begin{pmatrix} a_- \\ b_- \end{pmatrix}\ , \quad 0 \le t < T/2 \tag{1.13}$$

and in the second half

$$\begin{pmatrix} y \\ v \end{pmatrix} = V_+(t - T/2) \begin{pmatrix} a_+ \\ b_+ \end{pmatrix}\ , \quad T/2 \le t < T \tag{1.14}$$

where

$$V_\pm = \begin{pmatrix} e^{\sqrt{\mu^\pm} t} & e^{-\sqrt{\mu^\pm} t} \\ \sqrt{\mu^\pm} e^{\sqrt{\mu^\pm} t} & -\sqrt{\mu^\pm} e^{\sqrt{\mu^\pm} t} \end{pmatrix} \tag{1.15}$$

and $\mu^\pm = -\alpha \pm \delta$. Since the eigenvalues of the monodromy matrix are independent of the initial value [Eq. (1.9)] one can set $t_0 = 0$. Following the definition of $U(T, 0)$ the time evolution of the two initial values is calculated

$$(y_0, v_0) = (1, 0) \quad \text{and} \quad (y_0, v_0) = (0, 1) \tag{1.16}$$

over one period. I will only show the steps of the calculation for the first initial value. For $(y_0, v_0) = (1, 0)$ and $a_- = b_- = 1/2$, which means that

$$\begin{pmatrix} y \\ v \end{pmatrix} = \begin{pmatrix} \mathrm{ch}(\sqrt{\mu^-} t) \\ \sqrt{\mu^-}\mathrm{sh}(\sqrt{\mu^-} t) \end{pmatrix}\ , \tag{1.17}$$

where ch = cosh and sh = sinh. Since (y, v) is continuous at $t = T/2$ the two solutions (1.17) and (1.14) connect at $t = T/2$:

$$\begin{pmatrix} \mathrm{ch}(\sqrt{\mu^-} T/2) \\ \sqrt{\mu^-}\mathrm{sh}(\sqrt{\mu^-} T/2) \end{pmatrix} = V_+(0) \begin{pmatrix} a_+ \\ b_+ \end{pmatrix}\ . \tag{1.18}$$

Because this fixes a_+ and b_+, the only thing left in the calculation is to evaluate (1.14) at $t = T$. For the first initial value $y(T)$ and $v(T)$ are

$$\begin{pmatrix} y(T) \\ v(T) \end{pmatrix} = V_+(T/2)V_+(0)^{-1} \begin{pmatrix} \mathrm{ch}(\sqrt{\mu^-}T/2) \\ \sqrt{\mu^-}\mathrm{sh}(\sqrt{\mu^-}T/2) \end{pmatrix} \tag{1.19}$$

This is the first column of $U(T, 0)$. The second column can be computed in exactly the same way starting with $a_- = -b_- = \sqrt{\mu^-}/2$. The monodromy matrix becomes

$$U(T,0) = \begin{pmatrix} \mathrm{ch}(\Gamma^-)\mathrm{ch}(\Gamma^+) + \frac{\sqrt{\mu^-}}{\sqrt{\mu^+}}\mathrm{sh}(\Gamma^-)\mathrm{sh}(\Gamma^+) & \frac{\mathrm{ch}(\Gamma^+)\mathrm{sh}(\Gamma^-)}{\sqrt{\mu^-}} + \frac{\mathrm{ch}(\Gamma^-)\mathrm{sh}(\Gamma^+)}{\sqrt{\mu^+}} \\ \sqrt{\mu^-}\mathrm{ch}(\Gamma^+)\mathrm{sh}(\Gamma^-) + \sqrt{\mu^+}\mathrm{ch}(\Gamma^-)\mathrm{sh}(\Gamma^+) & \mathrm{ch}(\Gamma^-)\mathrm{ch}(\Gamma^+) + \frac{\sqrt{\mu^+}}{\sqrt{\mu^-}}\mathrm{sh}(\Gamma^-)\mathrm{sh}(\Gamma^+) \end{pmatrix}$$

where $\Gamma^\pm = T\sqrt{\mu^\pm}/2$. The equation determining the eigenvalues and hence the stability of the system is

$$0 = 1 + \lambda^2 - 2\lambda\,\mathrm{ch}\left(\Gamma^-\right)\mathrm{ch}\left(\Gamma^+\right) - \lambda\,\mathrm{sh}\left(\Gamma^-\right)\mathrm{sh}\left(\Gamma^+\right)\frac{(\mu^- + \mu^+)}{\sqrt{\mu^-\mu^+}}\,. \tag{1.20}$$

Using the above expression one can determine the regions of stability of the Meissner equation. They are mapped out in Fig. 1.1 for a range of δ and T. The light orange areas indicate stability, which means that both eigenvalues of the monodromy matrix, i.e. solutions to (1.20), are smaller or equal to one.

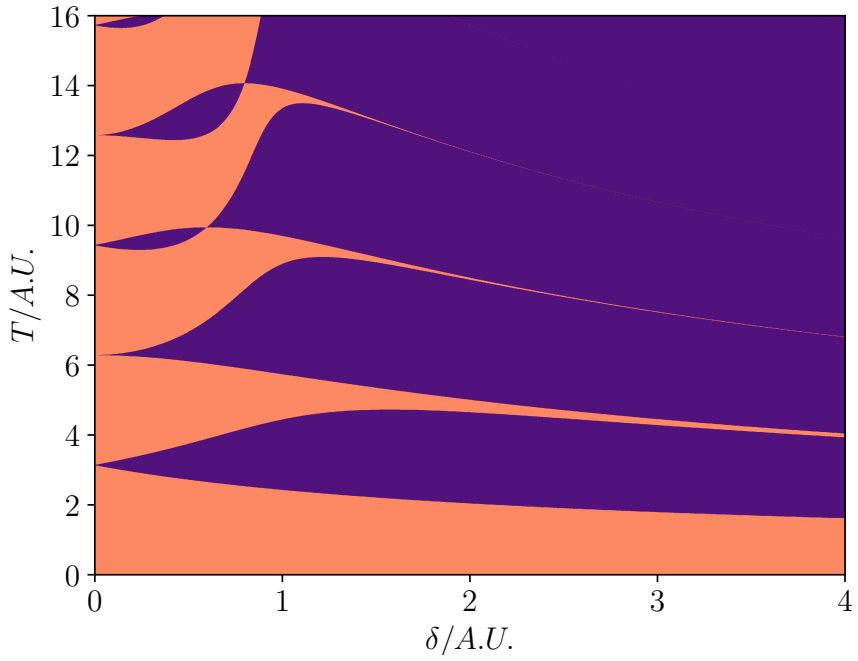

Figure 1.1: Regions of stability of the Meissner equation for $\mu_\pm = 1 \pm \delta$ and period T. The solutions are stable(unstable) in the light orange(dark violet) regions.

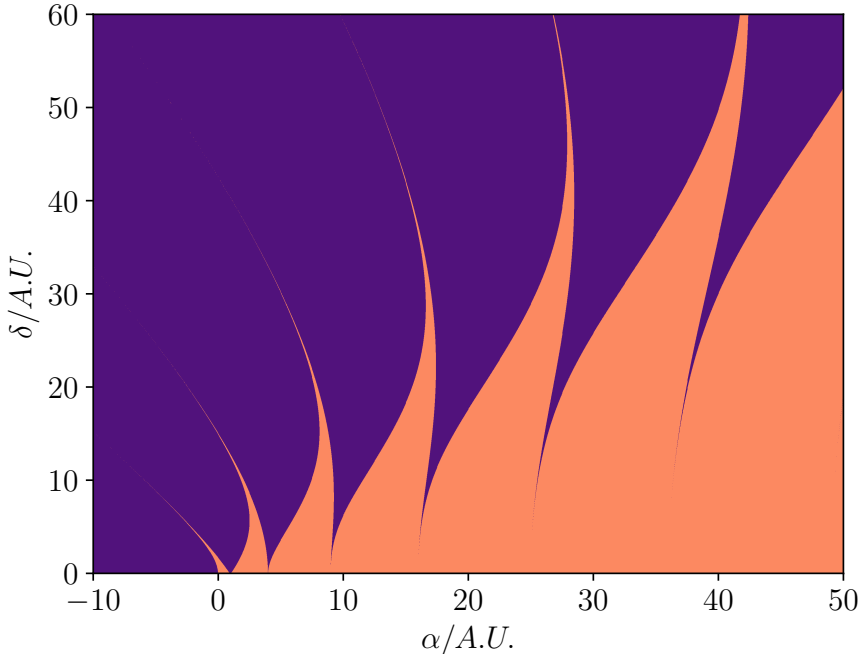

Figure 1.2: Regions of stability for the Mathieu equation for different values of α and δ ($\omega = 2$). The solutions are stable in the light orange and unstable in the dark violet regions.

Another very interesting example is a close relative of the Meissner equation and another special case of Hill's equation (1.1), the Mathieu equation [48]:

$$\ddot{y} + [\alpha + \delta \cos(\omega t)]y = 0 \ . \tag{1.21}$$

Unlike Meissner's equation (1.11), it cannot be explicitly integrated. Studying it with the help of numerical integration is of course always an option. As with the Meissner equation it is possible to map the regions of stability by calculating the eigenvalues of the monodromy matrix. As calculated above, the columns of the monodromy matrix are made up from the time evolution of the two initial values (1.16) over one period. This calculation was performed with a Fortran implementation of the Runge-Kutta-Fehlberg method (RKF45), which is described in Ref. [49]. The resulting stability diagram is shown in Fig. 1.2. The Mathieu equation has many applications in physics [50]. A couple of notable examples are: describing the inverted vertically vibrated pendulum [51, 52] for small angle oscillations, and describing the focusing of electrons in a quadrupole potential that is modulated in the radio frequency regime [53]. Most notably, the Mathieu equation describes the motion of a charge in a Paul trap [54], an achievement for whose experimental realization Wolfgang Paul was awarded the Nobel prize in 1989. In all of these systems certain driving parameters of the time periodic perturbation lead to some manifestation of stability or instability. In the case of the inverted pendulum, stability means that it remains upright. Stability for the radio frequency modulated quadrupole manifests itself as a focusing of the electron beam, whereas an instability can be used for acceleration. In the Paul trap, stability means that the charge does not escape, hence the name "trap".

The application of Floquet theory goes, of course, beyond that of stability considerations and this will be thoroughly explored in the following sections. The application of Floquet in quantum mechanics will now be addressed and, more specifically, the way it is used in the steadily growing field of Floquet engineering of ultra cold atoms.

1.2 Floquet theory in quantum mechanics

In quantum mechanics the time evolution of a state $|\Psi\rangle$ of a system is determined by the Schrödinger equation

$$\mathrm{i}\partial_t|\Psi(t)\rangle = H(t)|\Psi(t)\rangle \tag{1.22}$$

where Hamiltonian $H(t)$ is a time-dependent Hermitian operator (setting $\hbar = 1$). The following focuses on the subset of time periodic Hamiltonians where

$$H(t+T) = H(t)\ . \tag{1.23}$$

Since the Schrödinger equation is linear, it is immediately clear that it is of the same form as Eq. (1.2). Because it is of the same type, it connects to the more formal treatment in the previous section with many well established concepts in quantum mechanics. It is self evident that the time evolution operator

$$U(t,t_0) = \mathcal{T}\exp\left(-\mathrm{i}\int_{t_0}^{t}\mathrm{d}\tau H(\tau)\right)\ , \tag{1.24}$$

is the principal matrix solution of (1.22). $\mathcal{T}$ is the time-ordering operator. As its name suggests, the time evolution operator propagates a state from an initial time t_0 to some time t:

$$|\Psi(t)\rangle = U(t,t_0)|\Psi(t_0)\rangle\ . \tag{1.25}$$

The inverse of the time evolution operator is given by its Hermitian adjoint $U(t,t_0)^{-1} = U(t,t_0)^\dagger$. Applying Floquet's theorem (1.6) to (1.24) leads to

$$U(t,t_0) = \ P(t,t_0)e^{-\mathrm{i}H_\mathrm{F}(t-t_0)}, \tag{1.26}$$

where $P(t,t_0)$ is a periodic operator with period T. The general Floquet Hamiltonian is abbreviated as H_F. Identifying $Q_0 = -\mathrm{i}H_\mathrm{F}$ is justified because $U(t_0+T,t_0)$ is unitary. Additionally, it means that H_F can be assumed to be Hermitian. This in turn implies

$$P(t,t_0)P(t,t_0)^\dagger = \mathbb{1}\ . \tag{1.27}$$

The question of whether the exponential representation in Eq. (1.26) always exists in infinite dimensional Hilbert spaces [55, 56] is not entirely trivial. However, these subtleties are beyond the scope of this introduction and it will be assumed that $\log[U(t_0+T,t_0)]$, i.e. the logarithm of the monodromy, is defined. Since it will be important in the next section, it helps to point out that just as Q_0 depends on the initial time, so does H_F. As stated above, one can now relate the eigenvalues (characteristic exponents) of Q_0 with those of H_F. One can identify $\lambda_n = -i\epsilon_n$. The ϵ_n are commonly referred to as quasienergies. This term is analogous to the term quasimomentum appearing in Bloch's theorem. As

with the quasimomentum, the quasienergies are not uniquely defined. An easy way to see this is by examining the monodromy $\exp(-\mathrm{i}H_\mathrm{F}T)$. A shift in any of the eigenvalues of H_F by $\epsilon_n \to \epsilon_n + l\omega$, where $\omega = 2\pi/T$ and l is some whole number, would leave the monodromy invariant. In order for the logarithm of the monodromy to be single valued, i.e. H_F, the branch of the logarithm must be specified or, to put it in more physical terms, a Brillouin zone must be defined. The first Brillouin zone has width ω. For the time evolution operator (1.26) such a shift in the quasienergies can always be absorbed by $P(t, t')$, leaving the general properties of (1.26) unchanged.

For completeness' sake, Eq. (1.26) is connected to an equivalent formulation that is often used in the literature. Instead of specifying the form of the time evolution operator (1.26) the states are said to have a specific form. From Eq. (1.26) and the existence of a gauge transformation to a frame where the system's Hamiltonian is H_F (the Floquet frame - discussed in the next section), it follows that there exist solutions to the Schrödinger equation Eq. (1.22) that can be indexed by the quantum number n, and which have the form

$$|\Psi_n(t)\rangle = |u_n(t)\rangle e^{-\mathrm{i}\epsilon_n t} \ , \tag{1.28}$$

where the so-called Floquet modes $|u_n(t+T)\rangle = |u_n(t)\rangle$ are time periodic and the ϵ_n are the aforementioned quasienergies. The Floquet modes are eigenstates of the Hamiltonian

$$\mathcal{H}(t) = H(t) - \mathrm{i}\partial_t \ , \tag{1.29}$$

with the corresponding energies ϵ_n.

1.2.1 Effective and Floquet Hamiltonian

For a realistic experimental proposal of a Floquet system, the question of whether the specific starting point of a periodic manipulation has measurable consequences is very relevant. Theoretically this can either be addressed by demanding that the starting point of the protocol appeared in some infinite past $t_0 \to -\infty$ or at some specific point in time, e.g. $t_0 = 0$. In the first scenario the description of the system should be independent of the initial time, in the second it does have real physical significance. The second approach is more adjusted towards the realities of an experimenter, who commonly has to switch on his or her experiment at some moment in time. Take, for example, the following classical Floquet systems: a ball that is kicked left and right periodically. Even for this simple system, the initial kick has a significant effect on its trajectory (see e.g [57]). Another important issues is that T is often the shortest time scale in a given Floquet problem. This means that it can be very challenging to account for the initial time dependence of H_F in an actual experiment. It is therefore highly desirable to have a systematic way to account for the initial time, as well as the short and long term dynamics. Separating the short and long time dynamics will be one of the goals of the next two sections. The idea is to separate the time evolution into a part that is governed by a time-independent effective Hamiltonian sandwiched between two operators that account for the short term dynamics - sometimes referred to as the micromotion. The time-independent effective Hamiltonian will be the most important object in this and the following chapters.

In order to set the stage for the construction of said operators, some important precursory concepts related to gauge transformations will be reviewed. Some useful overviews on this topic can be found in Refs. [36, 57–59]. Here the work of [57, 58] and [59] is used.

The time-dependent effective Hamiltonian is constructed through an operator expansion in orders of $1/\omega$. The next paragraphs will begin with some remarks on the consequences of a key assumption necessary for this expansion: The existence of a gauge transformation $R(t) = \exp[iK(t)]$ that will lead to a frame in which the Hamiltonian no longer depends on time. A gauge transformation will change states according to

$$|\Psi'(t)\rangle = R(t)|\Psi(t)\rangle \ , \tag{1.30}$$

A change of gauge should have no effect on the outcome of measurements, which implies that $R(t)$ is unitary. In the following it is required that $K(t)$ is Hermitian, which is reasonable, given the unitarity of $R(t)$. For the time evolution operator one finds

$$U'(t, t_i) = R(t)U(t, t_i)R(t_i)^\dagger \ . \tag{1.31}$$

The initial time t_i is chosen, which can in general be different from t_0, which is kept as the time that fixes H_F. With the help of Schrödinger's equation (1.22) and either of the previous two equations, one can derive the Hamiltonian in the transformed frame

$$H'(t) = \mathrm{i}\dot{R}(t)R(t)^\dagger + R(t)H(t)R(t)^\dagger \ . \tag{1.32}$$

$R(t)$ is now fixed so that the $H'(t) = H_\mathrm{eff}$ is completely independent of time. In this work H_eff is called the effective Hamiltonian and it will be this Hamiltonian for which the expansion in $1/\omega$ is constructed. If ω is the largest energy in the system, $1/\omega$ is a good candidate for a small parameter for which this expansion will converge.

In the next few paragraphs the connection between the Floquet representation [Eq. (1.26)] and the effective Hamiltonian is made explicit. In the frame of H_eff the time evolution operator is simply $U'(t, t_i) = \exp[-\mathrm{i}H_\mathrm{eff}(t - t_i)]$. By inverting (1.31) one finds that

$$U(t, t_i) = R(t)^\dagger e^{-\mathrm{i}H_\mathrm{eff}(t-t_i)}R(t_i) \ . \tag{1.33}$$

In order to compare this with (1.26) (as in Ref. [59]) one has to reformulate the time evolution operator in (1.26) slightly

$$U(t, t_i) = U(t, t_0)U(t_i, t_0)^\dagger \tag{1.34}$$

$$= P(t, t_0)e^{-\mathrm{i}H_\mathrm{F}(t-t_i)}P(t_i, t_0)^\dagger \ . \tag{1.35}$$

This accommodates the initial time t_i and H_F, which depends t_0. The above equation adds a bit more meaning to $P(t, t_0)$ since it has the same form as (1.31). One can, together with (1.27), interpret $P(t, t_0)$ as a gauge transformation. Following Ref. [59] it is called the Floquet gauge. In the Floquet frame the time evolution is given by H_F. Since the choice of t_0 is arbitrary, it is clear that there are many gauge equivalent frames, i.e. t_0 spans a family of gauges. Having established that $P(t, t_0)$ represents a gauge transformation, one can simply compose the Floquet gauge with $R(t)$

$$\tilde{R}(t) = R(t)P(t, t_0) \tag{1.36}$$

to establish the connection between H_eff and H_F

$$H_\mathrm{eff} = \mathrm{i}\dot{\tilde{R}}(t)\tilde{R}(t)^\dagger + \tilde{R}(t)H_\mathrm{F}\tilde{R}(t)^\dagger \ . \tag{1.37}$$

Alternatively one can take $\partial_t U(t,t_i)$ in Eq. (1.33) and (1.35) and compare the results. Eq. (1.37) implies that there is a gauge transformation of $H_{\rm F}$, removing the dependence on t_0, that is, $H_{\rm eff}$ is assumed to be completely time-independent. With this, a subtlety comes to light: There are two different notions of gauge: The Floquet gauge and the gauge associated with $R(t)$. As intended, $R(t)$ removes the unwanted time dependence of $H_{\rm F}$ on the initial time. It also shows that in general $H_{\rm F}$ and $H_{\rm eff}$ are not the same and should not be mistaken for each other.

A very illustrative example of this was given in Refs. [58, 59]. They consider a two level system in a rotating magnetic field.

$$H(t) = B_z\sigma_z + B_\parallel[\sigma_x\cos(\omega t) + \sigma_y\sin(\omega t)] \ , \tag{1.38}$$

where the σ_i are the Pauli matrices. The transformation

$$P(t,t_0) = e^{-\mathrm{i}(\omega+\sigma_z\omega)(t-t_0)/2} \tag{1.39}$$

defines a Floquet gauge. It has all the properties required of $P(t,t_0)$, i.e. it is periodic in $P(t+T,t_0) = P(t,t_0)$ and $P(t_0,t_0) = \mathbb{1}$. The Floquet Hamiltonian [Eq. (1.32)] in this gauge is

$$H_{\rm F} = \frac{\omega}{2} + (B_z - \frac{\omega}{2})\sigma_z + B_\parallel[\cos(\omega t_0)\sigma_x + \sin(\omega t_0)\sigma_y]. \tag{1.40}$$

Removing the dependence on the initial time can be done with the transformation

$$R'(t_0) = e^{-\mathrm{i}\lambda[-\sin(\omega t_0)\sigma_x + \cos(\omega t_0)\sigma_y]} \tag{1.41}$$

One can calculate λ for which $R'(t_0)$ removes the dependence on t_0 by using the well-known properties of the Pauli matrices

$$[\sigma_i,\sigma_j] = 2\mathrm{i}\epsilon_{ijk}\sigma_k \ , \tag{1.42}$$

$$\sigma_i\sigma_j = \delta_{i,j} + i\epsilon_{ijk}\sigma_k \tag{1.43}$$

and

$$e^{\mathrm{i}\lambda\mathbf{n}\boldsymbol{\sigma}} = \cos(\lambda) + \mathrm{i}\mathbf{n}\boldsymbol{\sigma}\sin(\lambda) \tag{1.44}$$

where $\mathbf{n}$ is a three component vector with unit length and $\boldsymbol{\sigma} = (\sigma_x,\sigma_y,\sigma_z)$. For

$$\tan(2\lambda) = \frac{\omega/2 - B_z}{B_\parallel} \tag{1.45}$$

the transformed Hamiltonian becomes:

$$H'_{\rm eff} = \frac{\omega}{2} + \sigma_z\epsilon \ , \tag{1.46}$$

where

$$\epsilon = \sqrt{(\omega/2 - B_z)^2 + B_\parallel^2} \ . \tag{1.47}$$

The effective Hamiltonian is now manifestly independent of the initial time. Incidentally ϵ is one of the two quasienergies $\pm\epsilon$ of $H_{\rm F}$. This is not quite the effective Hamiltonian to be reviewed in the next section because it is clearly divergent in the limit $\omega\to\infty$. This

inconvenience is easily compensated for by an additional gauge transformation, which removes $\omega/2$ and eliminates the pathological behavior at $\omega \to \infty$,

$$R''(t) = e^{\mathrm{i}[\omega/2+(2\epsilon-\omega/2)\sigma_z]t} \ . \tag{1.48}$$

The final Hamiltonian thus is

$$H_{\text{eff}} = (\omega/2 - \epsilon)\sigma_z \ . \tag{1.49}$$

In the limit of $\omega \to \infty$, $\epsilon \to \omega/2$, which means that the above H_{eff} is does not diverge for large ω. The composition of all the transformations that lead up to this result is

$$R(t) = R''(t)R'(t_0)P(t,t_0) \ . \tag{1.50}$$

This example is one of the few cases where the exact Floquet and effective Hamiltonians can be derived. In the above, most of the important concepts needed to construct the expansion of H_{eff} were presented. The difference between the general Floquet Hamiltonian H_{F} and how they relate to each other were also detailed. Another difference that was not mentioned in the previous treatment is that H_{eff} does not necessarily generate the stroboscopic time evolution of the system. This is only always true for H_{F}.

1.2.2 Construction of the effective Hamiltonian

Now the construction of the effective Hamiltonian and the two operators that drive the short time dynamics is reviewed. Again the formalism in Ref. [57] is used. The time periodic Hamiltonian is defined as

$$H(t) = H_0 + V(t) \ , \tag{1.51}$$

where

$$V(t) = \sum_{j=1}^{\infty} V^{(j)} e^{\mathrm{i}j\omega t} + V^{(-j)} e^{-\mathrm{i}j\omega t} \tag{1.52}$$

The construction of the effective Hamiltonian relies on three assumptions: (i) The time evolution operator between an initial time t_i and a final time t_e has the form

$$U(t_e, t_i) = e^{-\mathrm{i}K(t_e)} e^{-\mathrm{i}H_{\text{eff}}(t_f - t_i)} e^{\mathrm{i}K(t_i)} \ . \tag{1.53}$$

In the following the naming convention in Ref. [57] of calling $K(t)$ the "kick" operator is maintained. When comparing it with Eq. (1.33) $R(t) = \exp[\mathrm{i}K(t)]$ is straightforward to identify. (ii) Furthermore it is imposed that the kick operator is periodic $K(t+T) = K(t)$ and (iii) has zero average over one period. The naming stems from interpreting the time evolution of Eq. (1.53) as a three step process: An initial kick with $K(t_i)$ is followed by the constant evolution with H_{eff} and a final kick with $K(t_f)$. As pointed out in the previous part, the effective Hamiltonian is assumed to be completely independent of t_i and t_f. One can now construct H_{eff} and $K(t)$ perturbatively. To that end both H_{eff} and $K(t)$ are expanded in orders of $1/\omega$.

$$H_{\text{eff}} = \sum_{n=0}^{\infty} \frac{1}{\omega^n} H_{\text{eff}}^{(n)} \tag{1.54}$$

and

$$K(t) = \sum_{n=1} \frac{1}{\omega^n} K^{(n)}(t) \ . \tag{1.55}$$

One then uses Eq. (1.32)

$$H_{\text{eff}} = e^{\mathrm{i}K(t)} H(t) e^{\mathrm{i}K(t)} + \mathrm{i}\left(\partial_t e^{\mathrm{i}K(t)}\right) e^{-\mathrm{i}K(t)} \tag{1.56}$$

In combination with the Baker-Campbell-Hausdorff series expansion of

$$e^{\mathrm{i}K} H e^{-\mathrm{i}K} = H + \mathrm{i}[K,H] - \frac{1}{2}[K,[K,H]] - \frac{i}{6}[K,[K,[K,H]]] + (\cdots) \ . \tag{1.57}$$

and

$$\left(\partial_t e^{\mathrm{i}K}\right) e^{-\mathrm{i}K} = \mathrm{i}\partial_t K - \frac{1}{2}\left[K, \partial_t K\right] - \frac{\mathrm{i}}{6}[K,[K,\partial_t K]] + (\cdots) \tag{1.58}$$

H_{eff} can be contructed to any desired order. For the sake of brevity the t dependence in the last two equations was dropped.

The calculation of the first order is briefly explained. Since it was assumed that the average over one period of $K^{(1)}(t)$ vanishes, its Fourier expansion can be written as

$$K^{(1)} = \sum_{j=1}^{\infty} K_j^{(1)} e^{\mathrm{i}\omega j t} + K_{-j}^{(1)} e^{-\mathrm{i}\omega j t} \ , \tag{1.59}$$

Inserting this into (1.56) together with (1.51), (1.57) and (1.58) gives in zeroth order in $1/\omega$

$$H_{\text{eff}}{}^{(0)} = H_0 + V(t) - \partial_t K^{(1)}(t) \ . \tag{1.60}$$

The second term in H_{eff} has to be time-independent to all orders, so it has to vanish:

$$K^{(1)} = \sum_{j=1}^{\infty} \frac{1}{\mathrm{i}j} \left(V^{(j)} e^{\mathrm{i}\omega j t} - V^{(-j)} e^{-\mathrm{i}\omega j t}\right) \ . \tag{1.61}$$

In conjunction with the second term in (1.58) one finds

$$H_{\text{eff}}^{(1)} = \sum_{j=1}^{\infty} \frac{1}{j} \left[V^{(j)}, V^{(-j)}\right] \ . \tag{1.62}$$

One can iterate this procedure to calculate H_{eff} up to arbitrarily high orders. To second order one finds [57]:

$$\begin{aligned} H_{\text{eff}} =& H_0 + \frac{1}{\omega} \sum_{j=1}^{\infty} \frac{1}{j} \left[V^{(j)}, V^{(-j)}\right] + \frac{1}{2\omega^2} \sum_{j=1}^{\infty} \frac{1}{j^2} \left(\left[\left[V^{(j)}, H_0\right], V^{(-j)}\right] + \text{H.c.}\right) \\ & \frac{1}{3\omega^2} \sum_{j,l=1}^{\infty} \frac{1}{jl} \left(\left[\left[V^{(j)}, V^{(l)}\right], V^{(-j-l)}\right] - \left[V^{(j)}, \left[V^{(-l)}, V^{(l-j)}\right]\right]\right) + \mathcal{O}(1/\omega^3) \end{aligned} \tag{1.63}$$

and the kick operator

$$\begin{aligned} K(t) = \frac{1}{\mathrm{i}\omega}\sum_{j=1}^{\infty}\frac{1}{j}\left(V^{(j)}e^{\mathrm{i}\omega jt} - V^{(-j)}e^{-\mathrm{i}\omega jt}\right) \\ +\frac{1}{\mathrm{i}\omega^2}\sum_{j=1}^{\infty}\frac{1}{j^2}\left([V^{(j)},H_0]e^{\mathrm{i}\omega jt} - \mathrm{H.c.}\right) \\ +\frac{1}{2\mathrm{i}\omega^2}\sum_{j,l=1}^{\infty}\frac{1}{j(j+l)}\left([V^{(j)},V^{(l)}]e^{\mathrm{i}(j+l)\omega t} - \mathrm{H.c.}\right) \\ +\frac{1}{2\mathrm{i}\omega^2}\sum_{j,l=1}^{\infty}\frac{1}{j(j-l)}\left([V^{(j)},V^{(-l)}]e^{\mathrm{i}(j-l)\omega t} - \mathrm{H.c.}\right) + \mathcal{O}(1/\omega^3) \end{aligned} \tag{1.64}$$

The convergence of this expansion is not guaranteed. As noted in Ref. [57] its convergence can, in general, only be determined after it's been explicitly worked out, and has been checked for whether it accurately describes the system. This will be commented on more in Section 1.4.

At this point, it is important to recognize that H_{eff} and H_F have the same quasienergy spectrum. This can be shown by computing the quasienergies through the time evolution operator after one period of the driving. Since $P(t,t_0)$ and $R(t)$ are both unitary and periodic, with the period T, $U'(T,0) = \exp(-\mathrm{i}H_{\text{eff}}T)$ and $U(T,0) = \exp(-\mathrm{i}H_{\text{F}}T)$, they must be similar matrices by construction ($U' = \tilde{R}^\dagger U\tilde{R}$). This in turn means that they have the same spectrum and hence produce the same quasienergies. The ambiguity in the quasienergies due to freedom of choice with regard to the Brillouin zone remains of course.

As a first example for the above expansion I want to come back to the spin in the rotating magnetic field Eq. (1.38). The identification of

$$H_0 = B_z\sigma_z \tag{1.65}$$

and

$$V^{(1)} = \frac{B_\parallel}{2}\left(\sigma_x - \mathrm{i}\sigma_y\right)\ , \quad V^{(-1)} = \frac{B_\parallel}{2}\left(\sigma_x + \mathrm{i}\sigma_y\right)\ , \quad V^{(j\neq\pm1)} = 0 \tag{1.66}$$

is straightforward. Calculating H_{eff} with (1.63) up to the first order correction gives

$$H_{\text{eff}} = \left(B_z - \frac{B_\parallel^2}{\omega}\right)\sigma_z \tag{1.67}$$

When expanding ϵ in (1.49) in orders of $1/\omega$ one finds

$$\epsilon = \frac{\omega}{2}\sqrt{\left(1-\frac{2B_z}{\omega}\right)^2 + \frac{4B_\parallel^2}{\omega^2}} \tag{1.68}$$

$$\approx \frac{\omega}{2} - B_z + \frac{B_\parallel^2}{\omega}\ . \tag{1.69}$$

The effective Hamiltonian in Eq. (1.49) is thus consistent up to first order with the one above (1.67).

At this point another important and interesting example is introduced: A Bose-Hubbard model with a periodic variation of the on-site potential. Such a system was considered by the authors of Refs. [60–63] and produces coherent destruction of tunneling (CDT). This is somewhat related to the notion of dynamical localization, which was formed in Ref. [64], where they studied a charged particle moving under the influence of an electric field. The difference between dynamical localization and CDT is that, in the first case, the dynamics appear to be frozen stroboscopically, whereas for the latter, the dynamics freeze for large frequencies entirely.

In this thesis, the time periodic modification of the on-site potentials is referred to as potential driving. The driven Hamiltonian is

$$H(t) = H_0 + V(t) \tag{1.70}$$

$$= -J \sum_{x=0}^{L-1} \left(a_{x+1}^\dagger a_x + a_x^\dagger a_{x+1} \right) + K \cos(\omega t) \sum_{x=0}^{L-1} x n_x \ . \tag{1.71}$$

The $a_x^\dagger, a_x$ are the bosonic creation and annihilation operators on a lattice site x and $n_x = a_x^\dagger a_x$ is the number operator. L is the number of sites of the lattice. They fulfill the usual bosonic commutation relations $[a_x, a_y] = [a_x^\dagger, a_y^\dagger] = 0$ and $[a_x, a_y^\dagger] = \delta_{x,y}$. J is the hopping energy and $K\cos(\omega t)$ is the energy offset between two adjacent sites. The time-dependent term can be generated by going into the rest frame of a shaking lattice, where it is interpreted as an inertial force. For example, in a one dimensional lattice shaking was studied experimentally in Ref. [63, 65–69]. Shaking will be discussed in detail in Chapter 2.

There are two routes to calculating the effective Hamiltonian. To begin, the first and second order terms in the inverse frequency expansion (1.63) are calculated. Here the lattice spacing is set to $a = 1$. Again, the Fourier components of (1.71) are identified as

$$H_0 = -J \sum_{x=0}^{L-1} \left(a_{x+1}^\dagger a_x + \text{H.c.} \right) \tag{1.72}$$

$$V^{(1)} = V^{(-1)} = \frac{K}{2} \sum_{x=0}^{L-1} x n_x \tag{1.73}$$

$$V^{(j \neq \pm 1)} = 0 \tag{1.74}$$

The first order contribution to H_{eff} vanishes, since $V^{(1)}$ and $V^{(-1)}$ commute. This is a general feature of drives that are symmetric under time inversion. The last term in Eq. (1.63) does not contribute as well. This leaves us with the second term. After evaluating the relevant commutators one finds

$$H_{\text{eff}} = -\left(1 - \frac{K^2}{4\omega^2}\right) H_0 + \mathcal{O}(1/\omega^3). \tag{1.75}$$

If $K \ll \omega$ this is a good approximation of the exact effective Hamiltonian.

The second way to derive the effective Hamiltonian begins with a gauge transformation (see for example Ref. [57])

$$W(t) = e^{\mathrm{i}K/\omega \sin(\omega t) \sum_{x=0}^{L-1} x n_x} \ , \tag{1.76}$$

Using Eq. (1.32) it is evident, that the transformed Hamiltonian is

$$H'(t) = \mathrm{i}\dot{W}(t)W(t)^\dagger + W(t)H(t)W(t)^\dagger \ . \tag{1.77}$$

The inertial term will be canceled by

$$-V(t) = \mathrm{i}\dot{W}(t)W(t)^\dagger \ . \tag{1.78}$$

The remaining term $W(t)H(t)W(t)^\dagger$ can be worked out by considering

$$f(\lambda) = e^{\mathrm{i}\lambda\sum_{x=0}^{L-1} xn_x} a_{x+1}^\dagger a_x e^{-\mathrm{i}\lambda\sum_{x=0}^{L-1} xn_x} \ . \tag{1.79}$$

and its derivative with respect to λ. It turns out that

$$\begin{aligned} \partial_\lambda f(\lambda) &= \mathrm{i}e^{\mathrm{i}\lambda\sum_{x=0}^{L-1} xn_x} \sum_{x=0}^{L-1} [xn_x, a_{y+1}^\dagger a_y] e^{-\mathrm{i}\lambda\sum_{x=0}^{L-1} xn_x} \\ &= \mathrm{i}f(\lambda) \end{aligned} \tag{1.80}$$

so that with $f(0) = a_{x+1}^\dagger a_x$ one finds

$$f(\lambda) = a_{x+1}^\dagger a_x e^{\mathrm{i}\lambda} \ . \tag{1.81}$$

The transformed Hamiltonian thus becomes

$$H'(t) = -J\sum_{x=0}^{L-1} \left(a_{x+1}^\dagger a_x e^{\mathrm{i}K/\omega \sin(\omega t)} + \mathrm{H.c.} \right) \tag{1.82}$$

The Jacobi-Anger expansion,

$$e^{\mathrm{i}z\sin(\theta)} = \sum_{n=-\infty}^{\infty} \mathcal{J}_n(z) e^{\mathrm{i}n\theta} \ , \tag{1.83}$$

where $\mathcal{J}_n(z)$ is the n-th Bessel function of the first kind, can be used to expand

$$H'(t) = -J\sum_{x=0}^{L-1}\sum_{n=-\infty}^{\infty} \left(\mathcal{J}_n(K/\omega) a_{x+1}^\dagger a_x e^{\mathrm{i}n\omega t} + \mathrm{H.c.} \right) \tag{1.84}$$

One can now time average the above Hamiltonian over one period of the driving to get the zeroth order Fourrier component of $H'(t)$ in the moving frame:

$$H_{\mathrm{eff}}{}' = H_0' = \frac{1}{T}\int_0^T \mathrm{d}t H'(t) \tag{1.85}$$

$$= -J\mathcal{J}_0(K/\omega)\sum_{x=0}^{L-1} \left(a_{x+1}^\dagger a_x + \mathrm{H.c.} \right) \ . \tag{1.86}$$

When compared with Eq. (1.63) it becomes clear that it is the zeroth order contribution to the expansion. Before it is justified that $H_{\mathrm{eff}} = H_{\mathrm{eff}}'$, a quick observation with regard to (1.63) is made: In fact, for an infinite lattice,

$$\sum_{x=0}^{L-1} \to \sum_{x=-\infty}^{\infty} \ , \tag{1.87}$$

periodic boundary conditions $a_L = a_0$, or hard wall boundary conditions $a_{-1} = a_L = 0$, the commutators of the Fourier components of $H'(t)$ [Eq. (1.52)]

$$\begin{aligned} V'^{(j)} &= -J\mathcal{J}_j(K/\omega)\sum_{x=0}^{L-1} a_{x+1}^\dagger a_x \\ V'^{(-j)} &= -J\mathcal{J}_j(K/\omega)\sum_{x=0}^{L-1} a_x^\dagger a_{x+1} \end{aligned} \tag{1.88}$$

vanish $[H_0', V'^{(\pm j)}] = [V'^{(j)}, V'^{(-j)}] = 0$. This implies that all higher order terms in the expansion (1.63) must vanish and the effective Hamiltonian is exact. One can check that by expanding the Bessel function up to the second order where it is consistent with the expression (1.75).

Since $W(t)$ is just a gauge transformation one can compose the transformation

$$R(t) = R'(t)W(t) \ , \tag{1.89}$$

where $R'(t)$ transforms the system in the moving frame into the frame of the effective Hamiltonian of the moving frame. The time evolution operator becomes

$$U(t_e, t_i) = R(t)^\dagger e^{-\mathrm{i}H'_{\mathrm{eff}}(t_e - t_i)} R(t_i) \ . \tag{1.90}$$

This means that $R(t)$ indeed determines the kick operator $K(t)$ and that, as promised, $H'_{\mathrm{eff}} = H_{\mathrm{eff}}$. Using Eq. (1.64) yields in the moving frame

$$R'(t) = e^{-iK'(t)} \tag{1.91}$$

where

$$K'(t) = \frac{\mathrm{i}J}{\omega}\sum_{n=1}^{\infty}\mathcal{J}_n(K/\omega)\sum_{x=0}^{L-1}\left[a_{x+1}^\dagger a_x e^{\mathrm{i}\omega n t} - a_x^\dagger a_{x+1} e^{-\mathrm{i}\omega n t}\right] \tag{1.92}$$

Here the method used in this example must, once more, be highlighted: the very helpful trick of transforming the system into a moving frame with $W(t)$ in Eq. (1.76). It will be one of the main tools to derive effective Hamiltonians in this thesis. This trick allows for either a non-perturbative treatment, or results in a clever partial resummation of (1.63). The key is the commutator that appears in (1.80). In the next section this trick is used extensively. If the inverse frequency expansion were to be derived starting with (1.96) without the transformation into the moving frame, it must be ensured that for the lower order corrections $\omega < K$, so that the expansion is justified.

Another interesting feature of H_{eff} in Eq. (1.86) is related to the prefactor $\mathcal{J}_0(K/\omega)$, which modifies or renormalizes the tunneling amplitude J:

$$J_{\mathrm{eff}} = J\mathcal{J}_0(K/\omega) \tag{1.93}$$

For certain values of the driving parameters K and ω, the J_{eff} is zero (Fig. 1.3), which means that tunneling is completely inhibited. In the context of ultracold quantum gases in lattices, this effect is known as coherent destruction of tunneling [60–62, 70, 71]. Experimental realizations related to coherent destruction of tunneling can be found in Refs. [63, 65, 72].

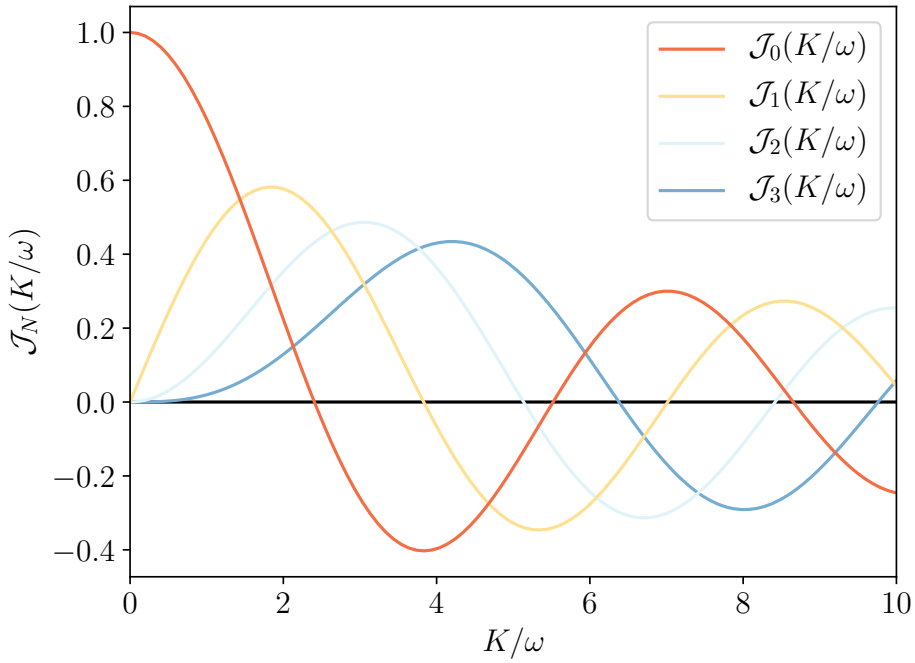

Figure 1.3: Shown are the first four Bessel functions of the first kind. The zeroth Bessel function renormalizes the hopping amplitude $J_{\text{eff}} = J\mathcal{J}_0(K/\omega)$ for the modulation in Eq. (1.71). The zeros of the Bessel mark the points where tunneling is inhibited, i.e. coherent destruction of tunneling. The higher order Bessel functions appear in the renormalization of the hopping for the driving in (1.101): $J_{\text{eff}} = (-1)^N J\mathcal{J}_N(K/\omega)$. The orders correspond to the condition $K_0 = N\omega$

1.3 Floquet engineering

In the previous section two examples of Hamiltonians with periodic variations were introduced. The derivation of the respective effective Hamiltonians primarily served as a way to familiarize the reader with various concepts such as the Floquet or effective Hamiltonian and the various gauge transformations. This part details how one can use periodic manipulations of quantum systems to engineer a specific behavior. The end goal is the generation of so called Peierls phases, which allow for the generation of artificial gauge fields [1]. Their origin is explained in detail in the next chapter, here it suffices to mention that Peierls phases $e^{\mathrm{i}\phi_{x,y}}$ accompany the hopping terms

$$H = \sum_{\langle x,y\rangle} \left(J_{xy} a_x^\dagger a_y e^{\mathrm{i}\phi_{x,y}} + \text{H.c.} \right) \ , \tag{1.94}$$

where J_{xy} is the hopping amplitude that connects the neighbors x, y in an arbitrary lattice.

To engineer these phases, modifications are introduced incrementally to the simple driven one dimensional Bose Hubbard model of the previous section. This allows for addressing each of the changes individually. Additionally, it retraces the chronology of theoretical and experimental advances concerning these types of drivings for ultracold atoms in optical lattices specifically.

The first modification is the introduction of interactions into Eq. (1.71).

$$H(t) = H_{\mathrm{T}} + H_{\mathrm{int}} + V(t) \tag{1.95}$$

$$= -J\sum_{x=0}^{L-1}\left(a_{x+1}^{\dagger}a_x + .\mathrm{H.c.}\right) + \frac{U}{2}\sum_{x=0}^{L-1} n_x(n_x-1) + K\cos(\omega t)\sum_{x=0}^{L-1} x n_x \ , \tag{1.96}$$

where U is the on-site interaction energy. Because $[H_{\mathrm{int}}, V(t)] = 0$ the gauge transformation (1.76) can be used to calculate the zeroth order contribution to the effective Hamiltonian by time averaging in the moving frame

$$H_{\mathrm{eff}}^{(0)} = \frac{1}{T}\int_0^T \mathrm{d}t H'(t) \tag{1.97}$$

$$= \mathcal{J}_0(K/\omega)H_{\mathrm{T}} + H_{\mathrm{int}} \ . \tag{1.98}$$

As shown in Fig. 1.3 there are values for which the tunneling is suppressed. This is what the authors of Refs. [70, 71] proposed. As mentioned earlier, the effects of this modulation were measured for example in the experiment reported in Ref. [65].

The result (1.98) is no longer non-perturbative. In the inverse frequency expansion (1.63) the Fourier components of $V'(t)$ [(1.88)] no longer commute with

$$H_0' = \mathcal{J}_0(K/\omega)H_{\mathrm{T}} + H_{\mathrm{int}} \ . \tag{1.99}$$

because the interactions in H_{int} are present. This means that the effective Hamiltonian in Eq. (1.98) is no longer exact and that H_{eff} only constitutes a partial resummation of the full inverse frequency expansion. The first correction to (1.98) due to the interactions is according to (1.63)

$$\begin{aligned} H_{\mathrm{eff}}^{(2)} = \frac{UJ^2}{2\omega^2}\sum_{j=1}^{\infty}\frac{1}{j^2}\mathcal{J}_j(K/\omega)^2 \\ \times\sum_{x=0}^{L-1}\big[-8n_x(n_x-1) + 16n_{x+1}n_x \\ - 4a_{x-1}^{\dagger}a_{x+1}^{\dagger}a_x a_x - 4a_x^{\dagger}a_x^{\dagger}a_{x+1}a_{x-1}\big] \ , \end{aligned} \tag{1.100}$$

where the first term second line is a renormalized addition to the interactions and the second term describes nearest neighbor interactions. The last line shows two correlated hopping processes: Two particles hopping from site x to the adjacent sites and vice versa.

$H_{\mathrm{eff}}^{(0)}$ remains a good approximation as long as the frequency of the driving sets the biggest energy scale $\omega > |\epsilon_{\max} - \epsilon_{\min}|$ where $\epsilon_{\max}$ and $\epsilon_{\min}$ are the biggest and smallest quasienergies respectively. The demand $\omega > J, U$ is slightly weaker. This doesn't eliminate the possibility of multiple particle hole excitations (many-body excitations in general) but it makes them unlikely and ensures that they contribute little in the inverse frequency expansion (1.63). A very detailed discussion of this was given in Ref. [73] and these processes will be commented on in greater detail in Section 1.4.

The last two Hamiltonians are already minimalist examples of Floquet engineering. They show how to use a periodic drive to attain a new time-dependent effective system.

The tunneling amplitude was modified by the driving, allowing for the localization of particles. It is well known that the Bose Hubbard model has a quasi quantum phase transition in one dimension ([74], more on that later). Depending on the filling and the ratio of U and J, the system is either a Mott insulator or it has the characteristics of a superfluid. The ability to tune the hopping amplitude in (1.98) allows the switch between the two. This is a remarkable interplay between theoretical prediction and experimental realization.

The next modification will help to produce Peierls phases. The first addition is a constant tilt in (1.71). Experimentally this can be achieved by tilting the lattice in a gravitational potential, or by a constant acceleration [75]

$$H(t) = -J\sum_{x=0}^{L-1}\left(a_{x+1}^{\dagger}a_x + \text{H.c.}\right) + [K_0 + K\cos(\omega t)]\sum_{x=0}^{L-1} x n_x \ . \tag{1.101}$$

The consequences of this type of driving were discussed in Ref. [76] and experimentally realized in Refs. [66, 77].

The effects of a constant tilt for an infinite chain (limits of the summation in (1.101) are $\pm\infty$) will be briefly reviewed in the following. For $\omega = 0$:

$$H_0 = -J\sum_{x=-\infty}^{\infty}\left(a_{x+1}^{\dagger}a_x + \text{H.c.}\right) + K_0\sum_{x=-\infty}^{\infty} x n_x \ . \tag{1.102}$$

It has been established that the Hamiltonian H_0 is diagonalizable [78] and resulting eigenstates are the so called Wannier-Stark states. The single-particle orbitals that diagonalize H_0 are

$$c_y^{\dagger} = \sum_{x=-\infty}^{\infty} \mathcal{J}_{y-x}(2J/K_0)a_x^{\dagger} \tag{1.103}$$

The completeness of the Bessel functions ([79], a special case of Neumann's addition theorem)

$$\sum_{x=-\infty}^{\infty} \mathcal{J}_{y+x}(\kappa)\mathcal{J}_{y'+x}(\kappa) = \delta_{y,y'} \tag{1.104}$$

guarantees that $[c_y, c_{y'}^{\dagger}] = \delta_{y,y'}$ and $[c_y, c_{y'}] = [c_y^{\dagger}, c_{y'}^{\dagger}] = 0$. In terms of the c_y the Hamiltonian H_0 becomes

$$H_0 = -\sum_{y=-\infty}^{\infty} \epsilon_y c_y^{\dagger}c_y \ , \tag{1.105}$$

where $\epsilon_y = yK_0$. The energy spectrum, customarily referred to as the Wannier Stark ladder, is composed of equally spaced energy levels, that are K_0 apart. For strongly tilted lattices $K_0 \gg J$ the Wannier-Stark states (1.103) are highly localized, which means that tunneling is inhibited. This is one of the reasons why it is difficult to observe the Bloch oscillations of an electron in a crystal [80]. The Hamiltonian that describes the electrons' motion is very similar to (1.102) where an externally applied electric field would correspond to the tilting term in (1.102). This leads to the following very non-intuitive prediction: A strong electric field localizes the electrons instead of exciting Bloch oscillations.

To continue with the time-dependent problem, one can transform $H(t)$ again with a variant of (1.76):

$$W(t) = e^{\mathrm{i}[K_0 t + K/\omega \sin(\omega t)] \sum_{x=0}^{L-1} x n_x} \ , \tag{1.106}$$

which changes the Hamiltonian (1.101) [Eq. (1.77)] into

$$H'(t) = -J \sum_{x=0}^{L-1} \left(a_{x+1}^\dagger a_x e^{\mathrm{i}[K_0 t + K/\omega \sin(\omega t)]} + \mathrm{H.c.} \right) \ . \tag{1.107}$$

Applying the Jacobi Anger expansion (1.83) leads to

$$H'(t) = -J \sum_{x=0}^{L-1} \sum_{n=-\infty}^{\infty} \left(\mathcal{J}_n(K/\omega) a_{x+1}^\dagger a_x e^{\mathrm{i}(K_0 + n\omega)t} + \mathrm{H.c.} \right) \ . \tag{1.108}$$

The time average determines the effective Hamiltonian. The additional tilt has an interesting consequence: It can be calibrated to be resonant with the driving frequency

$$K_0 = N\omega \ , \tag{1.109}$$

where $N \in \mathbb{Z}$. With this one finds

$$H_{\mathrm{eff}} = \frac{1}{T} \int_0^T \mathrm{d}t \, H'(t) \tag{1.110}$$

$$= (-1)^{N+1} J \mathcal{J}_N(K/\omega) \sum_{x=0}^{L-1} \left(a_{x+1}^\dagger a_x + \mathrm{H.c.} \right) \ . \tag{1.111}$$

This result is remarkable: In the effective Hamiltonian tunneling is restored. The resonance condition (1.109) can be interpreted as follows: The periodic drive provides quanta of energy $N\omega$ which are resonantly absorbed by the system. The localized states can use this energy to bridge the gaps K_0 in the Wannier-Stark ladder and reestablish tunneling with $J_{\mathrm{eff}} = (-1)^N J \mathcal{J}_N(K/\omega)$ (Fig. 1.3). For $N > 0$ the tunneling is suppressed in the limit of large frequencies $K/\omega \ll 1$, which is markedly different to the coherent destruction of tunneling discussed earlier. In the literature this is known as photo assisted tunneling [81] (see Fig. 1.4). Having established the mechanism behind photo assisted tunneling, the tool that will lead to the main idea behind the engineering of artificial gauge potentials can finally be introduced.

The next incremental change to (1.101) is a phase of the modulation:

$$V(t) = \sum_{x=0}^{L-1} \left\{ [K_0 + K \cos(\omega t + \theta)] x a_{x+1}^\dagger a_x + \mathrm{H.c.} \right\} \ . \tag{1.112}$$

Similar types of driving were discussed in Refs. [82–84]. In a ring it leads to the directed transport of particles. Proceeding as before one can transform the system into a moving frame with

$$W(t) = e^{\mathrm{i} \sum_{x=0}^{L-1} [K_0 t + K/\omega \sin(\omega t + \theta)] x n_x} \ . \tag{1.113}$$

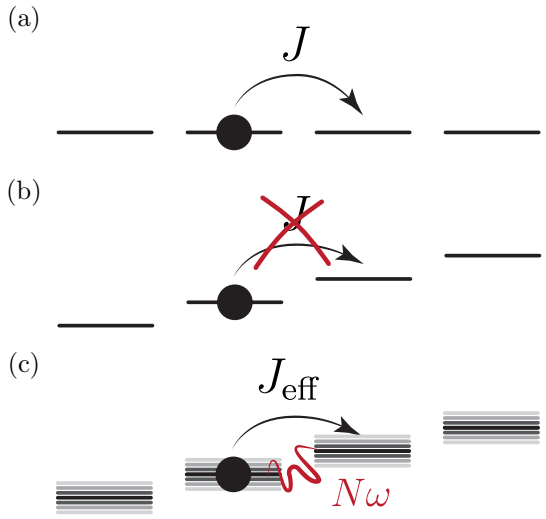

Figure 1.4: Illustration of photo assisted tunneling. Black bars represent the on site energies in a lattice. (a) No lattice tilt, tunneling with amplitude J. (b) Tunneling is inhibited by a constant tilt of the lattice K_0. (c) Photo assisted tunneling: Through the resonant absorption of $N\omega$ from the modulation (greyed out energy levels) tunneling is reinstated with the renormalized hopping amplitude $J_{\text{eff}} = (-1)^N J\mathcal{J}_N(K/\omega)$

Again, to calculate the Hamiltonian in the moving frame, a differential equation involving the appropriately modified version of (1.79) can be employed:

$$H'(t) = -J\sum_{x=0}^{L-1}\left(a_{x+1}^{\dagger}a_x e^{\mathrm{i}[K_0 t + n(\omega t+\theta)]} + \text{H.c.}\right) , \tag{1.114}$$

Combined with the resonance condition $K_0 = N\omega$ the effective Hamiltonian is

$$H_{\text{eff}} = (-1)^{N+1} J\mathcal{J}_N(\omega/K)\sum_{x=0}^{L-1}\left(a_{x+1}^{\dagger}a_x e^{i\theta N} + \text{H.c.}\right) . \tag{1.115}$$

This is essentially what was found before but with an additional phase accompanying the hopping term. It is the advertised Peierls phase, named after his work in Ref. [85]. As was discussed in Ref. [82], this result is surprising, since a shift of phase in the driving is simply a shift of the origin in time. The authors proceed to explain that at some point the driving field had to be turned on, and that event fixes a phase of the driving field. This initial condition is "remembered" in the coherent evolution of the system, and hence has real physical consequences. For ring (periodic boundary conditions) this leads to a ground state with non-zero current and similarly for open boundary conditions the presence of a phase θ will result in directed transport of particles. A simple way of understanding this is to transform the system into momentum space

$$a_x = \frac{1}{\sqrt{L}}\sum_{l=0}^{L-1} a_{k_l} e^{-\mathrm{i}k_l x} a_{k_l} , \tag{1.116}$$

$$a_{k_l} = \frac{1}{\sqrt{L}}\sum_{x=0}^{L-1} a_x e^{\mathrm{i}k_l x} a_{k_l} , \tag{1.117}$$

where

$$k_l = \frac{2\pi}{L} l \ , \quad l \in \mathbb{Z} \ . \tag{1.118}$$

After a bit of algebra the calculation concludes with

$$H_{\text{eff}} = (-1)^{N+1} J \mathcal{J}_N(\omega/K) \sum_{x=0}^{L-1} 2\cos(k_l + N\theta) a_{k_l}^\dagger a_{k_l} \ . \tag{1.119}$$

The addition of the Peirls phase in (1.115) shifts the minimum of the band. For most of the work in this thesis the first Brillouin zone is chosen to be either $[-\pi, \pi]$ or $[0, 2\pi]$. Both choices are equivalent and since $k_l + 2\pi \equiv k_l$, the non overlapping intervals $[-\pi, 0]$ and $[\pi, 2\pi]$ can be identified with each other. For $\theta = 0$ the crystal momentum of the ground states is either $k_l = 0$ if N is even or $k_l = \pm\pi$ if N is uneven. The term $N\theta$ in (1.119) shifts the ground state to momenta other than $0, \pm\pi$, which explains the occurrence of a non-zero current. Incidentally, in momentum space, the Bessel function flattens the band relative to the unmodulated, non-tilted lattice, which is how coherent destruction of tunneling appears in momentum space. Experimentally, this type of driving was studied in Ref. [86] where they found the center of mass oscillations of a cloud of ultra cold atoms in a driven optical lattice.

In summary: Despite the conceptually simple changes to the one dimensional Bose-Hubbard model, it was shown how slight modifications to the potential drive allowed to engineer precises changes to the tunneling amplitudes. Its control over the Peierls phases is what makes Floquet engineering an especially powerful tool. Crucially, they are the connection between the modulation of the lattice and the effect of gauge fields in Bose-Hubbard models. In the next chapter on the shaking of optical lattices, more time is spent on explaining this in detail.

The simple drive in (1.112) is not the only way to engineer Peirls phases. Just to give a few examples: The use of resonant two photon Raman transitions [41, 87] was one of the first proposed methods. This was studied experimentally by the authors of Refs. [88–91]. Another proposal involves the use of internal degrees of freedom of the trapped atoms [92] which was implemented in [93]. A more comprehensive overview of the arsenal of related theoretical and experimental techniques can be found in the Refs. [36, 42].

The above considerations are not limited to bosons. It is relatively straightforward to adapt the above analysis to fermions. Most systems studied in the literature are also not limited to one dimension. Most current research is geared toward two or more real or even synthetic dimensions. More involved driving schemes could also be imagined, such as

$$V(t) = \sum_{x=0}^{L-1} \Big(f(t,x) a_{x+1}^\dagger a_x + \text{H.c.} \Big) \ . \tag{1.120}$$

The transformation into the moving frame can be generalized to

$$W(t) = e^{\mathrm{i} \int_\vartheta^t \mathrm{d}\tau \sum_{x=0}^{L-1} f(\tau,x) x n_x} \ , \tag{1.121}$$

For which the zeroth order contribution to the effective Hamiltonian is

$$H_{\text{eff}} = \sum_{x=0}^{L-1} \Big[J_{\text{eff}}(x,\vartheta) a_{x+1}^\dagger a_x + \text{H.c.} \Big] \ . \tag{1.122}$$

with

$$J_{\text{eff}}(x,\vartheta) = \frac{1}{T}\int_0^T \mathrm{d}t\, e^{\mathrm{i}\lambda(x,\vartheta,t)} \ , \tag{1.123}$$

where

$$\lambda(x,\vartheta,t) = \int_\vartheta^t \mathrm{d}\tau\ \{x[f(x+1,t)-f(x,t)]+f(x+1,t)\}\ . \tag{1.124}$$

This opens up even more possibilities for band shaping. The authors of Ref. [94] used this more general approach as a proposal to study the zeros of the Riemans zeta function. The limits of this approach with regard to lattice shaking and the generation of homogeneous magnetic fields is explained in the next chapter. As a final remark, it should be noted that one can implement more complicated driving protocols by considering multiple discrete steps with different lattice modulations. Further discussion of these possibilities is included in the next chapter.

1.4 Heating

Heating in periodically driven interacting systems is not only of theoretical interest, it is very relevant for determining the feasibility of experimental proposals. If the effective Hamiltonian can only accurately describe the system dynamics on time scales that cannot be observed, then its relevance for real world experiments would be severely limited. This is of special importance for large systems and, in particular the thermodynamic limit $N, L \to \infty$. There are many examples of systems, for which it has been shown that in this limit a periodic drive will eventually cause heating to infinite temperatures [95–99].

The heating mechanism of main concern in Floquet systems is caused by the absorption of energy from the drive. In interacting systems many-body processes that are resonant with the driving frequency can constitute one such an absorption channel. As pointed out in Ref. [36], the Bose Hubbard model with potential driving and interactions serves as a good example for illustrating this. Ref. [36] explains in detail how the Floquet Magnus expansion [73] breaks down once the system is in the vicinity of avoided crossings [100] in the quasienergy spectrum. For the sake of completeness the first few orders of the Floquet Magnus [101, 102] expansion are given here

$$H_{\text{F}} = \sum_{i=0}^{\infty} H_{\text{F}}^{(i)} \tag{1.125}$$

$$H_{\text{F}}^{(0)} = \frac{1}{T}\int_{t_0}^{T+t_0} \mathrm{d}t H(t)\ , \tag{1.126}$$

$$H_{\text{F}}^{(1)} = \frac{1}{2!\mathrm{i}T}\int_{t_0}^{T+t_0} \mathrm{d}t \int_{t_0}^{t} \mathrm{d}t' [H(t),H(t')]\ , \tag{1.127}$$

$$H_{\text{F}}^{(2)} = \frac{1}{3!\mathrm{i}^2 T}\int_{t_0}^{T+t_0} \mathrm{d}t \int_{t_0}^{t} \mathrm{d}t' \int_{t_0}^{t'} \mathrm{d}t'' \Big([H(t),[H(t'),H(t'')]] + [H(t''),[H(t'),H(t)]] \Big)\ , \tag{1.128}$$

In the next paragraph the argument made in Ref. [36] is summarized in conjunction with Refs. [73] and [100]. In a way similar to the discussion in Ref. [36], Fig. 1.5 shows the

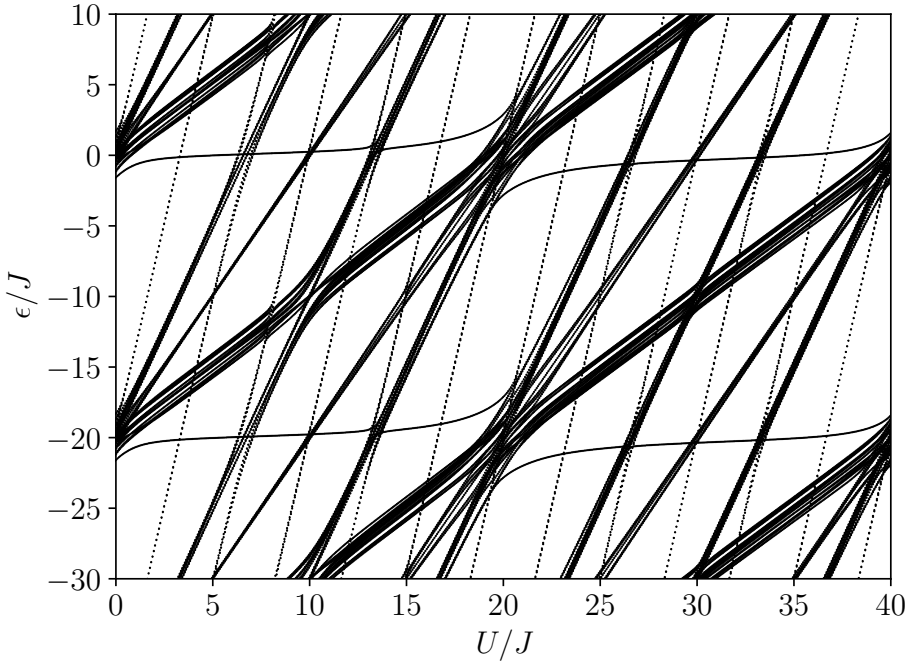

Figure 1.5: Quasienergy spectrum of (1.96) for four particles on four sites. The driving parameters are $\omega = 20J$ and $K = 2\omega$. The interaction U is changed in units of J. The first Brillouin zone is $\epsilon/J \in (-10, 10)$. The quasienergies are displayed in the extended zone scheme. They are clearly periodic with a period $20J$. First avoided level crossing with the Mott level $\epsilon/J \approx 0$ is visible at $U/J \approx 13$. The more significant crossing appears at $U/J \approx \omega/J = 20$.

quasienergy spectrum of a relatively small system of four particles of the Hamiltonian in Eq. (1.96). The quasienergies were calculated by evaluating $U(T, 0)$, after one period of the driving. To calculate $U(T, 0)$ the implementation of the explicit Runge-Kutta method of order $8(5, 3)$ [103] was used. It is provided by the *integrate* module in Python's *scipy* library [104]. The spectrum is displayed in the extended zone scheme. Displaying it this way has the advantage of displaying clearer origins of the quasienergy levels once they start to wrap around the first Brillouin zone $\epsilon \in (-10J, 10J)$. For $U/J \lesssim 1.6$ the quasienergies can be sorted into ground and excited states within their respective zones. Once the highest level of the second Brillouin crosses into the first one this ordering is no longer meaningful. For $1 < U/J < 10$ the level that lies close to $\epsilon \simeq 0$ is best characterized by the Mott state, i.e. a configuration with one particle on each site. This is to be expected for a strongly interacting system. The slanted levels clearly scale linearily with U. They are thus easily identified with states that can be traced back to those having particle hole excitations in the undriven Hamiltonian. The first few level crossings $U/J > 3$ barely interfere with the Mott state since they are exact level crossings. The first visible avoided crossing is visible at $U/J \approx 13$. It involves the Mott level and many levels featuring particle hole excitations. Since it is an avoided crossing, it is to be expected that the underlying Floquet Hamiltonian strongly couples the Mott configuration to configurations with particle hole excitations. As the author of Ref. [36] points out,

this is where the Floquet Magnus expansion (1.125) and (1.63) starts to break down. He asserts that the underlying perturbation theory of (1.125) (developed in Ref. [73]) requires a well ordered spectrum. Even though this ordering into ground and excited states stops being strictly meaningful for smaller interaction strengths $U/J < 13$, the coupling to configurations with higher particle hole excitations is small and interferes very little with the Mott level. In this regime H_{F} or H_{eff} still offer good effective descriptions of the system, i.e. the expansions (1.125) and (1.63) can be salvaged. The underlying perturbation theory and the Floquet Magnus expansion respectively completely break down once the coupling strengths between levels participating in a level crossing become significant, which is exactly what happens at the avoided crossings in Fig1.5. The next, much more significant avoided crossing appears once $U/J = 20$, i.e. where the drive is resonant with the interaction strength. This is not only the reason behind the breakdown of (1.125) but is also what is assumed to cause the heating to infinite temperatures. The cause of heating to infinite temperatures is not settled in the scientific community. In e.g. [105] the conclusion that the mixing of all available eigenstates of the unperturbed Hamiltonian at the large avoided crossings is really an expression of quantum ergodicity is contradicted by studying a one-particle problem with localization. An in-depth discussion of the current state of this discussion is beyond the scope of this work.

For bigger and bigger systems the spectrum in Fig. 1.5 will become more and more populated, which ultimately results in dense bands in the thermodynamic limit [2].

Despite the many-body resonances and the heating collapse of the inverse frequency expansion, there are examples of systems, where the spectrum remains within the first Brillouin zone [98] in the thermodynamic limit. Furthermore, even if heating occurs, there is a pre-thermal regime in which $H_{\mathrm{eff}}, H_{\mathrm{F}}$ accurately describe the systems evolution [96, 107–110]. There is more evidence that the timescale of the pre-thermal regime grows exponentially with ω [109]. Whether or not there is a usable frequency regime is of course always limited by the approximations underlying the model. Increasing the frequency of the driving might cause inter band transitions, which are not accounted for in the simple Bose-Hubbard models of the previous sections.

As a takeaway message it should be noted that as long as the drive frequency $\omega > |\epsilon_{\mathrm{min}} - \epsilon_{\mathrm{max}}|$ where the $\epsilon_{\mathrm{min/max}}$ are the biggest and smallest quasienergies of the spectrum of the effective Hamiltonian, it will provide an adequate description of the system. For large interacting systems this is still true for a reasonably long time as long as $\omega \gg U$.

1.5 Summary

This chapter has aimed at providing a thorough introduction to Floquet theory for classical and quantum mechanical systems. A stability analysis of two specific examples of Hill's equation showed the elegance of Floquet theory in the context of time periodically varied classical systems. Section 1.2 explained how both worlds, the classical and the quantum mechanical, are linked by the monodromy matrix, which becomes the time evolution

[2] Closely related to the dense bands is the discussion around the adiabatic limit [106] in Floquet systems. The question is whether an energy eigenstate will end up in a well-defined state once the drive is slowly switched on and dense bands form. The authors of Ref. [106] argue that in general the formation of bands make the adiabatic limit ill defined, but that is of no concern for most realistic scenarios of this limitation.

operator after one period of the variation. This relationship helps connect the abstract math with concepts that are more common in physics, such as the Floquet Hamiltonian and the effective Hamiltonian. The following section reviewed the approaches developed in Refs. [57–59]. The most notable approach mentioned is the construction of the effective Hamiltonian, which allows for the systematic separation of the short and long term dynamics. This characteristic expresses itself explicitly in the effective Hamiltonian's independence from the initial time and the so-called "kick"-operators. In the review of the effective Hamiltonian, many examples were provided, a pattern that continued throughout Section 1.3 where, among other things, the use of Floquet engineering to generate Peierls phases was explained. The chapter concluded with a brief discussion of heating, an essential concern for proposals related to Floquet engineering.

Chapter 2

Artificial magnetic fields

2.1 Quantum simulation

The method of simulating one system with the help of another system is well established and has long been used by physicists, engineers and architects. A notable recent fluid dynamic example is the simulation of the hexagonal cloud formation on Saturn (see e.g. [111]) with a laboratory model [112]. A remarkable example of simulation in civil engineering is the U.S. Army Corps of Engineer's physical model of San Francisco Bay [113]. It was completed in 1957 and was used to study the impact of two large dams in the area. An intriguing example of simulation in architecture is the hanging chains Antoni Gaudi used to model the structural design of the Sagrada Familia [114]. Nowadays, in the realm of classical physics, real world models are often replaced by computer simulation. This approach quickly fails in quantum physics due to the vast size of many-body Hilbert spaces, even when the systems are relatively small. The Hilbert space of qubits scales as 2^N, with the number of bits N. Achievements in the simulation of quantum circuits with classical methods of computations are with 45 qubits [115] and more recently with 49 qubits [116]. The size of the Hilbert space of N bosons on L lattice sites is

$$\dim\mathcal{H}^{N,L} = \binom{N+L-1}{L} . \tag{2.1}$$

Even for a relatively small system of 38 particles on 38 sites it would take roughly twelve zetabytes to store the coefficients of a state with single precision. This is roughly the total annual cloud data traffic of 2018 [117]. Since real world quantum systems involve many more particles, a more efficient means of analyzing larger systems would be very useful. It is not only the size and the limits of classical computation that make quantum simulation preferable. Another reason is that some quantum systems lie in a range of parameters that are as impossible to study in a laboratory as Saturn's atmosphere is to scale on earth.

As noted in the previous chapter, the idea of quantum simulation was popularized by Feynman [24]. The continuous advancement of experimental control over a diverse set of quantum systems makes this a highly interesting and rapidly growing field of research [118–122].

Roughly speaking, quantum simulation can be split into two approaches: Digital quantum simulation and analog quantum simulation. In digital quantum simulation a quan-

tum computer is used as a universal quantum simulator. To perform a simulation physical states are encoded in quantum bits. Their evolution is then controlled subsequently applying quantum gates [123–125]. Refs. [37, 124, 126, 127] are often cited in this context because, they appear to be promising platforms for scaling to meaningful system sizes. Analog simulation is more in vein with the non quantum examples mentioned above: One quantum system whose properties can be precisely controlled emulates another system whose parameter regime lies out of reach. This is especially relevant for ultracold gases [17, 40, 128, 129]. Superconducting circuits [38] and photonics [39] are used for both, digital and analog simulation approaches. There also proposals for hybrid simulators such as photons and polaritons [130] of a hybrid system consisting of photons and superconducting qubits [131]. These are just a few examples and this list is by no means comprehensive.

2.2 Artificial magnetic fields

The challenge at the center of this chapter is simulating the spectrum of electrons moving on a lattice under the influence of a uniform magnetic field. The intricate fractal structures that these spectra show are known as "Hofstadter Butterflies" [132, 133]. The parameter that determines the visibility of the fine fractal features is the ratio (see e.g. [132])

$$\alpha = T_{\text{cyclotron}}/T_{\text{qm}} = \left(\frac{a^2 m}{2\pi\hbar}\right) \Big/ \left(\frac{mc}{eB}\right) = \frac{a^2 B}{2\pi\hbar c/e} \tag{2.2}$$

where $T_{\text{cyclotron}}$ is the period of the cyclotron orbit of a free electron with charge e subject to a uniform magnetic field with strength B (c is the speed of light) and T_{qm} as the period associated with the time it takes an electron with crystal momentum $p = 2\pi\hbar/a$ to traverse a lattice spacing a. Once α is markedly different from zero, the fractal structures in the spectrum become visible. Since lattice spacings in typical crystals are only a few angstrom wide it takes enormous field strengths of the order $B = 10^5 T$ to achieve this. This is in the range of field strengths encountered close to neutron stars. To create the Hofstadter butterfly with electrons in a laboratory, lattices with larger spacings must be used. For example in [134] they exploited moiré superlattices to make the Hofstadter butterfly appear.

This is where ultra cold quantum gases present an opportunity. Compared to typical condensed matter systems, their environment is much more easily manipulated by the laser fields that hold them in place. The caveat is of course, that neutral atoms only interact weakly with magnetic fields. This shortcoming can be overcome with Floquet engineering, because it can be used to engineer an artificial magnetic field. In our work on realizing uniform synthetic magnetic fields by periodically shaking an optical square lattice [1] we made a detailed proposal on how a periodic modulation can be used to simulate a magnetic field with ultra cold atoms. This chapter is devoted to reporting on this work in more detail.

The field of research investigating the generation of artificial magnetic fields and artificial gauge fields in general, is steadily growing. This is not surprising given their ubiquity and importance in fundamental physics. They are most prominently featured classical electrodynamics. The concept of gauge invariance and its connection to the gauge fields

is indeed so fundamental, that it is one of the unifying features when physics is described on both cosmological scales and those of elementary particles. The modern mathematical framework of fiber bundles [135] elegantly connects these concepts to the Berry phase [136], which is a geometric phase that plays a major role in the quantum Hall effect [137] and more generally in the description of the topological aspects of matter. The possibility of developing a tool-box to access these phases makes this research very enticing, since it has the potential to open the doors to hitherto inaccessible or uncontrollable energy scales. In addition to the cold atoms systems [41, 90, 138–145], (some recent reviews [42, 146–148]), other platforms for simulating these phases include light in photonic lattices [149–153], phonons in ion traps [154, 155], microwave networks [156], sound and light in cavity optomechanics [157], and mechanical systems [158, 159]. A detailed review of these efforts can be found in [160].

This chapter mostly focuses on the shaking of optical lattices [139–142, 145] as a method for creating uniform artificial magnetic fields. In the section on Floquet engineering (1.3) in the previous chapter, it was briefly explained how the periodic acceleration of a lattice can be used for engineering the tunneling terms of a lattice Hamiltonian. In this chapter, this method will be studied in much greater detail. Shaking is one of the simplest methods, because it does not require the use of additional lasers (see Section 2.4). It also does not require any knowledge of the internal structure of the atoms beyond trapping and cooling them, and is thus a very general method that can be applied to different species of fermions and bosons alike. The driving schemes in this chapter are based on resonant shaking [90, 139, 142–144, 155, 161]. As in the examples in the previous chapter, these schemes involve some resonance of the shaking frequency with a static tilt. This chapter presents both, uniform and split shaking schemes and highlights some of their advantages and disadvantages.

Another method of generating and controlling Peierls phases involves two photon Raman transitions. A laser-induced tunneling scheme was employed e.g. in [90, 143, 144]. The effect of the additional Raman lasers can be seen as a moving lattice on top of a static one [1]. One can also make use of the internal structure of atoms to generate the relevant phases [41, 92, 138]. The generation of a magnetic field is not limited to ultracold atoms in optical lattices, creating Peierls phases in photonic crystals is detailed in [151, 162, 163].

The rest of this chapter is structured as follows: First the effect of a magnetic field on a charged particle in a lattice is explained in detail. Then a thorough account of the transformations of the laboratory frame into the moving frame of the shaking lattice is given. After that the observation that uniformly shaken lattices are not sufficient to simulate a homogeneous magnetic field will be discussed. Then more elaborate schemes to compensate for the shortcomings of the uniform shaking schemes are presented. The more elaborate schemes are evaluated with respect to their performances. Finally, the moving lattice method is contrasted with the shaking method.

2.3 Peierls phases and magnetic fields

In this section the effect of a magnetic field on a charge confined to a lattice will be reviewed. A charge is coupled to a magnetic field via the standard method of minimal

coupling. The magnetic field and the vector potential are related by

$$\mathbf{B}(\mathbf{x}) = \nabla \times \mathbf{A}(\mathbf{x}) \tag{2.3}$$

The Hamiltonian for a charge exposed to a lattice potential in the presence of a magnetic field is thus

$$H(q) = \int \mathrm{d}x\, \Psi^\dagger(\mathbf{x}) \left\{ \frac{1}{2m}[\mathbf{p} - q\mathbf{A}(\mathbf{x})]^2 + V(\mathbf{x}) \right\} \Psi(\mathbf{x}) \ , \tag{2.4}$$

$\Psi(\mathbf{x})$ is the field operator in position space with

$$[\Psi(\mathbf{x}), \Psi(\mathbf{x}')] = [\Psi^\dagger(\mathbf{x}), \Psi^\dagger(\mathbf{x}')] = 0 \ , \quad [\Psi(\mathbf{x}), \Psi^\dagger(\mathbf{x}')] = \delta(\mathbf{x} - \mathbf{x}') \tag{2.5}$$

and the lattice potential is spatially periodic $V(\mathbf{x} + \mathbf{a}) = V(\mathbf{x})$ where $\mathbf{a}$ is some lattice vector. The integration, if not otherwise indicated, encompasses the crystal volume. To establish the link between the tight-binding approximation of this Hamiltonian and the regular tight-binding approximation for $H(0)$, the latter will be reviewed first.

The regular tight binding approximation can be found by expanding the field operators into Wannier states [22]

$$\Psi(\mathbf{x}) = \sum_j w(\mathbf{x} - \mathbf{x}_j) a_j \ , \tag{2.6}$$

where the sum runs over all lattice sites x_j. and $[a_j, a_k] = [a_j^\dagger, a_k^\dagger] = 0$ and $[a_j, a_k^\dagger] = \delta_{jk}$. The Wannier functions are defined as (see e.g. [164])

$$w(\mathbf{x} - \mathbf{x}_j) = \frac{\mathrm{V}}{(2\pi)^3} \int_{\mathrm{BZ}} \mathrm{d}\mathbf{k}\, \psi_{0k}(\mathbf{x}) e^{\mathrm{i}\mathbf{k}\cdot\mathbf{x}_j}. \tag{2.7}$$

where the $\psi_{0k}(\mathbf{x})$ are the Bloch functions belonging to the lowest lying Bloch band, V is the volume of the unit cell in the lattice and BZ refers to the first Brillouin zone. The energies involved are assumed to be small, so that no mixing with higher bands occurs. This justifies dropping the band index. The tight binding approximation is then

$$H(0) = \sum_{\langle j,k \rangle} J_{jk} a_j^\dagger a_k + \sum_j \epsilon_j n_j \tag{2.8}$$

where the first sum runs over all neighbors $\langle j, k \rangle$ and it is assumed that due to the strong localization of the Wannier orbitals long range tunneling no longer occurs.

$$J_{jk} = \int \mathrm{d}x\, w(\mathbf{x} - \mathbf{x}_j)^* \left[\frac{\mathbf{p}^2}{2m} + V(\mathbf{x}) \right] w(\mathbf{x} - \mathbf{x}_k) \ , \tag{2.9}$$

$$\epsilon_j = \int \mathrm{d}x\, w(\mathbf{x} - \mathbf{x}_j)^* \left[\frac{\mathbf{p}^2}{2m} + V(\mathbf{x}) \right] w(\mathbf{x} - \mathbf{x}_j) \ . \tag{2.10}$$

In order to accommodate the vector potential one can choose a different local gauge of the Wannier orbitals and expand the field operator according to

$$\Psi(\mathbf{x}) = \sum_j w(\mathbf{x} - \mathbf{x}_j) e^{\mathrm{i}q \int_{\mathbf{x}_j}^{\mathbf{x}} \mathrm{d}\mathbf{x}' \cdot \mathbf{A}(\mathbf{x}')} a_j \tag{2.11}$$

Inserting this expansion into $H(q)$ then modifies the hopping amplitudes

$$J_{jk}(q) = \int \mathrm{d}x\, w(\mathbf{x}-\mathbf{x}_j)^* \times e^{-\mathrm{i}q\int_{\mathbf{x}_j}^{\mathbf{x}} \mathrm{d}\mathbf{x}'\cdot\mathbf{A}(\mathbf{x}')} \left\{ \frac{[\mathbf{p}-q\mathbf{A}(\mathbf{x})]^2}{2m} + V(\mathbf{x}) \right\} e^{\mathrm{i}q\int_{\mathbf{x}_k}^{\mathbf{x}} \mathrm{d}\mathbf{x}'\cdot\mathbf{A}(\mathbf{x}')} \times w(\mathbf{x}-\mathbf{x}_k)\ . \tag{2.12}$$

The exponential can be commuted with the momentum operator by using

$$\mathbf{p}e^{\mathrm{i}q\int_{\mathbf{x}_j}^{\mathbf{x}} \mathrm{d}\mathbf{x}'\cdot\mathbf{A}(\mathbf{x}')} = e^{\mathrm{i}q\int_{\mathbf{x}_j}^{\mathbf{x}} \mathrm{d}\mathbf{x}'\cdot\mathbf{A}(\mathbf{x}')}[\mathbf{p}+q\mathbf{A}(\mathbf{x})] \tag{2.13}$$

which eliminates the vector potential in the parenthesis in (2.12). Combining the remaining exponentials yields

$$J_{jk}(q) = e^{\mathrm{i}q\int_{\mathbf{x}_k}^{\mathbf{x}_j} \mathrm{d}\mathbf{x}'\cdot\mathbf{A}(\mathbf{x}')} \int \mathrm{d}x\, e^{\mathrm{i}q\oint_\gamma \mathrm{d}\mathbf{x}'\cdot\mathbf{A}(\mathbf{x}')} w(\mathbf{x}-\mathbf{x}_j)^* \left[\frac{\mathbf{p}^2}{2m} + V(\mathbf{x})\right] w(\mathbf{x}-\mathbf{x}_k) \tag{2.14}$$

where the path $\gamma : x_j \to x \to x_k \to x_j$. It is assumed that the flux encapsulated by this path vanishes, since it assumed that $\mathbf{A}(\mathbf{x})$ does not vary much on the scale of a lattice site. Under this assumption, the on-site energies ϵ_j remain unchanged. Finally it can be shown that

$$J_{jk}(q) = e^{\mathrm{i}q\int_{\mathbf{x}_k}^{\mathbf{x}_j} \mathrm{d}\mathbf{x}'\cdot\mathbf{A}(\mathbf{x}')} J_{jk} \tag{2.15}$$

$$= e^{\mathrm{i}\phi_{j,k}} J_{jk} \tag{2.16}$$

The phases

$$\phi_{j,k} = \mathrm{i}q \int_{\mathbf{x}_k}^{\mathbf{x}_j} \mathrm{d}\mathbf{x}' \cdot \mathbf{A}(\mathbf{x}') \tag{2.17}$$

are called the Peierls phases and they are the key ingredient to describe the effect of a magnetic field on a charge in a lattice. The substitution

$$a_j^\dagger a_k = T_{jk} \to T_{jk} e^{\mathrm{i}\phi_{j,k}} \tag{2.18}$$

is commonly reffered to as the Peierls substitution [132]. With this change, the tight binding Hamiltonian becomes

$$H(q) = \sum_{\langle jk\rangle} J_{jk} a_j^\dagger a_k e^{\mathrm{i}\phi_{j,k}} + \sum_j \epsilon_j n_j \tag{2.19}$$

In the following the considerations above will be applied to a square lattice. In the calculation it is assumed that the on-site potential and the hopping amplitude is negative and constant. The tight binding model then becomes

$$H_{\mathrm{H}} = -J \sum_{j,k} \left(a_{j,k+1}^\dagger a_{j,k} e^{\mathrm{i}\theta_{j,k}^y} + a_{j+1,k}^\dagger a_{j,k} e^{\mathrm{i}\theta_{j,k}^x} + \mathrm{H.c.} \right)\ . \tag{2.20}$$

This is the famous Harper-Hofstadter Hamiltonian. Note that instead of summing over neighbors, the index j now explicitly indicates horizontally aligned sites (x-direction) and

k vertically aligned ones (y-direction). The Peierls substitution for the square lattice is given by

$$\hat{a}^{\dagger}_{j+1,k}\hat{a}_{j,k} = \hat{T}^{x}_{j,k} \longrightarrow \hat{T}^{x}_{j,k}\, e^{\mathrm{i}\theta^{x}_{j,k}} \ , \tag{2.21}$$

$$\hat{a}^{\dagger}_{j,k+1}\hat{a}_{j,k} = \hat{T}^{y}_{j,k} \longrightarrow \hat{T}^{y}_{j,k}\, e^{\mathrm{i}\theta^{y}_{j,k}} \tag{2.22}$$

and the phases are (see Eq.(2.17))

$$\theta^{x}_{j,k} = q \int_{\mathbf{x}_{j,k}}^{\mathbf{x}_{j+1,k}} \mathrm{d}\mathbf{x} \cdot \mathbf{A}(\mathbf{x}) \ , \tag{2.23}$$

$$\theta^{y}_{j,k} = q \int_{\mathbf{x}_{j,k}}^{\mathbf{x}_{j,k+1}} \mathrm{d}\mathbf{y} \cdot \mathbf{A}(\mathbf{x}) \ , \tag{2.24}$$

where $\mathrm{d}\mathbf{x}(\mathrm{d}\mathbf{y})$ indicates integration along the $x(y)$-direction. It is sometimes desirable to connect both the Peierls phases and the vector potential to a manifestly gauge invariant quantity. It's common to choose a closed loop to determine the flux

$$\Phi_{\gamma} = \int_{S} \mathbf{B} \cdot \mathrm{d}\mathbf{S} = \oint_{\gamma} \mathbf{A}(\mathbf{x}) \cdot \mathrm{d}\mathbf{l} \ , \tag{2.25}$$

where Φ_{γ} is the flux passing through the surface S which is bounded by the path γ. A characteristic flux increment in the lattice is the flux per plaquette of the lattice. It is given by the accumulated phase of a particle traveling counter clockwise around one plaquette of the lattice (Fig. 2.1).

$$\Phi(j,k) = \theta^{x}_{j,k} + \theta^{y}_{j+1,k} - \theta^{x}_{j,k+1} - \theta^{x}_{j,k} \ . \tag{2.26}$$

Since the goal of this chapter is to present a way to generate Peierls phases through shaking, and since the phases are not themselves gauge invariant, the flux is a good way to characterize the synthetic field independent of the gauge.

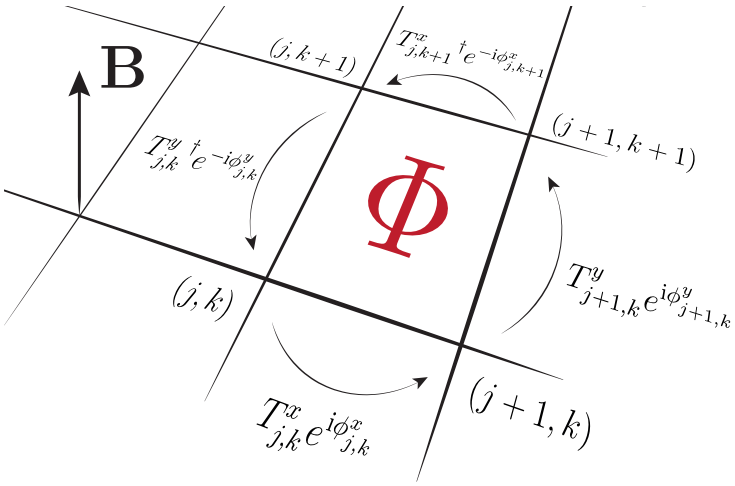

Figure 2.1: The accumulated phase of a particle looping around a plaquette of the lattice defines the flux per plaquette Φ.

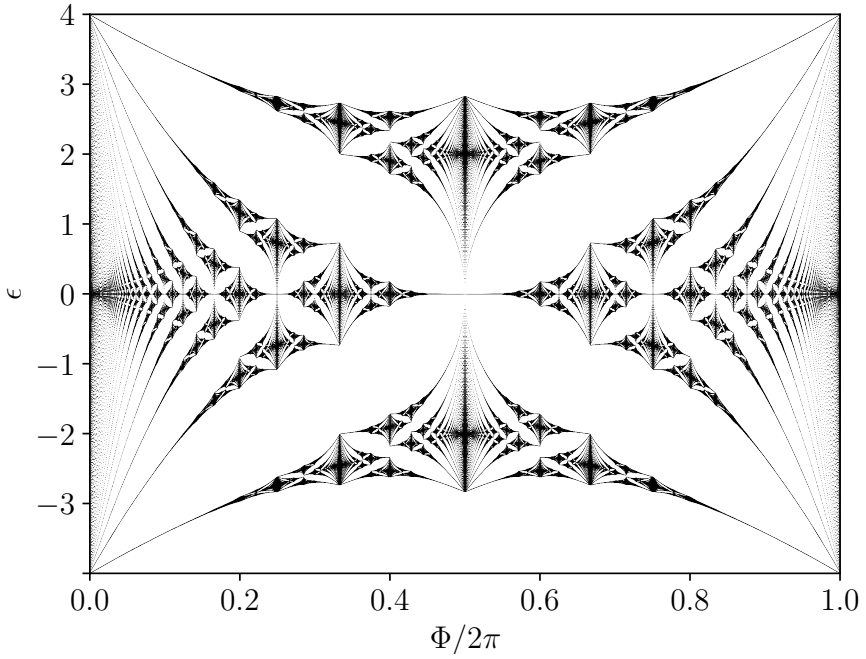

Figure 2.2: Hofstadter Butterfly. Energy spectrum of a charge on a square lattice for different values of the flux Φ with 2000×2000 sites and periodic boundary conditions in x- and y-directions. For $|\Phi| > 2\pi$ the spectrum repeats itself.

Additionally, theses phases are intended to simulate a uniform magnetic field. Two suitable choices for the vector potential are the symmetric gauge $\mathbf{A}(\mathbf{x}) = B/2(-y, x, 0)$ or the Landau gauge $\mathbf{A}(\mathbf{x}) = -B(y, 0, 0)$. Both of them generate a uniform magnetic field orthogonal to the lattice plane. The simplicity of the Landau gauge makes it the most suitable to be simulated through shaking. The phases in this gauge are

$$\theta^x_{j,k} = \Phi k \ , \quad \theta^y_{j,k} = 0 \ . \tag{2.27}$$

A particle moving along the x-direction picks up a y-dependent phase. Movement in the y-direction does not change the phase. In Fig. 2.2 the famous Hofstadter butterfly is shown. It displays the spectrum of the Harper-Hofstadter Hamiltonian (2.20) for a uniform magnetic field orthogonal to the lattice for a range of Φ. Periodic boundary conditions in both x- and y-direction were assumed. The spectrum repeats once $|\Phi| > 2\pi$, which can be seen in e.g. (2.27).

2.4 Lattice acceleration

Now the effects of a time dependent acceleration of the lattice in the x-direction is considered. There are various ways of achieving this experimentally: Either shaking can be generated through the introduction of the variation of a frequency difference in two counter propagating lasers with the help of acousto-optic modulators [63, 65, 66, 69], or if the lattice is created by reflection of a mirror, the mirror can be moved physically by

a piezo actuator [67, 68, 145]. In the rest frame of the lattice the periodic acceleration results in an inertial force. This section is dedicated to the discussion of the emergence of the inertial force. More specifically the focus will lie in motivating the transformations that take the system from the laboratory frame into the rest frame of the lattice. This section is based on the appendix in [1].

In [165] and [166] a unitary representation of the Galilean line group is constructed. This is the starting point of a many-body generalization. In [167] a summary of these transformation rules can be found. The classical Hamiltonian of a single-particle with mass m in one dimension, subject to a lattice potential that is shifted by the general displacement $d(t)$, is

$$H(t) = \frac{p^2}{2m} + V[x - d(t)] \tag{2.28}$$

The Galilean coordinate transformation into the rest frame of the lattice is

$$x' = x - d(t)\,, \quad p' = p - m\dot{d}(t)\,, \tag{2.29}$$

The Hamiltonian in the accelerated frame then becomes

$$H'(t) = \frac{{p'}^2}{2m} + V(x') + mx'\ddot{d}(t) + \frac{m}{2}\dot{d}(t)^2 + md(t)\ddot{d}(t)\,. \tag{2.30}$$

As expected, the potential no longer depends on time and an inertial force term $mx'\ddot{d}(t)$ appears. The last two terms do not couple to either p' or x' and represent a time dependent shift of the overall energy. In the following the representation of the Galilean line group derived in [165] is used to implement the transformation for a quantized version of (2.28):

$$\hat{U}_d(t) := e^{-\mathrm{i}\left(\frac{m}{2}\dot{d}(t)d(t) + m\dot{d}(t)\hat{x}\right)} e^{\mathrm{i}d(t)\hat{p}}\,. \tag{2.31}$$

$\hat{U}_d(t)$ is a unitary operator and $\hat{p}$ and $\hat{x}$ have the canonical commutation relations $[\hat{x}, \hat{p}] = \mathrm{i}$. To avoid confusion between the classical and the quantum mechanical variables, hats were introduced. $\hat{U}_d(t)$ is interpreted as the composition of a position shift by $d(t)$ followed by the shift of the momentum. The Hamiltonian in the moving frame is

$$\hat{H}'(t) = \mathrm{i}\left[\partial_t \hat{U}_d(t)\right]\hat{U}_d^\dagger(t) + \hat{U}_d(t)\hat{H}(t)\hat{U}_d^\dagger(t) \tag{2.32}$$

$$= \frac{\hat{p}^2}{2m} + V(\hat{x}) + m\ddot{d}(t)\hat{x} + \frac{m}{2}\ddot{d}(t)d(t) \tag{2.33}$$

The Hamiltonian in (2.30) can be converted into the one above by subtracting the total time derivative

$$\frac{d}{\mathrm{d}t}\frac{m}{2}d(t)\dot{d}(t)\,. \tag{2.34}$$

The authors of [168] argued that the last term in (2.33) is dependent on the cocycle representation and hence does not posses any physical significance. It should be noted however, that the authors of [169] argue that even for non-relativistic systems, terms that depend on the mass can potentially cause a phase difference if one keeps track of the proper time of two different systems. Without going into the subtleties of that discussion and for the sake of completeness the term is kept as is for now.

It is possible to adapt the transformation $\hat{U}_d$ to a many-body quantum formulation. In the continuum the many-body Hamiltonian of the shaken lattice is:

$$H(t) = \int \mathrm{d}x\, \Psi^\dagger(\mathbf{x}) \left[-\frac{\nabla^2}{2m} + V(\mathbf{x} - d(t)\mathbf{e}_x) \right] \Psi(\mathbf{x}) \,, \tag{2.35}$$

Hats were not used to indicate the quantum nature of e.g. the field operators Ψ. This helps to keep the notation consistent with the previous section and to sets the notation apart from the single-particle description. As before, the commutation relations in (2.5) hold. The generalization of (2.31) to a many-body formulation is

$$U_d(t) = U_1(t) U_2(t) U_3(t) \tag{2.36}$$

where

$$\begin{aligned} U_1(t) &= e^{-\mathrm{i}\frac{m}{2}\dot{d}(t)d(t)\int \mathrm{d}x\, \Psi^\dagger(\mathbf{x})\Psi(\mathbf{x})} \\ U_2(t) &= e^{-\mathrm{i}m\dot{d}(t)\int \mathrm{d}x\, \Psi^\dagger(\mathbf{x}) x \Psi(\mathbf{x})} \\ U_3(t) &= e^{\mathrm{i}d(t)\int \mathrm{d}x\, \Psi^\dagger(\mathbf{x})\frac{1}{\mathrm{i}}\partial_x \Psi(\mathbf{x})} \,. \end{aligned} \tag{2.37}$$

Transforming the Hamiltonian in Eq. (2.35) results in

$$H'(t) = \mathrm{i}[\partial_t U_d(t)] U_d^\dagger(t) + U_d(t) H(t) U_d^\dagger(t) \tag{2.38}$$

$$= \int \mathrm{d}x\, \Psi^\dagger(\mathbf{x}) \left[-\frac{\nabla^2}{2m} + V(\mathbf{x}) + m\ddot{d}(t)x + \frac{m}{2}\ddot{d}(t)d(t) \right] \Psi(\mathbf{x}) \,. \tag{2.39}$$

This equation is consistent with the single-particle result in Eq. (2.33). Assuming a square two dimensional lattice, in the tight binding approximation the above Hamiltonian is (2.6)-(2.8)

$$H(t) = H_0 + H_\mathrm{s}(t) \,, \tag{2.40}$$

where

$$H_0 = -J \sum_{j,k} (a^\dagger_{j,k+1} a_{j,k} + a^\dagger_{j+1,k} a_{j,k} + \mathrm{H.c.}) \,, \tag{2.41}$$

$$H_\mathrm{s}(t) = \sum_{j,k} \left[jm\ddot{d}(t) + \frac{m}{2}\ddot{d}(t)d(t) \right] n_{j,k} \tag{2.42}$$

where J was defined in (2.9). As before the lattice spacing was kept at $a = 1$. From now on the last term of $H_\mathrm{s}(t)$ is dropped, since for a single particle it only serves to contribute a global time dependent phase. This leaves the inertial term,

$$H_\mathrm{s}(t) = \sum_{j,k} jm\ddot{d}(t) n_{j,k} \tag{2.43}$$

which grows linearily along the x-direction of the lattice.

It is interesting to note that when taken by itself U_2 in (2.37) only regauges the momentum. This part of the transformation is renamed

$$W(t) = U_2(t) \tag{2.44}$$

$$= e^{-\mathrm{i}m\dot{d}(t)\int \mathrm{d}x\, \Psi^\dagger(\mathbf{x}) x \Psi(\mathbf{x})} \tag{2.45}$$

since it plays the exact same role as the gauge transformation (1.76). To show its full effect its inverse is applied, i.e. a shift of the momentum back into the laboratory frame:

$$H''(t) = \mathrm{i}\left[\partial_t W(t)\right] W^\dagger(t) + W(t)H'(t)W^\dagger(t) \tag{2.46}$$

$$= \int \mathrm{d}x\, \Psi^\dagger(x) \left[\frac{1}{2m}[\mathrm{i}\nabla + m\dot{d}(t)\mathbf{e}_x]^2 + V(x) + \frac{m}{2}\ddot{d}(t)d(t)\right] \Psi(\mathbf{x}) \ . \tag{2.47}$$

In this frame the connection between the acceleration, encoded in the lattice displacement $d(t)$, and a magnetic field is made explicit. Without the last term, the above Hamiltonian is just a version of (2.4) with a vector potential $\dot{d}(t)\mathbf{e}_x$, which couples to the mass of the particle. It is this term that makes shaking a viable contender for the simulation of a magnetic field.

Lattice shaking

In the previous paragraphs the effect of lattice acceleration on the rest frame of the lattice was explained in detail. In [1] shaking does not soley refer to a periodic displacement, but is rather more general. Apart from a periodic displacement it also features a constant acceleration and the temporal phase of the driving is allowed to vary in the y-direction. The introduction to Floquet engineering (Section 1.3) explained in detail the process of how a sinusoidal drive in combination with a constant acceleration causes a renormalization of the hopping amplitude [see e.g. (1.119)] and an accompanying phase. As will be explained later, unless the temporal phase of the drive is allowed to vary, the Peierls phases will end up uniform and the flux per plaquette (2.26) will vanish. With these assumptions the Hamiltonian in the shaking frame is

$$\begin{aligned} H'(t) &= H_0 + V(t) \\ &= H_0 + \sum_{j,k} j[K_0 + f(\omega t + \theta_k)]n_{j,k} \ , \end{aligned} \tag{2.48}$$

K_0 corresponds to a static tilt, and $f[\omega(t+T)] = f(\omega t)$ is a T periodic driving function with $\omega = 2\pi/T$. A comparison of Eq. (2.48) with Eq. (2.43) reveals that $f(\omega t)$ is the time dependent contribution to the acceleration of the displacement $d(t)$. Thus $f(\omega t)$ is associated with the inertial force resulting from shaking the lattice. H_0 is the same as the one in (2.42) . Just as in the section on Floquet engineering it can be used as a starting point to derive a time independent effective Hamiltonian. Also, as was explained above, the constant tilt is not necessarily generated by acceleration. The same effect can be achieved in a gravitational field gradient [86], a magnetic gradient [144] or by applying a dipole potential [143].

With this choice of the displacement $m\ddot{d}(t) = K_0 + f(\omega t + \theta_k)$ the inverse momentum-shift operator in (2.45) is

$$W(t) = e^{\mathrm{i}\sum_{j,k}[K_0 t + F(\omega t + \theta_k) - F(\theta_k)]jn_{j,k}} \ , \tag{2.49}$$

where

$$F(\omega t) = \int_0^t \mathrm{d}t'\, f(\omega t') \tag{2.50}$$

is identified as the velocity of the shaking.

2.5 Sinusoidal shaking

The following represents a simple continuous shaking scheme:

$$f(\omega t) = K\sin(\omega t)\ , \quad K_0 = N\omega\ . \tag{2.51}$$

Aspects of this scheme were already discussed in the section on Floquet engineering, albeit only in one dimension. The effective Hamiltonian (1.119) has renormalized tunneling amplitudes in x-direction $J_{\text{eff}} = J\mathcal{J}_N(\kappa)$ where $\kappa = K/\omega$ and a hopping term that was accompanied by a phase $\exp(\mathrm{i}\phi)$.

In two dimensions, the additional degree of freedom θ_k will introduce some important qualitative additions to the derivation of the effective Hamiltonian. These additions will be clarified in the next few paragraphs. Just as in the section 1.3 the Hamiltonian (2.48) can be transformed into a moving frame. As explained in Section 2.4, the transformation into the moving frame (2.49) is a momentum shift that will cause the appearance of Peierls phases in the transformed lattice Hamiltonian [(2.45) + tight binding approximation]. Together with the explicit form of the shaking (2.51), the momentum shift operator (2.49) that shifts the momenta back into the lab-frame is

$$W(t) = e^{\mathrm{i}\sum_{j,k} j n_{j,k}\{N\omega t - \kappa[\cos(\omega t+\theta_k)-\cos(\theta_k)]\}} \tag{2.52}$$

Using the formalism developed in section 1.3, the transformed Hamiltonian [see e.g. from Eq.(1.77) onward] is

$$H'(t) = H'_x(t) + H'_y(t) \tag{2.53}$$

$$H'_x(t) = -J\sum_{j,k} a^\dagger_{j+1,k}a_{j,k}f_x(t;j) + \text{H.c.}, \tag{2.54}$$

$$H'_y(t) = -J\sum_{j,k} a^\dagger_{j,k+1}a_{j,k}f_y(t;j,k) + \text{H.c.}, \tag{2.55}$$

$$\begin{aligned} f_x(t;k) &= \exp\Big(\mathrm{i}\left\{N\omega t - \kappa[\cos(\omega t+\theta_k)-\cos(\theta_k)]\right\}\Big), \\ f_y(t;j,k) &= \exp\Big(-\mathrm{i}\,j\kappa\{[\cos(\omega t+\theta_{k+1}) \\ &\qquad -\cos(\theta_{k+1})]-[\cos(\omega t+\theta_k)-\cos(\theta_k)]\}\Big). \end{aligned} \tag{2.56}$$

Shifting the $\sin(\theta)$ in (1.83) by $\pi/2$ yields the Jacobi-Anger expansion

$$e^{\mathrm{i}z\cos(\theta)} = \sum_{n=-\infty}^{\infty} \mathrm{i}^n\mathcal{J}_n(z)e^{in\theta}\ . \tag{2.57}$$

Using this expansion in (2.56) and averaging over one period of the driving will result in

the effective Hamiltonian

$$H_{\text{eff}} = H^x_{\text{eff}} + H^y_{\text{eff}} \tag{2.58}$$

$$\begin{aligned} &= -J^x_{\text{eff}} \sum_{j,k} a^\dagger_{j+1,k} a_{j,k} e^{-\mathrm{i}N\theta_k} e^{\mathrm{i}\kappa\cos(\theta_k)} + \text{H.c.} \\ &\quad - \sum_{j,k} J^y_{\text{eff}}(j,k) a^\dagger_{j,k+1} a_{j,k} e^{\mathrm{i}j\kappa[\cos(\theta_{k+1})-\cos(\theta_k)]} + \text{H.c.}, \end{aligned} \tag{2.59}$$

$$J^x_{\text{eff}} = J\mathcal{J}_N(\kappa),$$

$$J^y_{\text{eff}}(j,k) = J\mathcal{J}_0\left[2j\kappa\sin\left(\frac{\theta_{k+1}-\theta_k}{2}\right)\right], \tag{2.60}$$

Because of the phases accompanying the tunneling terms this already looks promising. This is a necessary condition for the simulation of a uniform magnetic field. The above Hamiltonian allows for the direct computation of the flux per plaquette as defined in (2.26)

$$\begin{aligned} \Phi(j,k) &= -N\theta_k + \kappa\cos(\theta_k) + N\theta_{k+1} - \kappa\cos(\theta_{k+1}) \\ &\quad + (j+1)K_0\Big[\cos(\theta_{k+1}) - \cos(\theta_k)\Big] \\ &\quad - jK_0\Big[\cos(\theta_{k+1}) - \cos(\theta_k)\Big] \\ &= N\left(\theta_{k+1} - \theta_k\right), \end{aligned}$$

In general this does not have to be a uniform flux. The Landau gauge (2.27) can be emulated by choosing

$$\theta_k = \alpha k \tag{2.61}$$

since θ_k, the temporal off-set of the shaking between different rows of the lattice, is a free parameter. With this choice, the flux per plaquette

$$\Phi = \alpha N \tag{2.62}$$

is uniform. The parameter with which an experimenter would control the field strength is α. It must be noted, that the sinusoidal shaking scheme produces a reasonable effective Hamiltonian within the constraints of the tight binding approximation. It does not suffer from potential divergences due to interactions and is an appropriate description of the system for large frequencies as long as ω does not excite transitions between higher lying Bloch bands.

The sinusoidal driving scheme was originally proposed in [139] and it does indeed generate a uniform flux. A simple scheme to generate the a synthetic uniform magnetic field would have been found had it not been for the non-uniform hopping amplitudes in (2.59). For the field to be truly uniform, the effective tunneling amplitudes $J^{x,y}_{\text{eff}}$ have to be uniform as well. While this is true for J^x_{eff}, J^y_{eff} is, however, strongly position dependent, as displayed in Eq.(2.60) after inserting (2.61). In Ref. [170] the authors clarified, that this method is only useful for a limited region around the origin of the lattice, where the non-uniformity is small.

In Ref. [1] we argue that this limitation cannot be overcome by using other forms of continuous driving schemes, such as the sinusoidal one explained above. In the next few paragraphs, this point will be reiterated. The goal is to prove that a non-zero uniform magnetic flux cannot coexist with uniform magnitude of effective hopping amplitudes, when considering a Hamiltonian with a periodic driving such as that shown in Eq.(2.48). The Hamiltonian is made a bit more concise by writing

$$\hat{H}_{\text{latt}}(t) = \hat{H}_0 + \sum jD(t,k)\hat{n}_{j,k} \ . \tag{2.63}$$

If $D(t,k)$ were dependent on j, shaking would no longer be an adequate description of the lattice manipulation. The unitary transformation in Eq. (2.49) is

$$W(t) = e^{\mathrm{i}\int_0^t \sum_{j,k} jD(t',k)\hat{n}_{j,k}\mathrm{d}t'} \ . \tag{2.64}$$

The transformed Hamiltonian becomes

$$H'(t) = -J\left(\sum_{j,k} f'_x(t;k)a^\dagger_{j+1,k}a_{j,k} + f'_y(t;j,k)a^\dagger_{j,k+1}a_{j,k} + \text{H.c.}\right) \tag{2.65}$$

where

$$f'_x(t;k) = e^{\mathrm{i}\int_0^t D(t',k)\mathrm{d}t'} \tag{2.66}$$

$$f'_y(t;j,k) = e^{\mathrm{i}\int_0^t j[D(t',k+1)-D(t',k)]\mathrm{d}t'} \ . \tag{2.67}$$

Again, the effective Hamiltonian is defined as $H'_{\text{eff}} = \frac{1}{T}\int_0^T \hat{H}'(t)\mathrm{d}t$. The following will show that uniformity of the magnitude of the effective hopping implies that the magnetic flux is zero everywhere. An important assumption for this statement is the time independence of $|J|$. This assumption is implicit in $\hat{H}_0$ of Eq. (2.48), which is a static tight-binding Hamiltonian with constant tunneling matrix elements [Eq. (2.42)].

Just as in Ref. [1], the focus will lie on the hopping matrix elements in the y-direction (this was the issue in Ref. [170]). To that extent, the squared modulus of the time-averaged (possibly complex), dimensionless effective hopping amplitude is considered

$$C = \left|J^y_{\text{eff}}(j,k)\right|^2 / J^2 \tag{2.68}$$

$$= \frac{1}{T^2}\int_0^T\int_0^T e^{\mathrm{i}j[G(t,k)-G(t',k)]}\mathrm{d}t\mathrm{d}t' \ , \tag{2.69}$$

where J is the (constant and uniform) magnitude of the hopping energy in the undriven Hamiltonian and

$$G(t,k) = \int_0^t [D(t',k+1) - D(t',k)]\mathrm{d}t' \ . \tag{2.70}$$

In this section the following condition will be proven: if C as defined in (2.69) is independent of j,k, then the magnetic flux of the time-averaged driven Hamiltonian must be zero.

If Eq. (2.69) is true for all j with C constant, then it must be true in particular for $j = 0$. This implies that $C = 1$. If $j = 2q$, $q \in \mathbb{Z}\backslash_0$, then from Eq. (2.69) follows

$$\begin{aligned} 1 &= \frac{1}{2T^2}\int_0^T\int_0^T \Big(e^{\mathrm{i}2q[G(t,k)-G(t',k)]} \\ &\qquad +e^{-\mathrm{i}2q[G(t,k)-G(t',k)]}\Big)\,\mathrm{d}t\mathrm{d}t' \\ &= \frac{1}{T^2}\int_0^T\int_0^T \cos\Big(2q[G(t,k)-G(t',k)]\Big)\mathrm{d}t\mathrm{d}t' \\ &= \frac{1}{T^2}\int_0^T\int_0^T \times \\ &\qquad \Big[1-2\sin^2\Big(q[G(t,k)-G(t',k)]\Big)\Big]\mathrm{d}t\mathrm{d}t' \ , \end{aligned} \tag{2.71}$$

and thus

$$0 = \int_0^T\int_0^T \sin^2\Big(q[G(t,k)-G(t',k)]\Big)\mathrm{d}t\mathrm{d}t' \ . \tag{2.72}$$

The integrand in the above equation is positive and the last equation only holds under the condition

$$G(t,k) - G(t',k) = \pi l(k) \ , \tag{2.73}$$

where $l(k) \in \mathbb{Z}$. Differentiating with respect to t leads to

$$D(t,k+1) - D(t,k) = 0\,. \tag{2.74}$$

Therefore it can be concluded that $D(t,k) = D(t)$ must be independent of k. This means that all the Peierls phases vanish and hence the magnetic flux is zero. In conclusion it has been shown that a uniform mass implies a zero flux, and thus a non-zero flux is incompatible with a uniform mass in this simple but general shaking scheme. Thus, it is clear, that more involved driving protocols are needed to generate an artificial uniform magnetic field. This will be investigated in the next section.

2.6 Split driving

In this section, more involved driving schemes will be presented. They circumvent the limitations created by the non-uniform tunneling amplitudes outlined above. In our work [1], several schemes in which one cycle of the driving is split into multiple operations were proposed. This avoids the non-uniformity caused by the continuous drive. Schemes of this type are aptly named "split driving" schemes. A thorough formalism of such schemes was developed in [57].

2.6.1 Two-step split driving

In the following the findings of Refs. [161] and our work in [1] are summarized. The two steps in their shaking protocol are: 1. Sinusoidal shaking of the system as in Eq. (2.48) sinusoidally but with the complete suppression of tunneling in the y-direction. This

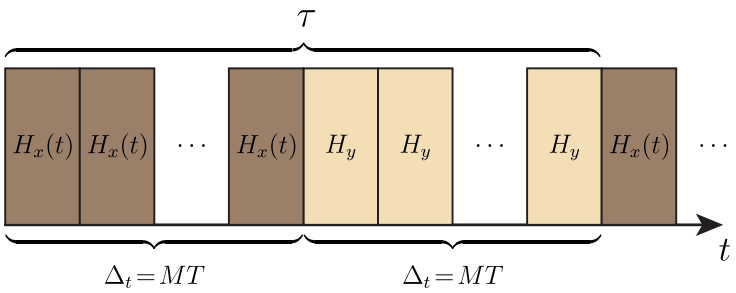

Figure 2.3: Two-step split driving. In the first step the system is evolved over M periods T with the sinusoidally shaken Hamiltonian $H_x(t)$ (2.48)(tunneling in the y-direction suppressed), and then it is evolved with $H_y(t)$ (no shaking, tunneling in the x-direction suppressed). This cycle repeats after $\tau = 2\Delta_t$, which is one period of the scheme.

can be accomplished by changing the lattice potential. 2. Reestablishing the tunneling in the y-direction, halting the shaking and suppressing the tunneling in x-direction. A driving protocol of this type breaks one of the assumptions made in the derivation of the impossibility of having uniform flux and uniform hopping at the same time: The kinetic energy is now time dependent.

First, in order to derive the effective Hamiltonian, one period of the driving is redefined as $\tau = 2\Delta_t = 2MT$, where $M \in \mathbb{Z}$ and $\Delta_t = MT$ is the duration of each of the split driving steps. This is illustrated in Fig. 2.3. The time-evolution operator over one period of the cycle τ is given by

$$U(\tau) = U_y U_x, \tag{2.75}$$

Again, U_x generates the time-evolution of the shaken system without tunneling in the y-direction and U_y without tunneling in the x-direction and shaking. The effective Hamiltonian during the first step of the cycle and hence the time evolution is given by Eq. (2.59)]:

$$U_x = e^{-\mathrm{i}\Delta_t H^x_{\mathrm{eff}}}. \tag{2.76}$$

With neither shaking nor tunneling in the x-direction the evolution in the second step is

$$\begin{aligned} U_y &= e^{-\mathrm{i}\Delta_t H_y}, \\ H_y &= -J_y \sum_{j,k} a^\dagger_{j,k+1} a_{j,k} + \mathrm{H.c.} \end{aligned} \tag{2.77}$$

With the use of the Baker-Campell-Hausdorff (BCH) formula both steps in (2.75) can be combined into a single approximate evolution over the period of one cycle τ:

$$U(\tau) = e^{-\mathrm{i}\Delta_t H_y} e^{-\mathrm{i}\Delta_t H^x_{\mathrm{eff}}} \simeq e^{-\mathrm{i}\Delta_t \left(H_y + H^x_{\mathrm{eff}}\right)} \tag{2.78}$$

$$= e^{-\mathrm{i}\tau H^{\mathrm{split}}_{\mathrm{eff}}}, \tag{2.79}$$

where $\tau = 2\Delta_t$ and the new split effective Hamiltonian was introduced

$$H^{\mathrm{split}}_{\mathrm{eff}} = -J^x_{\mathrm{eff}}/2 \sum_{j,k} a^\dagger_{j+1,k} a_{j,k} e^{\mathrm{i}N\theta_k} e^{-\mathrm{i}\kappa\cos(\theta_k)} - J_y/2 \sum_{j,k} a^\dagger_{j,k+1} a_{j,k} + \mathrm{H.c.} \tag{2.80}$$

The above approximation is the first order term in Δ_t in the Trotter expansion of

$$C = A + B + \frac{1}{2}[A, B] + \frac{1}{12}[A, [A, B]] - \frac{1}{12}[B, [A, B]] + \cdots \,, \tag{2.81}$$

where

$$e^A e^B = e^C \,. \tag{2.82}$$

As long as Δ_t is small enough this approximation is justified. For details see e.g. Ref. [57].

The split effective Hamiltonian $H_{\text{eff}}^{\text{split}}$ no longer possesses the non-uniformity of the tunneling. Both J_{eff}^x and J_y are independent of the lattice coordinates and since J_y is a free parameter the choice $J_{\text{eff}}^x = J_y$ can be made. The problem now is that the flux is no longer uniform. Calculation of the flux per plaquette [Eq.(2.26)] results in

$$\begin{aligned} \Phi(j,k) &= N\left(\theta_{k+1} - \theta_k\right) - \kappa\left[\cos(\theta_{k+1}) - \cos(\theta_k)\right]. \\ &= N\alpha - \kappa\left\{\cos[(k+1)\alpha] - \cos(k\alpha)\right\}, \end{aligned} \tag{2.83}$$

where the choice $\theta_k = \alpha k$ was made once again. The non-uniformity caused by

$$\kappa\left\{\cos[(k+1)\alpha] - \cos(k\alpha)\right\} \tag{2.84}$$

is bounded by κ and hence can be controlled and made small. In Fig. 2.4 the quasienergies ϵ_n of the fully time dependent system are plotted. As explained in Section 1.2 of Chapter 1 the ϵ_n can be calculated by taking the natural logarithm of the eigenvalues of (2.75) [1]. In Ref. [1] the first resonance $K_0 = \omega$ was examined and open boundary conditions were chosen. Fig. 2.4 shows that small amplitudes of the driving parameter $\kappa = 0.2$ reproduce the spectrum of the Harper-Hofstadter Hamiltonian (2.20). Since the system is quite small and because edges of the lattice are present, the fractal structures are much less pronounced than in Fig. 2.2. To make the wings of the butterfly appear more clearly, the quasienergies of the bulk and edge states were colored differently. Bulk states are marked with violet dots and edge states with orange ones. An edge state is considered to be any state, that has more than 50% of its weight on the edge of the lattice. The edge is taken to be two sites thick. In the present work the system size has been increased from 8×8 in Ref. [1] to 16×16 sites. This makes the butterfly more recognizable. Once the magnitude of the driving parameter κ increases the spectrum becomes visibly deformed and, as can be seen in Fig. 2.4 for $\kappa = 0.8$, the spectrum is severely distorted due to the non-uniformity of the flux.

In practice, being confined to small values of κ means that both J_{eff}^x and J_{eff}^y are small (see e.g. $\mathcal{J}_1(\kappa)$ in Fig. 1.3). This in turn implies that the system's dynamics is slow and the effective Hamiltonian has a relatively tight spectrum. This means lower temperatures are required to resolve the fine gaps. The next scheme will omit this short-coming by introducing two more steps in the driving procedure.

2.6.2 Four-step split driving

The impetus of this section is to present a solution for the removal of the inhomogeneous flux caused by (2.84) in (2.83). Two key insights helped to accomplish this in Ref. [1].

[1] The data for Fig. 2.4 was created with the implementation of the explicit Runge-Kutta method of order 8(5, 3) [103] provided by the integrate module of python's scipy library [104].

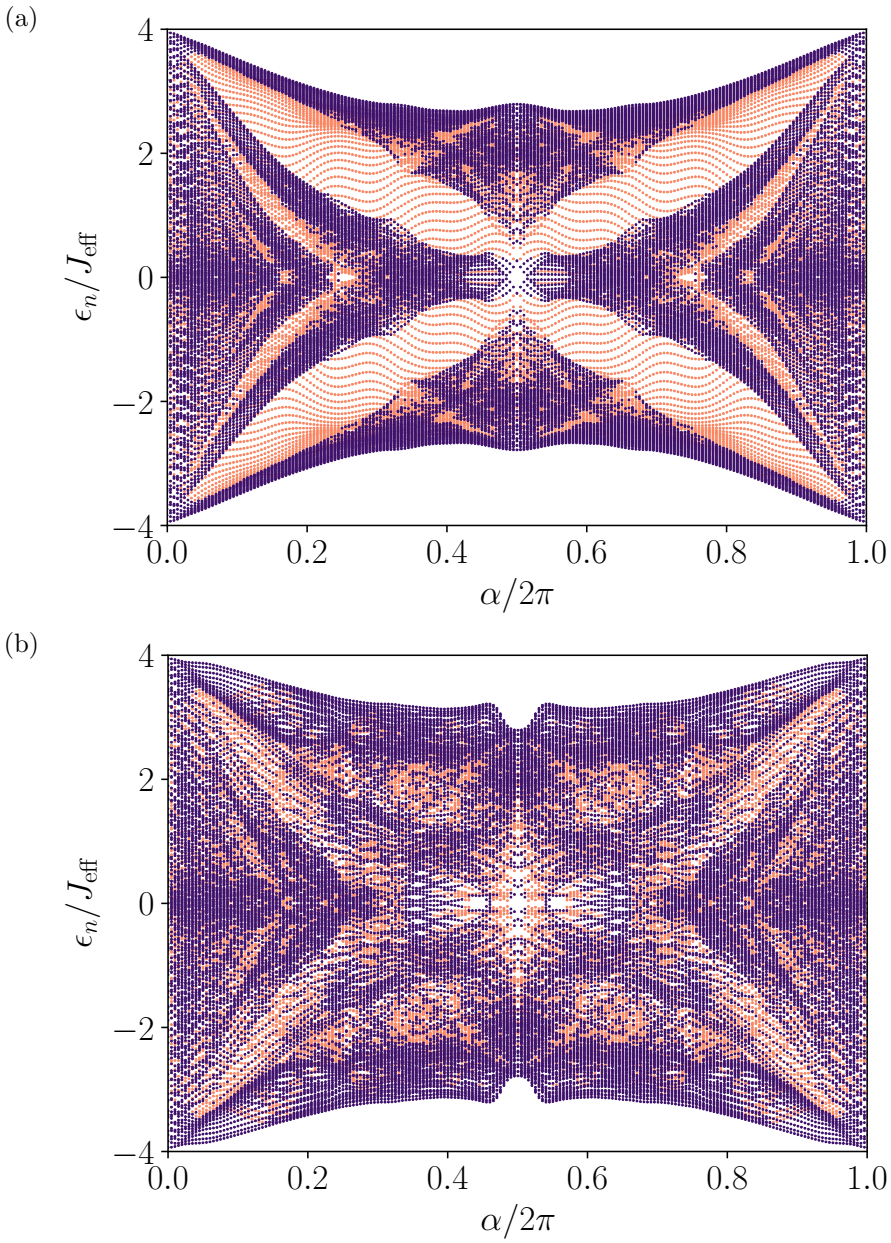

Figure 2.4: Quasienergies ϵ_n for a sinusoidal split driving. (a) Weak driving, $\kappa = 0.2$, The spectrum is almost exactly that of the Harper-Hofstadter Hamiltonian. (b) Stronger driving, $\kappa = 0.8$, the spectrum is visibly distorted. System parameters: 16×16 lattice, $J = 1$, $\omega = 1000J$. Violet/orange dots indicate edge/bulk states. An edge state has more than 50% of its weight on the edge.

The first is relatively simple and has already been mentioned here: it consists of extending (2.75) by introducing two additional steps. The second one is a bit more subtle and makes use of Eq. (1.81) to remove the unwanted phases. The four-step time evolution operator is defined

$$U(\tau) := U_y U_\beta U_x U_\alpha \ . \tag{2.85}$$

The two operators U_x, U_y are the same as in (2.75). The two new ones are given by

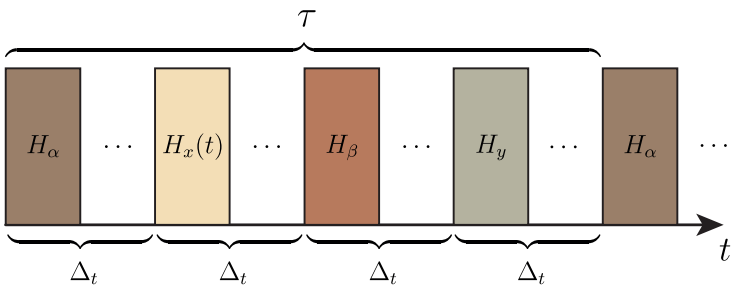

Figure 2.5: Four-step split driving: One cycle of the driving is divided into four-steps, where at first the system is pulsed by a linear potential H_α followed by shaking with tunneling in the y-direction suppressed [$(H_x(t)$], then pulsing with the linear potential H_β and finally evolving with H_y where tunneling in the x-direction is suppressed.

$$\begin{aligned} U_\alpha &= e^{-\mathrm{i}\Delta_t H_\alpha} \\ H_\alpha &= -\left(\kappa/\Delta_t\right) \sum_{j,k} j n_{j,k} \cos(\theta_k)\,. \end{aligned} \tag{2.86}$$

H_α is a linear potential along the x-direction lasting for a time Δ_t with no tunneling in either direction. The steepness of the linear ramp for each row k depends on θ_k. After evolving the system with U_x [Eq. (2.76)], the pulse

$$\begin{aligned} U_\beta &= e^{-\mathrm{i}\Delta_t H_\beta} \\ H_\beta &= \left(\kappa/\Delta_t\right) \sum_{j,k} j n_{j,k} \cos(\theta_k) = -H_\alpha\,. \end{aligned} \tag{2.87}$$

is applied and the final step is U_y as defined in Eq. (2.77). To calculate the four-step split effective Hamiltonian $U_\beta U_x U_\alpha$ has to be computed. Using Eq. (1.81) one finds

$$U_\beta H^x_{\text{eff}} U_\alpha = e^{\mathrm{i}\Delta_t H_\alpha} H^x_{\text{eff}} e^{-\mathrm{i}\Delta_t H_\alpha} \tag{2.88}$$

$$= -\left(J^x_{\text{eff}}/2\right) \sum_{j,k} a^\dagger_{j+1,k} a_{j,k} e^{\mathrm{i}N\theta_k} \tag{2.89}$$

So that

$$U(\tau) \simeq e^{-\mathrm{i}\tau H^{\text{4-split}}_{\text{eff}}}\,, \tag{2.90}$$

where $\tau = 4\Delta_t$ and the four-step split effective Hamiltonian is

$$H^{\text{4-split}}_{\text{eff}} = -\left(J^x_{\text{eff}}/4\right) \sum_{j,k} a^\dagger_{j+1,k} a_{j,k} e^{-\mathrm{i}N\theta_k} - \left(J_y/4\right) \sum_{j,k} a^\dagger_{j,k+1} a_{j,k} + \text{H.c.}\,. \tag{2.91}$$

Finally, the flux and the tunneling amplitudes are uniform over the entire lattice. Indeed, for $J^x_{\text{eff}} = J_y$ the Hamiltonian $H^{\text{4-split}}_{\text{eff}}$ is the Harper-Hofstadter Hamiltonian [(2.20)] for a uniform magnetic field that is perpendicular to the lattice [(2.27)]. In Fig. 2.6 the quasienergy spectrum[2] for $\kappa = 0.2$ is shown. As was the case for the two-step split driving, barely distinguishable from the energy spectrum of the Hofstadter model. A

[2]The data for Fig. 2.4 was created with the implementation of the explicit Runge-Kutta method of order 8(5, 3) [103] provided by the integrate module of python's scipy library [104].

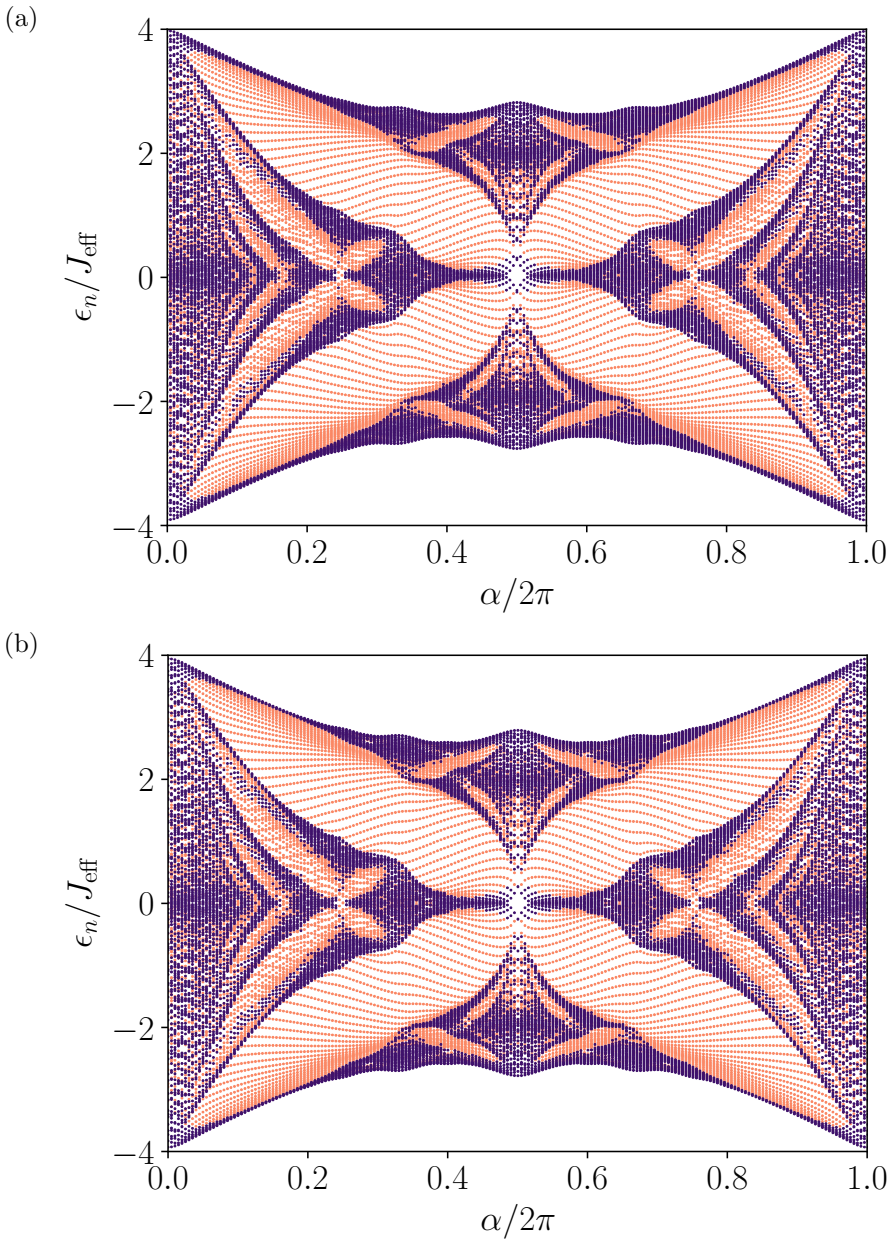

Figure 2.6: Quasienergies ϵ_n for the four-step split driving scheme. (a) Weak driving, $\kappa = 0.2$, The spectrum is almost exactly that of the Harper-Hofstadter Hamiltonian [(2.20)]. (b) Stronger driving, $\kappa = 1.841$, the spectrum almost exactly replicates that of the Harper-Hofstadter Hamiltonian. System parameters: 8×8 lattice, $J = 1$, $\omega = 1000J$. Violet/orange dots indicate edge/bulk states. An edge state has more than 50% of its weight on the edge.

detailed examination of the spectrum shows that it is as precise as the two-step scheme for weak driving. The situation drastically changes for strong driving: The spectrum agrees well with that of the Harper-Hofstadter Hamiltonian [see (2.20)]. In Fig. 2.6b the quasienergy spectrum for $\kappa = 1.841$ can be seen. This is where $J^x_{\text{eff}} = 0.582J$ takes its largest value. The four-step split driving fixes the problem of being confined to small

values of κ and in principle allows a speedup of the system's dynamics and hence permits an increase in the size of the gaps in the quasienergy spectrum.

As pointed out in Ref. [1], there is another four-step driving scheme, which also leads to a uniform flux. It was proposed in Ref. [171]. That proposal makes use of (real) oscillating magnetic fields and thus is different from the shaking scheme proposed here (see also Refs. [57, 172, 173]).

The four-step split driving results in the desired condition of completely eliminating the unwanted phase terms. However it introduces additional complexity into the experimental realization of the system, and so it is worth considering whether it is possible to find a means of suppressing these terms within the two-step approach, by altering the form of the periodic driving function $f(\omega t)$ in Eq. (2.48).

2.6.3 Two-step split driving with other waveforms

The added complexity in the four-step driving scheme results in an additional complication in eventual experimental implementations. Even though it completely eliminated non-uniformities in both the flux and the tunneling amplitudes it is worthwhile to see whether there are simpler two-step protocols. One way to make adjustments is to alter is the shape of the waveform of the driving. Interestingly, one can find an exact form of the effective hopping amplitude for a more general waveform. In Chapter 1, Section 1.2, a general expression for the hopping amplitude was given in Eq. (1.123). Continuing from there, the anti-derivative of the acceleration as defined in Eq. (2.50) is restated

$$F(\omega t) = \int_0^t \mathrm{d}t'\, f(\omega t') \ . \tag{2.92}$$

This implicitly entails that the shaking starts at $t = 0$, in contrast to other analyses, where shaking starts at $t = -\infty$. If furthermore a temporal phase is introduced, the above equation becomes

$$\int_0^t \mathrm{d}t'\, f(\omega t' + \theta) = F(\omega t + \theta) - F(\theta) \ . \tag{2.93}$$

With this the effective tunneling amplitude (1.123) for a single link, the following can be computed:

$$J^x_{\mathrm{eff}}/J = \frac{1}{T}\int_0^T dt \exp\left(-\mathrm{i}V_0 t - \mathrm{i}\int_0^t dt' f(\omega t' + \theta)\right) \ . \tag{2.94}$$

The tunneling in the other direction is given by the complex conjugate of this expression. The tilt $V_0 = N\omega$ is assumed to be resonant so that Eq. (2.92) can be written in terms of F as

$$\begin{aligned} J^x_{\mathrm{eff}}/J =& \frac{1}{T}\int_0^T dt \exp\left\{-\mathrm{i}N\omega t - \mathrm{i}\left[F(\omega t + \theta) - F(\theta)\right]\right\} \\ =& \frac{1}{T} e^{\mathrm{i}F(\theta)} \int_0^T dt \exp\left[-\mathrm{i}N\omega t - \mathrm{i}F(\omega t + \theta)\right] . \end{aligned} \tag{2.95}$$

The periodicity of $f(\omega t)$ implies that, $F(\omega t)$ and $\exp[\mathrm{i}F(\omega t)]$ are T-periodic. Therefore its Fourier series is

$$e^{\mathrm{i}F(\omega t)} = \sum_{m=-\infty}^{\infty} \gamma_m e^{\mathrm{i}m\omega t} \ . \tag{2.96}$$

For sinusoidal driving, this Fourier series is the Jacobi-Anger expansion (1.83). Substituting this expression in Eq. (2.95) results in the expression

$$J^x_{\mathrm{eff}}/J = \frac{1}{T} e^{\mathrm{i}F(\theta)} \int_0^T dt \exp\left(-\mathrm{i}N\omega t\right) \sum_m \gamma_m e^{\mathrm{i}m(\omega t+\theta)} \ . \tag{2.97}$$

After exchanging the order of integration and summation, the final expression reads

$$J^x_{\mathrm{eff}}/J = \gamma_N e^{\mathrm{i}(N\theta+F(\theta))} \ . \tag{2.98}$$

The hopping in the x-direction is modified by a factor γ_N and a phase of $N\theta + F(\theta)$ is acquired. For sinusoidal shaking the renormalization factor is $\gamma_N = \mathcal{J}_N(\kappa)$ and the phase is $N\theta - \kappa\cos(\theta)$ which is consistent with (2.59). The flux per plaquette is

$$\Phi(j,k) = N\alpha - \kappa\left[F((k+1)\alpha) - F(k\alpha)\right] \ . \tag{2.99}$$

Since $f(\omega t)$ and $F(k\alpha)$ are periodic, it is impossible to make a non-trivial choice $f(\omega t) \neq 0$ so that Φ is constant. It is possible, however, to design a function $f(\omega t)$ that produces a flux that is constant for large areas of the lattice and only deviates from this constant value for some k, as will be explained in the next section.

2.6.4 δ-kick driving

A candidate for such a function $f(\omega t)$ was given in Ref. [1]:

$$\begin{aligned} f(\omega t) =& K\{\delta[t - (T/2 - \Delta/2) - nT] \\ & - \delta[t - (T/2 + \Delta/2) - nT]\} \ , \quad nT < t \leq (n+1)T \ , \end{aligned} \tag{2.100}$$

where n is an integer and the ω dependence is implicit in $T = 2\pi/\omega$. Since $f(\omega t)$ is the acceleration of the shaking, this was named kicked driving [1]: In each interval of the protocol, two kicks separated by the interval Δ act on the system. Fig. 2.7 compares the velocity function $F(k\alpha)$ for kicked driving and sinusoidal driving. The non-uniformity in the flux of the sinusoidal protocol stems from the spatial dependence of $F(k\alpha)$. This is illustrated in Fig. 2.7a where the red dots indicate the spatial dependence for $\alpha = 2\pi/16$. This is what causes the distortions in the quasienergy spectra in Fig. 2.3. For kicked driving the flux remains mostly homogeneous, except for the values where $F(k\alpha)$ abruptly changes. This is exemplified in Fig. 2.8, where the flux per plaquette is plotet for a 16×16 lattice. For two-step split driving with a sinusoidal acceleration the areas over which the non-uniformity spreads is much larger than for the kicked drive. In addition the flux remained constant over large areas for the kicked driving protocol. The spatial dependence of the flux per plaquette can be made clearer by only analyzing its variation in the y-direction, since it does not depend on the x coordinate. This is done in Fig. 2.9. For three different values of α and δ. In Fig. 2.9a ($\Delta = 0.08T$) the value $\alpha = \pi/2$ is highly

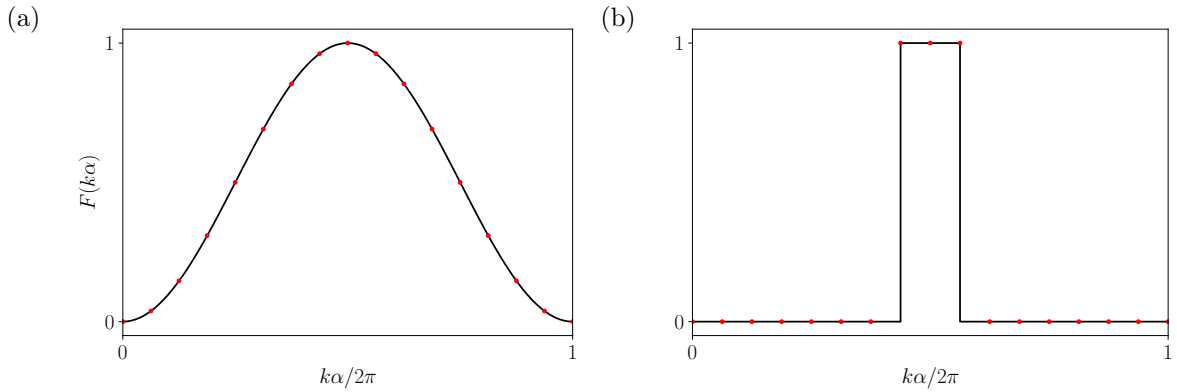

Figure 2.7: The velocity function $F(k\alpha)$ [(2.50)] for two different driving schemes: (a) In sinusoidal driving, the spatial inhomogeneity of the flux results from the values of $F(k\alpha)$ for $\alpha = 2\pi/16$ indicated by red dots. (b) In kicked driving the flux that results from this drive is mostly uniform, except for the k's that lie adjacent to the discontinuity.

commensurate with the driving period T and the flux oscillates rapidly. This would create a highly non-uniform magnetic field. The only way to lessen the impact of those oscillations on the uniform part of flux is by reducing κ (with the same caveat that this will also result in slowing the system's dynamics). Fig. 2.9b[$\Delta = 0.08T$] shows that the oscillation frequency can be reduced by tuning $\alpha = 0.55\pi$ slightly away from this value. In Fig. 2.9c the oscillations are reduced even further by keeping $\alpha = 0.55\pi$ and reducing $\Delta = 0.02T$. The flux remains uniform over almost 50 lattice sites, which means that for these sites the resulting synthetic magnetic field would behave as desired: Particles confined to these sites would behave as if they were exposed to a uniform magnetic field.

One way of studying this parameter space in a concise manner is by exploring the variance of the flux as a function of α and Δ. The variance is defined as

$$\sigma_\Phi^2 = \frac{1}{L}\sum_k (\Phi(j,k) - \bar{\Phi})^2 \tag{2.101}$$

where $\bar{\Phi}$ is the average flux and L is the number of sites of the lattice in the y-direction. In Eq. 2.101 j can be chosen arbitrarily, since $\Phi(j,k)$ in Eq. (2.99) is independent of j. In Fig. 2.10 an overview of the behavior of the flux is shown and illustrated for two different parameter regimes. Once α/T is tuned away from a highly commensurate value the variation of $\Phi(j,k)$ becomes much smoother as a function of α and Δ, and generally decreases as a function of Δ.

For kicked driving the effective tunneling amplitude can be calculated using (2.95):

$$J_{\text{eff}}^x = \frac{2J}{\pi}\sin(\pi\Delta/T)\sin(\kappa/2) \ , \tag{2.102}$$

where the same resonance condition $N = 1$ as for sinusoidal driving was used. In Fig. 2.11a the quasienergy spectrum is shown for a lattice with 16×16 sites. The driving parameter is $\kappa = 0.2$ and the kick-spacing has a value of $\Delta = T/32$. The spectra were computed with the same method as the previous spectra. The delta distribution was approximated with

$$\delta_N(\omega t) = \frac{1}{2\pi}\frac{\sin[(N+1/2)\omega t]}{\sin(\omega t/2)} \tag{2.103}$$

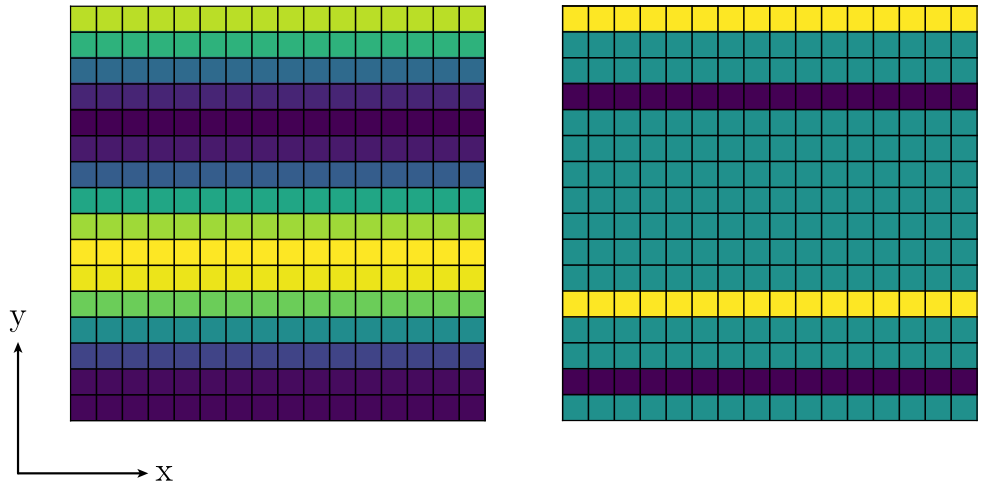

Figure 2.8: Flux in a 16×16 lattice for sinusoidal two-step split driving (left) and kicked two-step split driving (right). In the case of the kicked driving the non-uniformities only appear for certain values of k while they affect a larger area in the case of sinusoidal driving. Parameters of the system are: $\kappa = 0.5$, $\alpha = 0.6$, $T = 2\pi$ and $\Delta = T/4$

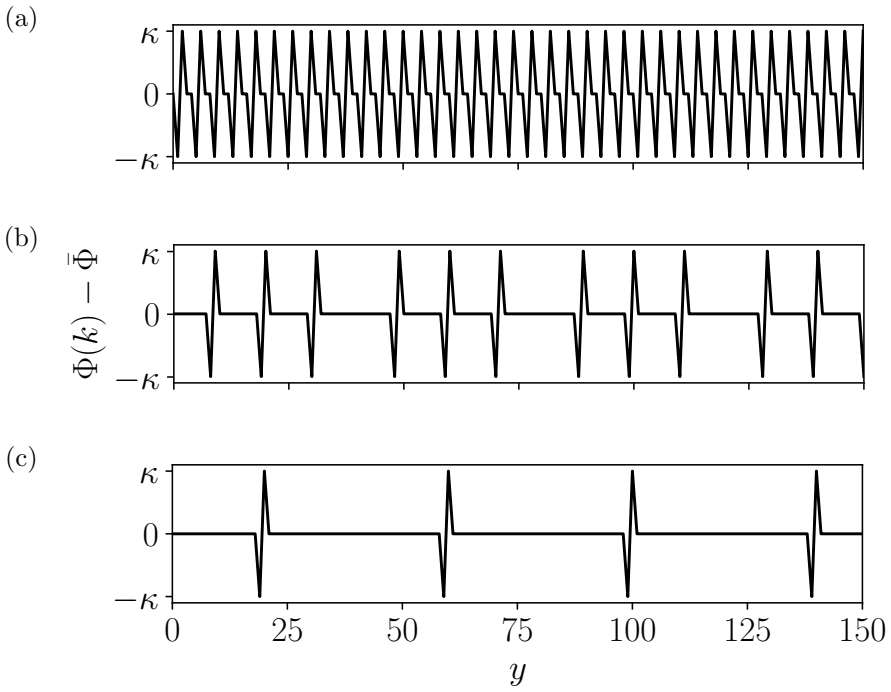

Figure 2.9: Here the variation of $\Phi(k)$ [see Eq. (2.99)] is shown in the y-direction for three different combinations of α and Δ. (a): $\alpha = \pi/2$ and $\Delta = 0.08T$ produced an highly oscillatory flux. This happens because α is highly commensurate with the period $T = 2\pi$ (b): $\alpha = 0.55\pi$ and $\Delta = 0.08T$. Tuning away from the highly commensurate value of α greatly reduces the frequency of the oscillations. (c): $\alpha = \pi/2$ and $\Delta = 0.02T$ reduces the oscillations even further. The flux remains uniform over a range of almost 50 sites.

where $N = 120$, and $J_y = J^x_{\text{eff}}$ (given by Eq. (2.102)). The result visibly agrees with the Hofstadter spectrum, but shows small distortions due to the discontinuities produced

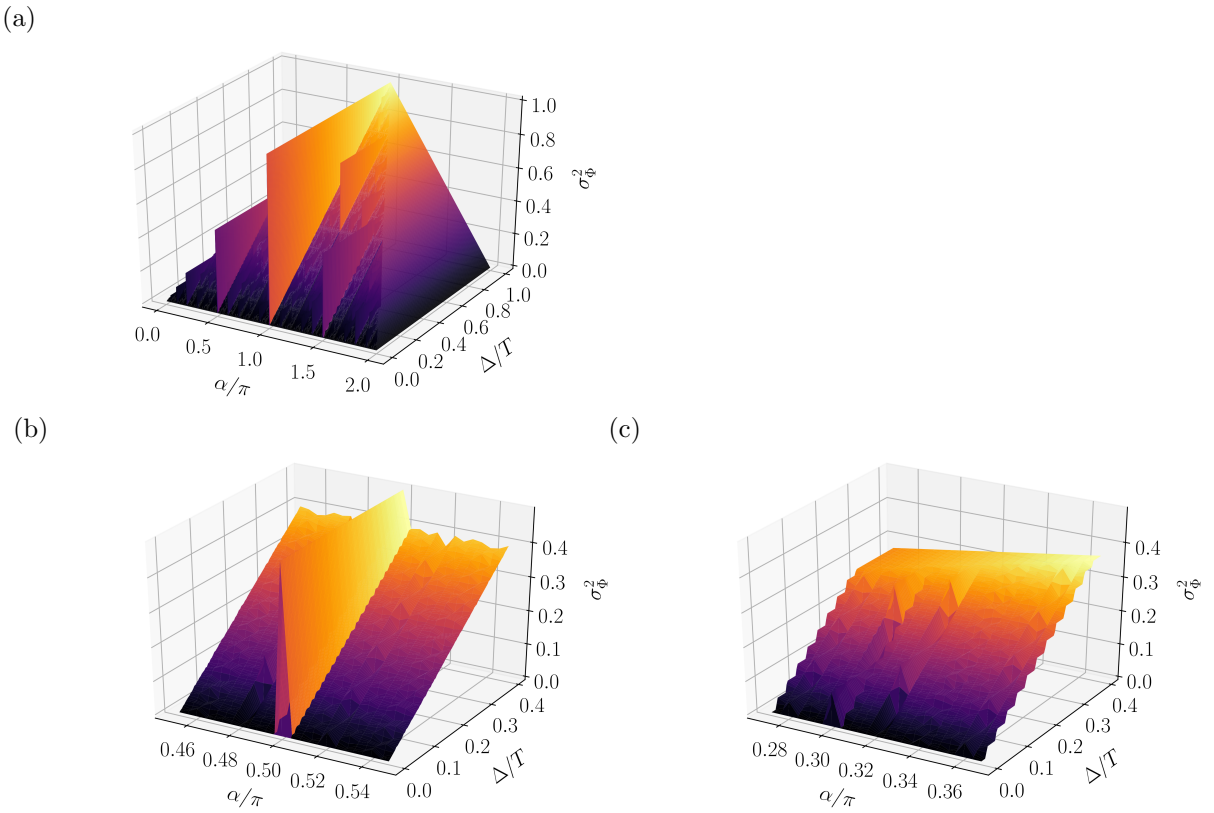

Figure 2.10: Shown is the variance of the flux per plaquette σ^2_Φ [see Eq. (2.101)] as a function of α and Δ. (a) Overview of σ^2_Φ for the entire meaningful parameter regime of α and Δ. Discontinuities arise for values where α and T are highly commensurate. (b) for the value $\alpha = \pi/2$ which is highly commensurate with the driving period T, σ^2_Φ is clearly peaked. The variation in $\Phi(j,k)$ is generally reduced by decreasing Δ once α is tuned away from this value. (c) In a regime, without any significant commensurate values of T/α the variance σ^2_Φ is much smoother. System parameters are: $T = 2\pi$, $\kappa = 1$ and $L = 1500$.

by commensurable values of α/T. These distortions are enhanced for $\kappa = \pi$, where J_{eff} reaches its highest value. Clearly most of the spectrum is still reproduced well except of course for the aforementioned discontinuities. Away from these discontinuities variations in the flux decay smoothly as explained in Fig. 2.10.

2.6.5 Benchmarking of driving schemes

To make the comparison of the various driving schemes more quantitative, a figure of merit was introduced in [1]:

$$\chi^2 = \sum_n |\epsilon_n^{\text{Hof}} - \epsilon_n|^2 \ , \tag{2.104}$$

where the ϵ_n^{Hof} are the energies of the Hofstadter Hamiltonian and the ϵ_n the quasi-energies belonging to the respective driving scheme. The apparent distinct appearance of the edge states generated by the individual shaking protocols (compare for example the orange

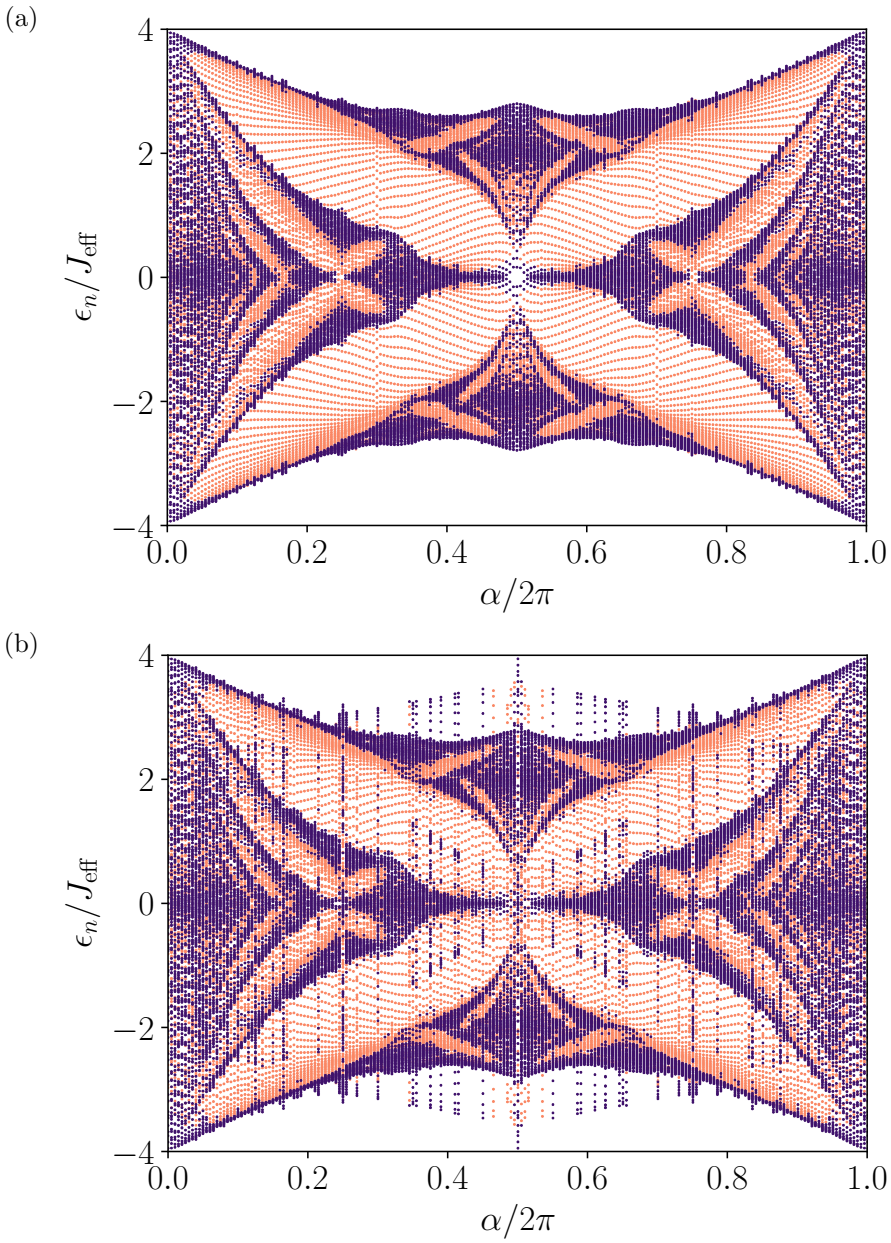

Figure 2.11: Quasienergies ϵ_n of the effective Hamiltonian for the kicked two-step split driving scheme. (a) Weak driving, $\kappa = 0.2$: The spectrum is very close to that of the Harper Hofstadter Hamiltonian [(2.20)]. Some slight deviations are visible due to the non-uniformity induced by the kicks. (b) Stronger driving , $\kappa = \pi$. The slight alterations of the spectrum produced by weak driving are much more pronounced. System parameters: 16×16 lattice, $J = 1$, $\omega = 1000J$ and $\Delta = T/32$.

colored points in Fig. 2.4a with the ones in Fig. 2.6a) is not addressed by χ^2 and will not be studied in this work. It would of course be an interesting extension of the benchmarking performed in this section. Fig. 2.12 shows χ^2 for the three different driving schemes as a function of the synthetic magnetic flux parameter α. The four step-split driving scheme and the two-step kicked scheme are comparable. The kicked driving scheme notably

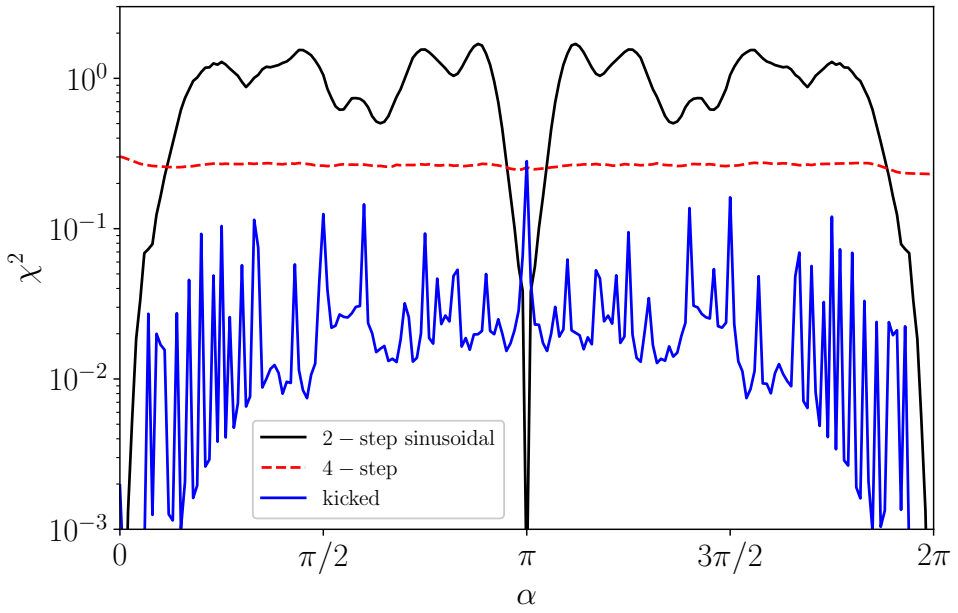

Figure 2.12: χ^2 is shown [Eq. (2.104)]. Two-step sinusoidal, kicked and four-step driving schemes are compared for $\kappa = 0.2$. The kicked driving scheme and the four-step driving scheme are comparable, apart from the values of α, where the spectrum shows discontinuities in the kicked drive case. The two-step sinusoidal scheme performs notably worse than the other two except for $\alpha = 0, \pi$.

deviates for sharply defined values of α, which originate from commensurate values of α and the period T. The four step driving is only matched by the two-step driving for the two values $\alpha = 0, \pi$. Otherwise, the two-step sinusoidal scheme is the least accurate out of the shaking protocols.

The previous analysis can be extended to studying the dependence of χ^2 on κ for a fixed value of α. This is shown in Fig. 2.13. This time, χ^2 is portrayed for the three driving schemes at a fixed value of the flux α. The error in the two-step sinusoidal protocol initially dips for very small values of κ, where it compares favorably with the four-step procedure. The error in two-step scheme then grows monotonically with κ. The error of the kicked protocol increases for $\alpha = \pi/2$. This value produces a large variation in the flux (see e.g. Fig. 2.9) whose amplitude grows with κ. Tuning away from this value to $\alpha = 51\pi/100$ improves the condition and it keeps decreasing as a function of κ. The four-step protocol decreases monotonically with κ. Even though the two energy scales of ω and K become eventually comparable, the high frequency approximation not only stays valid but actually improves. This is not uncommon in Floquet systems. Since both K and ω remain large compared to J, the hopping term in the time-dependent Hamiltonian is still dominated by the time dependent part which leads to the improvement in performance. The four-step driving protocol's error will eventually grow due to higher-order terms in the Trotter expansion (2.81). In the limit $\omega \gg J^x_{\text{eff}}, J_y$ these errors are very small. In the high frequency limit the errors in the other schemes are not due to the Trotter expansion result from non-uniformities of the flux. These grow as κ grows, which is what was confirmed in Fig. 2.13. It must be stressed, however, that χ^2 takes the entire spectrum

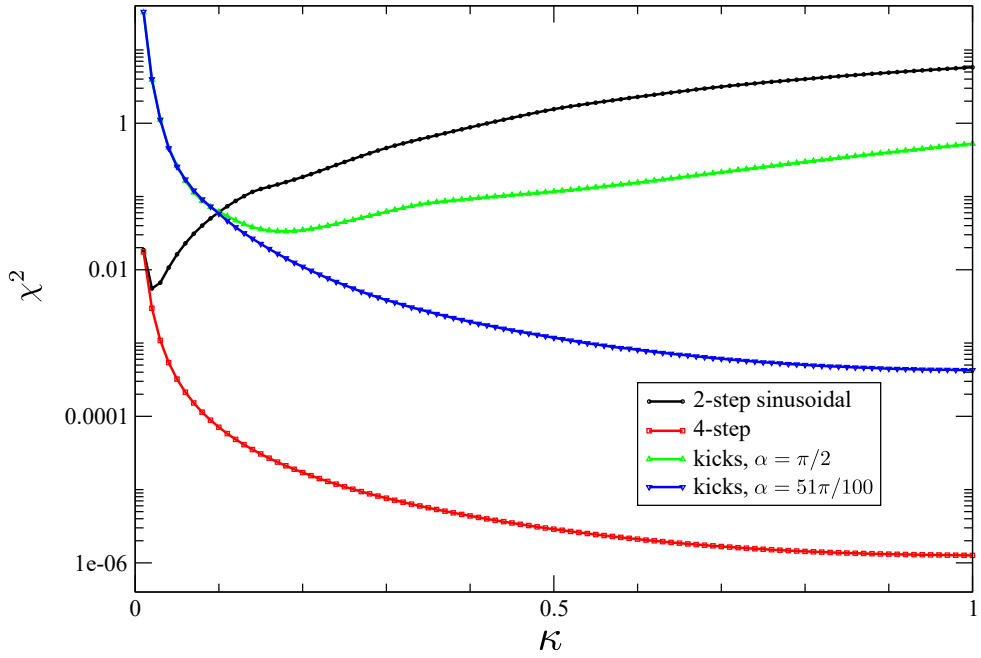

Figure 2.13: χ^2 for two-step sinusoidal, two-step kicked and four-step driving is shown as a function of κ for $\alpha = \pi/2$. The error in the four-step protocol decreases monotonically as κ grows. As predicted, the error grows for the two-step sinusoidal scheme. The kicked scheme performs equally poorly because α is highly commensurate with T. Tuning the flux slightly to $\alpha = 51\pi/100$ changes this behavior and the kicked protocol performs better as κ increases. The figure is taken from Ref. [1] and was compiled for lattices of 8×8 size.

into consideration. Even if a deviation described by χ is large this does not mean that there might not be other observables to that show no deviation. For the kicked system this could be the Hall drift [90, 174], in areas of the lattice where the flux remains uniform.

Moving Lattices

This section details another method to create Peierls phases. In [1] this method was presented as a moving potential on top of a static lattice. These moving lattices are typically generated by an additional set of lasers that interact via Raman transitions with the atoms trapped in the lattice [143, 144]. The frequency of the moving lattice is determined by the additional lasers by $\omega = \omega_1 - \omega_2$ and its position dependence is given by their wave vector difference $\mathbf{q} = \mathbf{k}_1 - \mathbf{k}_2$. In the tight binding approximation such a lattice potential manifests as

$$V(t) = 2K \sum_{j,k} n_{j,k} \cos(\omega t + q_x j + q_y k) \ . \tag{2.105}$$

Again, the lattice spacing is set to $a = 1$. Before the implication of this potential are explored the consequences of a more general term are explained. As in [1] it employs the

resonant single harmonic modulation of the form

$$V(t) = \sum_{j,k} j\omega n_{j,k} + K \sum_{j,k} \left[n_{j,k} v(j,k) e^{\mathrm{i}\omega t} + \text{H.c.} \right] \tag{2.106}$$

Using the same reasoning that lead to (2.59) an effective Hamiltonian can be derived ([1]):

$$H_{\text{eff}} = \sum_{j,k} \left(\mathcal{J}_x(j,k) a^\dagger_{j+1,k} a_{j,k} e^{\mathrm{i}\phi_{j,k}} + \mathcal{J}_y(j,k) a^\dagger_{j,k+1} a_{j,k} \right) + \text{H.c.} \ . \tag{2.107}$$

The renormalized hopping amplitudes are

$$\begin{aligned} \mathcal{J}_x(j,k) &= J_x \, \mathcal{J}_1 \left(2\kappa |\delta_x v(j,k)| \right), \\ \mathcal{J}_y(j,k) &= J_y \, \mathcal{J}_0 \left(2\kappa |\delta_y v(j,k)| \right), \qquad \kappa = K/\omega \end{aligned} \tag{2.108}$$

and the $\delta_{x,y}$ denote the operations:

$$\begin{aligned} \delta_x v(j,k) &= v(j+1,k) - v(j,k), \\ \delta_y v(j,k) &= v(j,k+1) - v(j,k) \ . \end{aligned} \tag{2.109}$$

The phase is given by

$$\phi_{j,k} = \arg[-\delta_x v^*(j,k)] \ . \tag{2.110}$$

The effective Hamiltonian for sinusoidal driving [Eq. (2.59)] is reproduced for

$$v(j,k) = j e^{\mathrm{i}\theta_k} / 2\mathrm{i} \ . \tag{2.111}$$

for the moving lattice potential

$$v(j,k) = e^{\mathrm{i}q_x j} e^{\mathrm{i}q_y k} \ . \tag{2.112}$$

This function does not increase in the x-direction as (2.111) does and keeps a constant modulus over the entire lattice. As a result of this the effective tunneling amplitudes are constant as a function of the lattice coordinates:

$$\begin{aligned} \mathcal{J}_x(j,k) &= J_x \, \mathcal{J}_1 \left(2\sqrt{2}\kappa \sqrt{1 - \cos q_x} \right) \ , \\ \mathcal{J}_y(j,k) &= J_y \, \mathcal{J}_0 \left(2\sqrt{2}\kappa \sqrt{1 - \cos q_y} \right) \ . \end{aligned} \tag{2.113}$$

When this result is compared with the tunneling amplitudes of the effective Hamiltonian of the sinusoidal shaking scheme Eq. (2.59) it's clear that both approaches produce a uniform flux but they remain very different. The moving lattice method thus does not have to grapple with the non-uniform tunneling amplitudes.

2.7 Summary and conclusions

In this chapter the effect of a magnetic field on a charge in lattice was introduced. The Hofstadter butterfly, i.e. the spectrum of such a system is incredibly difficult to observe in conventional systems where the charge carriers are electrons and the lattice spacings

are just a few Angstrom wide. This difficulty suggests that a possible solution would be to use a quantum simulator to generate such a spectrum. After a general introduction to the effect of a electromagnetic gauge potential on a charge in a two dimensional lattice was given, the process of how lattice acceleration can generate similar physics for neutral atoms trapped in a shaking optical lattice was explained. The schemes that were put forward in our work in Ref. [1] were then presented in detail. One of the most simple schemes, that of sinusoidal shaking, produced a uniform flux, but also came with the caveat of inhomogeneous tunneling amplitudes. This shortcoming could not be fixed by other wave-forms of the shaking, therefore more elaborate driving protocols are needed to generate the Harper-Hofstadter Hamiltonian. Two-step sinusoidal driving was explained as a scheme that showed promise, as it produced constant effective hopping amplitudes but a non-uniform flux still resulted. The severity of spatial variation in the flux could be controlled, however, by the magnitude of the driving parameter κ. To circumvent the slow dynamics, the two-split driving scheme was generalized to a four step variant, which produced an effective Hamiltonian with both a uniform flux and uniform hopping amplitudes. The two-step method could be improved upon by a kicked drive, which would show spatial variations of the flux for discrete values of one of the lattice coordinates, and would stay constant for areas in the lattice of a significant size, even for large values of the effective hopping amplitudes.

The focus on square lattices does not imply that these methods are limited to such. As long as the system permits shaking in one particular direction, the methods studied in this chapter should be generalizable to other forms of two or even three dimensional lattices. Some of potential two dimensional structures are triangular, honeycomb or brick wall lattices. The honeycomb lattice is important for simulating the Haldane model [145] and graphene [175, 176]. The brick wall lattice, which is topologically equivalent to the Haldane lattice was produced in [145, 177]. Triangular lattices produce their own challenges, as they produce staggered flux configurations [141]. In Ref. [178] the authors presented a scheme for realizing a uniform flux $\Phi = \pi/2$ with a time modulated triangular potential.

In conclusion, the methods that were presented in this chapter should be applicable to any system where shaking is a viable option. Possibly the most important systems are comprised of ultracold atoms in optical lattices. Apart from geometrical considerations, the system needs to allow for a parameter regime, where ω sets the biggest energy scale. In particular, omega should not drive inter band transitions, as this would break one of the assumptions implicit in the tight binding approximation. In the context of this chapter, this means that $\omega \gg J_{\text{eff}}, J_x, Jy$. In a typical lattice, $J \approx 100$Hz so a few kilohertz of the driving frequency should be sufficient. This should, in theory, allow for the study of the entire Hofstadter butterfly spectrum and respectively the Chern bands or Hall physics that are associated with it. Finally it should be noted that the resolution of the fine gaps in the Hofstadter spectrum is in principle limited by temperature of the lattice atoms, which can be as low as a few 10nK.

Chapter 3

Floquet magnetic monopole

3.1 Introduction

Ever since the surprisingly simple and elegant mechanism discovered by Paul A. M. Dirac [179] offered an explanation for the quantization of the electric charge, magnetic monopoles have become the subject of numerous investigations. Even before this renewed vigor in the search for magnetic monopoles, they presented a curious hypothetical case that would make Maxwell's equations more symmetric. In the following, a short, non-exhaustive summary of the historical developments and the motivation for the research of magnetic monopoles is given. An excellent review of the history, experimental and theoretic state of the research on magnetic monopoles can be found in this review article: Ref. [180]. A great overview on the theoretical front is provided in Yakov M. Shnir's book [181].

The study of magnetic monopoles revolves either around the implications of their existence or the question of if they appear in a field theory as a fundamental particle. These two focuses often go together, however, this chapter centers on the study of some of the consequences of the existence of a special case of monopole.

Dirac's work [179] investigated the consequences of a magnetic monopole within the context of quantum mechanics. Strikingly, he showed that the string-like singularity of the vector potential accompanying a monopole, even though highly contentious in classical theory, does not produce any fundamental problems in a quantum mechanical context. As noted earlier, the Dirac monopole mandates the quantization of the electric and magnetic charges. Some time passed before it could be shown that magnetic monopoles are indeed particle solutions appearing in a (Yang-Mill's) field theory. In honor of its discoverers it was named the Wu-Yang monopole [182]. After this discovery, a grand unified theory (GUT) also predicted monopoles. These, so-called t' Hooft monopoles [183], are super-heavy particles that would have been produced in a early universe and sparked a flurry of cosmological research [184–191] . Most notably, there is almost no trace of magnetic monopoles [185] in the universe, posing a formidable riddle as to why they are not observed [185, 186, 188]. With t' Hooft monopoles beyond the reach of the energy of earthbound accelerators, efforts continued to find monopoles in other field theories [192, 193].

The prediction of monopoles by GUTs, their mysterious absence and the fact that they offer a very simple explanation for the quantization of electric charge all explain the appeal of magnetic monopoles in fundamental physics research.

It is interesting to note that the study of magnetic monopoles is not limited to high energy physics and cosmology. The concept of topology links magnetic monopoles to condensed matter systems. As mentioned in Chapter 2, the role of topology in physics [135] provides a common framework for high energy physics, cosmology and certain phenomena in condensed matter physics. Topological phase transitions [194] are one famous example. D. J. Thouless, F. D. M. Haldane and J. M. Kosterlitz were awarded with the Nobel prize in 2016 for discovering these transitions. Magnetic monopoles represent one of the simplest expressions of a non-trivial topology. In this light, they also have enormous theoretical and experimental appeal in condensed matter systems. Indeed, even within the context of cosmology, condensed matter systems were explicitly proposed in Ref. [195] as a platform for analogous experiments.

There have been plenty of proposals recently for the realization of monopoles in solid state systems [196–202]. Those include spin ice [196, 197], artificial spin ice [203], spin liquids [200], charges close to surfaces [198, 202] and chiral magnets [199]. Some of these have been realized experimentally in both spin ice [204–206] and artificial spin ice [207–210]. A monopole was also simulated with a thin magnetic needle [211] and in a different experiment monopoles were connected to the unwinding of skyrmions [212].

Ultra cold atoms, with their high degree of tunability also attracted their share of proposals. The creation of magnetic monopoles was proposed for spinor condensates [213–215] and as an emergent quasiparticle from an impurity in a superfluid [201]. An experiment involving a spinor condensate is presented in [216].

With the promise of synthezising abelian and non-abelian gauge fields [146] with ultracold atoms, it even seems feasable to observe the emergence of monopoles through the simulation of gauge fields [146, 217–221] . Through the link with topoplogy, monopoles also arise in a more abstract parameter space, which also attracted attention [43, 222–227].

The new possibilities offered by ultra cold atom systems and their high degree of controllablility opens the window to the study of signatures of magnetic monopoles that do not have an immediate counterpart in GUTs. For example, monopoles that are simulated or appear as quasiparticles could become time dependent. In the context of Floquet engineering, the implications of a time periodic magnetic monopole, i.e. a Floquet magnetic monopole, has some merit as an interesting avenue of research. This will be the focus of this chapter. It is an initial look into the effects of a magnetic monopole whose charge has a simple periodic time dependence.

In Section 3.2 some introductory remarks on the Dirac monopole will be made. The appearance of magnetic charges in Maxwell's equations, as well as their quantum mechanical implications, are also commented upon. These remarks are mostly based on the treatment in [181]. Section 3.3 focuses on a charge coupled to a magnetic monopole with a rapidly oscillating magnetic charge. The quantum mechanical problem will be addressed in the large frequency limit. At the end of Section 3.3 these results are compared to an electric charge confined to a sphere, with a monopole at its center. The chapter concludes with a short discussion and outlook.

3.2 Magnetic monopoles

This section provides a short overview of some basic properties of magnetic monopoles. A more detailed analysis can be found in [180]. As mentioned in the introduction, the addition of magnetic monopoles into the Maxwell equations makes them more symmetric [228]

$$\partial_\alpha F^{\alpha\beta} = \mu_0 J_e^\beta \tag{3.1}$$

$$\partial_\alpha F^{\alpha\beta *} = \frac{1}{c} J_m^\beta \tag{3.2}$$

where $F^{\alpha\beta}$ is the Faraday tensor, $F^{\alpha\beta *} = \epsilon^{\alpha\beta\gamma\delta} F_{\gamma\delta}/2$ its dual, c is the speed of light, μ_0 the free space magnetic permeability, $J_e = (c\rho_e, \mathbf{j}_e)$ the electric four current density and $J_m = (c\rho_m, \mathbf{j}_m)$ the magnetic four current density. The Einstein summation convention is implied. In the manifest covariant form, the symmetry of Maxwell's equations is the most apparent. The Faraday tensor is related to the vector potential through

$$F^{\alpha\beta} = \partial^\alpha A^\beta - \partial^\beta A^\alpha \ . \tag{3.3}$$

The components of the vector potential are $A = (\phi/c, \mathbf{A})$, where the electric and magnetic field is given by

$$\mathbf{E} = -\nabla\phi - \partial_t \mathbf{A} \tag{3.4}$$

$$\mathbf{B} = \nabla \times \mathbf{A} \tag{3.5}$$

The modified Maxwell equations have an additional symmetry and are invariant under the transformation

$$\begin{pmatrix} \mathbf{E}' \\ \mathbf{B}' \end{pmatrix} = \begin{pmatrix} \cos[\theta] & \sin[\theta] \\ -\sin[\theta] & \cos[\theta] \end{pmatrix} \begin{pmatrix} \mathbf{E} \\ \mathbf{B} \end{pmatrix} \ , \quad \begin{pmatrix} \mathbf{j}'_e \\ \mathbf{j}'_m \end{pmatrix} = \begin{pmatrix} \cos[\theta] & \sin[\theta] \\ -\sin[\theta] & \cos[\theta] \end{pmatrix} \begin{pmatrix} \mathbf{j}_e \\ \mathbf{j}_m \end{pmatrix} \tag{3.6}$$

This symmetry is sometimes useful when performing specific calculations. This set of expressions marks the end of the presentation of the classical manifestation of a magnetic monopoles in Maxwell's equations in this chapter.

It is possible to just work with the physical fields and not worry about the issues arising from the fact that there is an apparent contradiction when combining the time-like component of Eq. (3.2) with (3.5), which results in

$$\nabla \cdot \mathbf{B} = \nabla \cdot \nabla \times \mathbf{A} \neq 0 \ . \tag{3.7}$$

The contradiction appears on the right hand side of this equation, which has to be zero, and thus forbids monopoles, if they are derived from a single vector potential. As written above this would not be an issue, if it wasn't for the Aharonov-Bohm effect in quantum mechanics: A charge that never directly couples to a magnetic field can acquire a phase through a vector potential. This phase acquisition can have real physical consequences. The gauge-independent so-called Aharonov-Bohm phase can be interpreted as a consequence of the topology of the gauge field, as will be explained shortly.

3.2.1 Dirac's monopole

A magnetic monopole can be reconciled with Maxwell's equations through several approaches. In the following paragraph, Dirac's solution is presented. The idea behind Dirac's approach is to remove the charges as sources from the Maxwell's equations and keep the original formulation intact. In practice this means that $J_m = 0$ in Eq. (3.2). The Coulomb like, spherically symmetric magnetic field originating from a magnetic charge at the origin is

$$\mathbf{B}_{\mathrm{m}} = \frac{g}{4\pi}\frac{\mathbf{r}}{r^3} \ , \tag{3.8}$$

where $\mathbf{r} = (x, y, z)$ denotes a position in space, $r = \sqrt{x^2 + y^2 + z^2}$ and g is the magnetic charge. The famous Dirac potential [179], which he proposed for the production of such a field is

$$\mathbf{A} = \frac{g}{4\pi}\left(\frac{-y}{r(r-z)}, \frac{x}{r(r-z)}, 0\right) \ , \tag{3.9}$$

which is singular along the positive z-axis. Carefully evaluating the curl of this field yields [181]

$$\mathbf{B} = \frac{g}{4\pi}\frac{\mathbf{r}}{r^3} - g\mathbf{z}\theta(z)\delta(x)\delta(y) \tag{3.10}$$

where $\mathbf{z} = (0, 0, 1)$. The first term corresponds to (3.8). The second one represents a line singularity, also known as the Dirac string, and is a consequence of the singular behavior of $\mathbf{A}$ along the positive z-axis. This singularity plays a crucial role in guaranteeing that $\nabla \cdot \mathbf{B} = 0$ and provides a physical interpretation of the origin of a monopole field. A quick calculation shows that, as demanded by Maxwell's equations,

$$\int_{B_\epsilon} \mathrm{d}V \nabla \cdot \mathbf{B} = \int_{\partial B_\epsilon} \mathrm{d}\mathbf{a} \cdot \left[\frac{g}{4\pi}\frac{\mathbf{r}}{r^3} - g\mathbf{z}\theta(z)\delta(x)\delta(y)\right] = g - g = 0 \ , \tag{3.11}$$

where B_ϵ is an infinitesimal ball with radius ϵ and ∂B_ϵ as its boundary and $\mathrm{d}\mathbf{a}$ is a surface increment. The singular nature of the vector potential "repairs" Gauss' law. Indeed, the Dirac potential can be shown to result from an infinitely tightly wound solenoid [229]

$$\mathbf{A} = -\frac{g}{4\pi}\int_0^\infty \mathrm{d}\mathbf{l}' \times \frac{\mathbf{r} - \mathbf{r}'}{(\mathbf{r} - \mathbf{r}')^3} \ , \tag{3.12}$$

where $\mathbf{r}'$ is a source point on the solenoid and $\mathrm{d}\mathbf{l}'$ is a line increment along the line going from $z = 0$ to $z = \infty$. In accordance with classical electromagnetism, it is thus appropriate to think about a monopole as an infinitely long and tight solenoid that ends at the position where the spherically symmetric magnetic field originates. The string can be of no physical significance, since its position can easily be changed with a gauge transformation: Take Eq. (3.9) and consider placing the singularity along the negative z-axis

$$\mathbf{A}' = \frac{g}{4\pi}\left(\frac{-y}{r(r+z)}, \frac{x}{r(r+z)}, 0\right) \ . \tag{3.13}$$

This potential is connected to (3.9) by the transformation

$$\mathbf{A}' = \mathbf{A} + \nabla\Lambda \ , \tag{3.14}$$

where

$$\Lambda = \frac{g}{2\pi}\phi \tag{3.15}$$

where ϕ is the polar angle in polar coordinates. This shows that the position of the string is completely arbitrary[180]. Even configurations where two strings join at the position of the pole's location exist [181]. This ambiguity is very problematic in classical physics. In the context of quantum mechanics this ambiguity is a blessing in disguise, because the Dirac string leads to the quantization of the charge. To be more precise: The requirement that it remains unobservable leads to the quantization of the charge.

The next paragraph explains how the charge quantization is derived. Schrödinger's equation for an electron coupled to a vector potential is expressed as:

$$H\Psi(\mathbf{r}) = \frac{1}{2M}\left(\mathbf{p} - e\mathbf{A}\right)^2 \Psi(\mathbf{r}) = E\Psi(\mathbf{r}) \tag{3.16}$$

where M is the mass of the charge e. The vector potential can be "gauged" away at the expense of a local phase of the wave function, so that the solution to (3.16) becomes

$$\Psi(\mathbf{r}) = \Psi_0(\mathbf{r}) e^{\mathrm{i}e\int_\gamma \mathrm{d}\mathbf{l}'\cdot\mathbf{A}(\mathbf{r}')} \tag{3.17}$$

where $\Psi_0(\mathbf{r})$ is a solution to (3.16) without $\mathbf{A}$, and $\mathrm{d}\mathbf{l}'$ is a line increment of the path γ. The contribution of the singular part of the vector potential now becomes of interest, i.e. that of the Dirac string.

Its contribution will be singled out through its magnetic field, which vanishes when outside the solenoid, and is of infinite strength inside. A charge taking a closed path around the string will pick up the phase

$$e\oint_\gamma \mathrm{d}\mathbf{l}'\cdot\mathbf{A}_{\text{string}} \tag{3.18}$$

where $\mathbf{A}_{\text{string}}$ indicates the singular part of the vector potential

$$\nabla\times\mathbf{A}_{\text{string}} = \mathbf{B}_{\text{string}} = g\mathbf{z}\theta(z)\delta(x)\delta(y)\ . \tag{3.19}$$

Now the restriction that the Dirac string is not observable will be applied. This condition is equivalent to demanding the singlevaluedness of the wavefunction after looping around the string. The single valuedness of the wavefunction translates into the condition

$$e\oint_\gamma \mathrm{d}\mathbf{l}'\cdot\mathbf{A}_{\text{string}} = 2\pi n\ , \quad n\in\mathbb{Z}\ . \tag{3.20}$$

The left hand side can be evaluated using Stoke's theorem, which results in

$$e\oint_\gamma \mathrm{d}\mathbf{l}'\cdot\mathbf{A}_{\text{string}} = e\int_S \mathrm{d}\mathbf{a}\cdot\mathbf{z}g\theta(z)\delta(x)\delta(y) \tag{3.21}$$

$$eg = 2\pi n\ , \tag{3.22}$$

where S is the surface enclosed by γ and pierced by the solenoid. This is the famous charge quantization condition. The above argument, however, is not the only possible way to argue for charge quantization. It might seem surprising, but other conceptions of monopoles lead to the same result. In the next section, the charge quantization is re-derived with the help of the Wu-Yang monopole.

3.2.2 Wu-Yang monopole

The Wu-Yang monopole differs from Dirac's monopole on a conceptual level. Dirac's potential (3.9) allowed the maintenance of Maxwell's equations without the addition of magnetic charges, through the introduction of classically meaningless singular strings. In a quantum mechanical context these strings are not a deficiency, since they imply the quantization of the electric charge. Just the existence of a single magnetic monopole in all of the universe would require that all electric charges are quantized.

The Wu-Yang monopole circumvents the singularities and maintains J_m in Eq. (3.2). The key difference lies in the choice to discard the use of a single vector potential [135]

$$\mathbf{A} = \begin{cases} \mathbf{A}^{\mathrm{S}} = \dfrac{g}{4\pi}\left(\dfrac{-y}{r(r-z)}, \dfrac{x}{r(r-z)}, 0\right) , & z \leqslant 0 \\ \mathbf{A}^{\mathrm{N}} = \dfrac{g}{4\pi}\left(\dfrac{-y}{r(r+z)}, \dfrac{x}{r(r+z)}, 0\right) , & z > 0 \ . \end{cases} \tag{3.23}$$

Note that $\mathbf{A}$ is not singular anywhere. As already mentioned in the previous section [Eq. (3.14)] $\mathbf{A}^{\mathrm{S}}$ and $\mathbf{A}^{\mathrm{N}}$ are connected by a gauge transformation

$$\mathbf{A}^{\mathrm{N}} - \mathbf{A}^{\mathrm{S}} = \nabla\Lambda \tag{3.24}$$

Indeed $\mathbf{A}$ is now in accordance with the extended Maxwell equations

$$\begin{aligned} \int_{B_\epsilon} \mathrm{d}\, V \nabla\cdot\mathbf{B} &= \int_{\partial B_\epsilon} \mathrm{d}\mathbf{a}\cdot\nabla\times\mathbf{A} \\ &= \oint_{\partial B_\epsilon^{\mathrm{N}}} \mathrm{d}\mathbf{a}\cdot\mathbf{A}^{\mathrm{N}} + \oint_{\partial B_\epsilon^{\mathrm{S}}} \mathrm{d}\mathbf{a}\cdot\mathbf{A}^{\mathrm{S}} \\ &= \oint_{\gamma_\epsilon} \mathrm{d}\mathbf{l}\cdot\left(\mathbf{A}^{\mathrm{N}} - \mathbf{A}^{\mathrm{S}}\right) \\ &= \frac{g}{2\pi}\oint_{\gamma_\epsilon} \mathrm{d}\mathbf{l}\cdot\nabla\phi \\ &= g \ , \end{aligned} \tag{3.25}$$

where $\partial B_\epsilon^{\mathrm{N,S}}$ denotes the northern and southern hemisphere of the B_ϵ and the γ_ϵ is a path running around the equator.

Arguing the charge quantization condition is even simpler for the Wu-Yang monopole than it was for Dirac's monopole.

Again a wavefunction fulfilling Eq. (3.16), but now with $\mathbf{A}$ as defined in (3.23), is considered. Consequently, this wavefunction can be split into a part Ψ^{N} that is defined on the northern hemisphere and Ψ^{S}, which is defined on the southern hemisphere. A gauge transformation connects the two functions according to

$$\Psi^{\mathrm{S}}(\mathbf{r}) = e^{-\mathrm{i}e\Lambda}\Psi^{\mathrm{N}}(\mathbf{r}) \ . \tag{3.26}$$

The entire wavefunction covering northern and southern hemisphere has to be single valued. Specifically at the equator ($\theta = \pi/2$) and for $\phi = 0, 2\pi$, single-valuedness is only possible if $eg = 2\pi n$, which again is the quantization condition derived for Dirac's

monopole. In conclusion, with Dirac's monopole no changes need to be made to Maxwell's equations, while Wu-Yang's monopole is consistent with the introduction of magnetic charges into Maxwell's equations. Both monopoles result in the same charge quantization condition.

3.3 A Floquet-Dirac monopole

In this section the quantum mechanical problem of a charge coupled to a time dependent magnetic monopole is examined. As before, minimal coupling is used to couple the charge to the time dependent vector potential

$$H(t) = \frac{1}{2M}[\mathbf{p} - e\mathbf{A}(t, \mathbf{r})]^2 \ , \tag{3.27}$$

where $\mathbf{A}(t, \mathbf{r})$ is Dirac's potential (3.9) with

$$g \to g\{1 - 2\Theta[\sin(\omega t - \pi)]\} = gf(t) \ , \tag{3.28}$$

where $\Theta(\cdot)$ is the unit step function (see Fig. 3.1). This means that the charge changes its polarity in a step-like manner from positive to negative with the frequency ω. This time dependence was chosen so that at each point in time, the charge quantization condition (3.22) is trivially fulfilled.

Expanding the square in Eq. (3.27) leads to

$$H(t) = \frac{1}{2M}\mathbf{p}^2 - \frac{e}{2M}[\mathbf{p}\mathbf{A}(t, \mathbf{r}) + \mathbf{A}(t, \mathbf{r})\mathbf{p}] + \frac{e^2}{M}\mathbf{A}(t, \mathbf{r})^2 \tag{3.29}$$

$A(t, \mathbf{r})$ can be shown to be in the Coulomb gauge by considering

$$\int_{B_\epsilon} \mathrm{d}\, V \nabla \cdot \mathbf{A} = \int_{\partial B_\epsilon} \mathrm{d}\mathbf{a} \cdot \mathbf{A} = 0 \ . \tag{3.30}$$

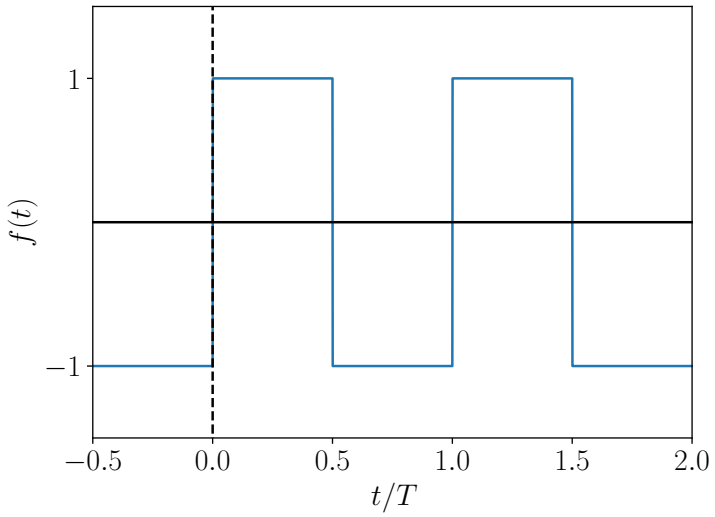

Figure 3.1: The magnetic charge $g(t) = gf(t)$ changes its polarity with the period $T = 2\pi/\omega$ in a step-like manner, to ensure that at each instance in time $eg = 2\pi n$.

The last equation holds thanks to the fact that $\mathbf{A} \propto \mathbf{e}_\phi$, where e_ϕ is the unit vector in the ϕ-direction. Conveniently this implies that $[\mathbf{p}, \mathbf{A}] = 0$:

$$\begin{aligned} \mathbf{pA}\Psi &= -\mathrm{i}\nabla \cdot (\mathbf{A}\Psi) && (3.31)\\ &= -\mathrm{i}\Psi\nabla \cdot \mathbf{A} - \mathrm{i}\mathbf{A} \cdot \nabla\Psi && (3.32)\\ &= \mathbf{Ap}\Psi \ . && (3.33) \end{aligned}$$

With the Coulomb gauge established, Eq. (3.29) simplifies to

$$H(t) = \frac{1}{2M}\mathbf{p}^2 - \frac{e}{M}\mathbf{pA}(t, \mathbf{r}) + \frac{e^2}{2M}A(t, \mathbf{r})^2 \tag{3.34}$$

Due to the step-like shape of $f(t)$ ($f(t)^2 = 1$ in Fig. 3.1), the last term is time independent. With the introduction of

$$\mathbf{C}(\mathbf{r}) = \left(\frac{-y}{r(r-z)}, \frac{x}{r(r-z)}, 0\right) \tag{3.35}$$

Eq. (3.34) can be written as

$$H(t) = \frac{\mathbf{p}^2}{2M} - \frac{1}{4\pi}\frac{ge}{M}f(t)\mathbf{p} \cdot \mathbf{C}(\mathbf{r}) + \frac{1}{32\pi^2}\frac{e^2g^2}{M}\mathbf{C}(\mathbf{r})^2 \ . \tag{3.36}$$

It is helpful to identify [57]

$$\begin{aligned} H_0 &= \frac{\mathbf{p}^2}{2M} + \frac{1}{32\pi^2}\frac{e^2g^2}{M}\mathbf{C}(\mathbf{r})^2 && (3.37)\\ V &= -\frac{1}{4\pi}\frac{ge}{M}\mathbf{p} \cdot \mathbf{C}(\mathbf{r}) \ . && (3.38) \end{aligned}$$

The goal of this section is to study the high frequency behavior of $H(t)$, so it is subjected to the expansion in Eq. (1.63). Considering the specific form of $f(t)$ and V, Eq. (1.63) becomes

$$\begin{aligned} H_{\text{eff}} &= H_0 + \frac{\pi^2}{24\omega^2}[[V, H_0], V] + \mathcal{O}(1/\omega^3) && (3.39)\\ &= H_0 + \frac{1}{768\omega^2}\frac{g^2e^2}{M^3}[[\mathbf{p} \cdot \mathbf{C}(\mathbf{r}), \mathbf{p}^2], \mathbf{p} \cdot \mathbf{C}(\mathbf{r})] \\ &\qquad + \frac{1}{768\pi^2\omega^2}\frac{g^4e^4}{M^3}[[\mathbf{p} \cdot \mathbf{C}(\mathbf{r}), \mathbf{C}(\mathbf{r})^2], \mathbf{p} \cdot \mathbf{C}(\mathbf{r})] \ . && (3.40) \end{aligned}$$

The above expression for H_{eff} reveals that H_0 is a highly non-trivial Hamiltonian featuring the singular static potential $e^2g^2/32\pi^2M\mathbf{C}(\mathbf{r})^2$. The Hamiltonian H_0 represents the time averaged Hamiltonian $H(t)$ and in the limit of $\omega \to \infty$. The following section is dedicated to solving the static Schrödinger equation $H_0\Psi = E\Psi$.

3.3.1 High frequency limit

The time-independent problem (3.16) has been solved classically as well as quantum mechanically. Both solutions are presented in [180, 181]. Extensive use of symmetries can

help in finding the classical trajectories or eigenfunctions of the stationary Schrödinger equation. Unfortunately, at the time this thesis was written, none of these symmetries seemed to apply to the problem described in this section. However, some strategies for finding exact solutions put forth in [181] proved tremendously helpful.

The stationary Schrödinger equation under consideration is

$$\begin{aligned} H_0\Psi &= E\Psi \\ \left[-\frac{\Delta}{2M}+\frac{1}{32\pi^2}\frac{e^2g^2}{M}\frac{1}{r^2}\frac{r+z}{r-z}\right]\Psi &= E\Psi \\ \left[-\frac{1}{r^2}\partial_r r^2\partial_r-\frac{1}{r^2\sin(\theta)}\partial_\theta\sin(\theta)\partial_\theta-\frac{1}{r^2\sin(\theta)^2}\partial_\phi^2+\frac{b}{a}\frac{1}{r^2}\frac{1+\cos(\theta)}{1-\cos(\theta)}\right]\Psi &= \frac{E}{a}\Psi\ . \end{aligned} \tag{3.41}$$

In the last equation the switch to spherical coordinates

$$\begin{aligned} x &= r\sin(\theta)\cos(\phi) \\ y &= r\sin(\theta)\sin(\phi) \\ z &= r\cos(\theta) \end{aligned} \tag{3.42}$$

was made and the constants

$$a=\frac{1}{2M}\ ,\quad b=\frac{e^2g^2}{32\pi^2M} \tag{3.43}$$

were introduced. No previous account of Eq. (3.41) or its solutions could be found at the time of writing this thesis. The only reference that provided some guidance to solving this problem was the solution to the static problem Eq. (3.16) given in e.g. Ref. [181]. This solution was then modified to accommodate the potential in Eq. (3.41)

$$V_{\rm s}=\frac{1}{32\pi^2}\frac{e^2g^2}{M}\frac{1}{r^2}\frac{r+z}{r-z}\ , \tag{3.44}$$

which is singular along the line $z>0$. This term is responsible for preventing the more elegant use of the algebraic methods made possible by making use of symmetries. In the following a detailed account of an explicit solution to Eq. (3.41) is given. Because no prior solution to this problem was known to the author, there is some additional merit in such an exhaustive treatment.

Separations of variable

The first step in finding the eigenfunctions of H_0 is separating the angular and radial variables of Ψ:

$$\Psi(r,\theta,\phi)=R(r)Y(\theta,\phi) \tag{3.45}$$

inserting this into (3.41) yields

$$\left[-\partial_r r^2\partial_r-r^2\frac{E}{a}\right]R(r)=\lambda R(r) \tag{3.46}$$

$$\left[\frac{1}{\sin(\theta)}\partial_\theta\sin(\theta)\partial_\theta+\frac{1}{\sin(\theta)^2}\partial_\phi^2-\frac{b}{a}\frac{1+\cos(\theta)}{1-\cos(\theta)}\right]Y(\theta,\phi)=\lambda Y(\theta,\phi) \tag{3.47}$$

where λ is the separation constant.

Furthermore, Ψ is separated into an azimuthal and a polar part

$$Y(\theta,\phi) = \vartheta(\theta)\varphi(\phi) \tag{3.48}$$

which leads to the two equations

$$\left[\sin(\theta)\partial_\theta \sin(\theta)\partial_\theta - \sin(\theta)^2 \frac{b}{a}\frac{1+\cos(\theta)}{1-\cos(\theta)} - \lambda\sin(\theta)^2\right]\vartheta(\theta) = \beta\vartheta(\theta) \tag{3.49}$$

$$-\partial_\phi^2\varphi(\phi) = \beta\varphi(\phi) \tag{3.50}$$

Angular part of Ψ

Eq. (3.50) can be integrated immediately, which results in

$$\varphi(\phi) = D_1 e^{\mathrm{i}\sqrt{\beta}\phi} + D_2 e^{-\mathrm{i}\sqrt{\beta}\phi} \tag{3.51}$$

Following the standard procedure, the choice $D_2 = 0$ can be made. This choice implies $\beta = m^2 \in \mathbb{Z}$, since the wave function has to be single valued.

This can be reinserted into (3.49). A change of variables will help to cast (3.49) into a form that will be more amenable:

$$z = \cos(\theta) \tag{3.52}$$

$$\partial_\theta = \frac{\mathrm{d}z}{\mathrm{d}\theta}\frac{\mathrm{d}}{\mathrm{d}z} = -\sqrt{1-z^2}\partial_z \tag{3.53}$$

Note that z is not the z-coordinate. Eq. (3.49) then becomes

$$\left[-2z\partial_z + (1-z^2)\partial_z^2 - \lambda - \frac{b(1+z)^2 + am^2}{a(1-z^2)}\right]\vartheta(z) = 0 \tag{3.54}$$

This is where the solution deviates from the method presented in [181]. Here, one has to look for solutions of the form

$$\vartheta(z) = (1-z)^\mu(1+z)^\nu F(z) \tag{3.55}$$

Inserting this expression into Eq. (3.54) will yield a condition for μ and ν , resulting in the elimination of the singularities at $z = \pm 1$. This is expressed as:

$$\left(\frac{-4\mu^2 + m^2 + 4b/a}{2(z-1)} + \frac{4\nu^2 - m^2}{2(z+1)} - \mu^2 - 2\mu\nu - \mu - \nu^2 - \nu - \lambda + b/a\right)F(z) \tag{3.56}$$

$$-2[\nu - \mu + (1-\mu-\nu)z]\partial_z F(z) + (1-z^2)\partial_z^2 F(z) = 0 \tag{3.57}$$

The aforementioned singularities are eliminated when making the choice

$$\mu = \pm\frac{1}{2}\sqrt{m^2 + 4b/a}\ , \quad \nu = \pm\frac{m}{2} \tag{3.58}$$

After making the substitution $x = (1-z)/2$ (x is just an ad-hoc variable) this can be brought into the form

$$\begin{aligned} -(2\mu\nu + \mu + 2\nu^2 + \nu + \lambda)F(x) + [1 + 2\mu - (2 + 2\mu + 2\nu)x]\partial_x F(x) \\ + x(1-x)\partial_x^2 F(x) = 0\ . \end{aligned} \tag{3.59}$$

This is the standard form of the hypergeometric differential equation

$$-ABF(x)+[C-(A+B+1)x]\partial_x F(x)+x(1-x)\partial_x^2 F(x)=0 \tag{3.60}$$

which is solved by

$$F(x)=D_1\,{}_2\mathrm{F}_1(A,B,C;x)+D_2\,(-1)^{1-C}x^{1-C}{}_2\mathrm{F}_1(1+A-C,1+B-C,2-C;x)\ , \tag{3.61}$$

where ${}_2\mathrm{F}_1(A,B,C;x)$ is the ordinary hypergeometric function. The constants are

$$AB=\lambda+\nu+2\nu^2+\mu+2\nu\mu \tag{3.62}$$
$$A+B=1+2\mu+2\nu \tag{3.63}$$
$$C=1+2\mu \tag{3.64}$$

which can be solved for A and B

$$A=\frac{1}{2}+\nu+\mu-\frac{\sqrt{a+4b-4a\lambda}}{2\sqrt{a}} \tag{3.65}$$
$$B=\frac{1}{2}+\nu+\mu+\frac{\sqrt{a+4b-4a\lambda}}{2\sqrt{a}} \tag{3.66}$$

As in [181] it can be demanded that the first argument of the hypergeometric function is some negative number $-l$ where $l\in\mathbb{N}_0$ to ensure that the expansion of ${}_2\mathrm{F}_1$ in z is finite. This is important in guaranteeing that Ψ is regular. For now

$$m\geqslant 0\ . \tag{3.67}$$

With this choice, the first independent solution of (3.61) ($D_2=0$) can be selected. Crucially, it fixes λ ($l>\mu$):

$$\lambda=\frac{a+4b}{4a}-\left(l+\frac{1}{2}+\nu+\mu\right)^2 \tag{3.68}$$

It is found that

$$F(z)\propto{}_2\mathrm{F}_1[-l,1+l+2\mu+2\nu,1+2\mu,(1-z)/2] \tag{3.69}$$

In the following, the use of the connection of the hypergeometric functions to the Jacobi polynomials is made [230]

$$P_n^{(\alpha,\beta)}(z)=\frac{\Gamma(a+n)}{\Gamma(a)\Gamma(n+1)}{}_2\mathrm{F}_1[-n,1+n+\alpha+\beta,1+\alpha,(1-z)/2]\ , \tag{3.70}$$

where $\Gamma(\cdot)$ denotes the gamma-function. The Jacobi Polynomials are represented as:

$$P_n^{(\alpha,\beta)}(z)=\frac{(-1)^n}{2^n n!}(1-z)^{-\alpha}(1+z)^{-\beta}\frac{\mathrm{d}^n}{\mathrm{d}z^n}\left\{(1-z)^{\alpha+n}(1+z)^{\beta+n}\right\} \tag{3.71}$$

Everything can now be put together ($\alpha=2\mu,\ \beta=m=2\nu>0$) resulting in the solution of the angular part of the wave function

$$\vartheta_{l,m}(z)\varphi_m(\phi)\propto e^{\mathrm{i}m\phi}(1-z)^{-\mu}(1+z)^{-\nu}(-1)^l\frac{\mathrm{d}^l}{\mathrm{d}z^l}\left\{(1-z)^{2\mu+l}(1+z)^{m+l}\right\}\ . \tag{3.72}$$

If it was only necessary to find a mathematical solution to Eq. (3.41) then the heavy lifting would be over. However, since this is a physical problem, the regularity of $\vartheta(z)$ at $z = \pm 1$ has to be guaranteed. Additionally, it must be shown that a complete orthonormal set can be constructed from $\vartheta(z)$, ensuring that the Hilbert space associated to H_0 is not trivially empty.

Indeed, from the above definition it can be shown that $\vartheta_{l,m}(z)$ is a regular function at the poles as long as $-l \leqslant m$. This extends the range of m for which the lower bound of zero was set in (3.67).

In the following the accordance of the lower bound $-l \leqslant m$ with the normalization condition will be demonstrated.

$$\int_0^{2\pi} \mathrm{d}\phi \varphi_m(\phi)^* \varphi_{m'}(\phi) \int_0^{\pi} \sin(\theta) \mathrm{d}\theta \, \vartheta_{l,m}(\theta) \vartheta_{l',m'}(\theta) = \delta_{m,m'} \delta_{l,l'} \tag{3.73}$$

The ϕ part is fulfilled so the more involved θ integral remains to be checked. Without loss of generality, it is assumed that $l' > l$

$$\begin{aligned} \int_{-1}^{1} \mathrm{d}z \, \vartheta_{l,m}(z) \vartheta_{l',m}(z) = \int_{-1}^{1} \mathrm{d}z \, (1-z)^{-2\mu} (1-z)^{-m} & \\ \times (-1)^{l+l'} \frac{\mathrm{d}^l}{\mathrm{d}z^l} \left\{ (1-z)^{2\mu+l} (1+z)^{l+m} \right\} & \qquad (3.74) \\ \times \frac{\mathrm{d}^{l'}}{\mathrm{d}z^{l'}} \left\{ (1-z)^{2\mu+l'} (1+z)^{l'+m} \right\} & \\ = \sum_{n=0}^{l} \binom{l}{n} \frac{(-1)^n (l+2\mu)!}{(l+2\mu-n)!} \frac{(l+m)!}{(m+n)!} & \\ \times \int_{-1}^{1} \mathrm{d}z \, (1-z)^{l-n} (1+z)^n & \qquad (3.75) \\ \times \frac{\mathrm{d}^{l'}}{\mathrm{d}z^{l'}} \left\{ (1-z)^{2\mu+l'} (1+z)^{l'+m} \right\} & \end{aligned}$$

The polynomial $(1-z)^{l-n}(1+z)^n$ can be expanded and partially integrated until the respective power of z is exhausted. The evaluation of terms such as

$$\frac{\mathrm{d}^{l'-k}}{\mathrm{d}z^{l'-k}} (1-z)^{2\mu+l'} (1+z)^{l'+m} \Big|_{-1}^{1} \tag{3.76}$$

is what remains. If the lower bound $-l \leqslant m$ is ensured, this expression always vanishes. The calculations above have established the following condition: as long as $l \neq l'$ the two solutions are orthogonal.

The final task is to find the normalization constant of of (3.72) for $l = l'$. The following calculation can be made:

$$\begin{aligned} \mathcal{N}^2 = \int_{-1}^{1} \mathrm{d}z \, \vartheta_{l,m}(z) \vartheta_{l,m}(z) = 2^{1+2l+m+2\mu} \frac{\Gamma(1+l)\Gamma(1+l+m)\Gamma(1+l+2\mu)}{\Gamma(2+2l+m+2\mu)} & \\ \times \left(\frac{\Gamma(1+l+2\mu)}{\Gamma(1+2\mu)} + \frac{\Gamma(1+l+m)}{\Gamma(1+m)} \right) & \qquad (3.77) \end{aligned}$$

So that for $-l < m$

$$Y_{l,m}(z,\phi) = \frac{e^{\mathrm{i}m\phi}}{\sqrt{2\pi}\mathcal{N}}(1-z)^{-\mu}(1+z)^{-m/2}(-1)^l \frac{\mathrm{d}^l}{\mathrm{d}z^l}\left\{(1-z)^{2\mu+l}(1+z)^{l+m}\right\} \ , \tag{3.78}$$

This completes the construction of the angular part of the wavefunction Ψ.

Connection to the free space solution

A simple check can be conducted to provide further support for the validity of $Y_{l,m}(z,\phi)$: It must reproduce the properties of the free space solution for $g = 0$. Superficially, the condition $-l < m$ is surprising, since it does not coincide with the commonly expected bounds $-l < m < l$. It is also not at all obvious that the free space separation constant in Eq. (3.68) will become $\lambda = -l(l+1)$ once $g = 0$.

For the lower bound $-l < m < 0$, an inspection of Eq. (3.68) reveals that:

$$\lambda = -l(l+1) \tag{3.79}$$

which correctly reproduces the free space limit. Since m has no upper bound it is not immediately evident how Eq. (3.68) fits the common free space bounds on m. The upper bound $0 < m < l$ is disguised by the way m is counted, and is not due to the regularity of $Y_{l,m}(z,\phi)$, which is always guaranteed for $m > 0$.

For $m > 0$ Eq. (3.68) implies

$$\lambda = \frac{1}{4} - \left(l + \frac{1}{2} + m\right)^2 \tag{3.80}$$

$$= -(l+m)(l+m+1) \tag{3.81}$$

$$= -l'(l'+1) \tag{3.82}$$

where $l' = l + m$ was introduced. This correctly reproduces the canonical form. $l \geqslant 0$ still has to hold true, which implies that all the allowed values of m for a fixed l' lie in the range $l' - l = m < l'$. This concludes the usual $2l+1$ degeneracy of the eigenvalue $\lambda = -l(l+1)$ and thus reproduces the free space result. It can further be shown that the wave function correctly reproduces the expected free space expressions.

Radial part of Ψ

The separation constant is $\lambda < 0$ for all values of the magnetic charge, m and l. This implies that the centrifugal potential is always repulsive [181]. Therefore it can be concluded that there are no bound solutions. The radial part of the Schrödinger equation is

$$\frac{-1}{2M}\left(\frac{2}{r}\partial_r + r^2\partial_r^2 + \frac{\lambda}{r^2}\right)R(r) = ER(r) \tag{3.83}$$

The physically viable solution to this equation is

$$R(r) \propto \frac{1}{\sqrt{kx}}\mathcal{J}_{1+4\lambda}(kx) \tag{3.84}$$

where $k = \sqrt{2ME}$

3.3.2 Charge confined to a sphere

A simple way to investigate the consequences of adding of the unusual potential (3.44) is to confine the charge to a sphere. In this way, the radial solution is no longer of interest and the problem above can be compared to a static monopole at a center of said sphere.

The latter system is described by the Hamiltonian

$$H_{\text{Haldane}} = \mathbf{\Lambda}^2/2MR^2 \tag{3.85}$$

where $\Lambda = \mathbf{r} \times [-i\hbar\nabla + e\mathbf{A}(\mathbf{r})]$. The spectrum of H_{Haldane} as found in [231] and [232] is given by the Landau levels

$$E_{\text{Haldane}} = [l(l+1) + (2l+1)s]/2MR^2 \ , \tag{3.86}$$

where l and $2s = n$ are integer.

What happens if (3.41) is constricted to a sphere? From Eq. (3.47) and Eq. (3.41) the energies come out to

$$E = \frac{-\lambda}{2MR^2} \tag{3.87}$$

At this point the quantization of the charge $eg = 2\pi n$ can be reintroduced into the equations, resulting in $\mu = \sqrt{m^2+n^2}/2$. As explained earlier, for $m > 0$ the change $l \to l - m$ with the upper bound $m < l$ can be made. Altogether this yields

$$\begin{aligned} E = \frac{1}{2MR^2}\Bigg\{ l(l+1) - \frac{1}{2}(2l+1)\left(|m| - \sqrt{m^2+n^2}\right) \\ + \frac{1}{2}\left(|m|\sqrt{m^2+n^2} - m^2\right)\Bigg\} \end{aligned} \tag{3.88}$$

It is interesting to note that the above equation coincides with Eq. (3.86) for $m = 0$. As m grows larger, it slowly approaches the free space solution. This can be seen in Fig. 3.2 where it is clearly shown that the degeneracy of the free space (or Landau levels) is partially lifted.

3.4 Summary and outlook

The main result of the work in this chapter is the construction of the Hilbert space belonging to an electric charge coupled to a Dirac monopole whose magnetic charge rapidly switches polarity. The surprising aspect of this result is that the Schrödinger equation could be solved, despite the line-like singularity in the potential V_{s} in (3.44). This problem and its solution in other contexts has not been previously published. That is not to say that the mathematical tools to find such a solution are not well established, because they are.

However, as in the case of the static monopole, no bound solutions to the problem exist. To ameliorate this fact and in order to study the discrete angular energy spectrum, the charge was confined to a sphere. The spectrum was compared to both sets of special conditions: A charge on a sphere with a regular magnetic monopole and that of the large frequency limit of an oscillating magnetic charge.

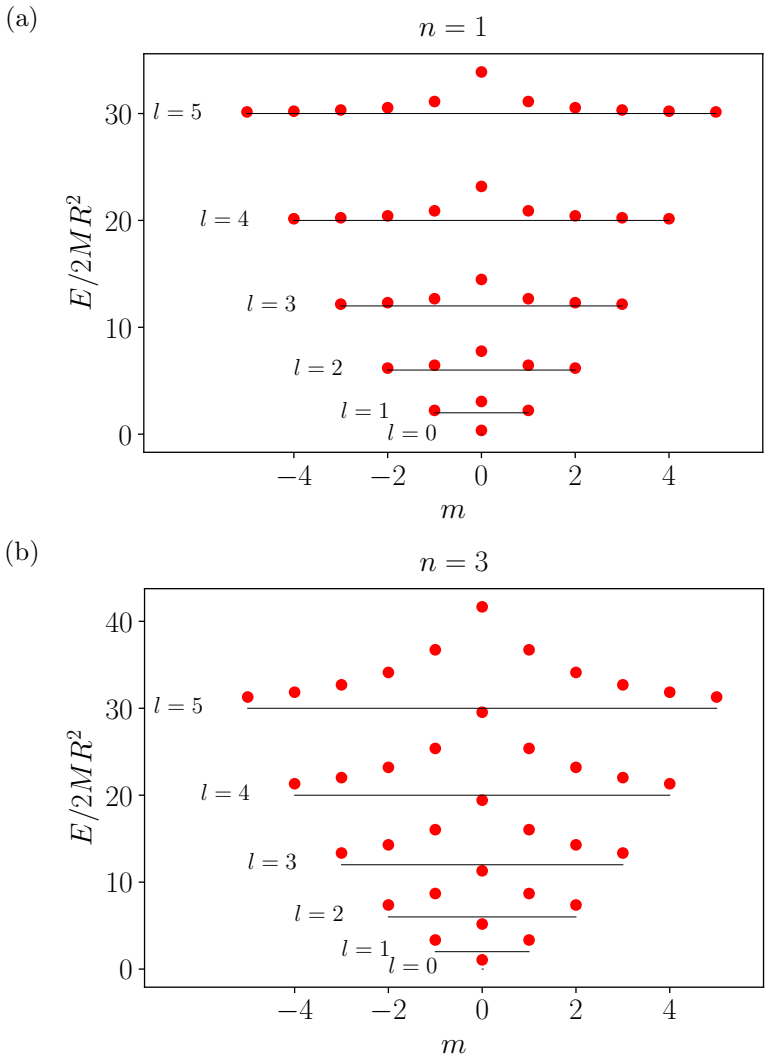

Figure 3.2: λ for two different values of (a) $n = 1$ and (b) $n = 3$. For $m = 0$ the energies E_{Haldane} and E are the same. As the value of $|m|$ increases, the energies approach the degenerate free space levels indicated by thin black lines. As opposed to the free space levels and the E_{Haldane} the modified energies partially lift the degeneracy for a given l.

The results presented in this chapter create a foundation on which to build a more comprehensive analysis of the Floquet magnetic monopole. Several things were not addressed with sufficient rigor, and are the subject of the author's ongoing research. Two of these are the convergence of the large frequency expansion in Eq. (3.39) and the identification of gauge invariant observables, which make a convincing case for the physical nature of the time independent Hamiltonian H_0. A appropriate candidate for such an observable would be the scattering cross-section of V_s.

Chapter 4

Kinetic driving

In Chapter 2 periodically shaking a two-dimensional lattice was investigated as a means for generating an artificial magnetic field. As noted in Chapter 2, shaking falls under the category of potential or diagonal driving, because the time periodic terms only affect the on-site potential terms for both the lab and the lattice frame. Naturally, other forms of driving have been considered experimentally and theoretically. Given the typical structure of tight binding models

$$H = H_{\mathrm{T}} + H_{\mathrm{pot}} + H_{\mathrm{int}} \ , \tag{4.1}$$

where H_{T} is the kinetic energy, H_{pot} describes the on-site energies and H_{int} the on-site interactions. Driving can be divided into three broad categories: 1. potential driving, 2. interaction driving and 3. kinetic driving. In the previous chapters, the way potential driving modifies the tunneling dynamics in the high-frequency limit was discussed in detail. The second category involves time-periodic manipulations of the interaction energy. Experimentally this manipulation can be accomplished via Feshbach resonances [18]. This type of periodic modulation was considered e.g. in Refs. [233–236] and it can produce dynamical gauge potentials: In the high frequency limit the hopping amplitudes aquire phases, depending e.g. on the number of particles occupying its neighboring site [237]. An interesting opportunity these unusual phase factors offer is the simulation of anyon physics [238]. Although these are not fundamental particles in three dimensions they can be fundamental in two. Apart from that, anyons are important quasiparticles in Hall-physics [239].

This chapter focuses on the study of the third category, namely kinetic driving. Oscillations of the tunneling amplitude are used in lattice modulation spectroscopy of cold atoms [240–243] and are usually done in such a way that the hopping amplitude is subject to a small variation around a large constant value. In the work presented here [2] the nearest-neighbor hopping amplitude is allowed to vary between negative and positive values. It is an unusual form of a periodic time dependence, which produces an equally unusual effective Hamiltonian. The new Hamiltonian will feature various long- and short-range interaction terms and different types of correlated hoppings. Because of its atypical nature, this effective Hamiltonian is an example of a periodically driven system that possesses new and interesting properties that warrant study for their own sake. This fact sets it apart from those used simply as tools for simulation. Indeed, as this chapter will show, this effective Hamiltonian produces a very intriguing ground state that will be investigated thoroughly in the next two chapters.

This chapter is structured as follows: In Section 4.1 the effective Hamiltonian is derived for periodic and hard wall boundary conditions. The section is completed by commenting on various extensions of the kinetically driven Bose-Hubbard model. In Section 4.2 the specific form of cosinusoidal driving is discussed by studying the effective Hamiltonian in position space as well as momentum space. In position space the large frequency approximation produces a host of correlated hoppings, as well as local and non-local interactions. The range of these interactions and hoppings is detailed for large system sizes. This is followed by an investigation of various momentum space observables, where strong evidence for quasi-condensation in two non-zero momentum modes has been compiled. From these preliminary observations a simple description of the ground state for small values of the driving parameter emerges. This is detailed in Section 4.2.3. An intuitive picture forms, explaining the peaks in the momentum density. For larger values of the driving parameter, this simple picture breaks down and a cat-like ground state emerges. In Section 4.2.5 this breakdown in the context of a quantum phase transition is investigated. Through the use of various measures, a Kosterlitz-Thouless transition from Mott to superfluid is found to take place in a physically meaningful regime of the driving. Section 4.3 is concerned with hard wall boundary conditions, in which the effective Hamiltonian for cosinusoidal driving is specified and the ground state properties are discussed once again. In Section 4.4 a potential experimental implementation of the proposed kinetic driving is discussed.

4.1 Kinetic driving of a Bose-Hubbard model

The model at the center of this chapter is the kinetically driven one-dimensional Bose-Hubbard model

$$H(t) = -J(t)\sum_x \left(a^\dagger_{x+1}a_x + \text{H.c.}\right) + \frac{U}{2}\sum_x^{L-1} n_x(n_x-1)\ . \tag{4.2}$$

The summation limits are not yet specified, in order to accommodate both periodic and hard wall boundary conditions. As in the previous chapters, the creation and annihilation operators are bosonic, U is the Hubbard interaction energy and $J(t)$ is some T-periodic function with zero time average. As in all previous models, the lattice spacing is set to $a = 1$, $\hbar = 1$. L is the number of lattice sites.

This section is dedicated to the derivation of the effective time independent Hamiltonian. Its quasienergy spectrum will then be compared to the spectrum calculated through $U(T, 0)$, the time evolution after one period of the driving. As explained in detail in Chapter 1, both the quasienergies calculated with $U(T, 0)$ and those of the exact effective Hamiltonian should coincide in the limit of large frequencies.

The methods used to derive the effective Hamiltonian are the same as the ones presented in Chapter 1 (see e.g. (1.77) and following). The effective Hamiltonian will be derived for both: periodic and hard wall boundary conditions (HWBC). The derivation begins with the introduction of periodic boundary conditions (PBC), i.e. a ring lattice or simply: a ring. The differences and similarities between both types of boundary conditions (periodic, hard walls) will become an important theme in this and the following chapter. The boundary conditions have significant consequences both physically and mathematically.

4.1.1 Periodic Boundary Conditions

The kinetically driven Hamiltonian for PBC, i.e. $a_L = a_0$, is

$$H_{\mathrm{pbc}}(t) = -J(t)\sum_{x=0}^{L-1}\left(a_{x+1}^{\dagger}a_x + \mathrm{H.c.}\right) + \frac{U}{2}\sum_{x=0}^{L-1} n_x(n_x-1)\ . \tag{4.3}$$

The calculation of the effective Hamiltonian proves to be simpler in the momentum representation, which differentiates it from the calculations in previous chapters. To that extent $a_x^{\dagger}, a_x$ have to be represented in momentum space. The difference between plane wave modes and stationary modes will become important later so Eq. (1.117) from Chapter 1 is repeated here:

$$a_x = \frac{1}{\sqrt{L}}\sum_{l=0}^{L-1} e^{-\mathrm{i}k_l x}a_{k_l}\ , \tag{4.4}$$

$$a_{k_l} = \frac{1}{\sqrt{L}}\sum_{x=0}^{L-1} e^{\mathrm{i}k_l x}a_x\ , \tag{4.5}$$

where

$$k_l = \frac{2\pi}{L}l\ , \quad l\in\mathbb{Z}\ . \tag{4.6}$$

The completeness of the plane wave mode functions $\exp(\mathrm{i}k_l x)$ in combination with the PBC guarantees the preservation of the commutation relations $[a_{k_l}, a_{k_m}] = [a_{k_l}^{\dagger}, a_{k_m}^{\dagger}] = 0$ and $[a_{k_l}, a_{k_m}^{\dagger}] = \delta_{km}$. In the momentum representation the Hamiltonian becomes:

$$H_{\mathrm{pbc}}(t) = -2f(t)\sum_{l=0}^{L-1}\cos(k_l)a_{k_l}^{\dagger}a_{k_l} + \frac{U}{2L}\sum_{l,m,n,p=0}^{L-1}\delta_{k_l+k_m,k_n+k_p}a_{k_p}^{\dagger}a_{k_n}^{\dagger}a_{k_m}a_{k_l}\ . \tag{4.7}$$

The $\delta_{k_l+k_m,k_n+k_p}$ ensures quasimomentum conservation. For all momenta the condition

$$k_{l+L} = k_l \tag{4.8}$$

is implied. The $\cos(k_l)$ in the first term in Eq. (4.7) together with $f(t)$ constitutes the instantaneous dispersion relation of the band. Kinetic driving is thus a specific form of direct band driving. For most numerical computations the Brillouin zone $[0, 2\pi)$ was chosen. This affects the summation limits and the specific numerical implementations, but has no bearing on the physical interpretation. To keep the presentation symmetric, all the figures and most of the text will reference the Brillouin zone $(-\pi, \pi]$. The two choices are switched between by identifying $(-\pi, 0]$ with $(\pi, 2\pi]$.

The unitary transformation

$$W(t) = e^{-2\mathrm{i}F(\omega t)\sum_{k_l=0}^{L-1}\cos(k_l)a_{k_l}^{\dagger}a_{k_l}}\ , \tag{4.9}$$

where

$$F(\omega t) = \int_0^t \mathrm{d}t'\, f(t) \tag{4.10}$$

facilitates the transformation into the moving frame. The transformed Hamiltonian is given by [see Eq. (1.77)]

$$H'_{\mathrm{pbc}}(t) = \mathrm{i}\dot{W}(t)W(t)^\dagger + W(t)H(t)W(t)^\dagger \ . \tag{4.11}$$

A slightly more involved calculation compared to that in Chapter 1 [(1.80)] has to be completed in order to find the Hamiltonian in the moving frame. One can reuse the technique however and define

$$\begin{aligned} f(\lambda) :&= e^{-\mathrm{i}\lambda\cos(k_u)a^\dagger_{k_u}a_{k_u}}a^\dagger_{k_p}a^\dagger_{k_n}a_{k_m}a_{k_l}e^{\mathrm{i}\lambda\cos(k_u)a^\dagger_{k_u}a_{k_u}} \\ &= U(\lambda)a^\dagger_{k_p}a^\dagger_{k_n}a_{k_m}a_{k_l}U^\dagger(\lambda) \ . \end{aligned} \tag{4.12}$$

Differentiation with respect to λ results in

$$\begin{aligned} \partial_\lambda f(\lambda) &= \mathrm{i}\cos(k_u)U(\lambda)\left[a^\dagger_{k_p}a^\dagger_{k_n}a_{k_m}a_{k_l}, a^\dagger_{k_u}a_{k_u}\right]U^\dagger(\lambda) \\ &= \mathrm{i}\cos\left(k_u\right)\left(\delta_{lu}+\delta_{mu}-\delta_{nu}-\delta_{pu}\right)f(\lambda) \ , \end{aligned} \tag{4.13}$$

which implies that

$$f(\lambda) = e^{\mathrm{i}\lambda\cos(k_u)(\delta_{lu}+\delta_{mu}-\delta_{nu}-\delta_{pu})}a^\dagger_{k_p}a^\dagger_{k_n}a_{k_m}a_{k_l} \ . \tag{4.14}$$

Using this in Eq. (4.11) gives

$$H'_{\mathrm{pbc}}(t) = \frac{U}{2L}\sum_{l,m,n,p=0}^{L-1}\delta_{k_l+k_m,k_n+k_p}e^{2\mathrm{i}F(\omega t)[\cos(k_l)+\cos(k_m)-\cos(k_n)-\cos(k_p)]}a^\dagger_{k_p}a^\dagger_{k_n}a_{k_m}a_{k_l} \ . \tag{4.15}$$

As in the previous chapter the periodicity of $f(t)$ implies that $F(t)$ is periodic as well. This means that the Fourier series

$$e^{2\mathrm{i}F(\omega t)g(k_l,k_m,k_n,k_p)} = \sum_{q=-\infty}^{\infty}\gamma_q(k_l,k_m,k_n,k_p)e^{\mathrm{i}q\omega t} \tag{4.16}$$

can be used. Here

$$g(k_l,k_m,k_n,k_p) = \cos(k_l)+\cos(k_m)-\cos(k_n)-\cos(k_p) \ . \tag{4.17}$$

Inserting the above expression into Eq. (4.15) and performing a subsequent time average over one period of the driving, results in the expression

$$\begin{aligned} H^{\mathrm{eff}}_{\mathrm{pbc}} &= \frac{1}{T}\int_0^T \mathrm{d}\tau H'(\tau) \\ &= \frac{U}{2L}\sum_{l,m,n,p=0}^{L-1}\delta_{k_l+k_m,k_n+k_p}\gamma_0(k_l,k_m,k_n,k_p)a^\dagger_{k_p}a^\dagger_{k_n}a_{k_m}a_{k_l} \ . \end{aligned} \tag{4.18}$$

This is the effective Hamiltonian. As long as $\omega \gg UN$ where N is the number of particles in the system, this time-independent effective Hamiltonian should be a good approximation. It guarantees that the quasienergies do not wrap around the zone edges of the

first Brillouin zone $(0, \omega)$ in the frequency domain. Consequently the quasienergies can be ordered and thus it is reasonable to identify ground and excited states. It is shown in Section 4.2 that the effective Hamiltonian resulting from cosinusoidal driving, which has a naturally well-ordered spectrum and possesses a well defined ground state, indeed reproduces the quasienergy spectrum, confirming that this interpretation is justified.

Unlike the result in the potential driving case, where only the nearest neighbor hopping amplitudes were renormalized, the situation is much more complicated for kinetic driving. In the momentum representation the $\gamma_0(k_l, k_m, k_n, k_p)$ are the scattering amplitudes of two particles with incoming momenta k_l, k_m and outgoing momenta k_n, k_p. The kinetic drive renormalizes those amplitudes, which very much depend on the incoming and outgoing momenta. For the time independent system the scattering amplitudes are constant $\gamma_0(k_l, k_m, k_n, k_p) = 1$, which reproduces the interaction term in momentum space. The renormalization of the scattering amplitudes has significant consequences: It produces non-local interactions and correlated hopping terms in position space. This effect is studied in detail in Section 4.2 (cosinusoidal driving).

The interaction energy U is a global scaling factor. A change of U results in a rescaling of time in the evolution of the system. The effect of a temporal off-set of the drive will be considered in the next chapter. In general, if a temporal offset were to be present, as defined in the previous chapters [see e.g. (2.93)] then the extra phase $\exp[-\mathrm{i}F(\theta)g(k_l, k_m, k_n, k_p)]$ would appear in the above summation [82].

4.1.2 Hard wall boundary conditions

A standard way to accommodate HWBC is to extend the lattice by two sites, on which the walls are assumed to be placed, i.e. $x = 0, L+1$. Placing the walls forces $a_0, a_{L+1} = 0$, so that the summation in Eq. (4.2) is changed to

$$H_{\mathrm{hw}}(t) = -J(t) \sum_{x=1}^{L} \left(a_{x+1}^\dagger a_x + \mathrm{H.c.} \right) + \frac{U}{2} \sum_{x=1}^{L} n_x(n_x - 1) \ . \tag{4.19}$$

A mode expansion satisfying these boundary conditions facilitates the derivation of the effective Hamiltonian. The natural choice is an expansion into stationary sinusoidal modes. The creation and annihilation operators in position space are expanded according to

$$a_x = \sqrt{\frac{2}{L+1}} \sum_{l=1}^{L} \sin(\tilde{k}_l x) a_{\tilde{k}_l} \tag{4.20}$$

$$a_{\tilde{k}_l} = \sqrt{\frac{2}{L+1}} \sum_{x=1}^{L} \sin(\tilde{k}_l x) a_x \tag{4.21}$$

where the new wave vector

$$\tilde{k}_l = \pi l/(L+1) \tag{4.22}$$

has to be defined so that $a_{\tilde{k}_l}$ and $a_{\tilde{k}_m}^\dagger$ satisfy the bosonic commutation relations and the boundary conditions. The first Brillouin zone now is $(0, \pi)$. The system is still periodic with respect to 2π, but the Brillouin zone is twice as dense as for PBC and $(\pi, 2\pi)$ is missing from it.

The derivation of the effective Hamiltonian is in perfect analogy to the one for PBC. The only difference is the reduced symmetry. A consequence of this is the loss of quasi-momentum conservation, leading to a more complicated effective Hamiltonian. In the stationary wave representation, after transforming into the moving frame and performing a subsequent time average over one period, the equation that results is:

$$\begin{aligned} H_{\mathrm{hw}}^{\mathrm{eff}} =& \frac{2U}{(L+1)^2} \sum_{x=1}^{L} \sum_{l,m,n,p=1}^{L} \sin(\tilde{k}_l x) \sin(\tilde{k}_m x) \sin(\tilde{k}_n x) \sin(\tilde{k}_p x) \\ & \times \gamma_0(\tilde{k}_l, \tilde{k}_m, \tilde{k}_n, \tilde{k}_p) a^\dagger_{\tilde{k}_p} a^\dagger_{\tilde{k}_n} a_{\tilde{k}_m} a_{\tilde{k}_l} \ . \end{aligned} \tag{4.23}$$

For PBC and the plane wave modes, the sum over x positions produced the Kronecker delta, ensuring momentum conservation. Here the sum remains and presents an additional complication in the renormalization of the scattering amplitudes. This has several consequences, one of them being that the numerical and analytic investigation of the problem becomes more difficult. This is the reason why the ring is more extensively discussed in this chapter. In Chapter 5 more importance is given to HWBC.

4.1.3 Stationary and truncated plane waves

Even though the plane wave representation is not the natural choice for HWBC it still is a valid expansion with a minor change: The plane wave modes have to be truncated at the positions of the walls:

$$\phi_{k_l}(x) = \begin{cases} e^{\mathrm{i}xk_l} \ , & x \leq L \\ 0 \ , & x = 0, L+1 \end{cases} \tag{4.24}$$

These mode functions preserve the bosonic commutation relations and help to compare observables in HWBC and PBC. Employing the truncated plane wave mode functions results in:

$$a_{\tilde{k}_l} = \sqrt{\frac{2}{L(L+1)}} \sum_{m=1}^{L} \sum_{x=1}^{L} \phi_{k_l} x \sin(\tilde{k}_l x) a_{k_m} \ , \tag{4.25}$$

Although this transformation is trivial in the continuum, the difference in the definitions of $\tilde{k}_l$ [(4.22)] and k_m [(4.6)] make it less trivial in discrete space.

4.1.4 Extensions

For PBC and HWBC it is possible to introduce complications into the driven Bose-Hubbard model in Eq. (4.2), such as an additional constant tunneling term, an on-site potential, a tilt or a single-site impurity. For all these cases it is still possible to derive an effective Hamiltonian. These complications introduce new energy scales, which have to comply with the high frequency regime. Without detailing their individual properties, it is still informative to state how kinetic driving affects their respective representations in momentum space.

The model that covers all the above complications is

$$\tilde{H}(t) = H_{\mathrm{kin}}(t) + H_{\mathrm{pot}} + H_{\mathrm{int}} \ . \tag{4.26}$$

The individual terms are

$$H_{\text{kin}}(t) = -[J_0 + J(t)] \sum_x (a^\dagger_{x+1} a_x + \text{H.c.}) \ , \tag{4.27}$$

$$H_{\text{pot}} = \sum_x K_x n_x \ , \tag{4.28}$$

$$H_{\text{int}} = \frac{U}{2} \sum_x n_x (n_x - 1) \ . \tag{4.29}$$

The renormalization of the scattering amplitudes in momentum space for the interaction term has been calculated in the previous sections. The new additions are a hopping term that is constant in time and the on-site potential term H_{pot}, which is the only term that requires some care when deriving the effective Hamiltonian. The transformation defined in Eq. (4.9) can be used to transform the system into the moving frame and perform a subsequent time average. The time independent term $-J_0 \sum_x (a^\dagger_{x+1} a_x + \text{H.c.})$ commutes with $W(t)$ so that it is not affected by the transformation.

When evaluating the transformation (4.11) an expression similar to Eq. (4.12) (PBC) is obtained:

$$\begin{aligned} f'(\lambda) &= e^{-\mathrm{i}\lambda a^\dagger_{k_u} a_{k_u}} a^\dagger_{k_l} a_{k_m} e^{\mathrm{i}\lambda a^\dagger_{k_u} a_{k_u}} \\ &= e^{\mathrm{i}\lambda \cos(k_u)(\delta_{mu} - \delta_{lu})} a^\dagger_{k_l} a_{k_m} \ . \end{aligned} \tag{4.30}$$

Periodic boundary conditions

The effective Hamiltonian for the PBC is

$$\tilde{H}^{\text{eff}}_{\text{pbc}} = H^0_{\text{kin}} + H^{\text{eff}}_{\text{pot}} + H^{\text{eff}}_{\text{int}} \ , \tag{4.31}$$

where

$$H^0_{\text{kin}} = -J_0 \sum_{x=0}^{L-1} (a^\dagger_{x+1} a_x + \text{H.c.}) \ , \tag{4.32}$$

$$H^{\text{eff}}_{\text{pot}} = \frac{1}{L} \sum_{x=0}^{L-1} \sum_{l,m=0}^{L-1} K_x e^{\mathrm{i}(k_l - k_m)x} \beta_0(k_l, k_m) a^\dagger_{k_l} a_{k_m} \ , \tag{4.33}$$

$$H^{\text{eff}}_{\text{int}} = H^{\text{eff}}_{\text{pbc}} \ , \tag{4.34}$$

where $\beta_0(k_l, k_m)$ is defined indirectly through the expansion

$$e^{2\mathrm{i}F(\omega t) h(k_l, k_m)} = \sum_{q=-\infty}^{\infty} \beta_q(k_l, k_m) e^{\mathrm{i}q\omega t} \tag{4.35}$$

and

$$h(k_l, k_m) = \cos(k_l) - \cos(k_m) \ . \tag{4.36}$$

The term $H^{\text{eff}}_{\text{pbc}}$ is given in Eq.(4.18)

Hard wall boundary conditions

For HWBC the expressions are very similar to those of the ring. The use of the new mode functions yields

$$\tilde{H}^{\text{eff}}_{\text{hw}} = H^{0}_{\text{kin}} + H^{\text{eff}}_{\text{pot}} + H^{\text{eff}}_{\text{int}} \ , \tag{4.37}$$

where

$$H^{0}_{\text{kin}} = -J_0 \sum_{x=1}^{L} (a^{\dagger}_{x+1} a_x + \text{H.c.}) \ , \tag{4.38}$$

$$H^{\text{eff}}_{\text{pot}} = \frac{2}{L+1} \sum_{x=1}^{L} \sum_{l,m=1}^{L} K_x \sin(\tilde{k}_l x) \sin(\tilde{k}_m x) \beta_0(\tilde{k}_l, \tilde{k}_m) a^{\dagger}_{\tilde{k}_l} a_{\tilde{k}_m} \ , \tag{4.39}$$

$$H^{\text{eff}}_{\text{int}} = H^{\text{eff}}_{\text{hw}} \ . \tag{4.40}$$

These expressions are the culmination of the derivations of general expressions for kinetic driving and will become useful in the next chapter.

4.2 Cosinusoidal driving of the ring

The specific waveform

$$f(t) = J \cos(\omega t) \tag{4.41}$$

and its general effects will now be studied in detail. This waveform is central to the discussion of our work in Ref. [2]. It produces a rich set of interesting effects that made its investigation a very fruitful process. The cosinusoidal waveform implies

$$F(\omega t) = \frac{J}{\omega} \cos(\omega t) \ . \tag{4.42}$$

In turn the expression

$$\gamma_0 = \mathcal{J}_0\{2\kappa[\cos(k_l) + \cos(k_m) - \cos(k_n) - \cos(k_p)]\} \tag{4.43}$$

is found. $\kappa = J/\omega$ will be referred to as the driving parameter. The effective Hamiltonian explicitly becomes

$$\begin{aligned} H^{\text{eff}}_{\text{pbc}} = \frac{U}{2L} \sum_{l,m,n,p=0}^{L-1} & \delta_{k_l + k_m, k_n + k_p} \\ & \times \mathcal{J}_0\{2\kappa[\cos(k_l) + \cos(k_m) - \cos(k_n) - \cos(k_p)]\} a^{\dagger}_{k_p} a^{\dagger}_{k_n} a_{k_m} a_{k_l} \ . \end{aligned} \tag{4.44}$$

The spectrum of quasienergies for $(N, L) = (8, 8)$ is shown in Fig. 4.1 (N is the number of particles).

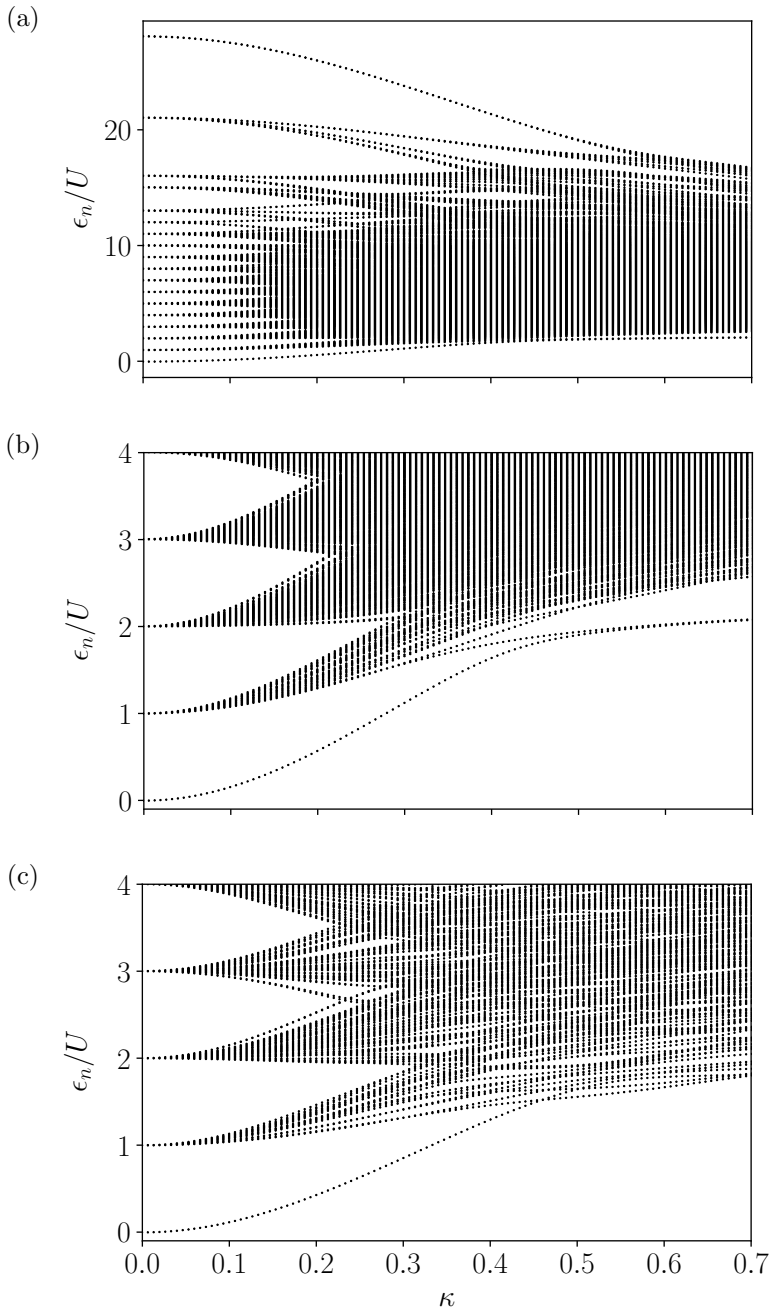

Figure 4.1: Quasienergies of $H^{\text{eff}}_{\text{pbc}}$ for (a),(b) $(N, L) = (8, 8)$ and (c) $(N, L) = (6, 6)$; $N =$ number of particles; $L =$ number of lattice sites. For $\kappa = 0$ the spectrum is gapped. Each level is characterized by a number of particle-hole excitations. $\epsilon_n = 0$ corresponds to the Mott state, which corresponds to a configuration with one particle per site. Once κ increases, the degeneracy of energy levels is lifted and dense bands start to form. In (a),(b) the ground and first excited state form their own band, which is clearly separated from the others. This feature depends on the available momenta. The momenta $k = \pm\pi/2$ must lie within the Brillouin zone, i.e $L/4 = n$, where n is an integer. (a) Entire spectrum for $(N, L) = (8, 8)$, (b) zoom-in for $(N, L) = (8, 8)$ and (c) zoom-in for $(N, L) = (6, 6)$. The gap between the first and second excited state is no longer present.

The spectrum is clearly gapped for $\kappa = 0$. Each level represents a set of particle-hole excitations. The ground state is the Mott state, in which each particle occupies exactly one site. The first excited energy is degenerate and is marked by at least one hole and one double occupation, contributing one unit of U to the energy. The higher excited, highly degenerate energy levels feature configurations of two, three or more particles on one site. The highest excited state has the energy $8(8-1)U/2 = 28U$. Once κ increases the degeneracy of the levels is lifted and dense bands start to form. For $\kappa > 0.4$ the ground and first excited state conspire to form a well separated level. This feature depends on the presence of $k = \pm\pi/2$ in the Brillouin zone, i.e. $L/4 = n$ with n some integer. This can be seen when comparing Fig. 4.1b and Fig. 4.1c. The gap between first and second excited state in Fig. 4.1b $[(N, L) = (8, 8)]$ is no longer visible in Fig. 4.1c $[(N, L) = (6, 6)]$. An explanation of this effect is given in the next chapter. It is quite involved and obscured by the effective Hamiltonian.

To see how well the quasienergies of the effective Hamiltonian agree with those obtained from the time evolution operator of the fully time-dependent system (4.2), the operator was evaluated after one period for various fillings and lattice sizes. For the time dependent calculation the parameters $\omega = 1000U$ and $J \in [0, 800U]$ were chosen. With $\omega \gg N(N-1)U/2$ there is no danger of the quasienergies wrapping around the zone edges of the first Brillouin zone and the spectrum is well ordered so that the identification of the ground and further excited states is meaningful. The figure of merit χ^2 [Eq. (2.104)]

$$\chi^2(\kappa) = \sum_n [\epsilon_n - \epsilon_n^{\mathrm{pbc}}(\kappa)]^2 \tag{4.45}$$

[Chapter 2, Eq. (2.104)] is used to quantify the agreement between the effective quasienergies $\epsilon_n^{\mathrm{pbc}}(\kappa)$ and the quasienergies ϵ_n derived from the time evolution. The results of this comparison can be seen in Fig. 4.2. The agreement is very good and even for moderate values of κ no significant deviation from the numerically calculated quasienergies can be detected. In conclusion, $H_{\mathrm{pbc}}^{\mathrm{eff}}$ can be confidently used to analyze the system for $\omega \gg UN$ and $\kappa < 0.8$ with this excellent agreement between the time dependent simulation and effective Hamiltonian.

4.2.1 Atypical hoppings and interactions

The effective Hamiltonian in the momentum representation does not provide intuitive access to the interpretation of the renormalized scattering amplitudes. It helps to consider $H_{\mathrm{pbc}}^{\mathrm{eff}}$ in the position representation to make the impact of the renormalization more transparent. To that extent, the expansion of the a_{k_l} in Eq. (4.5) can be used to revert to real space. In position space the effective Hamiltonian becomes

$$H_{\mathrm{pbc}}^{\mathrm{eff}} = \sum_{w,x,y,z=0}^{N-1} Q_{wxyz} a_w^\dagger a_x^\dagger a_y a_z \ , \tag{4.46}$$

where

$$\begin{aligned} Q_{wxyz} =& \frac{U}{2L^3} \sum_{l,m,n=0}^{L-1} e^{\mathrm{i}[k_l(x-z)+k_m(x-y)-k_n(x-w)]} \\ & \times \mathcal{J}_0\{2\kappa[\cos(k_l) + \cos(k_m) - \cos(k_l + k_m - k_n) - \cos(k_n)]\} \ . \end{aligned} \tag{4.47}$$

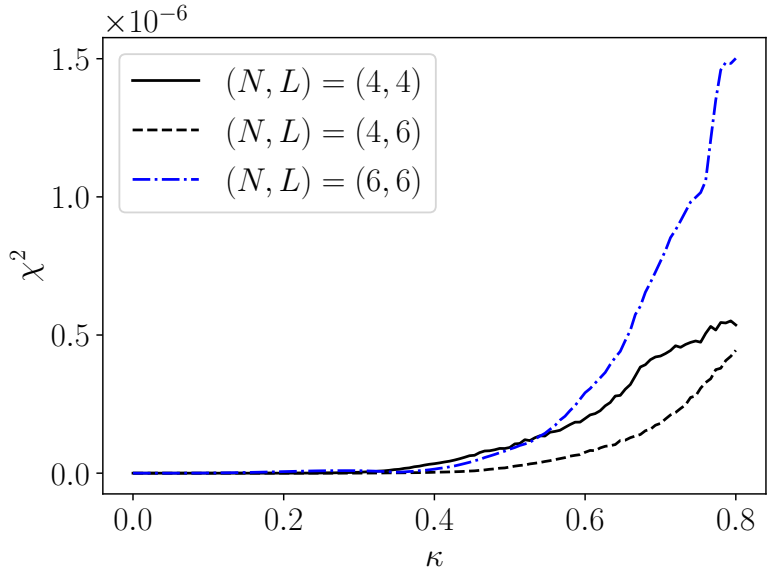

Figure 4.2: $\chi^2(\kappa)$ of Eq. (4.45) for various fillings. The agreement of the effective Hamiltonian with the numerical simulation is excellent for all values of κ

In Eq. (4.47) momentum conservation has been used. Despite the complicated nature of the amplitudes Q_{wxyz}, they are readily interpreted as representative of various correlated hoppings, as well as local and non-local interactions. In the following a range of processes that are important for small values of κ will be identified.

Some of the important correlated hopping processes, which are connected to specific Q_{wxyz}, are illustrated in Fig. 4.3. When inspecting Eq. (4.47), it can be seen that $Q_{w+d,x+d,y+d,z+d} = Q_{wxyz}$, where d is a lattice vector, which means that each specific Q_{wxyz} represents a whole class of processes. This is an expression of rotational symmetry in the ring. For example, the on-site energies Q_{xxxx} are all captured by Q_{0000}. Furthermore Q_{2121} represents nearest-neighbor interactions. Q_{1100} is a doublon hopping amplitude (two particles tunneling together). Q_{1120}, Q_{0312} are examples of correlated hopping amplitudes, where the former is the energy cost of two particles hopping on-top of each other, and the latter the cost for the inverse process. Q_{2220}, Q_{2110} both represent density dependent hopping terms. This can involve both neighboring and more distant sites. The magnitudes of these amplitudes can be seen in Fig. 4.3a and Fig. 4.3b. An illustration of these processes is shown in Fig. 4.3c. As expected, for $\kappa = 0$ only the on-site interaction energy $Q_{0000} = U/2$ is different from zero. Increasing κ renormalizes the on-site interaction potential and causes the appearance of a plethora of atypical hoppings and interaction amplitudes.

It is interesting to note that the nearest-neighbor hopping is completely eliminated from the effective Hamiltonian. This is not surprising, given that direct time averaging Eq.(4.2) eliminates nearest-neighbor hopping completely. The higher order terms in the expansion of $H^{\text{eff}}_{\text{pbc}}$ are naturally higher order processes. In principle all these processes are arbitrarily long ranged. For $\kappa < 0.3$ only a few of those make a significant contribution, which makes the problem tractable in this range. For $\kappa > 0.3$ more sophisticated methods

are required in order to explain the system's properties. In the next few paragraphs, a more detailed study of the range dependence of the Q_{wxyz} is given.

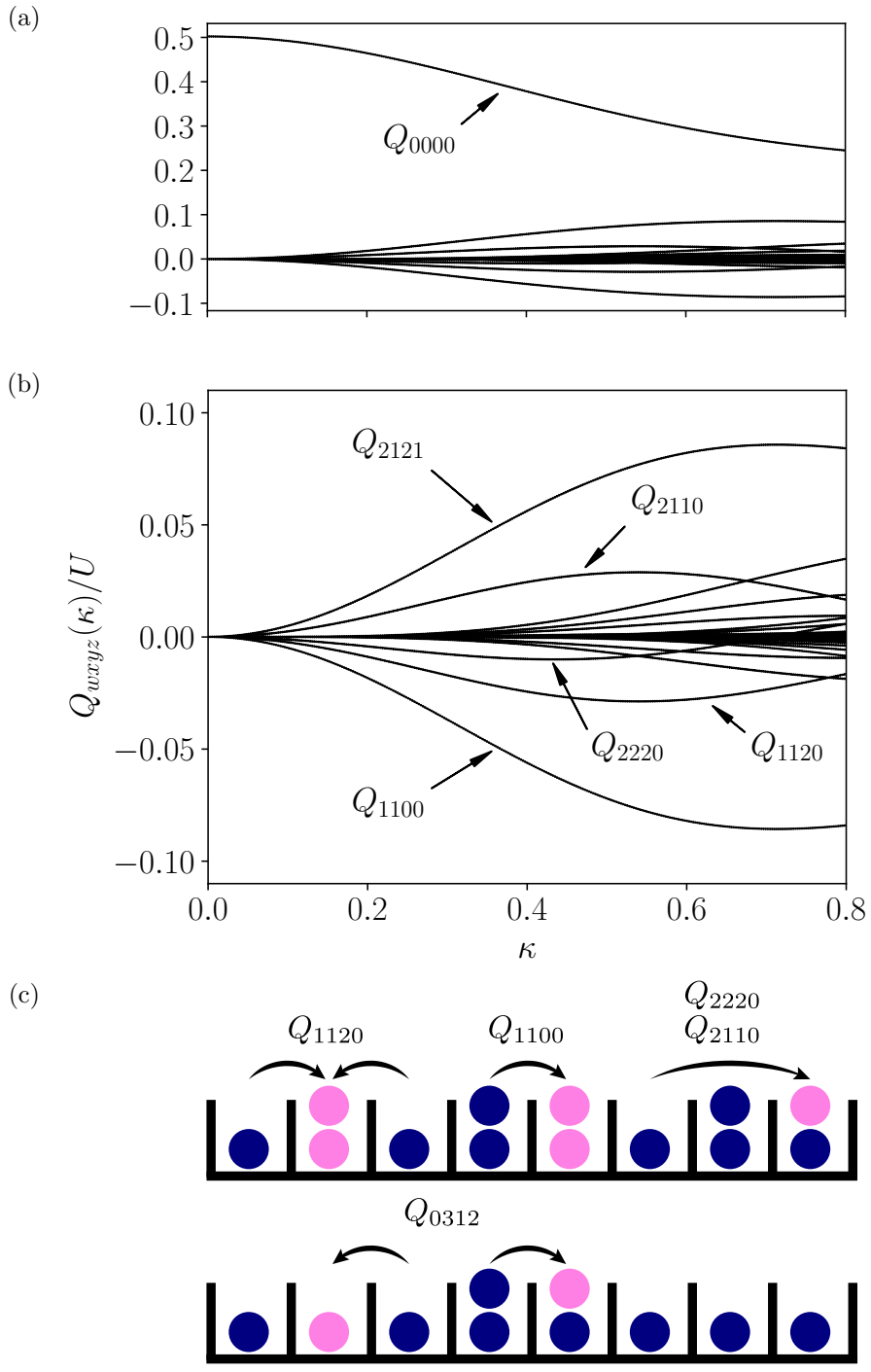

Figure 4.3: (a) All interaction/hopping energies for $L = 8$ in units of U. The renormalized on-site energy Q_{0000} dominates. Due to the rotational symmetry each Q_{wxyz} represents a whole class of processes. (b) Magnification of the hopping/interaction processes arising due to kinetic driving: Q_{2121} is the nearest-neighbor energy, the other Q_{wxyz} are explained in (c): Magenta (light gray) particles indicate positions after a hopping event.

The long range behavior of the Q_{wxyz} is now explored in a more systematic manner and in more detail than in [2]. In Fig. 4.4 w is fixed to zero [1], $\kappa = 0.5$ and a lattice with $L = 40$ sites was chosen. The biggest distance between two sites is 20 sites. In Fig. 4.4a

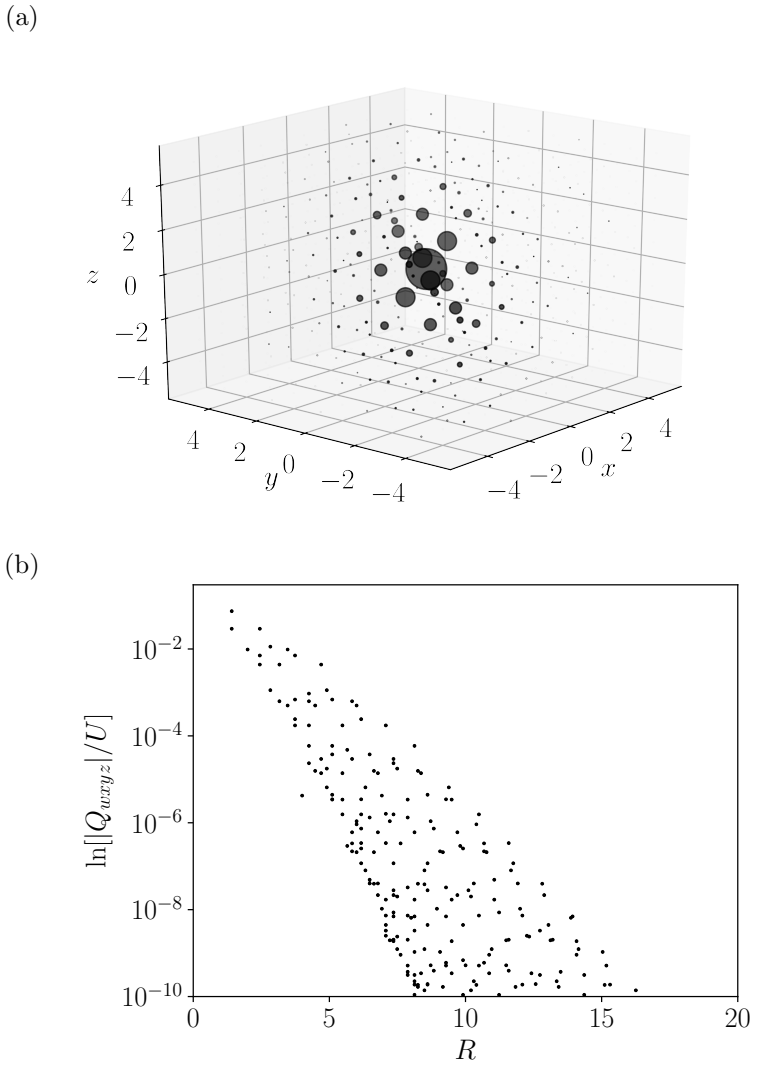

Figure 4.4: (a) $|Q_{0xyz}|$ for $\kappa = .5$ and $L = 40$ are shown. The size of the black spheres represent $|Q_{0xyz}|$.(b) log-plot of the $|Q_{0xyz}|$ as a function of $R = \sqrt{x^2 + y^2 + z^2}$. The amplitudes decrease exponentially indicating an effectively finite range of the atypical hopping and interaction terms.

the magnitudes $|Q_{wxyz}|$ represented by black spheres can be seen to decrease rapidly the further away they are from the origin. The log-plot in Fig. 4.4b shows the decrease of the amplitudes as a function of the distance $R = \sqrt{x^2 + y^2 + z^2}$. The slowest decaying points suggest an exponentially decaying upper bound for $|Q_{0xyz}|$ as a function of R:

$$\max_{\mathrm{R}}(|\mathrm{Q}_{0\mathrm{xyz}}|) = \mathrm{e}^{-\mathrm{aR}} \ , \tag{4.48}$$

[1] This choice equally represents all other w due to rotational symmetry

where $\max_R(\cdot)$ means the biggest value at a given distance R. In Fig. 4.5 the scaling of a as a function of lattice size is shown for the parameters $\kappa = 0.5$ for up to 48 sites. The decay rate $a_\infty = a(L \to \infty)$ approaches the value 1.73, which was calculated by averaging of the last three values of $a(L)$. The numerical evidence suggests that the atypical hoppings

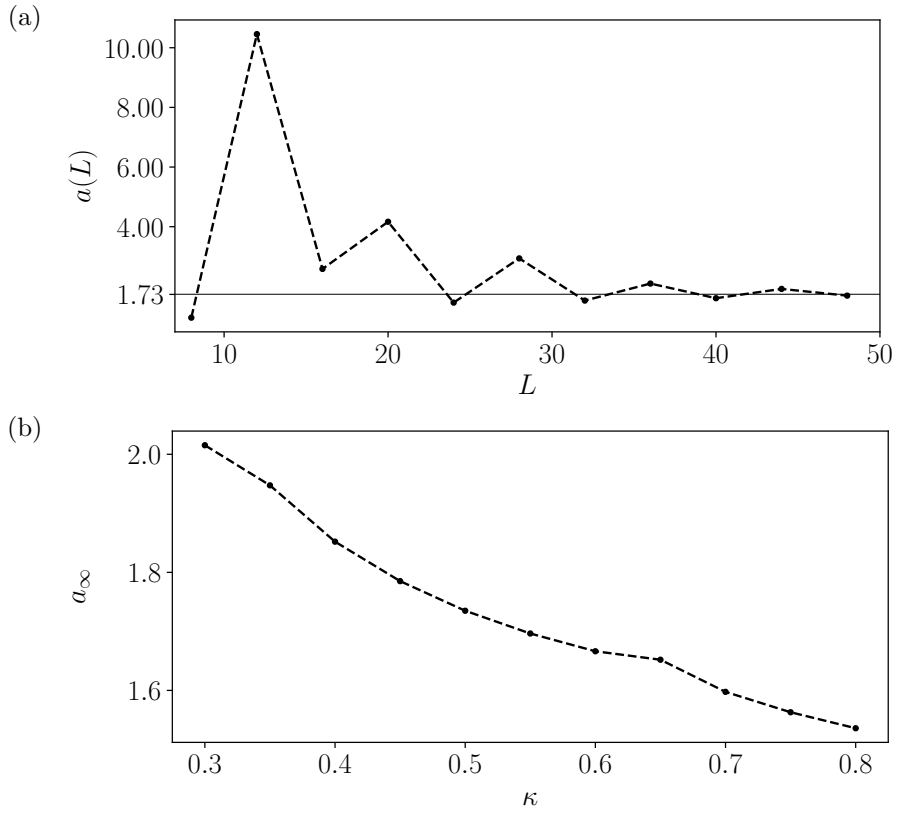

Figure 4.5: Decay rate of the slowest decaying $\max_{\mathrm{R}}(|\mathrm{Q}_{0\mathrm{xyz}}|) = \exp(-\mathrm{aR})$ for up to $L = 48$ ($\kappa = 0.5$). The decay rate a approaches $a_\infty = 1.73$. (b) The decay rates a_∞ for a range of values of κ.

and interactions are not infinitely long ranged. The findings also suggest that the decay is bound by an exponential law. The dependence of the decay rate on the system size shows a saturation of the decay, which points towards a well-defined limit of $a_\infty = a(L \to \infty)$. This limit was studied for a range of κ relevant to this work. The numerical findings imply that the Q_{wxyz} behave consistently over the parameter range that was studied. This concludes the study and discussion of the various amplitudes of the effective Hamiltonian in position space.

4.2.2 Momentum density

The impetus of this section is the analysis of the momentum density and the one-particle reduced density matrix (one-RPDM) of the ground state and first excited state of the effective Hamiltonian $H^{\mathrm{eff}}_{\mathrm{pbc}}$. Calculations with the effective Hamiltonian were performed using exact diagonalization (ED) techniques. More advanced numerical methods such as the density matrix renormalization group (DMRG) techniques are very difficult to use for

H_{pbc} due to the highly non-local nature of the effective Hamiltonian in position and or momentum space. ED was performed with either the "linalg.eig" routine of *NumPy* [244] or, when only the ground state or low lying excitations were required, the "linalg.sparse.eigsh" solver (implicitly restarted arnoldi method by [245]) from the *SciPy* module [104]. The limits for reasonable computation times given the available resources for this thesis are Hilbert space dimensions of $\dim(\mathcal{H}) < 12000$ which roughly corresponds to (N, L) in the range $(9, 8)$ or less. This section will focus on unit filling, which means that the biggest system under investigation will be $(N, L) = (8, 8)$.

The first observable of interest is the momentum density

$$\begin{aligned}\rho(k) &= \frac{1}{N}\langle n_k\rangle \\ &= \frac{1}{L}\sum_{j,l=0}^{L-1} e^{\mathrm{i}k(x-y)} P^{(1)}_{xy} \ ,\end{aligned} \tag{4.49}$$

where

$$P^{(1)}_{xy} = \frac{1}{N}\langle a^\dagger_x a_y\rangle \tag{4.50}$$

is the one-particle reduced density matrix. For $\kappa = 0$ the effective Hamiltonian is identical to

$$H_{\mathrm{pbc}}(0) = \frac{U}{2}\sum_{x=0}^{L-1} n_x(n_x - 1) \ . \tag{4.51}$$

For unit filling, i.e. one particle per site, the ground state of this Hamiltonian is simply the Mott state

$$|\mathrm{Mott}\rangle = |1_0, \cdots, 1_L\rangle \ , \tag{4.52}$$

with energy $\epsilon_0 = 0$. The momentum density of this state is constant $\rho_{\mathrm{Mott}}(k) = 1/8$. For a system size of size $(N, L) = (8, 8)$ (unit filling) the momentum density is shown in Fig. 4.6. Once κ increases, two peaks form at $\pm\pi/2$ for both the ground and first excited state. This feature is less visible for the third excited state. It is not present at all for the fourth and higher lying excited states.

The next section addresses the question of whether the formation of the peaks is correlated with some form of quasi condensation. In the following, for the sake of brevity, the term condensate is used, even though no true condensates can form in one dimension and therefore only quasi condensation exists.

Condensation is not only signaled by the formation of the peaks in $\rho(k)$ but also by the macroscopic occupation of one or more natural orbitals. The natural orbitals are the eigenvectors of the one-particle reduced density matrix. Their respective eigenvalues signify the orbitals' occupations. The one-RPDM in momentum space is defined as:

$$P^{(1)}_{q,k} = \frac{1}{N}\langle a^\dagger_q a_k\rangle \tag{4.53}$$

In Fig. 4.7 $P^{(1)}_{q,k}$ is illustrated for the ground state for four exemplary values of κ. The values represented on the diagonals in Fig. 4.7 correspond to the momentum density. The four points $(\mp\pi, \pm\pi)$ are repeated for a more symmetric appearance and belong to the diagonal. The one-particle reduced density matrices are all diagonal, which means that

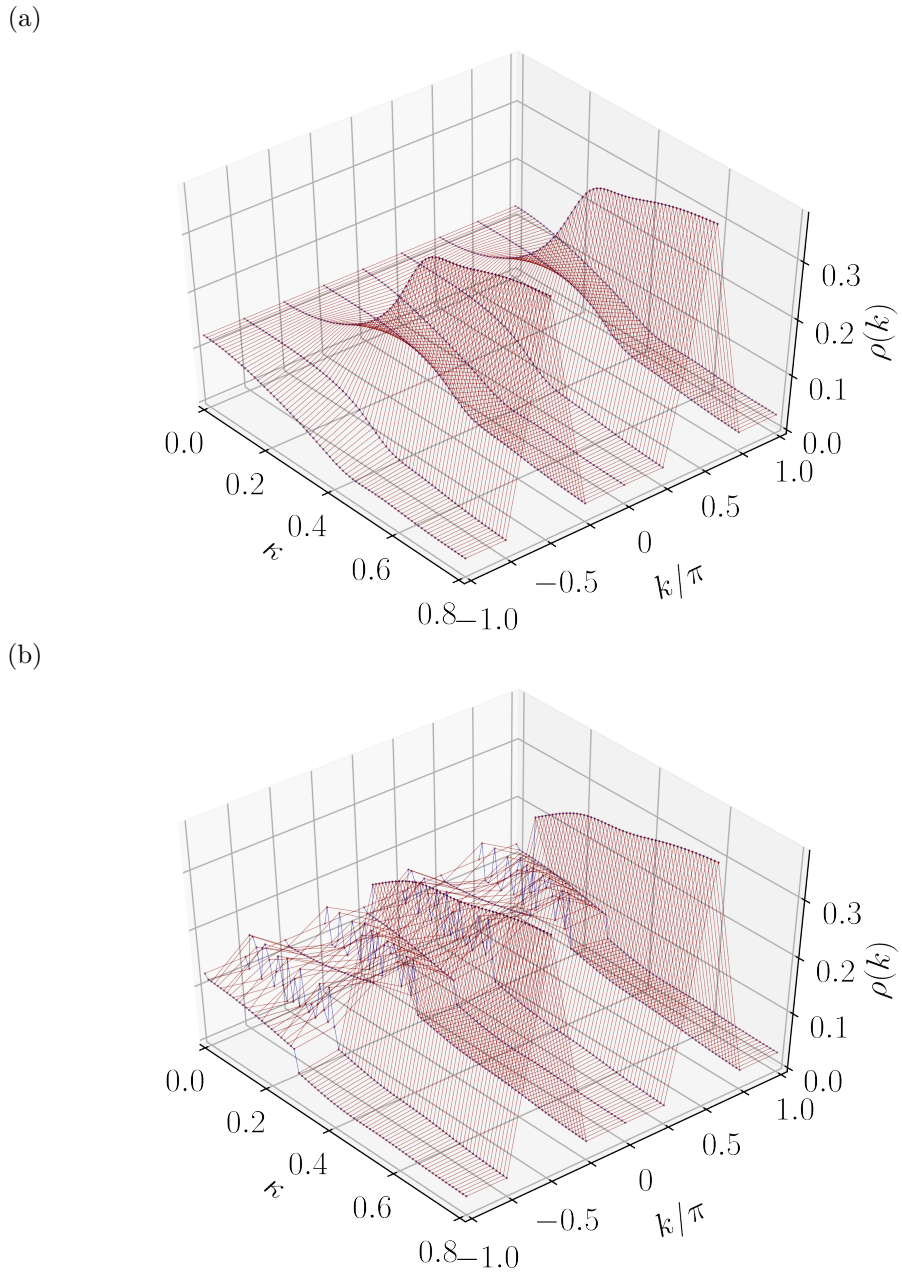

Figure 4.6: (a) Momentum density $\rho(k)$ of the ground state for $(N, L) = (8, 8)$ as a function of κ. Two peaks form at $k = \pm\pi/2$. (b) $\rho(k)$ of the first excited state shows very similar properties to that of the ground state, with the obvious difference that their formation is less smooth.

the natural orbitals are just plane waves. Their occupation as a function of κ is shown in Fig. 4.8. At $\kappa = 0$ all natural orbitals are equally occupied and the ground state is maximally fragmented. This is to be expected of the Mott state. Once κ increases a two-fold degenerate eigenvalue grows at the expense of the others. This indicates the formation of a fragmented condensate. The natural orbitals belonging to this eigenvalue are the plane waves with $k = \pm\pi/2$ (Fig. 4.7). This is in stark contrast to the more common Mott-superfluid transition of the undriven Bose-Hubbard model, where a single

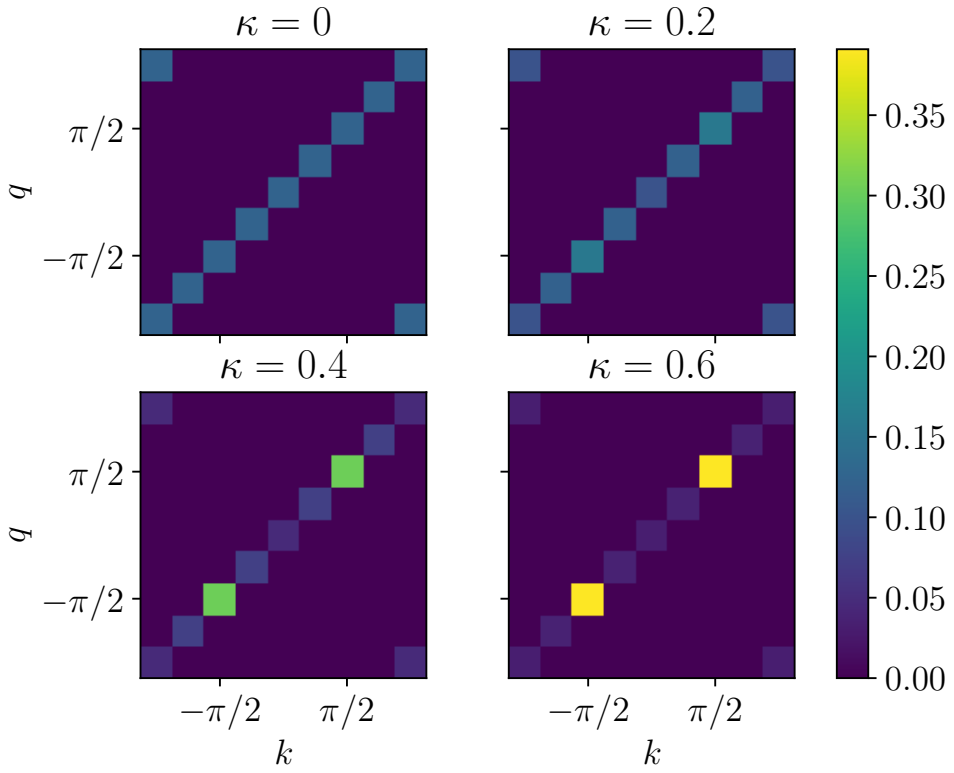

Figure 4.7: Shown is $P^{(1)}_{q,k} = \langle a^\dagger_q a_k \rangle / N$ in the ground state for four different values of the κ. Two clear peaks at $(p, q) = (\pm\pi/2, \pm\pi/2)$ form for increasing κ. For a more symmetric appearance the $(k, q) = \pm(\pi, \pi)$ and $(k, q) = \pm(\pi, -\pi)$ are repeated - hence the latter two points belong to the diagonal. The density matrices are diagonal, therefore the natural orbitals are just plane waves. The pictures are very similar for the first excited state

condensate forms at $k = 0$ if $J > 0$ (positive effective mass). A more detailed discussion of the properties of the Mott-superfluid transition is given in Section 4.2.5.

4.2.3 Dipole states

For values of $\kappa < 0.3$ it is possible to explain the formation of the peaks by closer examination of the numerically calculated ground state. In Fig. 4.9 the weights of various configurations for several values of κ are shown for the ground state. In the position representation the ground state is a superposition of

$$|\Psi_0\rangle = \sum_{\{n_\alpha\}} c_n |n_0, ..., n_N\rangle \tag{4.54}$$

where $\{n_\alpha\}$ means summing over all unique configurations for which $\sum_x n_x = N$. In Fig. 4.9 $|1012\rangle$, $|030\rangle$, etc. are shorthand for a single particle-hole pair, a single triple occupation and so forth. For $\kappa < 0.3$, states that we dub dipole states in [2] play the most important role, apart from the Mott state which is the biggest contributor to $|\Psi_0\rangle$ for all four values of κ. The plateaus in Fig. 4.9 are a manifestation of the rotational symmetry of $|\Psi_0\rangle$.

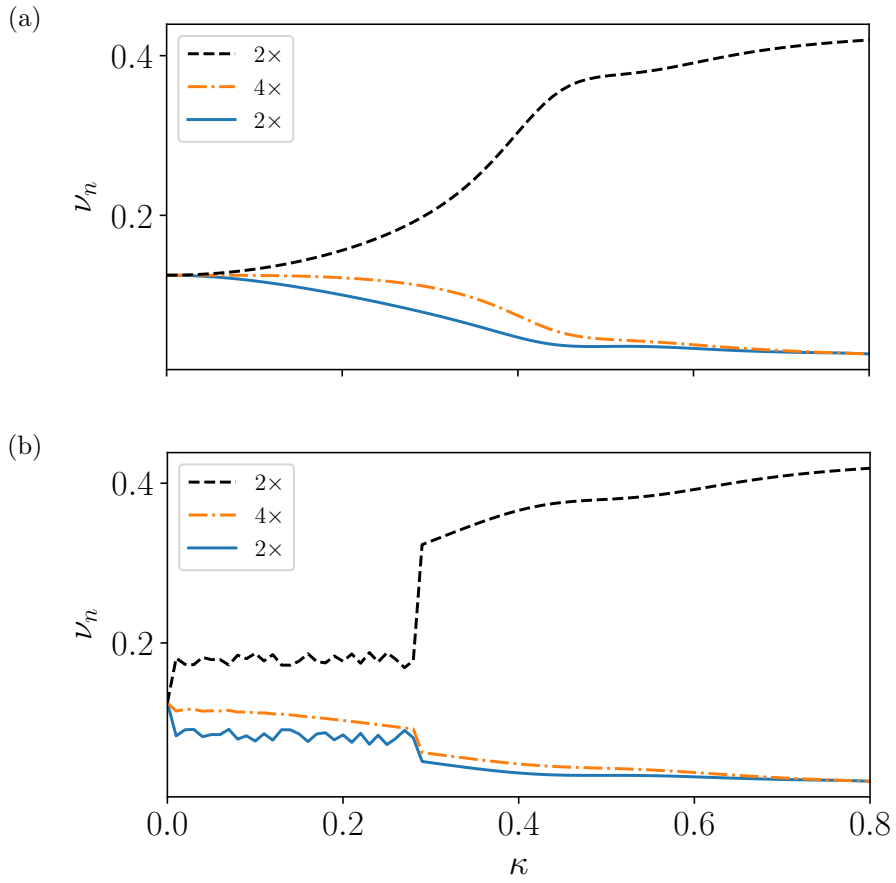

Figure 4.8: The eigenvalues ν_n of the one-RPDM for (a) the ground and (b) first excited state are shown here. (a) The magnitude indicates the occupation of the respective natural orbital. For $\kappa = 0$ all orbitals are equally occupied and the fragmentation of the ground state is maximal. As κ increases two degenerate orbitals emerge at the expense of the others, indicating the formation of a fragmented condensate. The degeneracy of each ν_n is listed in the legend. Except for the discontinuity, the first excited state (b) shows very similar behavior.

A more quantitative analysis for $\kappa < 0.3$ can be made by considering the variational ansatz

$$|\xi\rangle = \alpha|\text{Mott}\rangle + \beta|\text{D}\rangle \ , \tag{4.55}$$

where

$$|\text{D}\rangle = \frac{1}{\sqrt{2L}} \sum_{x=0}^{L-1} \left(D_x + D_x^\dagger\right) |\text{Mott}\rangle \tag{4.56}$$

and

$$D_x = a_x^\dagger a_{x+2} \ . \tag{4.57}$$

$|\text{D}\rangle$ is normalized and so is $|\text{Mott}\rangle$, which implies $\alpha^2 + \beta^2 = 1$. Since the numerical investigation showed all coefficients to be real α, β are taken to be real as well. Now the goal is to minimize the energy $\langle H_{\text{pbc}}\rangle$ with respect to $|\xi\rangle$ (the κ suppressed to minimize

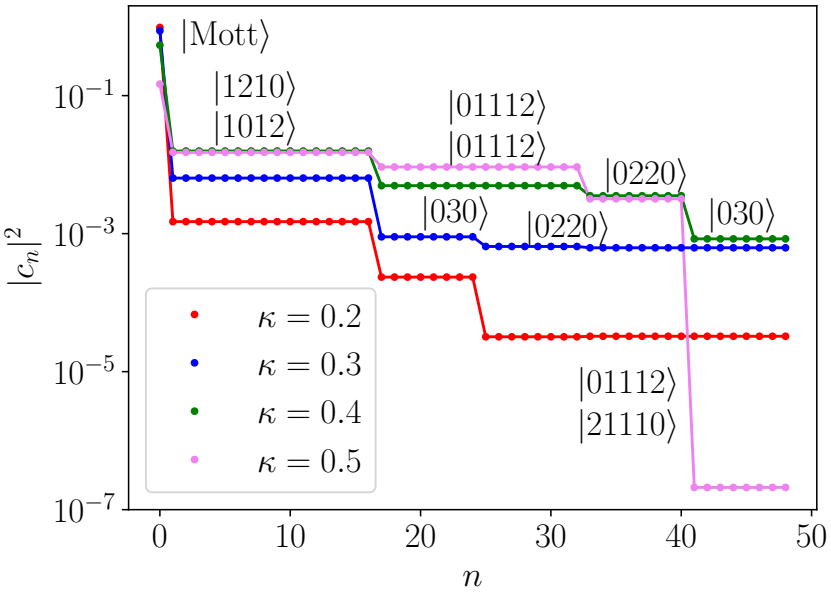

Figure 4.9: The weights $|c_n|^2$ of the configurations forming the ground state for $(N, L) = (8, 8)$ are shown. n indexes the configuration by weight. The $|\text{Mott}\rangle$ state has the largest weight for all four values of κ. For $\kappa < 0.3$, the second largest contribution to the $|\Psi_0\rangle$ is made by configurations with a doublon hole pair $|1012\rangle$, dubbed dipole states. For larger κ triple occupations $|030\rangle$, extended dipoles $|01112\rangle$ or multiple double occupations $|022\rangle$ become more important.

clutter):

$$\langle H_{\text{pbc}}\rangle = \alpha^2\langle\text{Mott}|H_{\text{pbc}}|\text{Mott}\rangle + \beta^2\langle\text{D}|H_{\text{pbc}}|\text{D}\rangle + 2\alpha\beta\langle\text{Mott}|H_{\text{pbc}}|\text{D}\rangle \tag{4.58}$$

This expression shows that if $\langle\text{Mott}|H_{\text{pbc}}|\text{D}\rangle > 0$ the energy is minimized for $\text{sgn}(\alpha\beta) < 0$.

Using the normalization of $|\xi\rangle$ α results in the expression (taken from the appendix of [2])

$$\langle H_{\text{pbc}}\rangle_\alpha = \alpha^2(A - C) + \alpha\sqrt{1-\alpha^2}B + C\ , \tag{4.59}$$

where

$$A = \langle \text{Mott}|H_{\text{pbc}}|\text{Mott}\rangle = 2\sum_{x\neq y} Q_{xyyx} \tag{4.60}$$

$$B = 2\langle \text{Mott}|H_{\text{pbc}}|\text{D}\rangle = 8\sqrt{N}\Big(\sum_{x\neq 0} + \sum_{x\neq 0,2}\Big)Q_{2xx0} \tag{4.61}$$

$$\begin{aligned} C = \langle \text{D}|H_{\text{pbc}}|\text{D}\rangle =& 2\sum_{x\neq y} Q_{xyyx} + 4\sum_{x\neq 0,2,4} Q_{4xx0} + 4\sum_{x\neq 0,2,4} Q_{4,x,x+2,2} - 4\sum_{x\neq 0,2} Q_{0xx0} \\ &+ \Big(2\sum_{\substack{x\neq 2\\ x\neq N-2}} + 6\sum_{\substack{x\neq 0,2\\ x\neq N-2}}\Big)Q_{2,x+2,x,0} + \Big(8\sum_{x\neq 0} - 4\sum_{x\neq 2}\Big)Q_{2xx2} \\ &+ 2\Big(\sum_{x\neq 0} + \sum_{x\neq 0,2} + \sum_{\substack{x\neq 0\\ x\neq N-2}} + \sum_{\substack{x\neq 0,2\\ x\neq N-2}}\Big)Q_{2xx,N-2} + 8Q_{4220} \\ &- 4Q_{2442} - 6Q_{2222}\ . \end{aligned} \tag{4.62}$$

Minimizing Eq. (4.59) with respect to α yields

$$\alpha_0 = \begin{cases} \sqrt{\frac{1}{2} + \frac{1}{2}\left(1 + \frac{2B^2}{(A-C)^2}\right)^{-\frac{1}{2}}} & \text{for } B < 0 \\ -\sqrt{\frac{1}{2} + \frac{1}{2}\left(1 + \frac{2B^2}{(A-C)^2}\right)^{-\frac{1}{2}}} & \text{for } B > 0 \end{cases} \tag{4.63}$$

The comparison $\langle H_{\text{pbc}}\rangle_{\alpha_0}$ with the exact ground state energy can be seen in Fig. 4.10 For values of $\kappa < 0.3$ the energy of the variational state and the exact ground state agree reasonably well, beyond that value of the driving parameter the variational approximation fails. The term that is key in reducing the energy is

$$\langle \text{Mott}|H_{\text{pbc}}|\text{D}\rangle = 4\sqrt{N}\left(\sum_{x\neq 0} + \sum_{x\neq 0,2}\right) Q_{2xx0}\ . \tag{4.64}$$

The amplitude Q_{2xx0} mediates between Mott and Dipole states. It also represents a density dependent next-to-nearest neighbor hopping of a single particle. The momentum density of the variational state is given by

$$\rho(k) = \frac{1}{N}\left(1 + \frac{4\alpha\beta}{\sqrt{N}}\cos(2k) + \frac{3\beta^2}{N}\cos(4k)\right) \tag{4.65}$$

$\langle \text{Mott}|H_{\text{pbc}}|\text{D}\rangle > 0$ for lattices with up to 90 sites, and therefore $\text{sgn}(\alpha\beta) < 0$. This implies that $\rho(k)$ develops two peaks at $\pm\pi/2$ just as it did for the ground state of the full effective Hamiltonian.

From the above analysis an intuitive physical picture emerges. If the assumption is made that the Mott state serves as a background of constant density for a single particle, then that particle can become delocalized through next-to-nearest neighbor hopping. In the language of an oversimplified one-particle model, this can be summarized with

$$H = J(\kappa)\sum_x (a^\dagger_{x+2}a_x + \text{hc}) \tag{4.66}$$

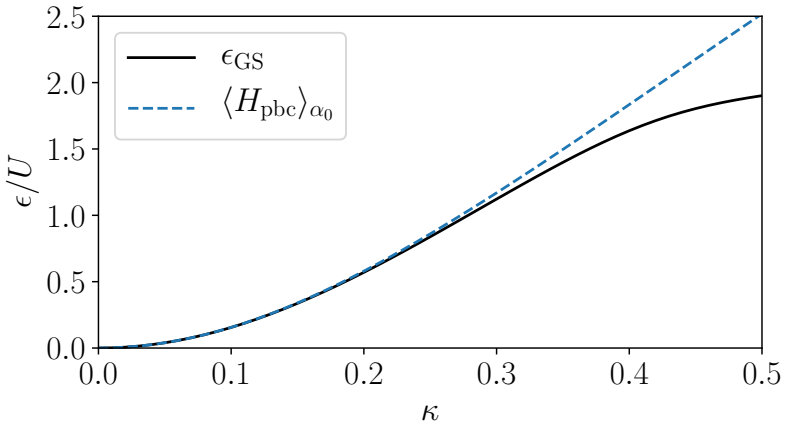

Figure 4.10: The exact ground state energy ϵ_0 of the effective Hamiltonian and the minimized variational energy $\langle H_{\mathrm{pbc}}\rangle_{\alpha_0}$ are shown. Around $\kappa \approx 0.3$ both energies start to diverge notably.

In the momentum representation this simply reads

$$H = 2J(\kappa)\sum_{k_l}\cos(2k_l)a^\dagger_{k_l}a_{k_l} \tag{4.67}$$

The dispersion is cosinusoidal but oscillates with twice the frequency of the one resulting from nearest-neighbor hopping (see Fig. 4.11). Depending on the sign of $J(\kappa)$ the lowest energies are either connected to the $k = 0, \pi$-orbitals if $J(\kappa) < 0$ (positive effective mass) or $k = \pm\pi/2$ orbitals if $J(\kappa) > 0$ (negative effective mass). When identifying $\langle \mathrm{Mott}|H_{\mathrm{pbc}}|\mathrm{D}\rangle > 0$ with the negative effective mass $J(\kappa)$ the simple picture of a ground state constituted by single particles preferring orbitals at $k = \pm\pi$ is confirmed. Once the driving strength increases past $\kappa \approx 0.3$, this picture breaks down. More and more configurations start contributing to the ground state and a fundamentally different description is needed to explain the emerging phenomena.

In part, this has to do with a phase transition occurring at $\kappa \approx 0.42$, which will be explored in great detail in Section 4.2.5. The dipole approximation described here belongs to the Mott-insulating regime, and it only partially accounts for the condensation at $\pm\pi/2$, as will be shown below. An extensive study has been performed with various Hilbert-space truncations to find a suitable approximation to the regime $\kappa > 0.3$, where the condensate forms. These efforts did lead to a better understanding of the nature of the fragmented condensate. This will be addressed in more detail in Chapter 5

4.2.4 Two-particle momentum density

The previous section detailed the evidence of the formation of a fragmented condensate at the momenta $k = \pm\pi/2$, which was signaled by two peaks in the momentum density.

The goal of this section is to further investigate the nature of the ground and first excited state. A natural extension of the previous measures is the two particle momentum density

$$\rho^{(2)}(q,k) = \frac{1}{N^2}\langle n_q n_k \rangle \tag{4.68}$$

$$= \frac{(N-1)}{NL^2}\sum_{w,x,y,z} e^{\mathrm{i}q(w-x)} e^{\mathrm{i}q(y-z)} P^{(2)}_{wyxz} + \frac{\delta_{kq}}{NL}\sum_{w,z} e^{\mathrm{i}q(w-z)} P^{(1)}_{wz} \ , \tag{4.69}$$

where

$$P^{(2)}_{wxyz} = \frac{1}{N(N-1)}\langle a^\dagger_w a^\dagger_x a_y a_z \rangle \tag{4.70}$$

is the two-particle reduced density matrix. For $\kappa = 0$ the system is in the Mott state and the two-particle momentum density is given by

$$\rho^{(2)}(q,k) = \frac{1}{N^2}[(N-2) + N^2\ \delta_{qk}] \ , \tag{4.71}$$

which implies peaks along the line $q = k$ and a constant background of $(N-2)/N^2$, and can be seen in Fig. 4.12. Once the driving parameter increases, two peaks develop at $(q,k) = \pm(\pi/2, \pi/2)$. This is clearly correlated with the onset of condensation at the two momenta $k = \pm\pi/2$. Again, this is due to the fragmentation of the condensate. Most notable is the absence of the peaks of the cross-correlations $(q,k) = \pm(-\pi/2, \pi/2)$. Unlike the one-PRDM this provides a crucial hint about the nature of the fragmentation.

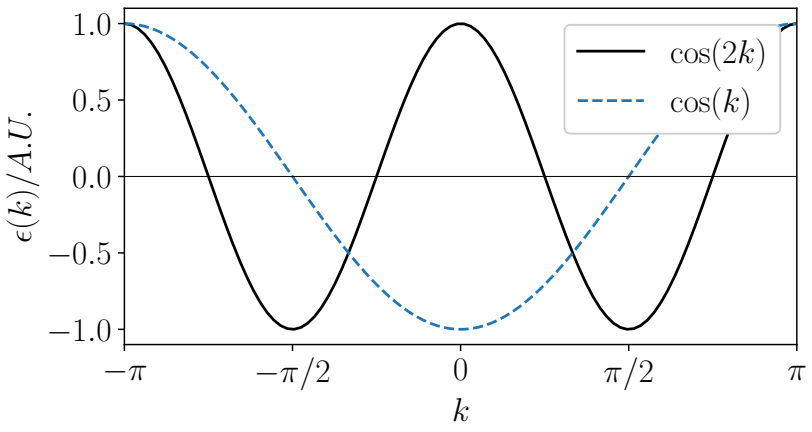

Figure 4.11: Dispersion relation for the undriven Bose-Hubbard model with next-to-nearest neighbor hopping (black solid line) $J > 0$ (negative effective mass), and nearest-neighbor hopping (blue dashed line) for $J < 0$ (positive effective mass).

In principle there are two types of idealized states, consistent with the fragmented nature of the condensate and the appearance of the one-PRDM in the regime where the

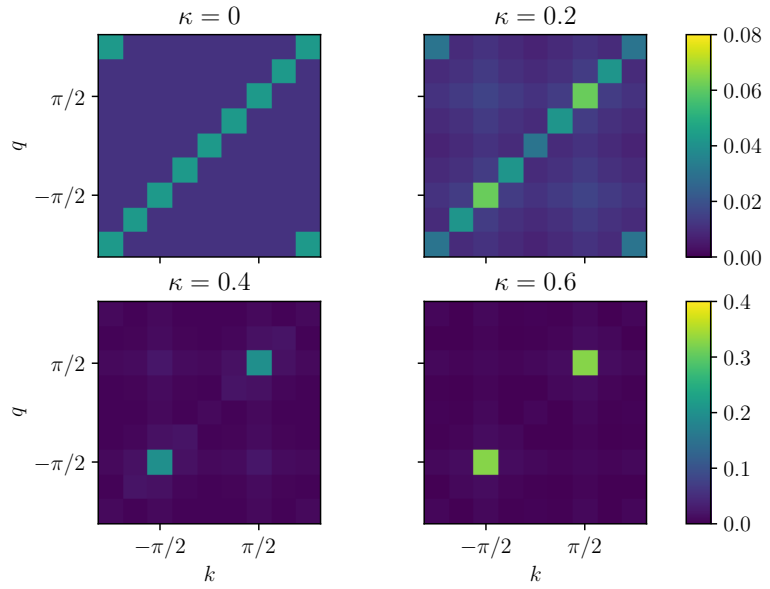

Figure 4.12: The figures show the two particle momentum density $\rho^{(2)}(q,k)$ in the ground state. Just as for the one-RPDM two distinct peaks emerge at $(q,k) = \pm(\pi/2, \pi/2)$. Unlike the one-RPDM the off-diagonal elements are not strictly zero for neither $\kappa = 0$ nor $\kappa = 0.6$. Most notable is the absence of cross-correlations at $(q,k) = (\mp\pi/2, \pm\pi/2)$ indicating a Schrödinger cat-like nature of the ground state for $\kappa \geq 0.5$.

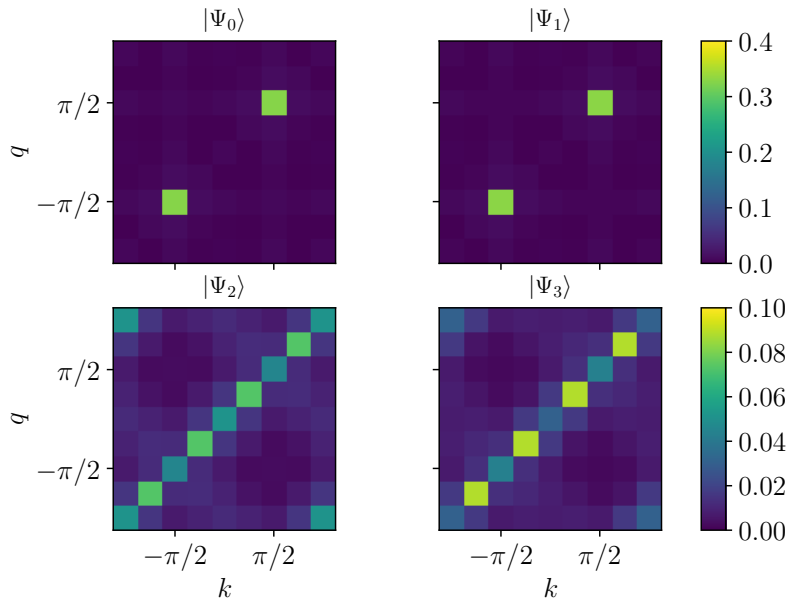

Figure 4.13: $\rho^{(2)}(q,k)$ at $\kappa = 0.6$ for the ground state $|\Psi_0\rangle$ to the third excited state $|\Psi_3\rangle$. The cat-correlations (see text or Fig. 4.12) are lost for the second and third excited state.

condensate has formed. The first is a simple product state, where half the particles occupy $-\pi/2$ and the other half are located in $\pi/2$

$$|\text{Fock}\rangle = \frac{1}{(N/2)!}\left(a^\dagger_{\pi/2}\right)^{N/2}\left(a^\dagger_{-\pi/2}\right)^{N/2}|0\rangle \ . \tag{4.72}$$

Crucially, this state would show four peaks in $\rho^{(2)}(q,k)$, two at $(q,k) = (\pm\pi/2, \pm\pi/2)$ and two at $(q,k) = (\mp\pi/2, \pm\pi/2)$. This is plainly not the case here, as can be seen in Fig 4.12. The other many-body state complying with strong fragmentation is the Schrödinger cat state

$$|\text{cat}\rangle = \frac{1}{\sqrt{2N!}}\left[(a^\dagger_{\pi/2})^N + (a^\dagger_{-\pi/2})^N\right]|0\rangle \ . \tag{4.73}$$

This state is consistent with both the one-RPDM and the two-particle momentum density. As shown in Fig. 4.13, the first excited state displays very similar behavior for $\kappa = 0.6$. The cat-like nature of ground and first excited state persists for even larger values of the driving parameter. The formation and properties of the cat-like ground and first excited state will be the center of attention in the next chapter.

The simple dipole approximation in Eq. (4.55) cannot account for the features of the ground state in the condensed regime. Even though its energy does not match that of the true ground state, other qualities might still be the same as those of the ground state. This is not true for the cross-correlations of $\rho(q,k)$, since they are not small enough when compared to the two peaks at $\pm(\pi/2, \pi/2)$. More importantly the dipole approximation does not have superfluid correlations. This will be addressed in the next section.

4.2.5 Mott to superfluid transition

This section is devoted to the study of a quantum phase transition of the effective Hamiltonian. In particular, the existence of numerical evidence of a Mott to superfluid transition, similar to that of the one-dimensional Bose-Hubbard model, will be investigated.

This section focuses on two measures, which characterize the Mott to superfluid transition. Both of them are known to work well with smaller system sizes. This is important in the context of this work, since more advanced numerical approximation schemes, that allow for larger system sizes such as DMRG, cannot be directly implemented for the effective Hamiltonian. The first method that is presented makes use of finite size scaling and the second is based on Luttinger liquid theory. Both of them are reviewed for the Bose-Hubbard model, to show that they produce adequate results, even for small systems.

Vanishing of the Mott gap

An important property of the superfluid phase is that in the thermodynamic limit a particle-hole excitation can delocalize with no energy cost. On the other hand, as the name Mott-insulator suggests, the same is not true in the Mott phase. Delocalization costs a finite amount of energy, which means that particle transport requires some amount of impetus. This finite amount (of energy) is the Mott gap Δ, and its presence is an important characteristic of the Mott phase. Following the procedure laid out in Ref. [246] this gap can be defined as

$$\Delta(N) = E(N, N+1) - 2E(N,N) + E(N, N-1) \ , \tag{4.74}$$

where $E(L, N)$ is the ground state energy of a system with L sites and N particles. $\Delta(N)$ thus compares the ground state energy of a system with N sites and N particles to a system that has an additional particle or hole. If $\Delta(N)$ vanishes in the thermodynamic limit $L, N \to \infty$, then a particle-hole excitation can delocalize at no energy cost and the system is superfluid. Here, the thermodynamic limit is extrapolated from finite size system scaling: the effective Hamiltonian (4.44) was diagonalized for increasing system sizes $N = 5, 6, 7, 8$ and the scaling of the gap was then fitted to

$$\Delta(N) = \Delta_\infty + d/N + \mathcal{O}(1/N^2) \ , \tag{4.75}$$

with a least-squares fit. Δ_∞ is then extracted from the intercept ($d/N = 0$). Even though the system sizes involved in this procedure are quite small, the point of transition is predicted quite well for the undriven Bose-Hubbard model $J(t) = J$ [Eq. (4.2)]. From

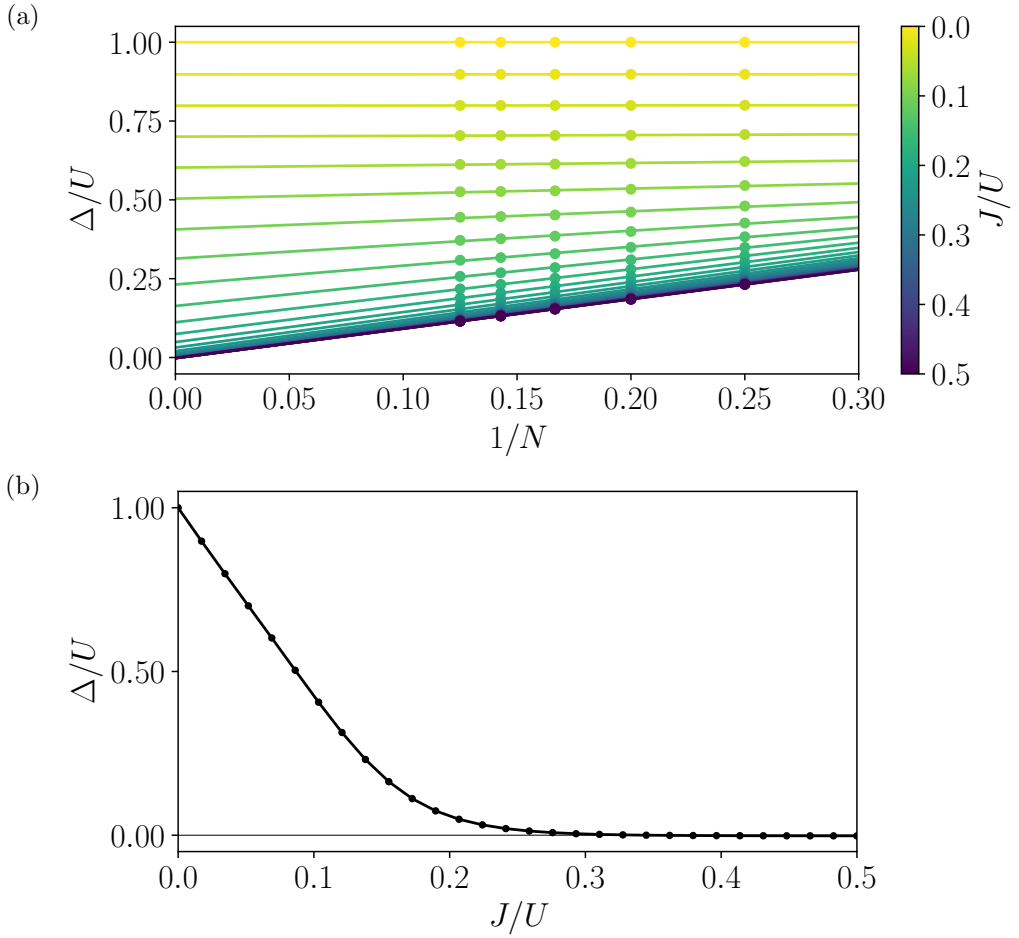

Figure 4.14: (a) Linear regression of $\Delta(N)$ [Eq. (4.75)] for $N = 5, 6, 7, 8$ for the undriven Bose-Hubbard model $J(t) = J$ [Eq. (4.2)]. The dots represent the numerically computed value and the lines the linear regresssion. The colors match the respective value of J/U. (b) Values of Δ_∞ represented by the intercept of the linear regression in (a). For $J/U \approx 0.32$ the gap vanishes, marking the Mott to superfluid transition

Fig. 4.14 the critical value $J/U \approx 0.32$ can be determined. This is very close to the critical value $J/U \approx 0.3$, that is found for much larger systems [247, 248]. For the effective

Hamiltonian, the same calculation was performed. The results are shown in Fig. 4.15. Fig.4.15a shows the gap $\Delta(N)$ as a function of $1/N$ for the system sizes $N = 5, 6, 7, 8$ and

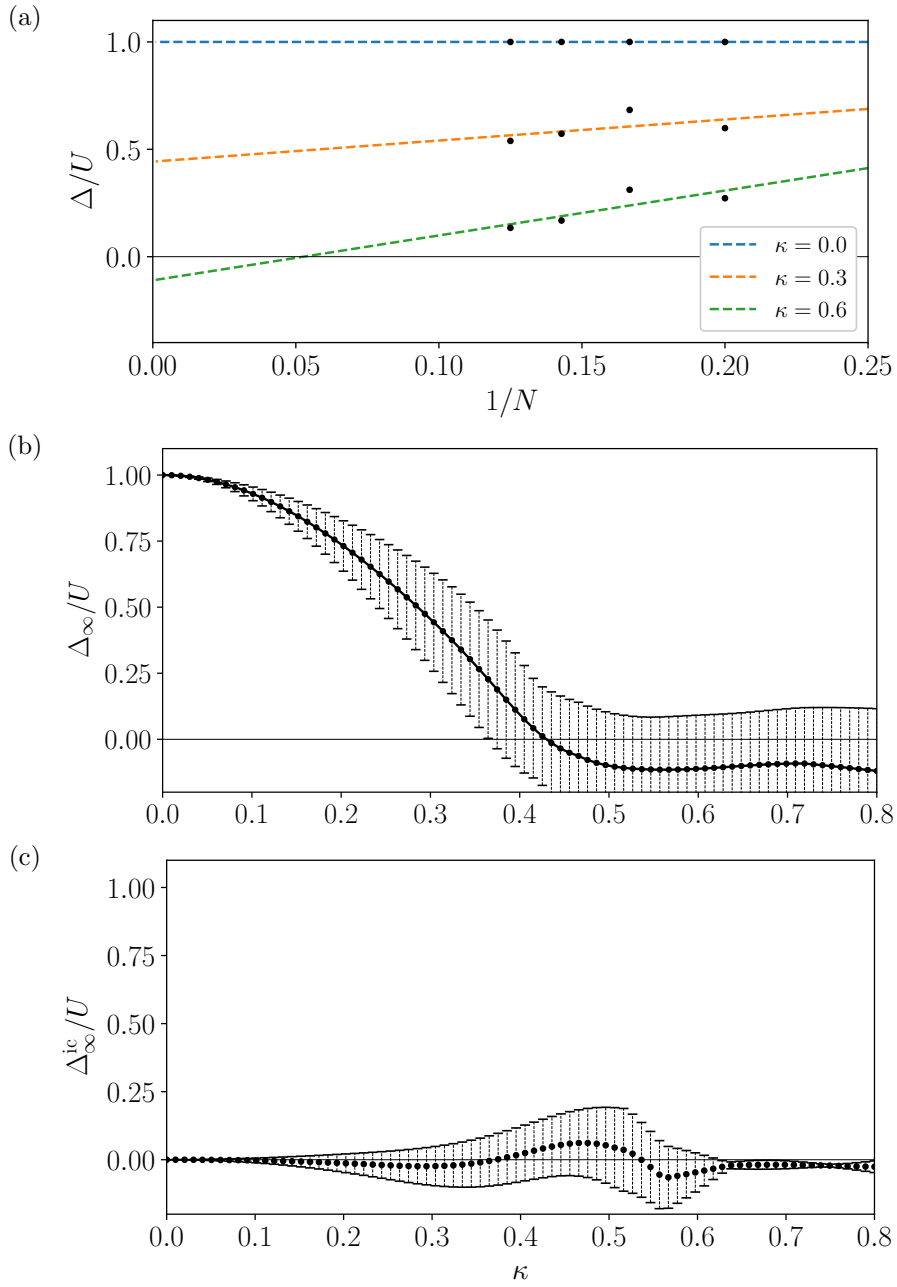

Figure 4.15: (a) The gap $\Delta(N)$ and its dependence on the lattice size N is displayed. Each point was calculated for unit filling. The lines represent the least squared fit used to calculate the Δ_∞ in the thermodynamic limit. (b) Δ_∞ corresponding to the intercept of the linear regression in (a). Error bars represent the statistical uncertainty of the fitting procedure. For $\kappa \approx 0.42$ the gap vanishes, signaling the transition from Mott to superfluid transition. (c) $\Delta_\infty^{\mathrm{ic}}$ for the case of incommensurate filling. In contrast to the commensurate case, the system remains superfluid throughout the driving range.

unit filling. As was calculated for the Bose-Hubbard model, linear regression was used to

extract Δ_∞ in the thermodynamic limit. The deviation from the fitting procedure can be seen in the error bars in Fig.4.15b, where Δ_∞ is shown over a range of κ. Even though the error is quite large, a clear trend can be seen. At $\kappa = 0$ the gap $\Delta_\infty = U$, which is the value it has to be for a Mott insulator. At $\kappa \approx 0.42$, the gap vanishes and remains closed, indicating a Mott to superfluid transition. To see whether or not this method produces consistent results with incommensurate fillings of $N - 2$, particles on N sites were investigated as well. The gap then becomes

$$\Delta^{\mathrm{ic}}(N) = E(N, N-1) - 2E(N, N-2) + E(N, N-3)\,. \tag{4.76}$$

In Fig. 4.15c the gap $\Delta^{\mathrm{ic}}_\infty$ remains consistently zero, signaling that the system remains superfluid over the entire range of driving. This is what would be expected from Luttinger liquid theory [248], where a non-commensurate system falls into a different universality class than the commensurate case and the system is expected to remain superfluid over the entire range of κ. Luttinger liquid theory will be the focus of the next section. Since the error in the gap calculation is quite large, another method is employed to locate the phase transition.

Luttinger liquid parameter

In one-dimensional interacting systems of bosons and fermions Tomonaga-Luttinger liquid (TLL) theory [249, 250] provides a unifying framework with which both particle types can be treated. An important tool for sorting out the properties of these systems are their various correlation functions. Most importantly, these correlations posses a power-law decay [251]. Another important feature is that the low-energy excitations of a TLL have a linear dispersion law, which, after Landau's superfluidity criterion [252], makes them true superfluids in one dimension. A TLL is described by two parameters: the interaction parameter (also called stiffness or Luttinger parameter K_b), which provides the asymptotic behavior of all correlation functions, and the velocity v of the phononic excitations, which have a linear dispersion relation. Both of these parameters enter the TLL Hamiltonian [74], describing the behavior of the collective excitations in the liquid (Ref. [74] uses the convention $K_b' = 1/K_b$):

$$H = \frac{v}{2\pi} \int \mathrm{d}x \left\{ \frac{1}{K_b} \Pi(x)^2 + K_b \left[\partial_x \Phi(x)\right]^2 \right\}\,, \tag{4.77}$$

where $\Phi(x)$ is the phase of the density modulations and $\Pi(x) = \partial_x \theta(x)$ its conjugate variable. $\theta(x)$ can be interpreted as the superfluid phase of the liquid. In the following, v and K_b are determined numerically, so their values in terms of e.g. the Fermi velocity and the magnitude of the interactions of the underlying particles are not of relevance here (for more information see e.g. [74]). The explicit value of the Luttinger parameter K_b depends not only on the interactions of the underlying particles but also on the presence of an underlying lattice and on the commensurability of its filling. The commensurability of the filling is defined by the ratio $p = L/N$. This ratio determines certain universal values of K_b which can be used to determine the phase of the liquid. Here two types of fillings are considered. For unit filling, K_b takes the universal value $K_b = \infty$ in the Mott-insulator regime. In the superfluid regime $K_b = 1/2$. For an incommensurate filling, $K_b = 1$, which implies superfluid correlations.

As in Ref. [2] K_b is extracted from the density-density correlation function [253]

$$N(r) = \frac{1}{N}\sum_{x=1}^{N}\langle n_x n_{x+r}\rangle - \langle n_x\rangle\langle n_{x+r}\rangle \ , \tag{4.78}$$

which asymptotically decays as [248]

$$N(r\to\infty) = \frac{-1}{2K_b\,(\pi r)^2} + A\frac{\cos(2\pi r)}{r^{2/K_b}} + \dots \ . \tag{4.79}$$

Instead of fitting $N(r)$ directly to Eq. (4.79), however, evaluating its Fourier transform, $N(k)$, and estimating K_b from its derivative yields more stable results [254]:

$$\frac{1}{2\pi K_b} = \lim_{k\to 0}\frac{N(k)}{k} \ . \tag{4.80}$$

In Fig. 4.16 this method is used to extract the phase transition for the undriven Bose-

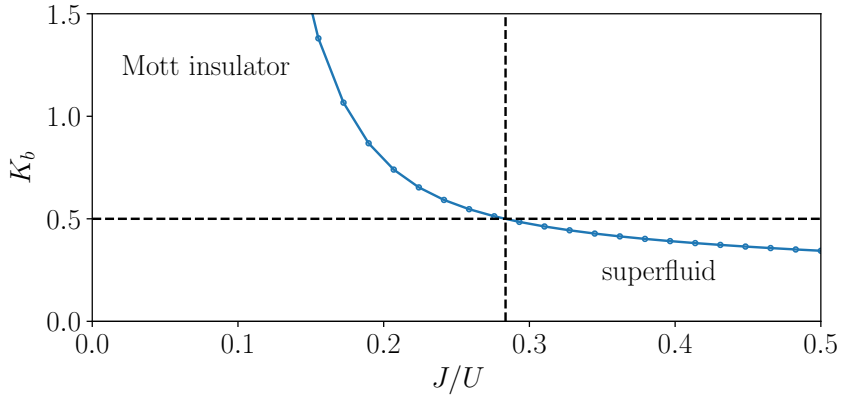

Figure 4.16: Using K_b in Eq. (4.80) determines the Mott to superfluid transition for the undriven Bose-Hubbard model [Eq. (4.2), $J(t) = J$]. The system size was set to $(N, L) = (8, 8)$. For $J/U < 0.28$ the values of K_b diverge. The Kosterlitz-Thouless transition from Mott to superfluid phase is taken to occur for $K_b = 0.5$. The value for which this happens is $\kappa \approx 0.283$ which is not far from the value found in Fig. 4.14.

Hubbard model for $(N, L) = (8, 8)$. For a finite sized system, the presence of the Mott phase in the thermodynamic limit is indicated by diverging values of K_b. These lie outside the range of K_b shown in Fig. 4.16 for $J/U < 0.15$. Once J/U increases K_b continues dropping in magnitude. The transition between the Mott state and the TLL is of Kosterlitz-Thouless type for all commensurate fillings. In the superfluid phase, for unit filling, the universal value is $K_b = 1/2$. For the finite sized system under consideration, this is the criterion that determines the critical point of the transition [74, 248]. In Fig. 4.16 it can be seen that this happens at $J/U = 0.28$, which is close to the value that was calculated in the previous section, where $J/U \approx 0.32$. This confirms that the TLL method is also adequate for determining the critical point of the phase transition.

In Fig. 4.17a $N(k)$ is shown for a few values of κ for the ground state of $H^{\text{eff}}_{\text{pbc}}$ for 8 sites and unit filling. It can be used as a proxy for the dispersion relation of the density

fluctuations. For small $\kappa < 0.3$ the system has a gap and the $N(k)$ displays quadratic behavior close to the origin, which corresponds to $K_b = \infty$. Beyond $\kappa = 0.3$ the linear behavior of $N(k)$ close to the origin becomes clear. This is correlated with the vanishing of the gap (Fig.4.15). This is additional evidence that justifies the use of TLL theory to determine the Mott-to-superfluid transition. In Fig. 4.17b the Mott to superfluid transition can be located at $\kappa \approx 0.48$. This is close to the value determined through the calculation of the Mott gap. Given that the gap calculation had quite large errors, this can still be considered a good agreement. Doping the system slightly immediately

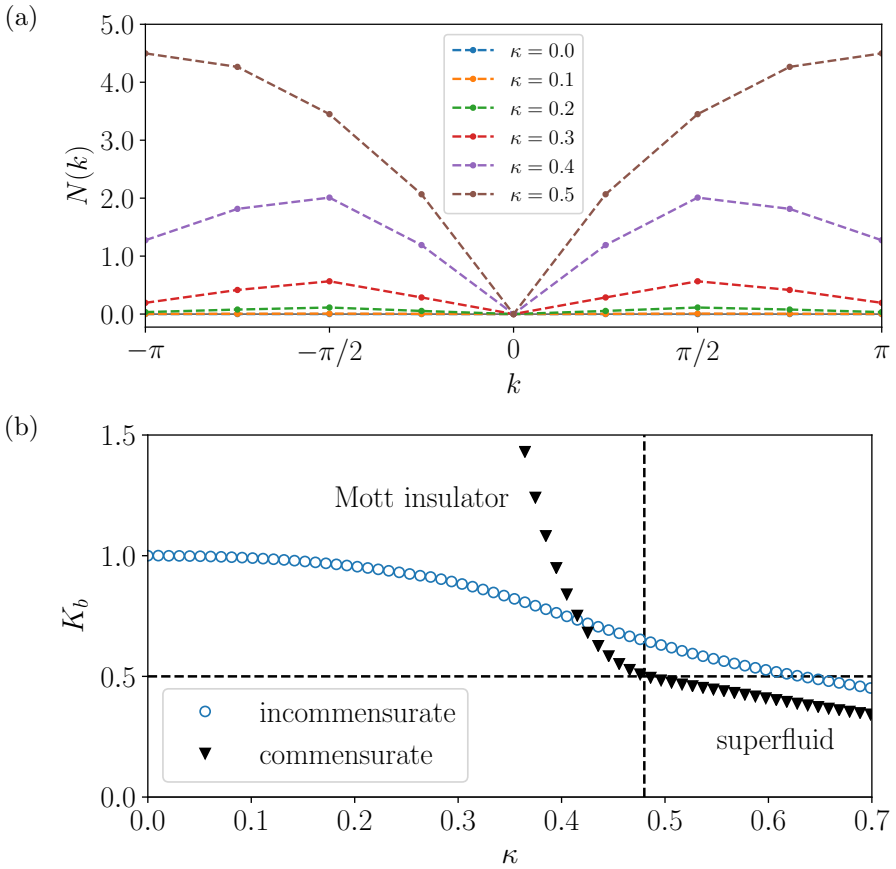

Figure 4.17: a) Fourier transformation of $N(r)$ for various driving amplitudes κ in the commensurate case of $(N, L) = (8, 8)$. For small values of κ (solid lines) the system is gapped, which is consistent with the quadratic behavior of $N(k)$ close to the origin. For larger κ (dashed lines) the gap vanishes. For these values $N(k)$ is linear for small k. b) Luttinger parameter, K_b, calculated from the Fourier transformation of the density correlation Eq. (4.80). For commensurate filling (black triangles) K_b diverges as κ reduces, indicating the Mott phase. When K_b passes through the universal value $K_b = 1/2$, the system transitions to the superfluid phase. By contrast, an incommensurate system of 6 bosons in an 8-site lattice (blue circles) is superfluid for all non-zero values of κ. In this case, as $\kappa \to 0$, K_b approaches unity, as expected for a such a system (for incommensurate fillings the universal value is $K_b = 1$).

produces superfluidity. The system will only be Mott insulating for $\kappa = 0$. Once κ grows,

superfluid correlations become instantly apparent. This is marked by $K_b < 1$ [248]. In Fig. 4.17b the blue circles shows the Luttinger parameter for an incommensurate filling $(N, L) = (6, 8)$. For all values of $\kappa > 0$ the blue circles are consistently smaller than 1, indicating superfluid correlations. As expected, this is consistent with the universality class of $K_b = 1$. This further strengthens the reliability of this manner for extracting K_b.

The superfluid correlations appearing in the numerical investigation of our system are another reason why the variational ansatz in Eq. (4.55) has to fail for $\kappa > 0.4$. Evaluation of $N(r)$ for $|\xi\rangle$ gives

$$N(r) = \frac{1}{N}(1 - \alpha^2)(2\delta_0 - \delta_{r,2} - \delta_{r,-2}) \tag{4.81}$$

which is short ranged and cannot produce the types of correlations described by Eq. (4.79).

4.2.6 Spectral function

The unusual nature of the system prompted an additional test of the TLL picture in Ref. [2]. The goal was to determine the linearity of the dispersion relation of the low lying excitations through an additional method, which in theory would allow for the determination of the second parameter describing the TLL v, i.e. its group velocity. In [2] this was achieved by using the method developed in [254, 255]. They made use of a spectral function to determine the dispersion relation of the low lying excitations.

The zero temperature spectral density function used here is defined as

$$A(\omega, k) = \sum_n \left| \langle \Psi_n | a_k^\dagger | \Psi_g \rangle \right|^2 \delta(\omega - \omega_n) \ . \tag{4.82}$$

where $|\Psi_n\rangle$ is the n-th excited state in the $N+1$ particle system, $|\Psi_g\rangle$ is the ground state of N particles and $\omega_n = E_n(N, N+1) - E_0(N, N)$. $E_n(N, N+1)$ is the energy of the n-th excited state in the $N+1$ particle system. To smooth out the spectral function $A(\omega, k)$, it was convoluted with a narrow Lorentzian. Sharp peaks in $A(\omega, k)$ indicate quasiparticle excitations, from which the dispersion relation $\omega(k)$ can be inferred. In the upper panels of Fig. 4.18, the results obtained for a system clearly located in the superfluid regime ($\kappa = 0.53$) are shown. For each value of momentum, the spectral function shows a single sharp peak, whose location shifts as the momentum changes. The contour plot of $A(\omega, k)$ reveals that this momentum dependence corresponds to two regions of linear dispersion, centered on $k = \pm\pi/2$ exactly where the two condensates formed. Even though the double dip structure is unusual, it is consistent with a picture where the low lying excitations have a linear dispersion.

As explained in Chapter 1 (Section 1.4), the thermodynamic limit of a Floquet system with interactions is not necessarily well defined because of the many-body resonances that occur once $UN(N-1)/2$ is of the order of the driving frequency. However, due to the existence of a long pre-thermal regime, an investigation of the thermodynamic limit is not completely unreasonable. An in-depth study of the heating that occurrs in a kinetically driven Hamiltonian would be an interesting endeavor by itself, but it is beyond the scope of this thesis.

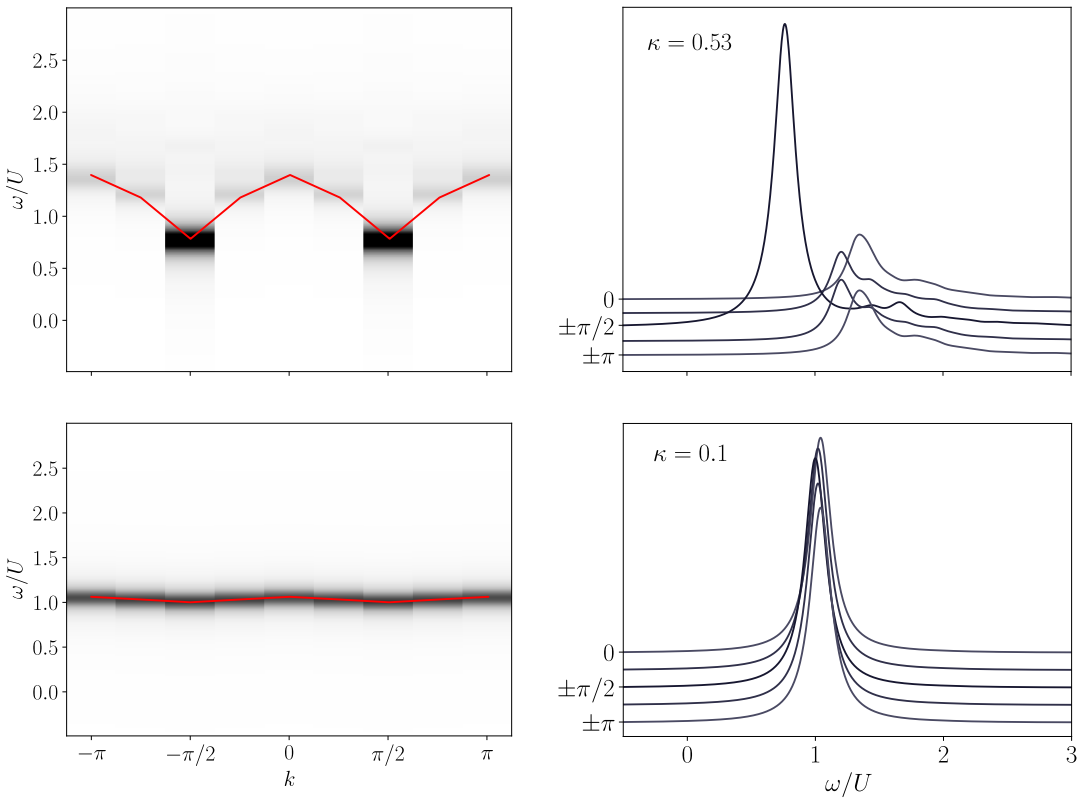

Figure 4.18: The spectral density (left panels) and line shape (right panels) $A(\omega, k)$ of a single quasiparticle excitation. The red lines in the left panels indicate the dispersion relation $\omega(q)$; the velocity of excitations (the other Luttinger parameter) being given by the slope of these curves at $k = \pm\pi/2$. Upper plots are for the superfluid regime $\kappa = 0.53$, the lower panels for the Mott insulating regime $\kappa = 0.1$ for $N = 8$.

4.3 Cosinusoidal driving with hard wall boundary conditions

The effective Hamiltonian for HWBC and cosinusoidal driving (4.43) in the stationary wave representation is [Eq. (4.23)]

$$\begin{aligned} H_{\mathrm{hw}}^{\mathrm{eff}} = & \frac{2U}{(L+1)^2} \sum_{x=1}^{L} \sum_{l,m,n,p=1}^{L} \sin(\tilde{k}_l x) \sin(\tilde{k}_m x) \sin(\tilde{k}_n x) \sin(\tilde{k}_p x) \\ & \times \mathcal{J}_0\{2\kappa[\cos(\tilde{k}_l) + \cos(\tilde{k}_m) - \cos(\tilde{k}_p) - \cos(\tilde{k}_n)]\} \\ & \times a_{\tilde{k}_p}^{\dagger} a_{\tilde{k}_n}^{\dagger} a_{\tilde{k}_m} a_{\tilde{k}_l} \ . \end{aligned} \tag{4.83}$$

Some important differences between $H_{\mathrm{hw}}^{\mathrm{eff}}$ and $H_{\mathrm{pbc}}^{\mathrm{eff}}$ were already mentioned at the end of Section 4.1. An important difference to the ring is the lack of momentum conservation, which can be seen in the residual sum over x and the explicit appearance of the stationary waves. Other changes due to the boundary conditions are the momenta $\tilde{k}_l = \pi l/(L+1)$. With the reduction of symmetry it is also not possible to study the effective hopping and interaction terms as concisely as in Section 4.2. The Q_{wxyz} defined in Eq. (4.47) can no

longer be chosen in such a way that Q_{0xyz} is representative for all possible hopping and interaction terms since those will clearly depend on where w is positioned relative to the walls.

Furthermore, the presence of the walls alters the density correlation functions [248] in such a way that the numerical study of the phase transition is no longer applicable, since the system now really is too small. Some measures remain useful however, and they help to analyze and understand the system. These include the momentum density, the one-RPDM and the two particle momentum density. The spectrum shows some interesting differences to PBC. The well separated ground doublet that formed for increasing κ is no longer present for HWBC.

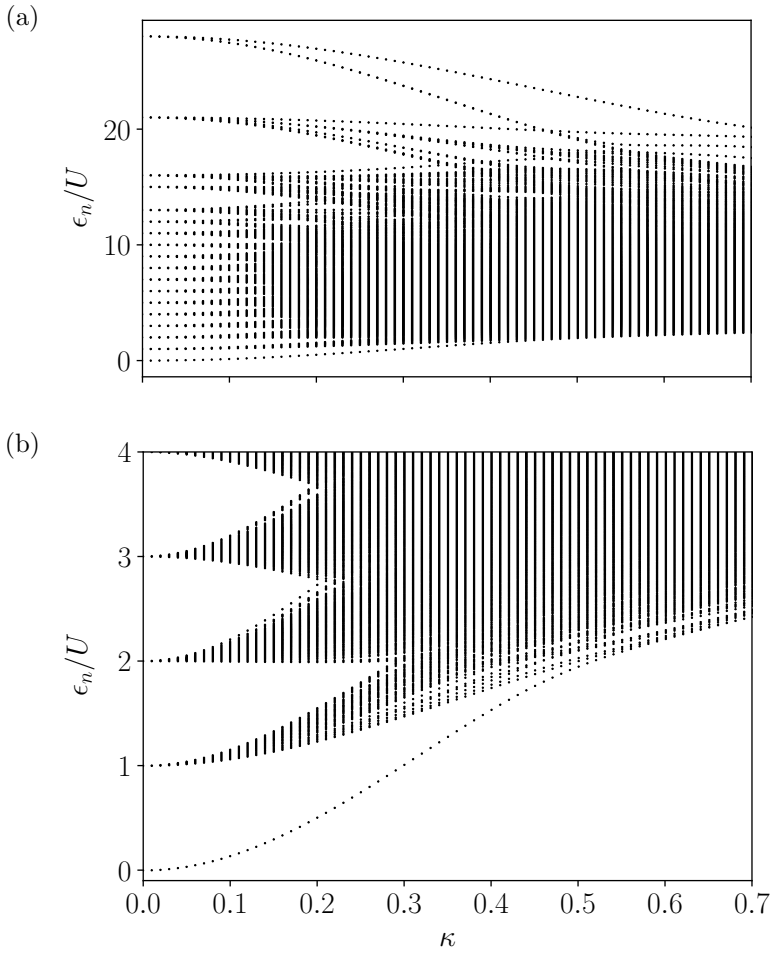

Figure 4.19: Quasienergies of $H_{\mathrm{hw}}^{\mathrm{eff}}$ for (a),(b) $(N, L) = (8, 8)$. For $\kappa = 0$ the spectrum is gapped. Each level is characterized by a number of particle-hole excitations. $\epsilon_n = 0$ corresponds to the Mott state implying one particle per site. (b) zoom-in for $(N, L) = (8, 8)$.

4.3.1 Momentum density

In the same way as for PBC, the momentum density for HWBC of the ground and first excited state can be calculated as a function of the driving parameter κ. For a

better comparison with PBC, the truncated plane wave transformation (4.25) was used for the computation of the momentum density. This is shown in Fig. 4.20. Curiously, the momentum density $\rho(k)$ for HWBC behaves in a very similar way to those of the ring. Incidentally there is no visible discontinuity in $\rho(k)$ for the first excited state as there was for PBC. Another difference to PBCs is that the peaks are not quite as pronounced and consequently momenta other than $k = \pm\pi/2$ contribute more. Again, higher excited states lose the double peak feature. The natural orbitals are no longer just plane waves in the

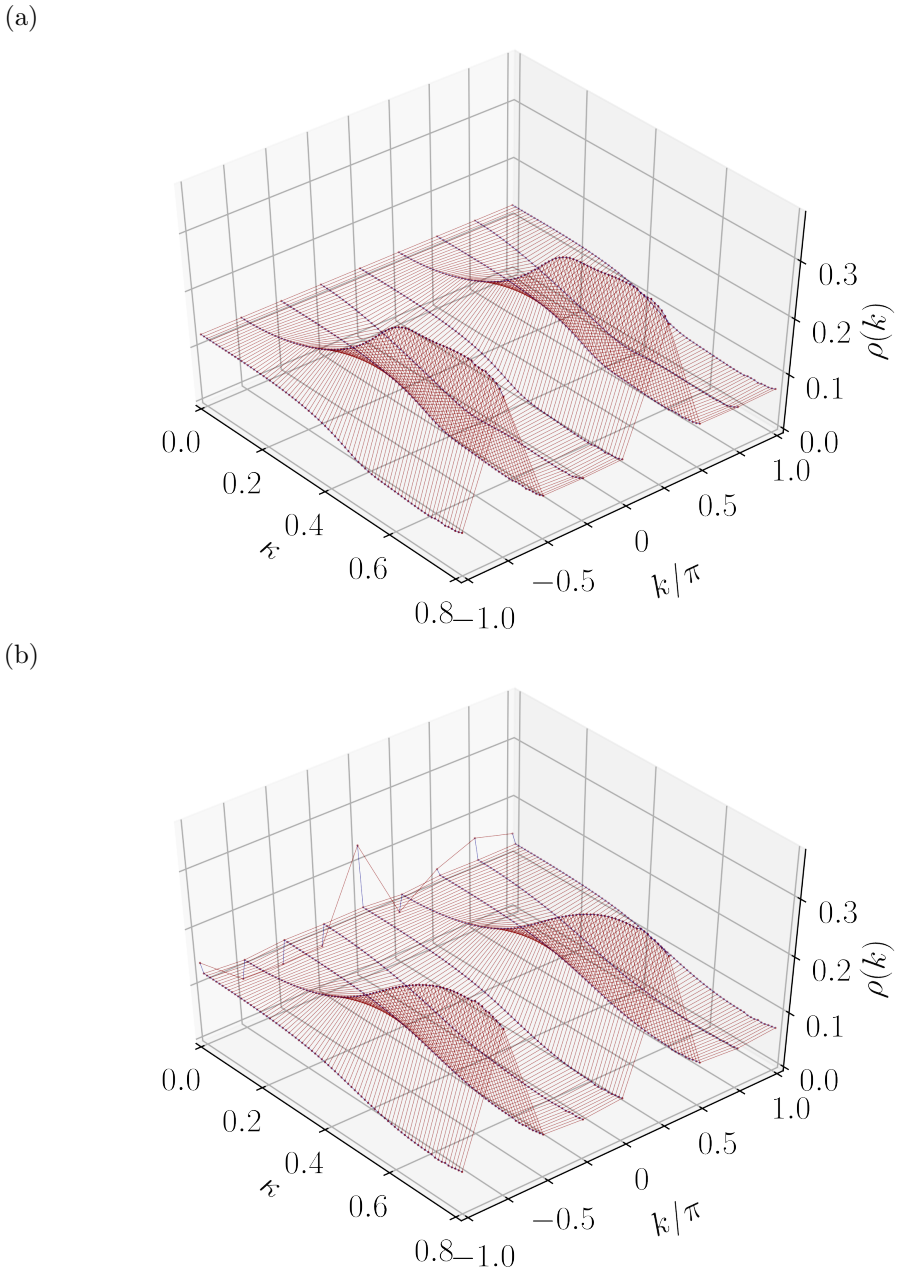

Figure 4.20: (a) Momentum density $\rho(k)$ of the ground state for $(N, L) = (8, 8)$ as a function of κ for HWBC. Just as for PBC two peaks form at $k = \pm\pi/2$. (b) $\rho(k)$ of the first excited state shows the same behavior as the ground state. In contrast to PBC, there is no discontinuity at $\kappa = 0.2$.

truncated plane wave representation. As a general rule it can be stated that interactions with the wall are energetically costly so the system tries to avoid them. In the bulk of the lattice the natural orbitals behave more like plane waves again. In standard Bose-Einstein condensate (BEC) theory, the distance required for the condensate to "repair" the presence of an obstacle is known as the healing length. In the numerical calculation of one-PRDM in the truncated plane wave representation, non-negligible imaginary off-diagonal contributions are present. This is illustrated in Fig. 4.21. For PBC this was not the case and in the plane wave representation the one-PRDM is a real valued diagonal matrix (Fig. 4.7). In the next chapter the nature of the natural orbitals will be discussed in greater detail. Fig. 4.22 shows that the occupation of the natural orbitals displays an

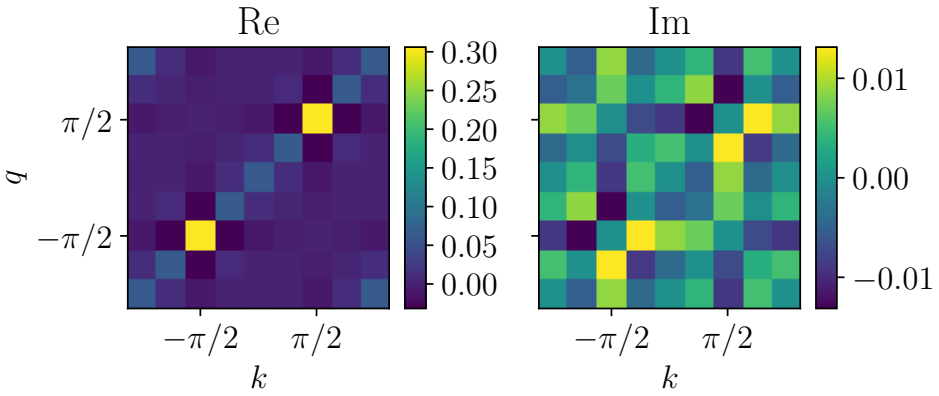

Figure 4.21: One-RPDM evaluated for the ground state for $\kappa = 0.75$ and HWBC in the truncated plane wave representation. When compared with Fig. 4.7, the matrix is no longer diagonal and real. This is due to the fact that the truncated plane waves are not a natural choice for HWBC and that the density close to the walls is reduced in the ground state.

on-set of condensation for $\kappa > 0.3$, as for PBC. Each of the four eigenvalues of the one-PRDM is two-fold degenerate. Together with the momentum density these two findings present remarkable similarities to the ring.

4.3.2 Two-particle momentum density

As computed for the PBC the two-particle momentum density was calculated for HWBC. The results can be seen in Fig. 4.23. An easy comparison with PBC is ensured by using the truncated plane wave representation. It is notable that the ground state for HWBC remains Schrödinger cat-like. The first excited state shows very similar correlations to that of the ground state. In Fig. 4.24 the higher excited states are shown for $\kappa = 0.6$. As for PBCs the cat like correlations disappear for the second and higher excited states. These findings will be discussed in greater detail in the following chapter.

4.4 Experimental implementation

The cosinusoidal kinetic driving proposed in this chapter is quite unusual as it requires a sign change of the tunneling amplitude. The method proposed in [2] makes use of

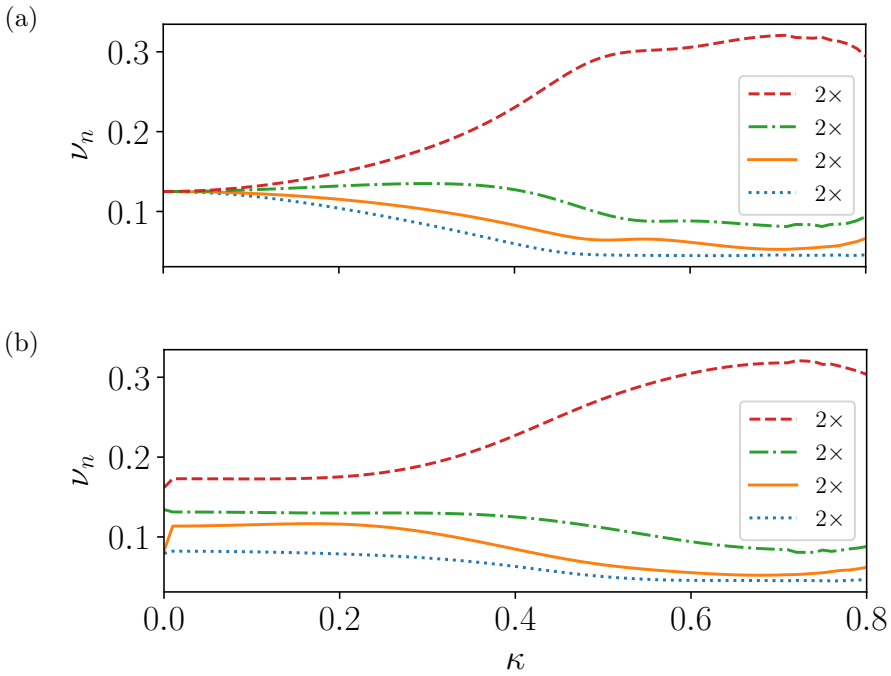

Figure 4.22: The eigenvalues ν_n of the one-RPDM for (a) the ground and (b) first excited state with HWBC are shown. (a) The magnitude indicates the occupation of the respective natural orbital. As for the ring, an increase in κ produces two degenerate orbitals that are more and more occupied. Again, this indicates the formation of a fragmented condensate. The degeneracy of each ν_n is listed in the legend. The most occupied orbitals are also not quite as populated as for the ring.

the lattice shaking technique. As discussed in detail in Chapter 1 and Chapter 2, this technique allows for the precise control of the tunneling amplitude. When the lattice is shaking with a large enough frequency Ω, the effective value of the tunneling amplitude is renormalized to an effective value. For sinusoidal shaking the effective tunneling amplitude is $J_{\text{eff}} = J\mathcal{J}_0\left(K/\Omega\right)$, where the amplitude of the shaking K was first introduced in Eq. (1.71). Fig. 4.25 shows J_{eff} for a range of Ω/K. At $K/\Omega \simeq 2.404$ the zeroth order Bessel function passes its first zero and the effective tunneling amplitude vanishes.

A slow alternation of the shaking parameters can now be envisioned [256], so that J_{eff} follows the change of the parameter $K(t)/\Omega$ on a time scale much larger than the shaking period $\tau = 2\pi/\Omega$. If this is done periodically with a frequency $\omega \ll \Omega$ around the first root of the Bessel function, the effective tunneling amplitude will become time dependent and it will oscillate between positive and negative values. If a suitable choice of $K(t)$ is made, a waveform of the driving such as in Eq. (4.2) with $J(t) = J\cos(\omega t)$ can be envisioned. For the applicability of the effective Hamiltonians (4.44) and(4.23) in the large frequency regime, the hierarchy of the driving frequencies $J, UN(N-1) < \omega \ll \Omega$ has to hold true.

For example, systems in which these conditions can be implemented include those with 87ˆRb [65, 257] and potassium-39 [258]. For a single-band BH model optical lattice depths of $V_0 > 6E_r$ are required, where E_r is the recoil energy. All but the nearest-neighbor hopping terms are then suppressed. Since the shaking frequencies have to be smaller than

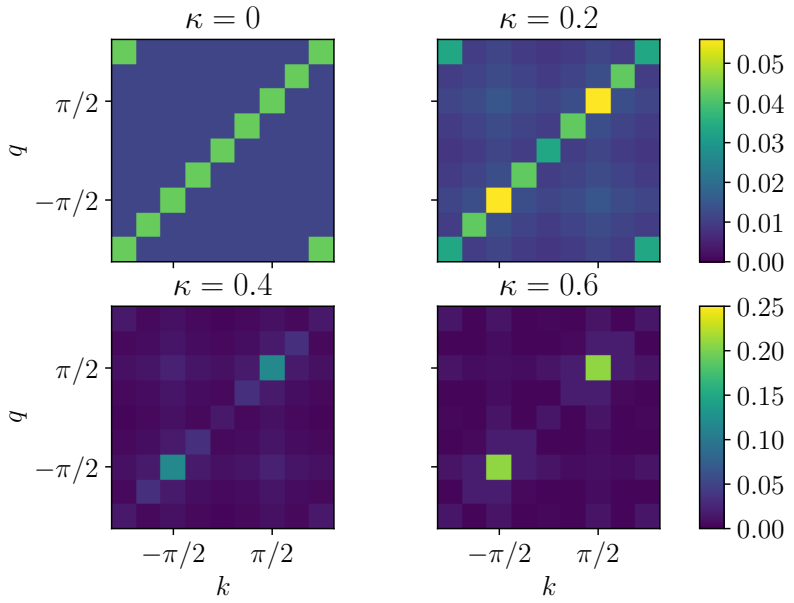

Figure 4.23: The two particle momentum density $\rho^{(2)}(q,k)$ of the ground state for HWBC is shown. As in PBC two distinct peaks emerge at $(q,k) = \pm(\pi/2, \pi/2)$. Again, most notable is the absence of cross-correlations at $(q,k) = \pm(-\pi/2, -\pi/2)$, indicating a Schrödinger cat-like nature of the ground state for $\kappa \geq 0.5$.

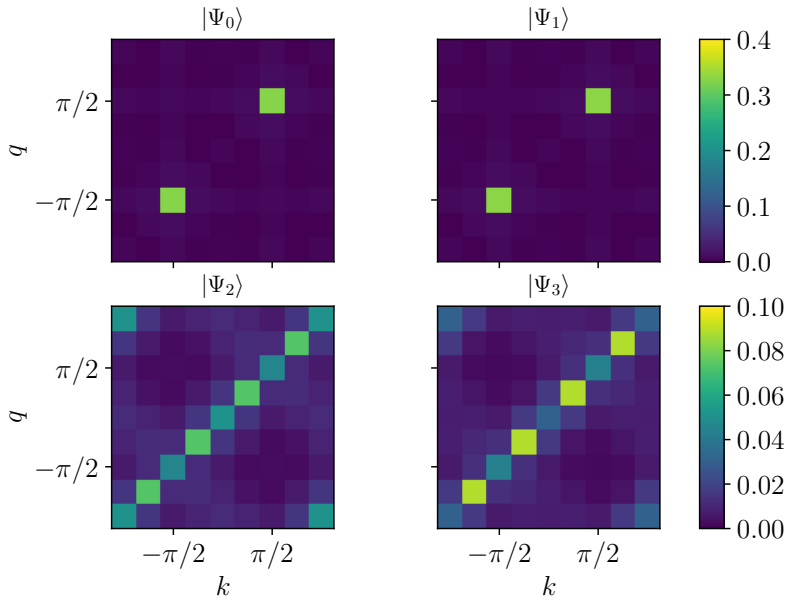

Figure 4.24: $\rho^{(2)}(q,k)$ at $\kappa = 0.6$ for the ground state $|\Psi_0\rangle$ to the third excited state $|\Psi_3\rangle$ with HWBC. The cat-correlations (see text or Fig. 4.12) are lost for the second and third excited state.

the excitation energy to the next band, several tens of kilohertz are permissible. The bare tunneling J that remains is of the order 100 Hz. This is sufficient to satisfy the first

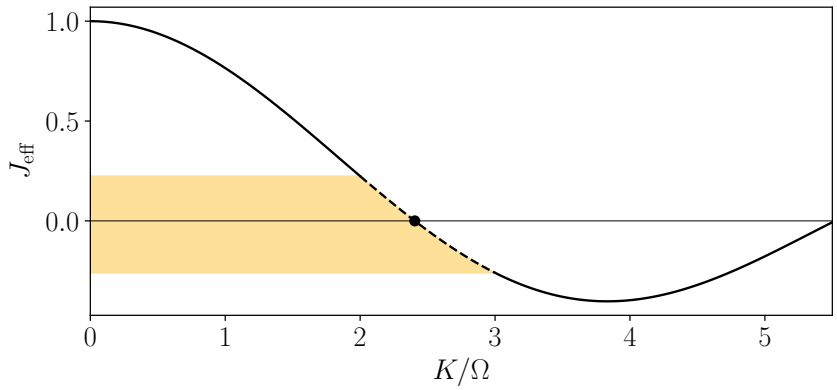

Figure 4.25: Sinusoidal lattice shaking produces an effective tunneling $J_{\text{eff}} = J\mathcal{J}_0(K/\Omega)$ where Ω is the frequency of the shaking and K is its amplitude. A periodic variation of K/Ω around the first root of the Bessel function results in an oscillation of J_{eff} with same periodicity in the shaded region. In the large frequency regime, this yields the Hamiltonians (4.44) or (4.23) depending on the boundary conditions.

condition, $J < \Omega$, and leaves a reasonable range of available frequencies for ω at which the tunneling is modulated. The interactions can be adjusted, by means of Feshbach resonances, to fit into the required hierarchy.

Heating due to the drive is another important aspect in a possible experimental implementation. As discussed in Chapter 1 (Section 1.4) heating to an "infinite temperature", known as the eigenstate thermalization hypothesis, is a serious obstacle to preserving the quantum coherence. As long as the driving frequencies are much larger than the energy scales given by the undriven Hamiltonian, a long-lived prethermal regime can be assumed [108, 110]. In this regime, heating is an exponentially small function of the driving frequency. This leaves a relatively long time-scale in which the dynamics of the system can be approximated well by the effective Hamilonian. The Bose-Hubbard model in particular is known to have this property [259], so there is a high level of confidence that there is sufficient time to observe some of the unusual properties discussed in this chapter.

The momentum density or the other signatures discussed in this chapter can be revealed experimentally. Time-of-flight methods are the most readily available for this. The stability of the states that were presented in this chapter will be a topic in the next chapter. All together an experimental realization and the observation of the properties presented in this chapter are feasible.

4.5 Summary and conclusions

In this chapter, the kinetically driven Bose-Hubbard model was studied. First, the general effective Hamiltonians for PBC and HWBC were derived without choosing a specific waveform. In Section 4.2 the ring was investigated with a cosine waveform. The analysis was based on the findings in [2]. The process by which renormalized hopping amplitudes produce atypical interactions and correlated hoppings was discussed. Numerical inspection showed that these interactions have a limited reach, and yet also have some

remarkable effects. A notable result was the formation of a fragmented condensate at $k = \pm\pi/2$. For $\kappa < 0.3$, with the help of a variational ansatz [dipole states Eq. (4.55)], an intuitive explanation for the formation of these peaks was given: $\sum_x Q_{2xx0}$ was interpreted as a next-to-nearest neighbor single-particle hopping amplitude giving rise to a negative effective mass, in conjunction with a dispersion relation that has two minima at $k = \pm\pi$. This simple picture had to be abandoned once the condensate fully formed. The dipole states cannot describe the two-particle momentum density nor the fluctuations that arise as $\kappa > 0.3$. The study of the Mott gap and TLL theory helped to unveil a Kosterlitz-Thouless phase transition from Mott to superfluid phase at $\kappa \approx 0.48$. The expected universal behavior of Δ and K_b for different commensurabilities of the filling reinforced the validity of the application of both approaches. Finally, the spectral function further solidified the linear dispersion of the energetically low lying density fluctuations.

The two-particle momentum density firmly ruled out a simple product state as an approximation for the ground state of the effective Hamiltonian. A much better candidate is the Schrödinger cat state in Eq. (4.73). This is quite remarkable by itself and a thorough explanation of its formation is given in the next chapter.

In Section 4.3 a similar analysis as that for the ring was performed for HWBC. The presence of the walls made the study of the phase transition nearly impossible with the methods employed in this chapter. Despite this, evidence that condensation takes place was found. The momentum density and two particle momentum density for the ground and first excited states appeared to be in a similar range to those in PBC. This means that both the ground and first excited states are best described as Schrödinger cats. This will also be of interest in the next chapter.

Finally an experimental implementation was discussed and it was found to be feasible.

Chapter 5

Protected cat states from kinetic driving of a boson gas

5.1 Introduction

This chapter is based on the author's work in the article [3], which addresses the generation of cat states through kinetic driving. This work is a continuation of that presented in the previous chapter and provides substantial additions to the analysis presented in it. One of the most curious predictions of the laws of quantum mechanics is the existence of macroscopic superposition states (MQS). In the famous thought experiment by Erwin Schrödinger [260] a cat is locked up in a box with a devious mechanism that ties the demise of the cat to the decay of a small amount of radioactive substance. The quantum mechanical nature of the decay creates a superposition state of a dead cat and alive cat, a so-called Schrödinger cat state or simply cat state. This is very much at odds with humans' perception of macroscopic objects. The superposition of dead and alive would immediately turn into one of the two options if an attempt is made to observe the cat. This discontinuity in the evolution of the wave function [261] is known as wave function collapse. The Schrödinger cat paradox is often resolved by looking to the environment. Since the box is not a perfectly isolated system, its environment will become entangled with the cat state and produce a statistical mixture before an observer can cause the collapse. In fact, an observer or a measuring apparatus is often understood as a special kind of dissipative environment inducing the collapse [262–264]. In general, the bigger a system, the more difficult it is to shield it from such a dissipative environment, which in turn accelerates the effect of decoherence [263].

Cat states represent a form of entanglement where the amount of particles sharing their fate in a particular measurement is taken to an extreme. Even without the macroscopic aspect, entanglement induces a zoo of contradictions between classical and quantum logic. Some notable examples include the quantum eraser [265, 266], ghost imaging [267–269], delayed choice inference [270–273] and, arguably the most important, the violation of Bell's inequalities [274–277].

As a special form of extreme entanglement, cat states are of great fundamental interest themselves. They are central to proposals testing macroscopic realism [278–282]. At the heart of macroscopic realism lies the question of whether there can be an observer-independent description of macroscopic objects that keeps the laws of quantum mechan-

ics intact at the micro-level [281]. Other possible applications of cat states are atom interferometry beyond the Heisenberg limit [283], precision measurements [284], quantum information tasks [285] and quantum metrology [286].

The difficulty in creating and maintaining a cat state is produced by the coupling to the environment, which quickly decoheres the superposition into a statistical mixture [263, 264, 287]. The main challenge therefore is to overcome the decohering effects of the environment to make the state live long enough to permit the probing coherence between the two macroscopically distinct states.

This is the context in which the present work is best appreciated. The cat-like states of the previous chapter, which were found in a kinetically driven Bose-Hubbard model, show resilience against collapse into one of their branches in both the ring and hard-wall case. Most importantly, the circular boson superfluid preserves the MQS when subjected to a spurious flux. Similarly, the gas between hard walls is fundamentally unaltered by a velocity drift due to gauge invariance. Another important feature is that the two condensates share the depletion cloud (labeled reduction cloud here), which provides a degree of protection against atom losses. The findings in this chapter are the result of the work presented in Ref. [3].

This chapter is organized as follows: In Section 5.2, a non-exhaustive summary of theoretical and experimental research efforts concerning cat states is given. In Section 5.3 the generation of a cat state in the ring is discussed in detail. The section begins with the failures of various perturbative treatments of the effective Hamiltonian, most notably the failure of a naive application of Bogoliubov-de Gennes theory. In Section 5.3.3 a non-perturbative treatment of the strong driving limit is developed. It provides a solid qualitative understanding of the formation of the cat state through the interplay of attractive interactions in momentum space [288] and a particular case of a pairing interaction commonly encountered in the so-called Richardson-Gaudin pairing models. These play an important role in the context of nuclear physics and small grain superconductivity [289, 290]. According to the work presented here, the two condensates that participate in the ground state of the kinetically driven ring share a common reduction cloud that is a result of the pairing interaction. In the subsequent Section 5.4 the many-body properties of the true ground state in the ring case are highlighted. Since there are many Fock-configurations that contribute to both condensates, no simple criterion for assigning a single configuration to either branch of the cat exists. A symmetry argument helps to precisely define both branches that make up the cat state. For the ring, the effective Hamiltonian yields an unconventional particle current operator which yields a vanishing expectation value for the ground state and the cat branches. In a time-of-flight experiment, however, the behavior of the two cat branches would be markedly different. The same many-body plane wave analysis is performed for hard-wall boundary conditions which is followed by Section 5.5 on the study of harmonic confinement. Section 5.6 features a discussion of different figures of merit that help to characterize the quality of the cat state. The section includes a short review of various measures that were proposed in the literature and the introduction of a new measure. Section 5.7 investigates the preparation of the cat state for both hard walls and the ring. Finally in Section 5.8 the system's resilience with regard to collapse of the cat state is discussed. In particular, the possibilities for decay due to spurious rotations or velocity drifts, atom losses and diagonal impurities are discussed. Additionally, thermal excitations and coupling to an environ-

ment as possible causes of collapse are considered. The chapter ends with a summary and conclusions.

5.2 Literature overview

There has been continuous interest in proposals and experiments for the creation of superpositions of macroscopically distinct states, or cat states for short. Even though this seems to be a simple enough definition of what constitutes a cat state, the notion of 'macroscopic' and 'distinct' are by themselves a subject of debate. This is, in part, due to the complicated nature of quantum many-body systems, in which many different configurations can intervene in any given state. Some aspects of these complications are reviewed in Section 5.6. Cat states have also been proposed and produced for a considerable variety of systems. Continuous superpositions of macroscopically distinct states (i.e. double condensates [291, 292]), not usually referred to as cat states, are not included in this discussion. They require a more specific treatment, like the one found in [293]. In the following a non-exhaustive overview of the literature on macroscopic quantum systems and cat states is given.

Over the past 25 years, many experiments have produced cat states. The first forays with cold atoms produced a correlated superposition of atoms in spatially separated states [294]. Although not yet macroscopic it was an important stepping stone. A mesoscopic superposition of internal states was realized in [295]. A promising avenue in superconducting devices for the generation of MQS is the use of superconducting quantum interference devices (SQUIDs) [296, 297] which are based on the earlier work on the macroscopic quantum behaviour in those systems [298–300]. Cooper pair boxes [301] are a related type of device. The quantum interference of very large molecules is another avenue to test size constraints on quantum coherence. Molecules as big as C60 [302] and beyond [303–305] are known to show quantum behavior in double-slit type experiments. Large molecules are also the subject of studies examining the transition of macroscopically distinct states involving different magnetic orientations [306–308]. Just like for ultracold atoms, trapped ion systems also offer a great level of control and tunability, which makes them a successful test-bed for cat state preparation. In [309] four ions were entangled. This number was increased from six [285] to up to fourteen [310]. Photonic systems also proved to be a successful platform for many cat state realizations. Small cat states were produced within the optical range [311, 312] and the microwave range [313, 314]. In the optical range these have been increased considerably to involve hundreds [315] or even hundreds of millions [316] of photons. In the microwave range the size of the cats has been increased up to hundreds of photons [317]. Cat states have also been produced for micromechanical oscillators [318]. An interesting example of such a preparation involves an optical levitating submicron particle [319]. In ultracold bosonic systems, a spinor cat was realized in a double-well [320].

A plethora of theoretical proposals have focused on the study and generation of cat states. Early studies focused on superconducting devices [278, 321] which also included the coupling to a micromechanical resonator [322]. Optomechanical oscillators that have been investigated can be found in [323–326]. Optical systems are equally great for exploring MQS. The superposition of coherent states was proposed in [327]. With the assistance of

cavity collisions, few-atom systems can also exhibit cat states of the Greenberger-Horne-Zeilinger (GHZ) type [328].

Given the excellent level of control that ultracold atoms offer, it comes as no surprise that a large number of proposals can be found in this category. Examples are found in Refs. [329–343]. Since this work is mostly centered around ultracold atoms, the characterization of these proposals provided here contains more detail. The various approaches can be divided according to the spatial distribution of the macroscopically distinct states and the macroscopic observable that differentiates the two branches of the cat state. Proposals where the position of two or more atom clouds is the observable distinguishing the branches are found in Refs. [329, 330, 333, 336, 342, 344]. The relative phase of two clouds may also play a role in distinguishing the branches [332, 335, 343] so that the spatial distribution of the atoms remains similar in either one. The branches may also occupy the same region of space but populating modes which differ in the density profile [345, 346]. In a manner similar to SQUIDs, superfluid currents can also occur for ultracold atoms confined to a ring [338–341]. The superposition of states with different phase profiles (and thus different superfluid currents) then constitutes the cat state. In ring lattices with attractive interactions, described by the attractive Bose-Hubbard model, a cat state may be expressed in the correlated hopping of atoms concentrated on a given site [334]. The atom spin is also a useful observable to distinguish cat branches [347] which can also be correlated with the position of the condensate [331].

Out of these proposals, various guiding principles for the preparation of a cat state can be summarized. Direct cooling to a ground state that is a MQS is very difficult. This is mainly due to the tiny difference in energy between ground and first excited state [348]. The other methods can be broadly split into the three categories: (i) projective measurement, (ii) dynamic evolution, and (iii) adiabatic preparation.

Examples for projective measurements can be found in Refs. [335, 349], where the authors proposed the creation of macroscopic superpositions of atoms by some form of measurement on a Bose Einstein condensate. These setups commonly begin with a continuous superposition of macroscopically different states, which is then subject to a limited measurement that is unable to resolve the difference between two distinct eigenvalues of the measured observable. A similar proposal was made in Ref. [332] for the relative phase of two interfering condensates.

Refs. [283, 327, 336, 341, 342] are in the second category. Dynamic preparation refers to an initial state evolving in such a way that a cat state appears during its evolution. Proposals of this type were realized in the photonic system found in Ref. [313]. The preparation of an initial state is sometimes achieved by abruptly changing a parameter. This can be a sign of the interaction in a bosonic atom gas [336], or a sudden change in the tunneling phase [341].

Adiabatic preparation refers to the slow change of a parameter of the system. If the system is initially prepared in the ground state, then during the change of a parameter the initial state follows the lowest lying energy level. This method has also been proposed to yield cat states [329, 336]. In Ref. [329] the authors propose producing the initial state through cooling, which is then adiabatically transformed into a cat state. This method was also implemented in [297], where a superposition of two macroscopically different flux states was created by driving a SQUID towards a level anti-crossing. The difficulties in preparing MQS states in rotating rings is discussed in Ref. [339].

Finally, the mechanisms that destroy the MQS state may be addressed. The main cause of the fast decay of a Schrödinger cat state is the collapse into one of its branches due to decoherence [262]. The detailed mechanism is very sensitive to the particular physical realization but, as already stated, it is a general trend that the larger and more different the superposed branches are, the faster the collapse is. Particle losses are known to be sources of such a collapse in ultracold atoms [329] or photonic systems [350]. The interaction of a BEC with its depeletion cloud can also play a role in the decoherence of a MQS of a boson condensate in two immiscible internal states [331]. In Ref. [336] both the lasers that trap a condensate and its thermal cloud are the main contributors to decoherence. There are also effects that counteract decoherence. The authors of [341] identified inhomogeneities in a ring and in [342] interactions help to delay the decay of the cat state. A discussion of the robustness of the more general concept of fragmented states, of which cat states are a subset, can be found in Ref. [351]. The resilience to collapse is one of the interesting features of the setups considered in this chapter. Section 5.8 contains a discussion of the possible mechanisms that may cause a collapse of the cat state.

5.3 Cat state from kinetic driving in the ring

In this section, a varied assortment of analytical tools are used to study the formation of the cat state. A brief review: The kinetically driven BH model in one dimension, with PBC (4.3) and unit filling went through a quantum phase transition of the Kosterlitz-Thouless type. The Mott-insulating state at $\kappa = 0$ ($\kappa = J/\omega$) transitioned to a fragmented superfluid state for $\kappa \simeq 0.48$. The fragmented quasi-condensate that formed condensed at the non-zero momenta $k = \pm\pi/2$. The condensation is clearly signaled by the formation of peaks in the momentum density at $k = \pm\pi/2$ and in the two-particle momentum density $\langle n(q)n(k)\rangle$ at $(q,k) = (\pm\pi/2, \pm\pi/2)$ (Figs. 4.6 and 4.13). The absence of peaks at $(q,k) = (\pm\pi/2, \mp\pi/2)$ was the first strong indication that the ground state in the strong driving regime is cat-like and not a mere product state.

For the undriven Bose-Hubbard model the occupation of the zero momentum state is favored due to the minimization of the kinetic energy between adjacent sites. Deep in the superfluid regime, interactions are a small perturbation to this state. Even though they are small, they are essential for superfluidity. For the kinetically driven model, however, it is much less clear why $\pm\pi/2$ is favored in the superfluid regime. Primarily this is because of the many correlated hoppings and local and non-local interaction terms in $H^{\text{eff}}_{\text{pbc}}$ [see Eq. (4.46)]. In fact, nearest-neighbor hopping is completely suppressed in $H^{\text{eff}}_{\text{pbc}}$.

Some important symmetries can be pointed out before reviewing the more detailed analysis. The Hamiltonian $H^{\text{eff}}_{\text{pbc}}$ is invariant under the transformation $k \to -k$ (time inversion) and $k \to \pm\pi + k$. Both these symmetries highlight the importance of the pairs of states with the momentum eigenvalues $0, \pi$ and $\pm\pi/2$. Both pairs remain invariant under the aforementioned symmetry transformations. This explains why a macroscopic occupation of $\pi/2$ has to go along with the equally occupied momentum $-\pi/2$. This does not explain, however, why they are macroscopically occupied in the first place.

In the Mott insulating regime, a qualitative explanation of the occupation for $\pm\pi/2$ has been developed. It involved the dipole states in Eq. (4.55), concluding that an effective

next to nearest-neighbor tunneling can explain the onset of the peaks for small values of κ. This picture, however, completely breaks down in the superfluid regime. The next few sections will be dedicated to elucidating a more apt description of the superfluid regime. To begin this analysis some insightful failures will be discussed.

5.3.1 Two-mode model

The simplest possible approximation assumes only two modes that intervene in the formation of the ground state in the superfluid regime. A radical truncation of the effective Hamiltonian in momentum representation $H^{\text{eff}}_{\text{pbc}}$ [Eq.(4.44)] to the two modes $k = \pm\pi/2$ yields

$$H_{2\text{LS}} = \frac{U}{2L}\left(2N^2 - N - n_a^2 - n_b^2 + a^{\dagger 2}b^2 + b^{\dagger 2}a^2\right) \ , \tag{5.1}$$

where $a = a_{\pi/2}$ and $b = a_{-\pi/2}$ and $n_{a,b}$ the respective number operator. This approximation is named the two-level approximation. Interestingly, the above Hamiltonian can be diagonalized exactly with the canonical transformation,

$$c = \frac{1}{\sqrt{2}}(a + b) \ , \tag{5.2}$$

$$d = \frac{1}{\sqrt{2}}(a - b) \ , \tag{5.3}$$

which leads to

$$H_{2\text{LS}} = \frac{U}{2L}(2N^2 - 2N - 4n_c n_d) \ , \tag{5.4}$$

The normalized ground state of the above Hamiltonian is

$$|\Psi\rangle = \frac{1}{(N/2)!}\frac{1}{2^{N/2}}(a^{\dagger 2} - b^{\dagger 2})^{N/2}|\text{vac}\rangle \ . \tag{5.5}$$

This state does not yield the two-particle momentum density, which was observed numerically. If one takes the ratio of cross to diagonal correlations

$$\chi = \langle n_a n_b\rangle / \langle n_a n_a\rangle \tag{5.6}$$

as a measure to compare the numerical results of the previous chapter to the state in Eq. (5.5) then one can show analytically that for (5.5) in the thermodynamic limit $\chi = 1/3$. This is much larger than the numerical results for the ground state of $H^{\text{eff}}_{\text{pbc}}$ where $\chi \ll 1$. For an ideal cat state

$$(2N!)^{-1/2}[(a^\dagger)^N \pm (b^\dagger)^N]|\text{vac}\rangle \tag{5.7}$$

this ad hoc measure would yield $\chi = 0$. The discrepancy between the state in Eq. (5.7) and Eq. (5.5) comes from the "center" configuration $|(N/2)_a, (N/2)_b\rangle$ when Eq. (5.5) is expanded by means of a binomial expansion. Its contribution is simply too large to accurately capture the two-momentum density of the state in (5.7). This can also be appreciated in Fig. 5.1. The failure of $H_{2\text{LS}}$ to accurately capture the properties of the ground state of $H^{\text{eff}}_{\text{pbc}}$ highlights the importance of modes other than $\pm\pi/2$. Taking these into account would result in a more accurate description.

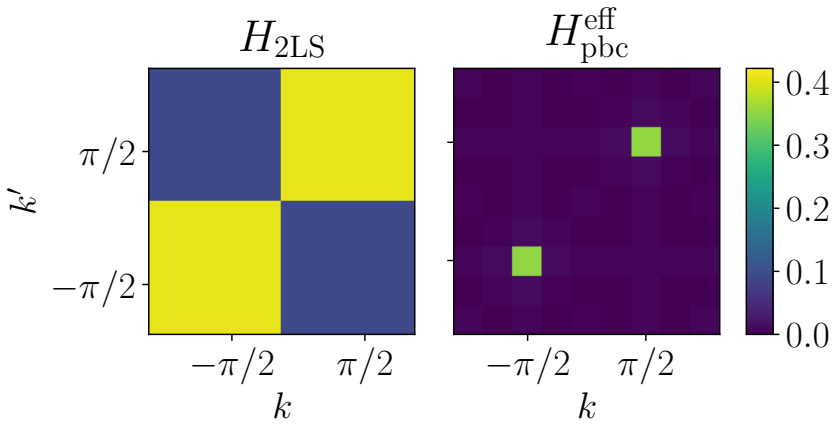

Figure 5.1: Two-particle momentum density for the two-mode approximation (left panel) and for the full effective Hamiltonian (right panel) at $\kappa = 0.7$. The ratios $\langle n_{\pi/2} n_{\pi/2}\rangle / \langle n_{-\pi/2} n_{\pi/2}\rangle$ are, respectively, 4.3 and 45.5. This implies that the ground state of the two-mode approximation is much less cat-like than that of the full model.

5.3.2 Failure of Bogoliubov-de Gennes theory

The previous two-mode approximation is the closest analog to the Gross-Pitaevskii (GP) solution of the undriven Bose-Hubbard model. For the GP a fully occupied mode

$$(N!)^{-1/2}(a^\dagger)^N|\text{vac}\rangle\,. \tag{5.8}$$

is considered. Using this as a point of departure and replacing the operators a, b in $H^{\text{eff}}_{\text{pbc}}$ or $H_{2\text{LS}}$ with c-numbers would only work if both modes a and b were macroscopically occupied in all the intervening configurations. This, however, is not the case for the ground state of either $H^{\text{eff}}_{\text{pbc}}$ or $H_{2\text{LS}}$, as can be seen numerically for the former, and analytically for the latter.

Regardless of these difficulties, the introduction of a depletion cloud for both modes $\pm\pi/2$ by performing a naive Bogoliubov calculation might yield meaningful results.

To start, a single condensate can be assumed to be in an unspecified momentum mode k_v, replacing $a_{k_v}, a^\dagger_{k_v} \to \sqrt{N_0}$ in $H^{\text{eff}}_{\text{pbc}}$ [Eq. (4.44)], where N_0 is the number of atoms in the condensate. Following the usual steps of Bogoliubov-de Gennes theory, terms of $\mathcal{O}(N_0^2)$ and $\mathcal{O}(N_0)$ are extracted from the effective Hamiltonian while neglecting higher order contributions. Retaining terms up to $\mathcal{O}(N_0^2)$ results in

$$h_{\text{mf}} = \frac{U}{2L} N_0^2 \tag{5.9}$$

The next leading order in N_0 is

$$h_{\text{bg}} = \frac{UN_0}{2L} \sum_{k_p \neq k_v} \left[4a^\dagger_{k_v} a_{k_v} + g(\kappa, k_p) \left(a_{k_p} a_{2k_v - k_p} + a^\dagger_{k_p} a^\dagger_{2k_v - k_p} \right) \right] \tag{5.10}$$

where

$$g(\kappa; k_v, k_p) = \mathcal{J}_0 \left\{ 2\kappa \left[2\cos(k_v) - \cos(k_p) - \cos(2k_v - k_p) \right] \right\} \tag{5.11}$$

In the following a non-number conserving variant of Bogoliubov theory is applied. This method reproduces the linear dispersion relation for the low-lying excitations of the depletion cloud of the undriven Bose-Hubbard model in one dimension. The non-number conserving variant requires the introduction of a chemical potential into (5.10)

$$h_{\mathrm{BdG}} = h_{\mathrm{mf}} + h_{\mathrm{bg}} - \mu N_0 \sum_{k_p} a^\dagger_{k_p} a_{k_p} \tag{5.12}$$

$$= h_{\mathrm{mf}} - \mu N_0 + h_{\mathrm{bg}} - \mu \sum_{k_p \neq k_v} a^\dagger_{k_p} a_{k_p} \tag{5.13}$$

Minimizing $h_{\mathrm{mf}} - \mu N_0$ with respect to N_0 yields $\mu = UN_0/N$. Inserting this back into Eq. (5.13) gives

$$h_{\mathrm{BdG}} = \frac{U}{2L}\left\{ -N_0^2 + N_0 \sum_{k_p \neq k_v} 2a^\dagger_{k_p} a_{k_p} + g(\kappa; k_v, k_p)\left(a_{k_p} a_{2k_v - k_p} + a^\dagger_{k_p} a^\dagger_{2k_v - k_p}\right)\right\} \tag{5.14}$$

This can now be subjected to the Bogoliubov transformation

$$a_{k_p} = \alpha c_{k_p} + \beta c^\dagger_{2k_v - k_p} \ . \tag{5.15}$$

From this choice follows $[a_{k_p}, a^\dagger_{k_p}] = \alpha^2 - \beta^2 = 1$. This calls for the parameterization

$$\alpha = \cosh(\phi) \ , \quad \beta = \sinh(\phi) \tag{5.16}$$

The diagonalization of h_{BdG} requires

$$2\alpha\beta + g(\kappa; k_v, k_p)(\alpha^2 + \beta^2) = 0 \tag{5.17}$$

which implies that

$$\tanh(2\phi) = -g(\kappa; k_v, k_p) \ . \tag{5.18}$$

Finally one finds for h_{BdG}

$$\begin{aligned} h_{\mathrm{BdG}} = \frac{U}{2L}\Bigg\{ -N_0^2 + N_0 \Bigg[& \sum_{k_p \neq k_v} (-1 + \sqrt{1 - g(\kappa; k_v, k_p)^2} \\ & + \sum_{k_p \neq k_v} 2\sqrt{1 - g(\kappa; k_v, k_p)^2} c^\dagger_{k_p} c_{k_p} \Bigg] \Bigg\} \end{aligned} \tag{5.19}$$

The first interesting feature of this Hamiltonian is that the first sum is minimized for $k_v = \pm\pi/2$, since the root vanishes for these two values of k_v. This is a strong hint that $k_v = \pm\pi/2$ plays a special role in the formation of the condensates. There is, however, an immediate issue with this result: the excitation energy of all the quasiparticles c_{k_p} vanishes, which makes the model nonsensical.

The introduction of a second condensate by making the substitutions

$$a_{\pi/2} \to \sqrt{N_0} e^{\mathrm{i}\varphi_+} \ , \quad a_{-\pi/2} \to \sqrt{N_0} e^{\mathrm{i}\varphi_-} \ , \tag{5.20}$$

where the $\varphi_\pm$ allows for a possible phase between the condensates does not fare better. The reason for this is that it takes into account terms such as $a^\dagger_{\pi/2}a^\dagger_{-\pi/2}a_k a_{-k} \to N_0 a_k a_{-k}\exp[\mathrm{i}(\varphi_+ - \varphi_-)]$. The numerical studies, however, have shown that these terms barely contribute to the ground state. Neglecting terms of this type assumes condensates that are completely independent, which is equivalent to studying a single condensate and its depletion cloud. Since the single condensate approach already failed, a more sophisticated method is required.

5.3.3 Large κ limit

The simple Bogoliubov-de Gennes approach of the previous section did not advance the understanding of the large κ limit. In the following a new concept will help to understand the formation of the cat state. Going back to $H^{\mathrm{eff}}_{\mathrm{pbc}}$ in Eq. (4.44) one can identify the scattering processes that dominate when κ becomes comparable to 1 or larger. Since the $\mathcal{J}_0(x)$ has its largest value for $x = 0$ one can take the argument of the Bessel function in Eq. (4.44) and set it to zero

$$\cos(k_l) + \cos(k_m) - \cos(k_m + k_l - k_n) - \cos(k_n) = 0 \ , \tag{5.21}$$

a condition that is independent of κ and which includes momentum conservation $k_l + k_m = k_n + k_p$. The above condition is fulfilled by the three equations:

$$k_l = k_n \ , \quad k_m = k_n \ , \quad k_l + k_m = \pm\pi \ . \tag{5.22}$$

The first two conditions mark the absence of collisions. The three equations can be viewed as four planes in the first Brillouin zone of (k_l, k_m, k_n)-space. This is illustrated in Fig. 5.2. A point on any of these planes represents a scattering event with an amplitude $U/2L$. These events are the dominant contributors to $H^{\mathrm{eff}}_{\mathrm{pbc}}$ for large κ. In the limit $\kappa \to \infty$ they

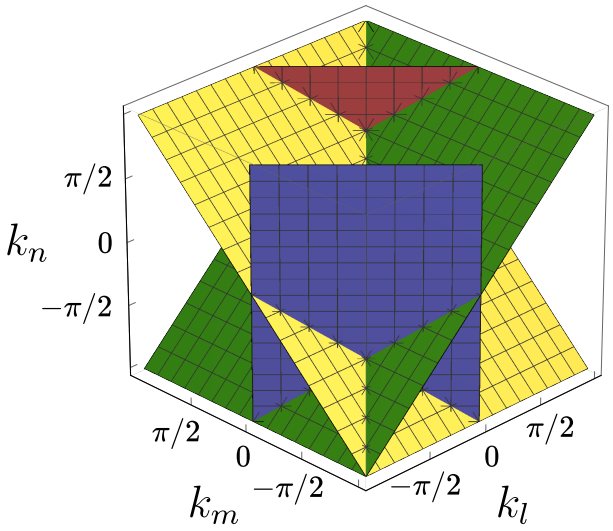

Figure 5.2: The four planes (each plotted with a different color) containing the scattering amplitudes in H_{eff} which are independent of κ. Only the first Brillouin zone in k_l, k_m, k_n-space is shown.

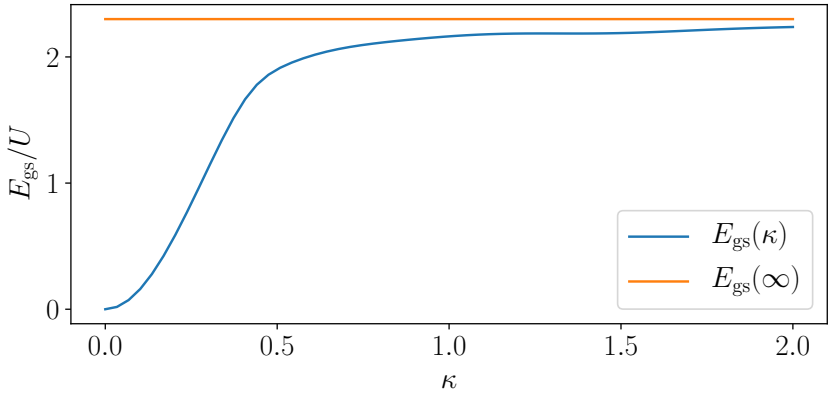

Figure 5.3: Ground state energy comparison of $H^{\mathrm{eff}}_{\mathrm{pbc}}$ and H_∞ for $(N, L) = (8, 8)$. For increasing κ the ground state energy of $H^{\mathrm{eff}}_{\mathrm{pbc}}$ approaches that of the asymptotic model. This convergence was checked for multiple system sizes and fillings.

are the only amplitudes surviving since $\lim_{x\to\infty} \mathcal{J}_0(x) = 0$. The effective Hamiltonian in this limit is

$$H_\infty = \frac{U}{2L}\left(2N^2 - N - \sum_k n_k^2 + \sum_{\substack{k\neq k'\\ k+k'\neq\pi}} a^\dagger_{\pi-k}a^\dagger_k a_{\pi-k'}a_{k'}\right) . \tag{5.23}$$

Even though this Hamiltonian is technically only exact for $\kappa = \infty$ it aptly describes many of the properties of $H^{\mathrm{eff}}_{\mathrm{pbc}}$ even for more moderate values of κ. Figs. 5.3 and 5.4a reveal that, for $0.5 < \kappa < 1$, the ground state energy and the momentum density of $H^{\mathrm{eff}}_{\mathrm{pbc}}$ are very close to those of H_{inf}. A comparison of Fig. 4.12 and Fig. 5.4b shows that the two-particle momentum densities are also very similar. This justifies making H_{inf} a reference for the parameter regime of moderate κ. H_∞ is simplified by removing the scaling factor $U/2L$, and the terms that are constant for a given N:

$$h_\infty = -\sum_k n_k^2 + \sum_{\substack{k\neq k'\\ k+k'\neq\pi}} a^\dagger_{\pi-k}a^\dagger_k a_{\pi-k'}a_{k'} . \tag{5.24}$$

The first term is an attractive on-site interaction in momentum space (as noted in Ref. [288]). The second term in Eq. (5.24)

$$h_{\mathrm{pf}} = \sum_{\substack{k\neq k'\\ k+k'\neq\pi}} a^\dagger_{\pi-k}a^\dagger_k a_{\pi-k'}a_{k'} \tag{5.25}$$

will be referred to as the pairing force term. In H_{pf} a pair of particles is defined as any two particles whose momenta sum up to π. This is different for a normal superfluid where pairs interact in collisions of momenta $k' + k = 0$. This Hamiltonian, referred to as the toy model from this point on, qualitatively captures the properties of the true ground state in the superfluid sector for a broad range κ ($\kappa \sim 0.5$ and larger).

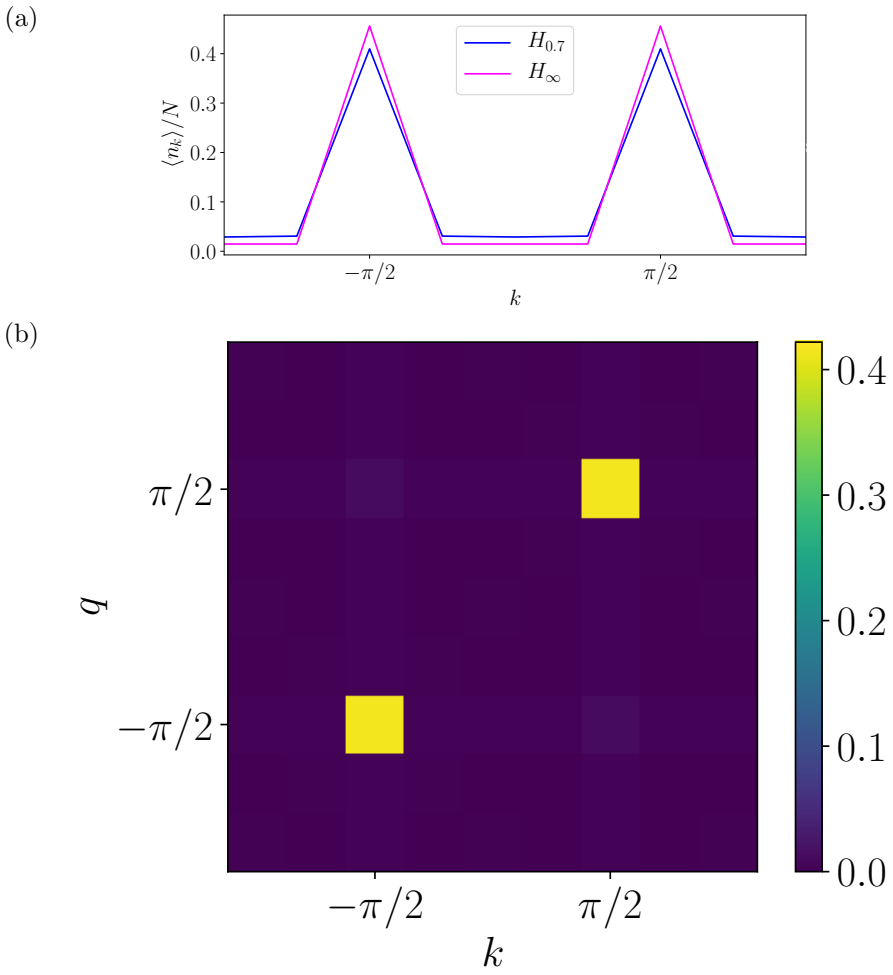

Figure 5.4: (a) Momentum density $\langle n_k \rangle / N$ for the ground state of $H^{\text{eff}}_{\text{pbc}}$ for $\kappa = 0.7$ and H_{inf} for $(N, L) = (8, 8)$. For both of them clearly separated peaks around $k = \pm\pi/2$ are visible. Bottom: two-particle momentum density for the ground state of H_{inf}. Again, two peaks around $\pm\pi/2$ are visible with negligible cross correlations, indicating a cat-like ground state.

5.3.4 Connection to the Richardson model

The toy model (5.24) has some very interesting connections to other fields of physics. h_{pf} is a variant of the second term of the pairing-force Hamiltonian

$$H = \sum_k 2\epsilon_k n_k - g \sum_{k',k} a^\dagger_k a^\dagger_k a_{k'} a_{k'} \ . \tag{5.26}$$

An exact solution for this Hamiltonian was found by Richardson in Ref. [289]. Ever since this work, models of this type that can be solved exactly, have been found, which are known under the umbrella term Richardson-Gaudin models. His theory was rediscovered and successfully applied to mesoscopic superconducting metallic grains [352, 353]. It also plays an important role in nuclear physics and in the theory of superconductivity. An excellent review on exactly diagonalizable Richardson-Gaudin models can be found in Ref. [290]. Despite the sophistication of the strategies that are used to solve Hamiltonians,

such as the one detailed in Eq. (5.26), they are of no help with regard to the full diagonalization of h_∞. The main reason for this failure is the first term in h_∞ which is quadratic in n_k. Despite this shortcoming, many of the techniques developed by Richardson in [289] can be employed to further understand the properties of h_∞.

A particle pair in the toy model is created by

$$B_k^\dagger = a_{\pi-k}^\dagger a_k^\dagger \tag{5.27}$$

Following Ref. [289], a seniority operator

$$\nu_k = |n_k - n_{\pi-k}| \tag{5.28}$$

can be defined which counts the number of unpaired particles with momentum k [1]. It should be noted that

$$[h_\infty, \nu_k] = 0 \ , \tag{5.29}$$

which leads to the definition of the seniority of an eigenstate of h_∞ as its eigenvalue with respect to

$$\nu = \frac{1}{2}\sum_k \nu_k \ . \tag{5.30}$$

This operator measures the total number of unpaired particles. The factor $1/2$ accounts for double counting.

Because seniority is a constant of motion, $[h_\infty, \nu] = 0$, it allows for a helpful block-diagonalization of h_∞, since only configurations with the same seniority are connected by h_∞. In particular, states that do not contain any pairs ($\nu = N$) are eigenstates of the pairing term with eigenvalue 0 and thus eigenstates of h_∞. States with the lowest energy within the class of $\nu = N$ are of the type $|N_{k\neq\pm\pi/2}\rangle$. Their energy is $-N^2$, where $|N_q\rangle$ is a state with N particles in momentum q.

With regard to the ground state, an important sector in the block-diagonalized Hamiltonian is $\nu = 0$. This is the set of states that only contains configurations with paired particles. These states are referred to as fully paired states. Within this set of states, only $|N_{\pm\pi/2}\rangle$ involves the exclusive occupation of a single mode, since $\pm\pi/2$ are the only two momenta in which two particles can occupy the same mode and be paired at the same time. Similarly to $|N_{k\neq\pm\pi/2}\rangle$, these modes benefit the most from the "on-site" attractive interaction in momentum space. Unlike $|N_{k\neq\pm\pi/2}\rangle$, they are not eigenstates of the repulsive pairing term h_{pf}. This is because of the contribution

$$\sum_{k\neq\pm\pi/2} a_{\pi-k}^\dagger a_k^\dagger \left(a_{\pi/2}a_{\pi/2} + a_{-\pi/2}a_{-\pi/2}\right) + \mathrm{H.c.} \tag{5.31}$$

included in h_{pf}. States involving only $\pi/2$ or $-\pi/2$ or both are expected to further lower their energy by mixing with configurations which include pairs with $k \neq \pm\pi/2$. These states will be referred to as the reduction cloud of the $\pm\pi/2$ condensates. This is to emphasize that the reduction cloud is qualitatively different from the conventional depletion cloud.

[1] Seniority in Ref. [289] was defined formally differently because of its application to fermions.

The differences between the reduction cloud and the depletion cloud are: Pairs of the reduction cloud have a total momentum π (in contrast to zero for the depletion cloud) and, most importantly, the reduction cloud is shared by the two condensates. This can be seen in Eq. (5.31): a pair $(k, \pi - k)$ does not carry information on whether or not it originated from a condensate pair $(\pi/2, \pi/2)$ or $(-\pi/2, -\pi/2)$.

A simple variational calculation shows that mixing $|N_{\pm\pi/2}\rangle$ with other fully paired configurations (but containing at least one $k \neq \pm\pi/2$) further lowers the energy beyond $-N^2$.

5.3.5 Variational ground state

A variational calculation similar to the one in Section 4.2.3 can be performed to further elucidate the role of the reduction cloud. The calculation starts with the state

$$|\Psi(\alpha)\rangle = \alpha|F\rangle + \beta|R\rangle \tag{5.32}$$

$$\begin{aligned} =&\frac{\alpha}{\sqrt{2}}(|N_{-\frac{\pi}{2}}, 0\rangle + |0, N_{\frac{\pi}{2}}\rangle) \\ &+ \frac{\beta}{\sqrt{2(L-2)}}(|(N-2)_{-\frac{\pi}{2}}, 0_{\frac{\pi}{2}}\rangle + |0_{-\frac{\pi}{2}}, (N-2)_{\frac{\pi}{2}}\rangle \\ &\times \sum_{k\neq\pm\frac{\pi}{2}} |1_k, 1_{\pi-k}\rangle\,, \end{aligned} \tag{5.33}$$

where α, β are real and $\alpha^2 + \beta^2 = 1$. Here F stands for fragmented condensates and R for reduction cloud. The energy of this state is

$$E(\alpha) = \langle\Psi(\alpha)|h_\infty|\Psi(\alpha)\rangle \tag{5.34}$$

$$= \alpha^2(E_F - E_R) + \alpha\sqrt{1-\alpha^2}\,V + E_R\,, \tag{5.35}$$

which is minimized for $\alpha = \alpha_0$ with

$$\alpha_0 = -\mathrm{sgn}(V)\sqrt{\frac{1}{2} + \left(1 + \frac{2V^2}{(E_F - E_R)^2}\right)^{-1/2}}\,. \tag{5.36}$$

The various parameters are

$$E_F = \langle F|h_\infty|F\rangle = -N^2\,, \tag{5.37}$$

$$\begin{aligned} V &= 2\langle F|h_\infty|R\rangle \\ &= \sqrt{N(N-1)(L-2)}\,, \end{aligned} \tag{5.38}$$

$$\begin{aligned} E_R &= \langle R|h_\infty|R\rangle \\ &= -N^2 + 4N + L - 9\,. \end{aligned} \tag{5.39}$$

For unit filling ($N = L$) the energy reduction $(N, L) = (8, 8)$ due to the reduction cloud is $E(\alpha) - E_R = -8.19$ (here, $E_F = -64$, $E(\alpha_0) = -72.2$ and the numerically exact ground state energy is $E_{\mathrm{gs}} = -83.2$). For $N > 9$ one can prove generally that

$$E(\alpha) < E_F\,. \tag{5.40}$$

In the limit of large N, one obtains

$$E(\alpha_0) - E_F = -N\sqrt{N}\,. \tag{5.41}$$

This clearly shows how the mixing with a cloud of pairs lowers the energy of the fully occupied modes $\pm\pi/2$. For simplicity the inclusion of $|(N-2)_{-\pi/2}, 2_{\pi/2}\rangle, |2_{-\pi/2}, (N-2)_{\pi/2}\rangle$ was omitted, as it would have necessitated the introduction of yet another independent parameter, without further elucidating the effect of interactions of the condensate with its cloud.

In order to better understand the benefit of the cat state nature of the condensate, a product state may be chosen as $|F\rangle$ in Eq. (5.33):

$$\begin{aligned} |\Psi_{\rm c}(\alpha)\rangle &= \alpha|\tilde{F}\rangle + \beta|\tilde{R}\rangle \qquad (5.42)\\ &= \alpha|(N/2)_{-\frac{\pi}{2}}, (N/2)_{\frac{\pi}{2}}\rangle \\ &+ \frac{\beta}{\sqrt{2(L-2)}}(|(N/2-2)_{-\frac{\pi}{2}}, (N/2)_{\frac{\pi}{2}}\rangle \\ &+ |(N/2)_{-\frac{\pi}{2}}, (N/2-2)_{\frac{\pi}{2}}\rangle) \sum_{k\neq\pm\frac{\pi}{2}} |1_k, 1_{\pi-k}\rangle\,. \qquad (5.43) \end{aligned}$$

The key difference between (5.43) and (5.33) is that the two condensate terms in the reduction cloud of (5.43) can mix because of the pair interaction term, namely,

$$\begin{aligned} &\langle (N/2-2)_{-\frac{\pi}{2}}, (N/2)_{\frac{\pi}{2}}|h_\infty|(N/2)_{-\frac{\pi}{2}}, (N/2-2)_{\frac{\pi}{2}}\rangle \\ &= N/2(N/2-1) \neq 0\,. \end{aligned} \tag{5.44}$$

By contrast, this mixing does not affect (5.33) because their counterparts are not connected by h_∞:

$$\langle (N-2)_{-\frac{\pi}{2}}, 0_{\frac{\pi}{2}}|h_\infty|0_{-\frac{\pi}{2}}, (N-2)_{\frac{\pi}{2}}\rangle = 0\,. \tag{5.45}$$

Again

$$\tilde{E}(\alpha) = \alpha^2(E_{\tilde{F}} - E_{\tilde{R}}) + \alpha\sqrt{1-\alpha^2}\,\tilde{V} + E_{\tilde{R}} \tag{5.46}$$

is minimized, where

$$\begin{aligned} E_{\tilde{F}} &= \langle\tilde{F}|h_\infty|\tilde{F}\rangle = -N^2/2\,, \qquad (5.47)\\ \tilde{V} &= 2\langle\tilde{F}|h_\infty|\tilde{R}\rangle \\ &= \sqrt{N(N/2-1)(L-2)}\,, \\ E_{\tilde{R}} &= \langle\tilde{R}|h_\infty|\tilde{R}\rangle \\ &= -N^2/4 + 3N/2 + L - 9\,. \qquad (5.48) \end{aligned}$$

The $\tilde{\alpha}_0$ that minimizes $\tilde{E}(\alpha)$ can be calculated using (5.36), with Eqs. (5.37)-(5.39) replaced by (5.47)-(5.48).

Not only is $\tilde{E}(\tilde{\alpha}_0) > E(\alpha_0)$ but the overall contribution of the reduction cloud to the state is altered. For unit filling $N = L$, the change introduced to $E_{\tilde{R}}$ due to the overlap in Eq. (5.44) causes $\lim_{L\to\infty}\tilde{\alpha}_0^2 = 1$ as opposed to $\lim_{L\to\infty}\alpha_0^2 = 1/2$. The closer $\tilde{\alpha}_0$ is

to one, the less important the contribution of the reduction cloud to $|\Psi_c\rangle$ and to $\tilde{E}_{\tilde{\alpha}_0}$, as can be seen in Eq. (5.46) and the normalization condition for α, β. This means that the reduction cloud in $|\Psi_c(\tilde{\alpha}_0)\rangle$ loses importance once the system size increases, which is not the case for $|\Psi(\alpha_0)\rangle$. Even for moderate sizes, such as $(N, L) = (8, 8)$, $\tilde{\alpha}_0^2 = 0.92$, whereas $\alpha_0^2 = 0.76$ (the bigger α the smaller the weight of the reduction cloud). It should be noted that (5.33) and (5.43) are just approximate ansätze, hence the weight of the condensate does not need to vanish in the thermodynamic limit, as would be expected for an exact description.

It is important to emphasize that there is a possibility for $|N_{\pm\pi/2}\rangle$ to mix with other fully paired states of the type $|(N-2)_{\pm\pi/2}, 1_k, 1_{\pi-k}\rangle$ with $k \neq \pm\pi/2$ as the reason for reducing the energy thanks to the pairing interactions in $H^{\text{eff}}_{\text{pbc}}$. By contrast, states of the type $|N_k\rangle$ with $k \neq \pm\pi/2$ cannot lower their energy, since the pairing term does not allow them to mix with other configurations. As already noted, they are eigenstates of h_∞.

5.3.6 Exact ground state in the large κ limit

Both an inspection of the numerically-found ground state and the fact that all the momenta $k \neq \pm\pi/2$ play an equivalent role suggest that the ground state of h_∞ (for $L/4$ an integer) can be written as the fully paired state

$$|\Psi_0\rangle = \sum_{m=0}^{N/2} \sum_{l=0}^{(N-2m)/2} C_{m,l} \left[|(N-2m-2l)_{-\frac{\pi}{2}}, (2l)_{\frac{\pi}{2}}\rangle + |(2l)_{-\frac{\pi}{2}}, (N-2m-2l)_{\frac{\pi}{2}}\rangle \right] \times \sum_{\sum n_k = m} Q_{\{n_k\}} \sum_P |P\{n_k\}\rangle \ . \tag{5.49}$$

The sum over $\{n_k\}$ contains all possible occupation numbers n_k of the pairs $(k, \pi - k)$, each one characterized by the momentum k satisfying $0 \leq k < \pi/2$, so that in each sequence $\{n_k\}$, a given number n_k represents the two-mode state $|n_k, n_{\pi-k}\rangle$ containing n particles in momentum k and n particles in momentum $\pi - k$. The sum over P represents a summation over all possible permutations of the sequence of pair occupation numbers. Each permutation P acting on $\{n_k\}$ yields a unique sequence of the respective sequence of pair occupations $\{n_k\}$ distributed throughout the set available momenta (always with $k \neq \pm\pi/2$). The resulting configuration represented by $|P\{n_k\}\rangle$ must have the same weight as $|\{n_k\}\rangle$. This ansatz (5.49) is expected to be the exact ground state of the toy model.

The above state may be elucidated further by expanding it according to its leading contributions. If Q_m is defined as $Q_{\{n_k\}}$ for the particular sequence in which m particle pairs transferred to the reduction cloud are concentrated in one mode pair [as usual,

labeled $(k, \pi - k)$ with $k \neq \pm\pi/2$], then it is found that

$$\begin{aligned}|\Psi_0\rangle =& C_{0,0}Q_0\Big(|N_{-\frac{\pi}{2}}, 0_{\frac{\pi}{2}}\rangle + |0_{-\frac{\pi}{2}}, N_{\frac{\pi}{2}}\rangle\Big) + \\ & C_{1,0}Q_1\Big(|(N-2)_{-\frac{\pi}{2}}, 0_{\frac{\pi}{2}}\rangle + |0_{-\frac{\pi}{2}}, (N-2)_{\frac{\pi}{2}}\rangle\Big) \sum_{k\neq\pm\pi/2} |1_k, 1_{\pi-k}\rangle \\ & + C_{0,1}Q_0\Big(|(N-2)_{-\frac{\pi}{2}}, 2_{\frac{\pi}{2}}\rangle + |2_{-\frac{\pi}{2}}, (N-2)_{\frac{\pi}{2}}\rangle\Big) \\ & + C_{1,0}Q_2\Big(|N-4)_{-\frac{\pi}{2}}, 0_{\frac{\pi}{2}}\rangle + |0_{-\frac{\pi}{2}}, (N-4)_{\frac{\pi}{2}}\rangle\Big) \sum_{k\neq\pm\pi/2} |2_k, 2_{\pi-k}\rangle + \dots ,\end{aligned} \tag{5.50}$$

where the terms are written in order of decreasing value of $|C_{m,l}Q_m|^2$, as obtained numerically for the case of $(N, L) = (8, 8)$ [2].

The expansion (5.50) explains most of the features that were observed for the ground state of $H^{\text{eff}}_{\text{pbc}}$. The first term can be identified as the ideal Schrödinger cat-like superposition of the two macroscopically occupied orbitals $\pm\pi/2$ (sometimes called a NOON state). The second term is the largest contribution to the reduction cloud. The third term represents an internal exchange of one pair between the two main configurations of the fragmented condensate, without the reduction cloud intervening. The fourth term represents the exchange of four particles between the fragmented condensate and the reduction cloud all going to the same mode pair.

The many-body states (5.49) and (5.50) show very clearly that the reduction cloud is shared by the two branches (or macroscopically distinct configurations) of the cat state. This fact eliminates the naive picture of the cat state formed by two macroscopic branches each carrying its own depletion cloud.

As was noted earlier, when a pair of total momentum π is created, it can originate from either condensate at $\pi/2$ or $-\pi/2$. This implies that, as shown in Eqs. (5.49) and (5.50), such a pair (with $k \neq \pm\pi/2$) factors out from a coherent, still cat-like superposition of the two different macroscopic branches.

It must be noted that block diagonalization is of great help in reducing the numerical overhead when studying the ground states. For $\nu = 0$ and unit filling, one only has to consider $\binom{N-1}{N/2}$ configurations instead of $\binom{2N-1}{N}$ [3]. For $(N, L) = (8, 8)$ this already makes a big difference. Instead of 6435 configurations, one only has to work with 70. This allows the system size to be increased up to 18 particles on 18 sites. Fig. 5.5 shows the scaling of the energy per particle as a function of the system size. The energy drops in a zig-zag pattern. This is connected to the fact that only when $\pm\pi/2$ are among the allowed momenta, do fully paired states involving the occupation of just two modes, namely, $\pm\pi/2$ appear. This is possible only when $L/4$ is an integer.

5.3.7 First excited state

Numerical inspection shows that the ground and the first excited states of both $H^{\text{eff}}_{\text{pbc}}$ and h_∞ differ in their behavior under time reversal, i.e., the transformation that changes the

[2] Since they are multiplying non-normalized many-body states, these decreasing coefficients are not necessarily correlated with the relative weight, within the many-body ground state, of a given type of configuration.

[3] N bosons distributed in L sites yield $\binom{N+L-1}{N}$ distinct configurations.

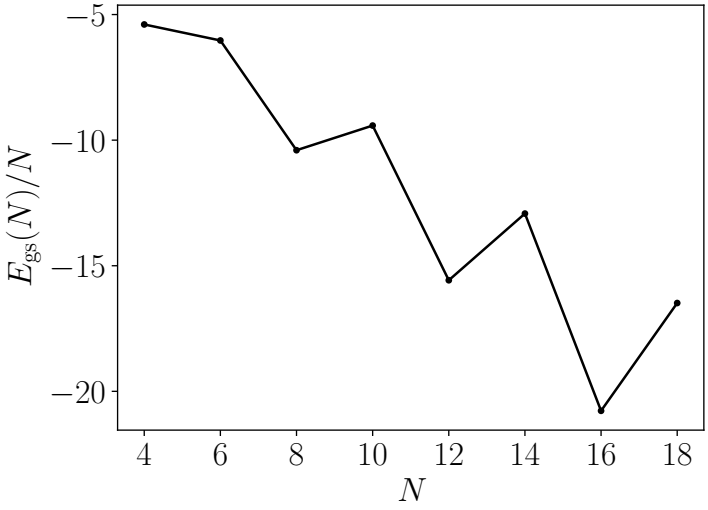

Figure 5.5: Energy per particle of the ground state of h_∞ for different system sizes with unit filling $N = L$. Sizes for which $L/4$ is not an integer, $k \pm \pi/2$ is not part of the set of momenta and its ground state has therefore a slightly higher energy per particle than an adjacent system for which $L/4$ is an integer.

sign of all momenta ($k \to -k$)

$$T a_k T^\dagger = a_{-k}\,. \tag{5.51}$$

While the ground state is symmetric with regard to time inversion, the first excited state is antisymmetric. For the toy model, the first excited state is very similar to (5.49) and (5.50) except for the relative sign between $|(N-2m-2l)_{-\pi/2}, (2l)_{\pi/2}\rangle$ and $|(2l)_{-\pi/2}, (N-2m-2l)_{\pi/2}\rangle$, which is flipped. As a consequence, the first excited state does not have any configurations for which $N - 2m - 2l = 2l$.

The energy spectrum for a few low-lying energy levels of $H^{\rm eff}_{\rm pbc}$ for $\kappa = 0.8$ is shown in Fig. 5.6. The lowest-lying doublet formed by the two very similar states is isolated from the higher-lying excited states. The values of $|C_{m,l}|$ in (5.49) for a given m, l are different in the ground and the first excited state. This is correlated with the fact that the two lowest-energy states are not degenerate (see Fig. 5.6). The non-degeneracy is discussed in the next section.

5.4 Many-body plane waves

5.4.1 Many-body plane waves in the ring

As pointed out in Section 4.2.2, the natural orbitals (defined as the eigenstates of the reduced one-particle density matrix) of $H^{\rm eff}_{\rm pbc}$ have been found to be just plane waves. Of them, the two most occupied ones have momenta $\pm\pi/2$ for both the ground state and the first excited state. Moreover, it was also found that the ground state and the first excited state are symmetric and antisymmetric under time reversal for $H^{\rm eff}_{\rm pbc}$ in the superfluid regime. Importantly, this result coincides with the fact that the coefficients of the ground state wave function in the momentum Fock representation are real. These properties

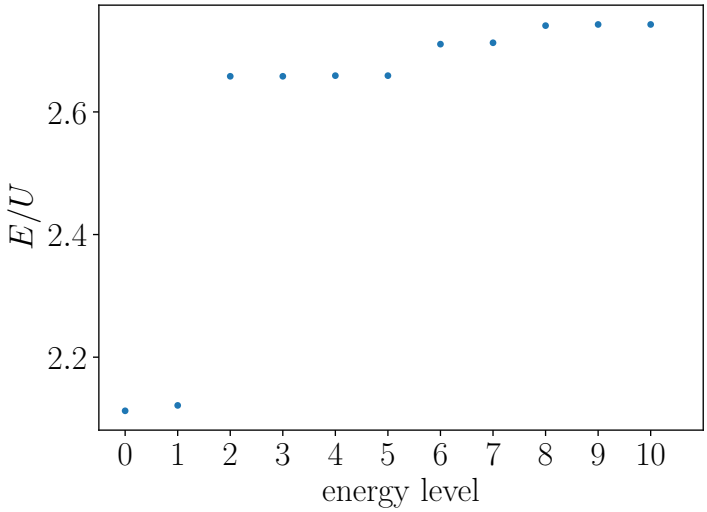

Figure 5.6: Low-lying energy levels of $H^{\text{eff}}_{\text{pbc}}$ for $\kappa = 0.8$ for $(N, L) = (8, 8)$. The lowest two energy levels form an almost degenerate doublet, separated by a large energy gap from the rest of the spectrum.

suggest an interesting relation between the ground state $|\Psi_0\rangle$ and the first excited state $|\Psi_1\rangle$, namely, as the symmetric and antisymmetric superposition of two collective plane waves with average momentum $\pm\pi/2$. This leads to the following approximation:

$$\begin{aligned} |\Psi_0\rangle &\simeq |C(\pi/2)\rangle \\ |\Psi_1\rangle &\simeq \mathrm{i}|S(\pi/2)\rangle \end{aligned} \tag{5.52}$$

where

$$\begin{aligned} |C(k)\rangle &\equiv \frac{1}{\sqrt{2}}\left[|\Phi(k)\rangle + |\Phi(-k)\rangle\right] \\ |S(k)\rangle &\equiv \frac{-\mathrm{i}}{\sqrt{2}}\left[|\Phi(k)\rangle - |\Phi(-k)\rangle\right] , \end{aligned} \tag{5.53}$$

and $|\Phi(k)\rangle = |N_k\rangle$ is a many-body state with all particles in momentum k, its wave function being

$$\langle x_1, \ldots, x_N|\Phi(k)\rangle = L^{-N/2} \exp(\mathrm{i}k \sum_i x_i) , \tag{5.54}$$

where x_i is the space coordinate of the $i-$th boson. Here letters C and S were chosen to signal the $\sin(kx)$ and $\cos(kx)$ wave functions that these states become in the single-particle ($N = 1$) case. In this limit, $|\Phi(k)\rangle$ is the single-particle state with the wave function $L^{-1/2}\exp(\mathrm{i}kx)$.

In Fig. 5.7 the wave function of the numerical and ideal plane wave orbitals for $(N, L) = (8, 8)$ are plotted. The difference between the numerical and the ideal cannot be distinguished with the naked eye. The highly correlated nature of the macroscopic occupation of momenta $\pm\pi/2$, as shown in Fig. 5.1 on the right, is not produced by an exact cat state such as that in (5.53), but a more complicated superposition that is best approximated by Eq. (5.49). A relevant question at this point is whether or not it

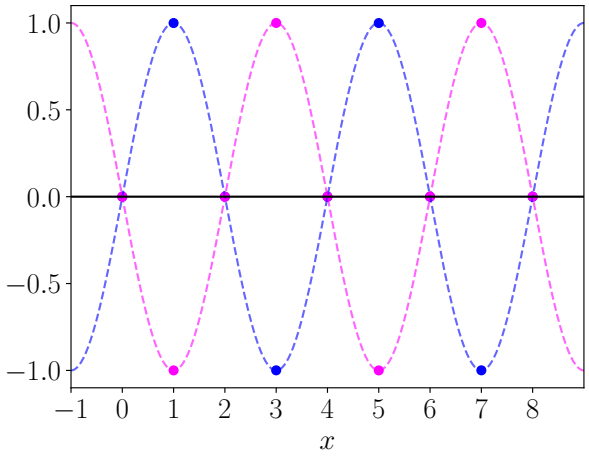

Figure 5.7: Exact (dots) and ideal (dashed lines) natural orbitals in the ring. The real part of the wave function is plotted.

is possible to separate the two branches of the cat-like state without having to invoke any approximation. Remember, the numerically obtained states involve thousands of momentum configurations.

Equations (5.52) and (5.53) give a simple way out: The two cat branches can be identified if $|C(\pi/2)\rangle$ and $|S(\pi/2)\rangle$ are replaced by the true ground and first excited states. Inverting (5.53) leads to the proposal

$$|\Psi_\pm\rangle = \frac{1}{\sqrt{2}}\left(|\Psi_0\rangle \pm |\Psi_1\rangle\right) \tag{5.55}$$

and the expressions

$$|\Psi_0\rangle = \frac{1}{\sqrt{2}}\left(|\Psi_+\rangle + |\Psi_-\rangle\right) \tag{5.56}$$

$$|\Psi_1\rangle = \frac{1}{\sqrt{2}}\left(|\Psi_+\rangle - |\Psi_-\rangle\right) \tag{5.57}$$

with the orthogonality of $|\Psi_0\rangle$ and $|\Psi_1\rangle$ guaranteeing

$$\langle\Psi_+|\Psi_-\rangle = 0\,. \tag{5.58}$$

In Fig. 5.8 the two-particle momentum density of $|\Psi_\pm\rangle$ is shown. The distinct single peaks at $\pm(\pi/2, \pi/2)$ clearly confirm that the criterion (5.55) is adequate for cleanly constructing the two cat branches. It should be emphasized that Fig. 5.8 shows $\langle n_q n_k\rangle/N^2$ for a numerically obtained state $|\Psi_\pm\rangle$ involving thousands of momentum configurations of which $|N_{\pm\pi/2}\rangle \equiv (N!)^{-1/2}(a^\dagger_{\pm\pi/2})^N|\text{vac}\rangle$ is only that with the largest weight. Specifically, for $N = L = 8$, the states $|N_{\pm\pi/2}\rangle$ add up to a normalization weight of approximately 50%.

The remarkable result is that a decomposition in cat branches such as that shown in (5.56) with the results of Fig. 5.8 is also possible for a boson gas between hard walls, as will be discussed in the next section.

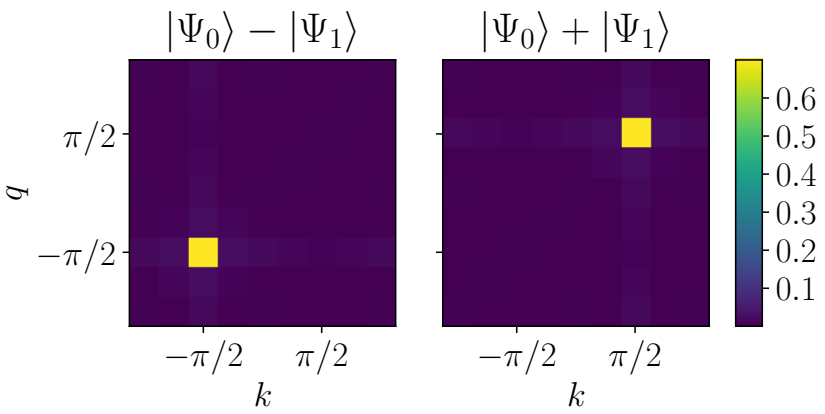

Figure 5.8: Two-particle momentum density of $|\Psi_\pm\rangle = \frac{1}{\sqrt{2}}(|\Psi_0\rangle \pm |\Psi_1\rangle)$ constructed from the superposition of the ground and first excited states. The isolated peaks clearly suggest that the ground state is formed by two many-body configurations akin to collective plane waves. Here $\kappa = 0.7$.

Before analyzing the hard-wall boundary conditions, the nondegeneracy of the ground state doublet shown in Fig. 5.6 should be commented on: In the particular case of $N = 1$, (5.52) yields two degenerate states, since $\cos(\pi x/2)$ and $\sin(\pi x/2)$ are wave functions connected by a symmetry operation, namely, a space translation of one lattice spacing. Interestingly, the same analysis for N particles shows that $|C(\pi/2)\rangle$ and $|S(\pi/2)\rangle$ differ by a global $1/N$ translation. For $N > 1$, $1/N$ is less than a lattice spacing and thus such a translation does not yield a degenerate state. However, practical degeneracy is obtained for $N \gg 1$. This argument, developed for noninteracting bosons, provides a semiquantitative explanation of the small but nonzero splitting of the interacting ground state doublet shown in Fig. 5.6. It also suggests that this splitting vanishes in the thermodynamic ($N \to \infty$) limit.

Particle current

It is tempting to view the branches (5.55) as many-body plane waves traveling with an average momentum of $\pm\pi/2$. This picture is, however, proved invalid under closer inspection. The already unusual effective Hamiltonian (4.44) yields an equally unconventional particle current operator $I^{\text{eff}}_{\text{pbc}}$. If, as a result of a twist in the periodic boundary conditions ($a_L = e^{-i\theta}a_0$), all allowed momenta are shifted by an amount θ, the matrix elements in $H^{\text{eff}}_{\text{pbc}}$ change accordingly. The space-averaged particle current operator, $I = L^{-1}\partial H^{\text{eff}}_{\text{pbc}},/\partial\theta$ can thus be written as

$$I^{\text{eff}}_{\text{pbc}} = \frac{U\kappa}{L^2} \sum_{l,m,n,p=0}^{L-1} \mathcal{J}_1[2\kappa F(k_l,k_m,k_n,k_p)] \times G(k_l,k_m,k_n,k_p) a^\dagger_{k_p} a^\dagger_{k_n} a_{k_m} a_{k_l} \delta_{k_l+k_m,k_n+k_p}\,, \tag{5.59}$$

where $\mathcal{J}_1$ is the first-order Bessel function and

$$G(k_l,k_m,k_n,k_p) = \sin(k_l) + \sin(k_m) - \sin(k_n) - \sin(k_p)\,. \tag{5.60}$$

Clearly, the expectation value of $I^{\text{eff}}_{\text{pbc}}$ vanishes for a state of the type $|\Phi(k)\rangle = |N_k\rangle$ where all particles have the same momentum k. Numerically, it is confirmed that

$$\langle \Psi_\pm | I^{\text{eff}}_{\text{pbc}} | \Psi_\pm \rangle = \langle \Psi_{0,1} | I^{\text{eff}}_{\text{pbc}} | \Psi_{0,1} \rangle = 0\,. \tag{5.61}$$

However, despite this apparent lack of dynamics, the two branches $|\Psi_\pm\rangle$ will behave very differently in a time-of-flight experiment in which the crystal momentum in the lattice becomes the linear momentum in the vacuum as the confining optical lattice is switched off. Moreover, it is found, that in the presence of a finite twist in the periodic boundary conditions, the ground state carries a nonzero current, which is to be expected of a superfluid. Interestingly, the nonzero value of the current depends crucially on the presence of the reduction cloud.

5.4.2 Many-body plane waves for hard walls

In Section 4.3 a remarkable discovery was made. Even for hard wall boundary conditions the two-particle momentum density showed correlated peaks at $\pm\pi/2$ in the truncated plane wave representation. This of course means that the state remains cat-like even though the hard walls introduce a strong coupling between single-particle modes with momentum k and $-k$. As noted in Section 4.3, a lot of the numerical tools to study the hard wall case are no longer applicable for an investigation of the effective Hamiltonian $H^{\text{eff}}_{\text{hw}}$ in Eq. (4.83). For example, it was no longer computationally affordable to investigate the Mott to superfluid transition with the methods used for the ring. Less hampered by system size are, of course, the analytic approaches developed here. The analytic methods strongly relied on momentum conservation, which ultimately facilitated the derivation of h_∞. For example, the use of momentum conservation is crucial for deriving Eq. (5.22). Only in the high frequency limit was it possible to develop a microscopic picture of the ground state and explain the cat-like features of $H^{\text{eff}}_{\text{pbc}}$ in the superfluid regime. This is no longer possible for $H^{\text{eff}}_{\text{hw}}$ due to the residual sum over x in Eq. (4.83) and the use of stationary waves [see Eq. (4.21)]. The difference between HWBC and PBC is also present in the numerical analysis. For $(N, L) = (8, 8)$ the double peak structure of the momentum density in Fig. 4.20 does collapse for $\kappa > 0.8$ into a single peak at $k = 0$ (not shown). Not all is lost however: since large values of κ are inherently less physical (see Section 4.4 of the previous chapter), $\kappa < 0.8$ is still the physically most relevant regime of the driving, and it is this regime where the system displays its most interesting properties. The numerical methods developed in the previous section still apply as well. In fact, they were originally developed to deal with the HWBC and to reach a better numerical understanding of the cat-like nature of the ground state in a box.

As in Eq (4.83), the wave vector $\tilde{k}_l = \pi/(L+1)$ references the stationary waves in Eq. (4.21) as opposed to the plane wave expansion (4.5). As in the ring case, symmetry can be used. Space inversion around the midpoint of the chain is represented by the transformation

$$I a_{\tilde{k}_l} I^\dagger = \begin{cases} -a_{\tilde{k}_l} & l \text{ even} \\ a_{\tilde{k}_l} & l \text{ uneven}\,, \end{cases} \tag{5.62}$$

where I is the spatial inversion operator. It was confirmed numerically that the ground state is symmetric under I, while the first excited state is antisymmetric. As shown in

Section 4.3 of the previous chapter, the momentum density of both the ground and first excited state are very similar.

As in the previous section, these properties can be used to form an approximate picture of the wave function of the ground and first excited states. Specifically the approximations

$$|\Psi_0\rangle \simeq |C(\pi/2)\rangle \tag{5.63}$$
$$|\Psi_1\rangle \simeq |S(\pi/2)\rangle\,, \tag{5.64}$$

can be made. The coordinates in (5.54) refer to the midpoint between the walls. For hard walls, the appropriateness of this approximation can, once again, be inferred from an analysis of both the approximate and numerically-exact natural orbitals. The reduced one-particle density matrix for $|C(k)\rangle$ and $|S(k)\rangle$ is

$$\rho^{(1)}(x,x') = \frac{1}{L}\cos[k(x-x')] \tag{5.65}$$
$$= \frac{1}{L}[\cos(kx)\cos(kx') + \sin(kx)\sin(kx')]\,. \tag{5.66}$$

This result means that the natural orbitals are

$$\phi_0(x) = \cos(kx)\,, \quad \phi_1(x) = \sin(kx)\,. \tag{5.67}$$

These can then be compared with the numerically obtained natural orbitals. In Fig. 5.9 a direct comparison between the degenerate, most occupied orbitals for $(N,L) = (8,8)$ and the approximate natural orbitals in (5.67) is drawn. For $k = \pi/2$ the numerically exact and the approximate solutions are very similar. The numerically exact state obeys the boundary conditions, so its orbitals decline more gradually close to the walls. This can be ameliorated by multiplying the truncated plane waves implicit in (5.63) and (5.64) by an envelope function that smoothly goes to zero at the walls. This envelope function is also one of the reasons for the broken symmetry between 0 and π, since the envelope function's discontinuity at the walls will imbalance the momentum distribution.

The above analysis of symmetries and natural orbitals strongly supports the relevance of the approximate picture (5.63) proposed above. As was done for the ring, the relations (5.53) can be employed to identify the cat branches between hard walls.

The above findings strongly support the approximate picture given in Eqs. (5.63) and (5.64). This conclusion is further strengthened by the fact that the ground state and the first excited state are, respectively, even and odd under space inversion (always within the convention that, when expanded into momentum Fock states in the stationary wave representation, the ground and first excited state only have real coefficients).

These symmetry considerations then imply that the ground state and the first excited state are, respectively, cosine-like and sine-like (with respect to the midpoint). Therefore the cat branches can be expected to be:

$$|\Psi_\pm\rangle = \frac{1}{\sqrt{2}}(|\Psi_0\rangle \pm \mathrm{i}|\Psi_1\rangle)\,. \tag{5.68}$$

This expectation is confirmed in Fig. 5.10, where the numerical momentum-momentum correlation is shown for the branches $|\Psi_\pm\rangle$. As argued for the ring, the orthogonality of

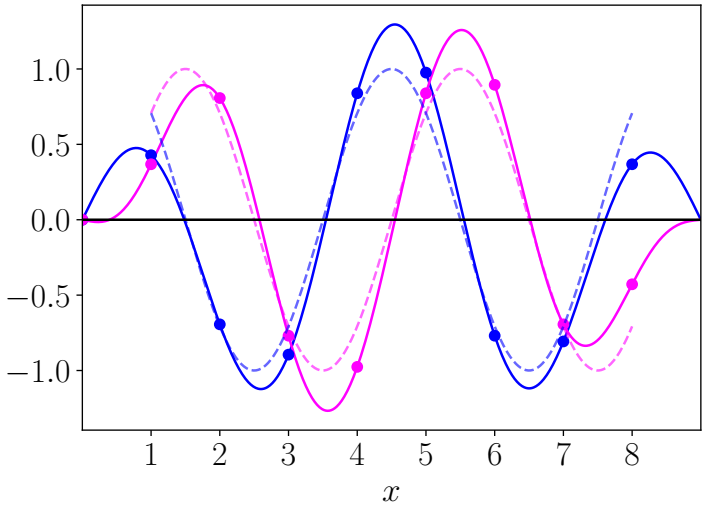

Figure 5.9: The solid lines represent the two most occupied natural orbitals at $\kappa = 0.8$ for 8 particles on 8 sites. They are plotted continuously to better compare them with the analytically obtained orbitals from the ansatz in (5.63). Points indicate the value of the wave function at the sites. The numerically exact orbitals and the approximation show good agreement in the center of the lattice. At the edges the agreement fades. This is due to the highly discontinuous nature of the truncated plane waves at the edges, while the stationary waves are not discontinuous at all.

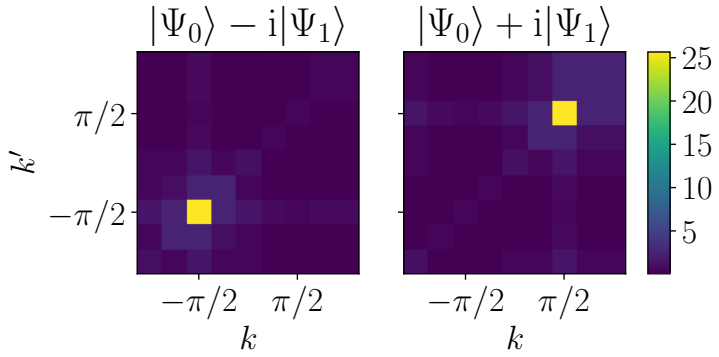

Figure 5.10: Momentum correlations of the states $|\Psi_\pm\rangle$ constructed from the superposition of the ground and first excited states [see (5.68)] for $\kappa = 0.8$. The isolated peaks clearly indicate that the ground state can be viewed as the superposition of two collective plane waves between the walls.

$|\Psi_0\rangle$ and $|\Psi_1\rangle$ guarantees $\langle\Psi_+|\Psi_-\rangle = 0$. The outcome is such that for the hard-wall case the ground and first excited states can again be written as

$$|\Psi_0\rangle = \frac{1}{\sqrt{2}}(|\Psi_+\rangle + |\Psi_-\rangle) \tag{5.69}$$

$$|\Psi_1\rangle = \frac{-\mathrm{i}}{\sqrt{2}}(|\Psi_+\rangle - |\Psi_-\rangle)\,, \tag{5.70}$$

where $|\Psi_\pm\rangle$ represent complex but strictly orthonormal many-body configurations with

a preferential occupation of momenta $\pm\pi/2$. The two orthonormal branches of the cat state are identified with $|\Psi_\pm\rangle$.

As for the ring, the states $|\Psi_\pm\rangle$ yielding the simple-looking result in Fig. 5.10 involve thousands of momentum configurations.

The low-lying excitation energies are shown in Fig. 5.11. The ground state and first excited state are much less separated from the higher-lying excitations than for the ring. The comparison of the various energy differences in the ring and in the hard-wall cases takes us to the question of the fragility of the cat-like correlations against temperature and finite-time state preparation. This problem is addressed in Section 5.7.

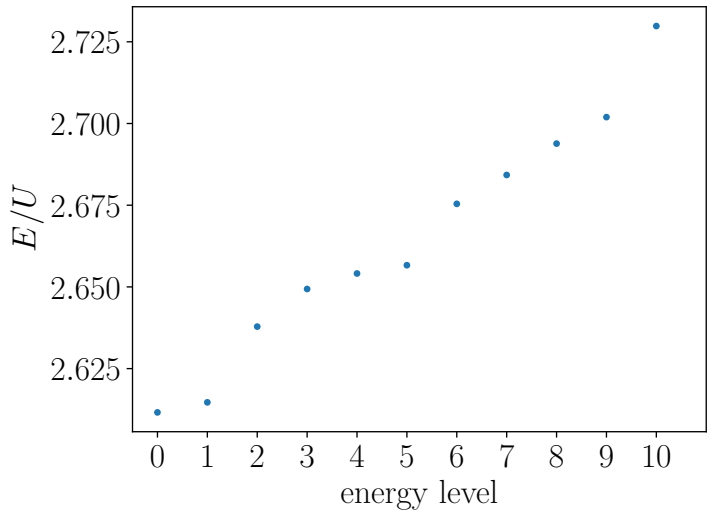

Figure 5.11: Low-lying energy levels for $H_{\rm hw}^{\rm eff}$ and $\kappa = 0.8$. The gap between the lowest two states and the rest of the spectrum is considerably smaller than it is for the ring-case (Fig. 5.6).

5.5 Harmonic confinement

Although the trapping of ultracold atoms between hard-wall boundaries has been realized experimentally [354], the more common trapping potential is of parabolic shape. In [3] the surviving properties of the effective Hamiltonians discussed previously were analyzed by the addition of

$$V(x_j) = V_0 \sum_j (x_j - x_0)^2 \, n_j \ , \tag{5.71}$$

to the fully time dependent Hamiltonian in Eq. (4.2). The center of the box is indicated by x_0 and n_j is the standard number operator.

To analyze the system, it was initially prepared in the Mott state. Then the amplitude of the time dependent driving was slowly ramped up. In [3] it was reported that the momentum density function and the natural orbital occupation strongly mimics that of a flat potential $V_0 = 0$. When κ is ramped up from zero, two natural orbitals become more and more occupied once again. As for the ring and the hard walls, these orbitals correspond to the momenta $\pm\pi/2$. This points toward the formation of a cat state. For the

larger values of $V_0 = 0.04/U$ and $V_0 = 0.08/U$ these features continue to be pronounced. The cat-like features even survive random potentials. This remains true, as long as the amplitude of the energy of the disorder potential does not cause a localization of the particles. With this it can be concluded that the cat state features are preserved in spite of these local on-site potentials.

5.6 Measuring "cattiness"

Quantifying a given state's cat-like quality or "cattiness" [355] is neither a simple nor a straightforward task. A number of measures for the quality of cat states have been proposed in the literature [278, 356, 357]. A rough categorization of the various ways to gauge the quality of a cat state can be drawn from the summary in Ref. [356]. Measures that define the effective size of a superposition compare it to a perfect cat state, which is made from a orthonormal superposition of two macroscopic states. The work in Refs. [358–361] can be filed under this category. Fluctuations of the relative particle numbers are used as a characterization in Refs. [347, 362]. In Refs. [342, 363, 364] information-theoretical considerations form the base of quantifying "cattiness". The magnitude of the off-diagonal correlations is used to distinguish between mixed and pure states in Refs. [279, 280, 344, 365]. Finally, the more measurement-based approaches are discussed in Refs. [337, 366–369].

The characterization of the various ground states in this section is based on the measurement-based definition of cat quality introduced in [337]. Their measure is best fitted to the situation encountered in the previous sections. This is mostly because it allows the inclusion of more than two modes and it requires the identification of the respective branches of the cat state. If the superposition

$$|\Psi\rangle = |A\rangle + |B\rangle \tag{5.72}$$

is considered then the method in Ref. [337] rates a cat state by how well branch A and B can be distinguished from each other after a measurement. A and B do not have to be orthogonal. More precisely, it quantifies the probability of successfully inferring the two n-particle reduced density matrices (n-PRDMs) $\rho_A^{(n)}$ and $\rho_B^{(n)}$ [370] related to the respective branches after a n-particle measurement. Formally this translates to

$$P^{(n)} = \frac{1}{2} + \frac{1}{4}||\rho_A^{(n)} - \rho_B^{(n)}|| \ . \tag{5.73}$$

where $||\cdot||$ is the trace norm $||\rho|| = \sum_i |\lambda_i|$ with λ_i the eigenvalues of ρ. Identical branches would mean that the probability of inferring the branch from an n-particle measurement is $P = 1/2$. This means that performing a measurement does not increase the knowledge about either branch. A perfect cat state collapses the probability to $P^{(1)} = 1$ after a single measurement. The effective size of the superposition is determined by the amount of measurements it takes to differentiate the branches. The more particles it takes, the smaller is its size.

As in Ref. [3], Eq. (5.73) is used without invoking an effective cat size. This would require a value of confidence which is an additional parameter determined by the user of

the measure. Only measurements up to two particles are considered. Both branches A and B are sharply defined by the splitting in Eq. (5.56) in the plane wave representation.

The properly normalized components of the one-PRDM and two-PRDM are

$$\rho_{il}^{(1)} = \frac{1}{N}\langle a_{k_i}^\dagger a_{k_l}\rangle \tag{5.74}$$

$$\rho_{ijlm}^{(2)} = \frac{1}{N(N-1)}\langle a_{k_i}^\dagger a_{k_j}^\dagger a_{k_l} a_{k_m}\rangle \tag{5.75}$$

In Fig. 5.12 $P^{(n)}$ is presented as a function of κ for $n = 1, 2$. As κ grows, the probability of inferring A or B evidently rises in both the ring and the hard walls. For $\kappa < 0.75$ the biggest probabilities reached for the ring are $P^{(1)} = 0.93$ and $P^{(2)} = 0.98$, whereas for the hard walls they are $P^{(1)} = 0.88$ and $P^{(2)} = 0.95$. In the ring, $P^{(n)}$ closely approaches the theoretical limit $P^{(1)} = 0.94$ ($P^{(2)} = 0.98$) given by the pairing model. Even in the limit $\kappa \to \infty$, the ground state is not a perfect cat, since the pairs in the reduction cloud are shared by both condensate branches. A measurement of the momentum of a particle in the reduction cloud carries no information about which branch it belongs to.

The probability of collapsing the state after a two-particle measurement is consistently higher in both the ring and the hard walls. The apparent discontinuity in the ring for low values of κ stems from a discontinuity in the first excited state, which does not develop its peaks at $\pm\pi/2$ in the momentum density gradually (see Fig. 4.6). This discontinuity was not investigated in detail.

Finally, in Fig. 5.13 the scaling of $P^{(1)}$ as a function of increasing system size is shown. The pairing model predicts that $P^{(1)}$ increases with N but it appears to be bounded by a value below unity for $N \to \infty$. This is due to the presence of the reduction cloud.

An additional, complementary figure of merit C was defined in [3] to quantify cattiness:

$$C \equiv \sum_k p_k(|\langle A|\xi_k\rangle| - |\langle B|\xi_k\rangle|)^2 \tag{5.76}$$

where

$$p_k = \langle\Psi|n_k|\Psi\rangle/N \tag{5.77}$$

is the probability of finding momentum k in a one-particle measurement, and

$$|\xi_k\rangle = \frac{n_k}{\mu_k^2}|\Psi\rangle\ , \tag{5.78}$$

with $\mu_k^2 \equiv \langle\Psi|n_k^2|\Psi\rangle$, is the normalized many-boson state after projecting out configurations with momentum k unoccupied. The cattiness C is an intuitively constructed measure. As in Ref. [337], it is designed to be based on a measurement procedure. The idea is to infer the quality of the superposition by correlating it with the extent to which $|\xi_k\rangle$ overlaps with $|A\rangle$ or $|B\rangle$, i.e., with the ability to predict the outcome of the second one-particle measurement from the result of the first measurement.

For an ideal cat, $C = 1$. For a non-cat state ($|A\rangle = |B\rangle$ in (5.72)), $C = 0$. In Fig. 5.14 the results for the ring and hard-wall boundary conditions are shown. Again, the discontinuity for the ring stems from a discontinuity in the nature of the first excited state. In the Mott insulating regime C is very close to zero and increases notably after

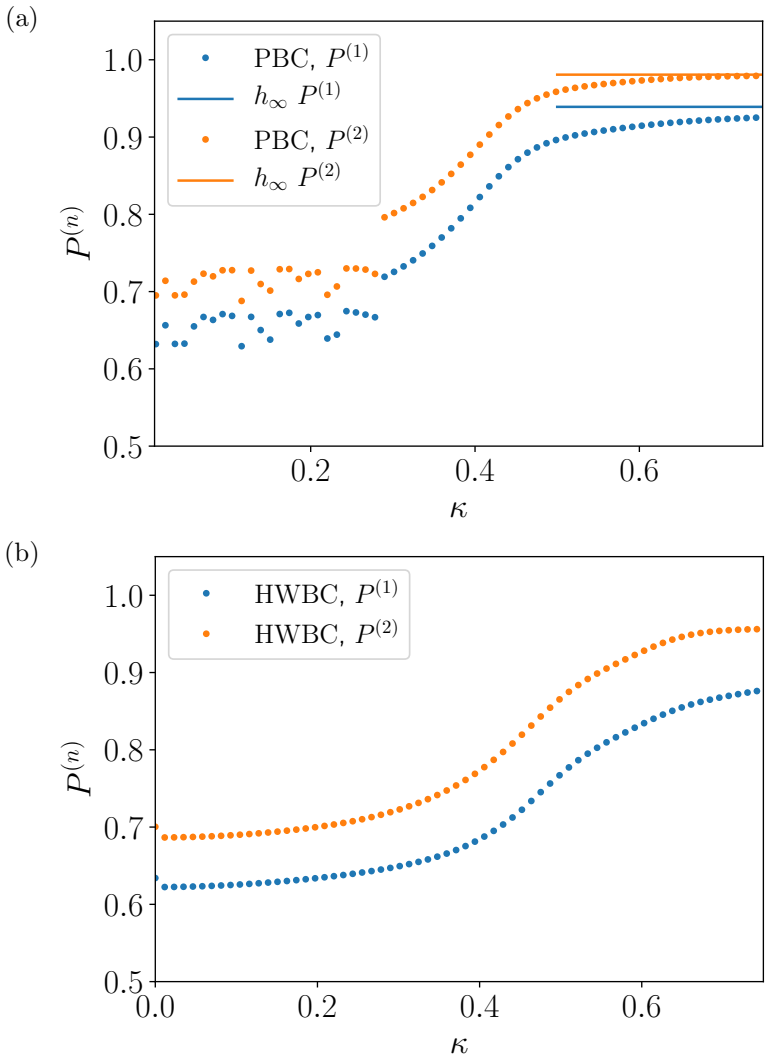

Figure 5.12: Figure of merit based on the probability $P^{(n)}$ of inferring the branch A or B after an n particle measurement: (a) ring, (b) hard walls. The apparent discontinuity in the ring at $\kappa \simeq 0.3$ is due to a discontinuity in the behavior of the first excited state. The probabilities of inferring the cat state for the hard-wall case is consistently lower than for the ring.

the transition. As for (5.73), the fact that $C < 1$ for large κ is related to the presence of the reduction cloud, i.e., the multi-mode nature of the ground state.

The quantitative measure (5.76) is particularly simple to apply when only two modes are involved. In the following C is calculated for one of the states proposed in [358]

$$|\Psi\rangle = \frac{1}{K}(|A\rangle + |B\rangle) \tag{5.79}$$

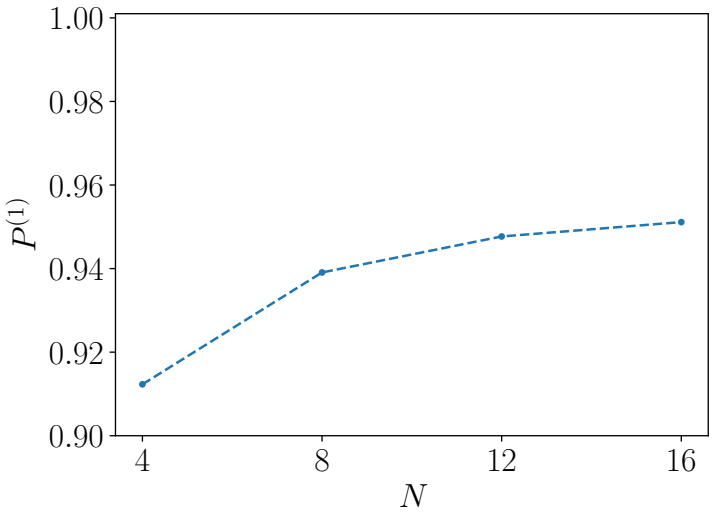

Figure 5.13: Scaling of $P^{(1)}$ with system size for the pairing model. For up to 16 particles on 16 sites the probability steadily increases.

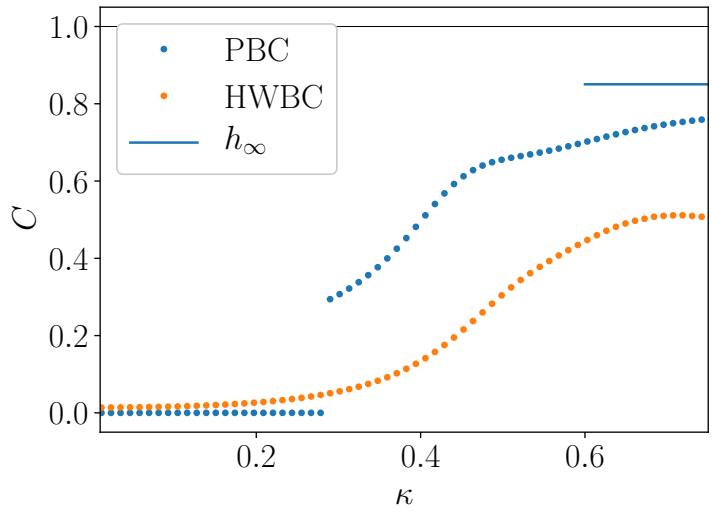

Figure 5.14: Figure of merit C, defined in Eq. (5.76). As before, the discontinuity in the ring result arises from the behavior of the first excited state. $C < 1$ for large κ because both branches share the reduction cloud. The largest values reached are: $C = 0.79$ for the ring, $C = 0.85$ for the pairing model and $C = 0.51$ for hard walls.

where

$$|A\rangle = |N, 0\rangle \ , \tag{5.80}$$

$$\begin{aligned} |B\rangle &= \frac{1}{\sqrt{N!}}(c_\theta a^\dagger + s_\theta b^\dagger)^N |\text{vac}\rangle \\ &= \frac{1}{\sqrt{N!}} \sum_l \binom{N}{l} c_\theta^l s_\theta^{N-l} \sqrt{l!(N-l)!} |l, N-l\rangle \ , \end{aligned} \tag{5.81}$$

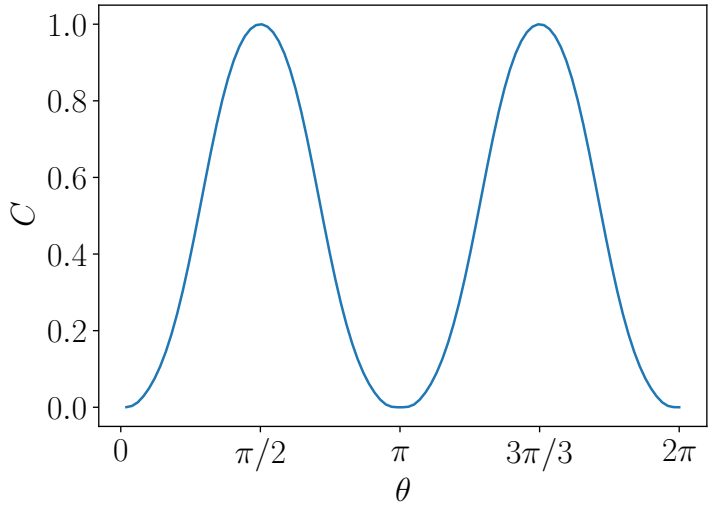

Figure 5.15: Cattiness C for (5.79). For $\theta = \pi/2, 3\pi/2$ the state is a perfect cat, for $\theta = 0, \pi$ it has no cat state feature.

where $c_\theta \equiv \cos\theta$ and $s_\theta \equiv \sin\theta$. With this the closed expressions

$$C(\theta) = \sum_k f_k(|\langle A|\xi_k\rangle| - |\langle B|\xi_k\rangle|)^2 \tag{5.82}$$

$$= \frac{1}{NK^4}\left(\frac{1}{\mathcal{M}_1^2}(N + 2Nc_\theta^N + g_1)(N - g_1)^2 + \frac{g_2^3}{\mathcal{M}_2^2}\right) \tag{5.83}$$

can be calculated, where

$$\mathcal{M}_1^2 = \frac{1}{K^2}\left(N^2 + 2N^2 c_\theta^N + \frac{1}{N!}\sum_{l=0}^{N}\binom{N}{l}^2 c_\theta^{2l} s_\theta^{2(N-l)} l^2 l!(N-l)!\right) \tag{5.84}$$

$$\mathcal{M}_2^2 = \frac{1}{N!K^2}\sum_{l=0}^{N}\binom{N}{l}^2 c_\theta^{2l} s_\theta^{2(N-l)}(N-l)^2 l!(N-l)! \tag{5.85}$$

and

$$g_1 = \frac{1}{N!}\sum_{l=0}^{N}\binom{N}{l}^2 c_\theta^{2l} s_\theta^{2(N-l)} l!(N-l)!l \tag{5.86}$$

$$g_2 = \frac{1}{N!}\sum_{l=0}^{N}\binom{N}{l}^2 c_\theta^{2l} s_\theta^{2(N-l)} l!(N-l)!(N-l) \tag{5.87}$$

5.7 State preparation

Based on the analysis provided in our work in Ref. [3], the preparation of the cat state is now analyzed. As it is the ground state of the system, it can be expected to naturally fall into this state as the system is cooled. However, the cat state consists of a superposition of two branches which are degenerate in energy and yield a splitting that vanishes in the

thermodynamic limit. As a consequence, cooling the system towards zero temperature will just result in a classical mixture of the two branches [348]. Here the feasibility of preparing the cat state will be studied by adiabatic manipulation, as considered in [329, 336]. Working with the full time-dependent Hamiltonian (4.3), the system is initialized in the Mott state, with one particle occupying each lattice site, and κ is slowly ramped up over many thousands of driving periods from an initial value of zero to a final value of $\kappa = 0.8$, as shown in Fig. 5.16a. When this final value is reached, κ is held constant.

To give an indication of the degree to which the instantaneous state of the system exhibits cat correlations during this process, the two-particle reduced density matrix at momenta $(\pi/2, \pi/2)$ is evaluated, that is $\chi \equiv \langle n_{\pi/2} n_{\pi/2} \rangle$ is computed. As was seen above, this quantity has a large value when the system is in a cat-like state and is small otherwise. So it acts as a reasonable alternative figure of merit to characterize the expected cat nature of the state that is reached by slowly ramping up the driving amplitude.

Fig. 5.16b shows the behaviour of χ for periodic boundary conditions (the ring) for various ramp speeds. It can clearly be seen that as the ramp speed decreases, the final value of χ increases, indicating that the cat state is being prepared with greater fidelity. This can be understood from the quasienergy spectrum of the system, shown in Fig. 5.17a. For small κ the system is a Mott insulator, and so the ground state is separated from the next excited states by a gap of order U. Accordingly, as long as the ramp-speed is sufficiently slow with respect to the gap, $\Delta/\dot{\Delta} \gg 1$, the adiabatic approximation holds and the system safely remains in the ground state. Once the Mott gap closes, and the system becomes superfluid, the two lowest-lying states become an almost degenerate doublet. To form the cat correlations, the system must remain in this doublet, without being excited to higher excited states, which again imposes an adiabatic limit on the speed of the ramp (actually, as noted below, the system barely occupies the first excited state due to symmetry). As the gap is smaller here than in the Mott regime, the adiabaticity requirement is more stringent, and it is only fulfilled when the ramp-time is of the order of $6400T$. For more rapid ramps, χ shows an oscillatory behaviour arising from the excitation of higher states, which decreases the value of the cat correlations. To confirm this interpretation, the overlap (squared) of the final state with the true ground state of the system for $\kappa = 0.8$ was examined. For a ramp-time of $1600T$, for example, this takes a value of 0.842, indicating that a substantial proportion of the state has been excited out of the ground state. For the slowest ramp, however, this value rises to 0.999, demonstrating that the procedure indeed has excellent fidelity.

Fig. 5.16(c) shows the corresponding results for the hard-wall case. In contrast to the ring, however, even the slowest ramp speeds used are not able to prepare a cat state with comparable fidelity. As is shown in Fig. 5.17b, this is a consequence of the differences in the energy spectrum produced by the change in boundary conditions. For hard walls the lowest doublet of states in the superfluid regime is barely separated from the next-highest states, as can be seen explicitly by comparing Fig. 5.11 with Fig 5.6. Again the overlap of the obtained state with the actual ground state of the system is examined. It reveals that even for a ramp-time of $6400T$ the fidelity is substantially lower ($\simeq 0.902$) than for the corresponding case of the ring, As a result, slower ramp-speeds would be needed to prepare a cat state, with time scales at least an order of magnitude longer than for the case of a ring.

Interestingly, for both the ring and the hard-wall case, the overlap of the final state

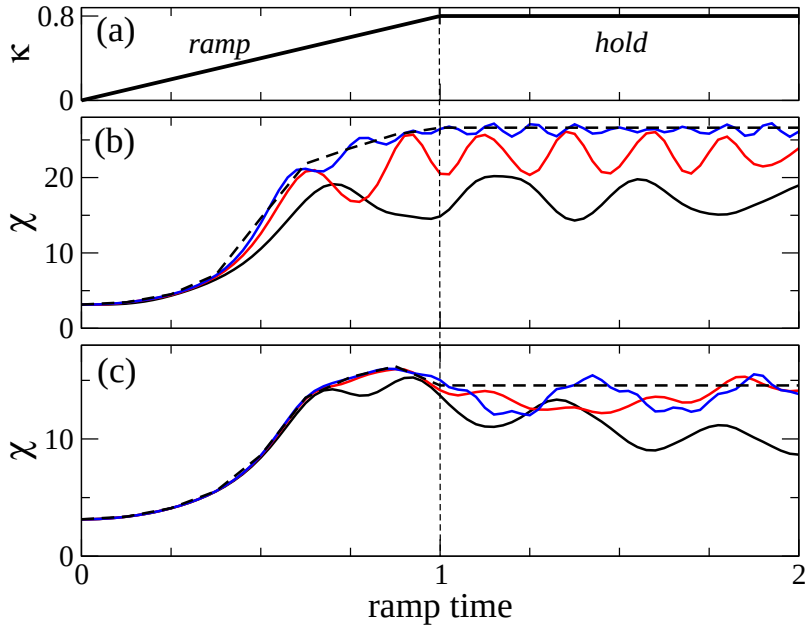

Figure 5.16: The full time-dependent system is initialized in a Mott state, and κ ramped linearly from 0 to a value of 0.8 over a time-interval (the ramp-time), and then held constant for the same time interval (a) Time-dependence of the driving parameter, κ. (b) Cat correlation χ for a ring system. The black line is for a ramp-time of $1600T$, the red line for $3200T$ and the blue line for $6400T$. As the ramp-time is increased, the final value of χ becomes closer to that of the system's true ground state (dashed curve), and the oscillations reduce in amplitude, indicating that the cat state is being prepared with greater fidelity. (c) As in (b) but for a hard-wall system. The final value of χ is lower, and even for the slowest ramp-time, the oscillations in χ remain significant. Even slower ramps would be needed to prepare the cat state with adequate fidelity. Physical parameters: $U = 1$, $\omega = 50$. The figure is taken from [3].

with any single excited state is very small. In particular, the overlap with the (also cat-like) first excited state is essentially zero because the ramp-up driving respects the symmetry of the ground state.

5.8 Resilience to collapse

This section focuses on the resilience of the cat state against collapse into one of its branches once it has been prepared. Here collapse or decay means its projection into one branch due to energy lowering or information retrieval. In this context the meaning of collapse is extended to include a long period of time, in which the state remains in either of its branches after the decay takes place.

For a boson gas in a ring, one possible cause of collapse is the appearance of a spurious external flux (i.e. a rotation drift of the optical lattice) that breaks the degeneracy of the opposite-momenta condensates. This mechanism may be relevant in a SQUID [296, 297], where the Josephson coupling generates a periodic flux dependence, which yields a double-

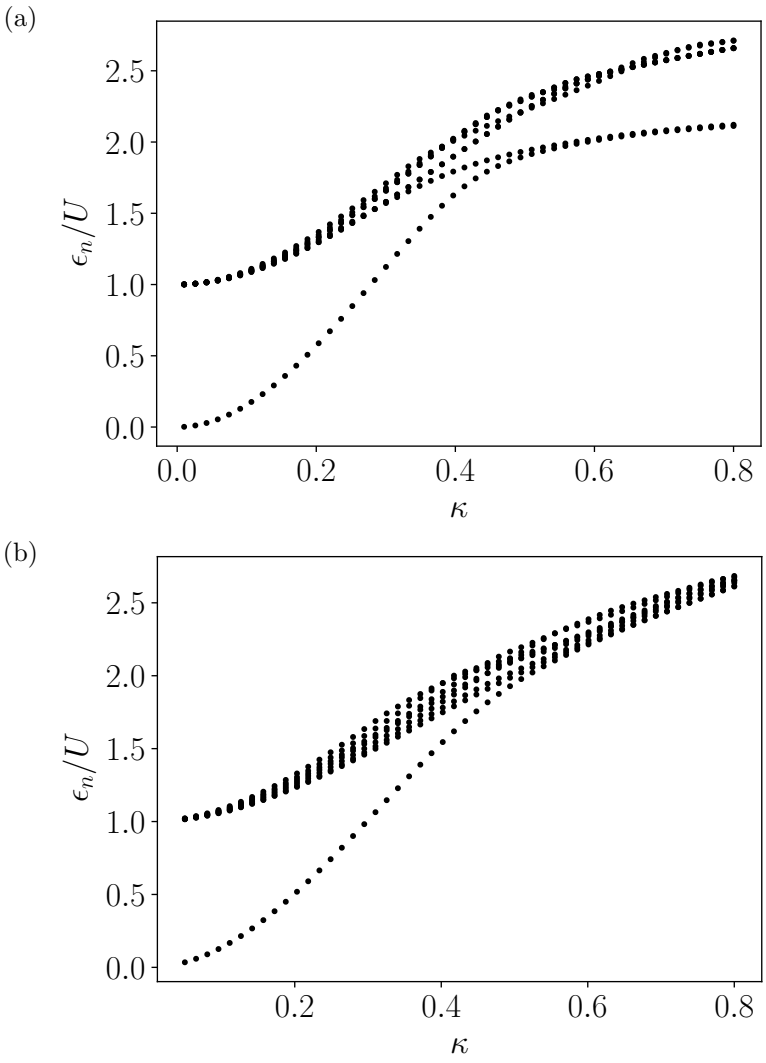

Figure 5.17: Quasienergy spectrum as a function of κ for (a) periodic boundary conditions, and (b) hard walls. Note how in (a) the ground state manifold is always isolated from the rest of the spectrum, but that in (b) the ground-state merges into the spectrum as κ increases. This makes adiabatic preparation of the cat state far more challenging for the case of hard walls.

well potential that can be easily imbalanced. Here the physics is different: an external flux merely introduces a shift in the average momentum of the two condensates while preserving the cat structure. In the case of a box (hard wall), the situation is even simpler, as any velocity drift can be gauged away.

Particle losses can be a cause of MQS collapse [329, 350]. In order for this to be an efficient decay mechanism it is necessary for the emitted atom to carry information on the cat branch it comes from. Assuming that it is possible upon detection to know the momentum the atom had in the optical lattice, that information retrieval might be sufficient to cause the collapse. However, this is not clearly the case if the atom with nonzero momentum in the lattice actually had zero group velocity before being emitted (see section 5.4.1). For the reduction cloud, the situation is more radical: even if one

was able to know the initial crystal momentum of the detected atom, if this momentum happens to belong to the reduction cloud (i.e. it is different from $\pm\pi/2$), then it carries no information whatsoever on the branch state, since the reduction cloud is identically shared by the two $\pm\pi/2$-momentum condensates.

A similar discussion of atom losses applies to a kinetically-driven boson gas between hard walls.

The interaction with the thermal cloud has sometimes been identified as a possible cause of cat state collapse [336]. Thermal excitations have not been investigated here, but the existing experience on conventional boson gases teaches that quasiparticles often tend to reflect the structure of the depletion cloud. The fact that the reduction cloud is common to the two macroscopic condensates strongly suggests that the same is true for the quasiparticles. Thus the assertion that the thermal cloud cannot cause the decay of the MQS state appears to be an educated conjecture.

Diagonal impurities may also break the cat structure. Both for impurity disorder (see section 5.7) and for isolated impurities, the cat structure remains intact within a range of nonzero impurity strength.

Finally, standard decoherence can be a cause of preventing the preparation of a pure cat state, i.e., dephasing caused by coupling to an external dissipative environment [261–264]. Cold atom systems tend to be quite isolated and thus quite insensitive to external sources of dissipation. For the present system, there is an additional, more profound reason to believe that dynamic decoherence is not operating here. A necessary condition for an environment to cause the collapse of a cat state is that it couples to the system observable whose eigenstates (the "pointer basis" of Ref. [262]) characterize the cat branches. It is difficult to think of a dissipative environment that meets those requirements here, considering that the branches of the present state collectively populate nonzero momentum states while yielding individually a zero current average, due to the counterintuitive current operator (see section 5.4.1).

Altogether, there seem to be a number of reasons for asserting that the cat states in the ground doublet of a kinetically driven boson gas are quite resilient. Although it has not been explicitly investigated, it seems reasonable to venture that this unusual MQS robustness will survive in the thermodynamical limit. Thus a picture emerges of a many-body state with a practically hidden cat structure that only blossoms when subject to the invasive momentum-measurement of a time-of-flight experiment.

5.9 Summary and conclusions

This chapter investigated, in detail, the Schrödinger cat state that is produced by kinetically driving a Bose-Hubbard model. As noted in Ref. [2] and in the previous chapter, such a boson system has a preference for collectively populating the states of momentum $\pm\pi/2$ (in units of the inverse lattice spacing). The main feature of the kinetic driving and the cat states which it generates, are several mechanisms that offer protection from collapse.

The exploration of the cat-like nature of the ground state has provided a deeper understanding of the atypical many-body problem it was based on. It is fortunate that the ring system can be approximated by a Hamiltonian that has properties already encoun-

tered in the Richardson-Gaudin model, for medium and large driving amplitudes. The effective system also includes an attractive interaction in momentum space [288] and a peculiar pairing rule that links momenta $k, \pi - k$ (instead of the conventional $k, -k$). This unusual pairing interaction gives rise to a modified depletion cloud which is shared by the two condensate branches and which is called a "reduction cloud" to clearly distinguish it from the qualitatively different depletion cloud of the conventional, undriven BH model.

The simplified toy model just described does not apply so well to the boson gas between hard walls. Yet many of its features can still be qualitatively understood in terms of an ensemble of atoms with highly correlated momenta. This picture is quantitatively confirmed by analyzing the many-body ground state in the representation of truncated plane waves (see Fig. 5.10). The case of harmonic confinement was also studied and the same structure of many atoms with a high momentum correlation was found, which underlines the robustness of the effect.

The aspects of the ground state that have been investigated include its intrinsic quality as a cat state, the feasibility of its preparation, and its resistance to collapse. The emerging picture is that of a boson system whose ground doublet is formed by two cat-like states. It must be asserted that the ground states' preparation is feasible, its cat quality is acceptable and its resilience to collapse is remarkable.

The cat branches differ in the momentum that is macroscopically occupied. Despite their nonzero momentum, each cat branch has, separately, a zero average current. This counterintuitive result is directly linked to the exotic character of the effective Hamiltonian, which results in an atypical current operator as well. The atom momenta can be measured in a time-of-flight experiment, since upon removal of the confining optical lattice the crystal momentum within the lattice becomes the linear momentum in free space. In such an experiment the majority of atoms are expected to flock in a given direction that varies randomly from run to run. In such a scenario one could investigate the statistics of correlations between detected momenta at different times, thus probing the reduction cloud of the fragmented condensate and its resulting correlations.

In the presence of a finite effective flux, the kinetically driven boson gas displays a nonzero current whose very existence is crucially dependent on the presence of the reduction cloud. This may be viewed as a new form of superfluidity. There are two main differences with conventional superfluidity which were identified so far. First of all, the pairing in the reduction cloud binds particles with momenta k and $\pi - k$, unlike in the conventional case, where pair particles have momenta k, $-k$. Secondly, in the conventional case, the condensate is able to carry current by itself, the depletion cloud being necessary only for making that current robust, which is the essence of superfluidity. In the system investigated here, preliminary results (which have not been reported here in detail) suggest that a non-zero current in the presence of an external flux is obtained only from the interference between the reduction cloud and the (condensate) branches of the cat state.

The present work paves the way for the study of a novel class of low-energy robust cat states that can be realized in cold atom setups and other similar systems.

Conclusions and Outlook

This thesis has investigated three highly intriguing systems that have time periodic variation as a central feature.

In Chapter 2 shaking was used as a means to create a uniform synthetic magnetic field for ultra cold atoms in a square optical lattice. Various driving schemes were investigated and compared. The comparison of the shaking protocols exposed their various strengths and weaknesses with regard to potential experimental implementations. Various gauge transformations, which helped in the derivation of the effective Hamiltonians, as well as transformations representing a change of a frame of reference, were identified.

These results support the conclusion that no simple continuous shaking protocol can produce a strictly uniform field and therefore more involved schemes, such as split driving protocols, are required.

The two-step split driving scheme with a sinusoidal waveform performs well for small values of the driving parameter but, as the driving parameter is increased, it produces visibly distorted spectra when compared to the Hofstadter butterfly. Small values of the driving parameter imply that the dynamics in the shaken system are slower than those in the static system. In an experimental implementation, this leads to long observation times that can be problematic because of heating.

The four-step split driving protocol produces spectra that are in excellent agreement with the Hofstadter butterfly. It performs well over a broad range of driving parameters and, in particular, for larger values of the effective hopping amplitude when compared to the two-step sinusoidal shaking. This fixes the shortcoming of slow system dynamics.

The two-step kicked driving scheme improves the sinusoidal wave-form at the expense of producing strong isolated discontinuities in the magnetic flux.

There are several subjects of further study that would complement the research presented in this chapter. An experimentally relevant factor would be the inclusion of interactions and the heating that is caused by the shaking. As mentioned at the end of Chapter 2, this research could be extended to other lattice geometries and possibly even three dimensions.

The theme of magnetic fields and, more broadly, that of gauge potentials was continued in Chapter 3. It focused on a rapidly oscillating charge in a magnetic monopole. This Floquet magnetic monopole is purely hypothetical, but recent advances in designing and creating artificial gauge potentials might make the realization of such a system possible. Some foundations were laid in the analysis of this system and the spectrum of a charge coupled to such a monopole was derived. This system is the subject of an on-going investigation with the goal of identifying and calculating gauge invariant quantities such as the scattering cross section.

Chapters 4 and 5 continue the investigation of unusual Floquet systems. Here, a

Bose-Hubbard chain with a time periodically modulated kinetic energy was studied.

In the ring, the system produces a very interesting transition from a Mott insulator to a fragmented superfluid that condenses at non-zero momenta. In position space, the effective model describing the system produces a multitude of local and non-local interactions as well as correlated hoppings. This complexity was manageable in the Mott insulating regime, but a more involved approach based on the momentum representation was required to explain the features of the superfluid. In the end, it was concluded that the state in the superfluid regime is best described by a Schrödinger cat state.

The formation of this state and its properties were at the center of Chapter 5. Its formation is explained as resulting from the interplay of on-site attractive interactions in momentum space and a pairing interaction term. The analysis also exposes the role of a special type of depletion cloud, labeled as the reduction cloud, and which is shared by both condensates.

The ground state was investigated with respect to its intrinsic quality as a cat state, the feasibility of its preparation, and its resistance to collapse. A picture of a boson system emerges whose ground doublet is formed by two cat-like states. It can be fairly asserted that their quality and preparation feasibility are acceptable and its resilience to collapse is remarkable.

In the presence of a finite effective flux, the kinetically driven boson gas displays a non-zero current whose sheer existence depends crucially on the presence of the reduction cloud. This may be viewed as a new form of superfluidity. The highly interesting mechanism responsible for supporting superfluidity in the kinetically driven boson gas is actively being investigated. This subject is a natural and exciting extension of the work presented here.

There are many other possible extensions of the work on kinetically driven boson gases: A rigorous investigation of the thermodynamic limit; a study of different waveforms of the driving; the effects of kinetic driving in two or more dimensions; boson mixtures; and a more comprehensive study of the decoherence of the cat-like ground state.

As mentioned in the introduction, this thesis has focused solely on bosons, so another logical and exciting extension of the present work would be the investigation of similar questions in fermion systems.

Finally, the experimental implementation of the peculiar kinetic driving presented in this thesis would be highly intriguing, because it would reveal whether or not the intriguing properties that have been discovered theoretically can be replicated in the real world.

Appendix

Numerical methods

General remarks

A brief overview of the numerical methods used in this thesis will be provided here. The two languages that were chosen to perform most of the numerical computations are *Python* [371] and *Fortran*. *Python* is an interpreted (no compilation step), general purpose language. Because *Python* is a strongly and dynamically typed language with high level features, it is ideal for quickly implementing ideas and prototyping algorithms.

These characteristics also make it a powerful scripting language that can be used to interface with programs written and compiled in other languages. *Python* comes with very well-developed and documented scientific libraries, as well as libraries for data visualization. The two scientific libraries essential to this thesis were *NumPy* [244] and *SciPy* [104]. Data visualization in this thesis was performed with the *Matplotlib* library [372].

Despite the performance features of *NumPy* and *SciPy*, Python is slow when large dense matrices have to be generated from scratch. *Fortran* was chosen to complement *Python* to compensate for this shortcoming. In some instances an increase in speed of 100× or better was achieved by switching to *Fortran*.

Fortunately, *NumPy* contains the module "f2py" (*Fortran* to *Python*) that allows for a simple compiling and wrapping of *Fortran* subroutines, so that they can be imported and executed within a *Python* script. This allowed for the seamless generation and handling of large matrices with *Fortran* subroutines and their subsequent processing with the convenience of *Python*. This interplay between the two languages also facilitated the prototyping of algorithms with *Python* and their implementation in *Fortran*.

Another major benefit of *Python* and *Fortran* are their cross platform capabilities. Most of the scripts and *Fortran* routines for this thesis were written on a *Windows* machine. The compilers and interpreters for both languages work just as well, if not better on *Unix* based machines. This meant that it was no problem to use the same unmodified code developed on a *Windows* machine on a cloud computing instance with *Linux*.

The rapid and efficient deployment of both languages was facilitated by using the free student edition of *Pycharm*. *Pycharm* is an integrated development environment (IDE) that supports window splitting, automatic indentation, code completion, and many more advanced features that help in writing and executing *Python* scripts.

Some resource intensive calculations were outsourced to cloud computing platforms such as Amazon's aws cloud computing services (*aws.amazon.com*) and sabalcore (*sabalcore.com*). The first one offers free and for-pay services whereas the second had an offer

of 500 core hours of free usage for students.

Specific numerical methods

In the early stages of this work, *QuTiP* [373] was an immensely useful library for both quickly grasping principles of scientific programming in the context of quantum mechanics and quickly generating results without in-depth knowledge of the various algorithms and routines. This is an honorable mention, since *QuTiP* was not used to generate published results and was discarded in favor of more specialized tools early on in the thesis.

The numerical methods used frequently that were not written from scratch are eigensolver routines integrated in *NumPy* and *SciPy*. For full exact diaogonalization the "linalg.eig" routine of *NumPy* was used. For determining only the lowest few eigenvalues and eigenstates the "sparse.linalg.eigsh" solver (implicitly restarted arnoldi method by [245]) of *SciPy* was employed.

Three different methods for time evolution purposes were used throughout the thesis: The first is a self implemented Runge-Kutta-Fehlberg method (RKF45) with step size control in Fortran (described in Ref. [49]), the second is the explicit Runge-Kutta method of order $8(5,3)$ [103] provided by the integrate module of *Python*'s *SciPy* library ("integrate.ode") and the third is the "integrate.odeint" routine of the same module.

Remarks Hilbert space basis and Hamiltonian construction

Two items that produced significant improvements in the speed of my calculations will be commented on briefly here. Both of them might be of relevance for projects that deal with small-sized bosonic systems. The Hilbert space basis in this thesis was constructed with an amazingly simple recursively defined (*Python*-)function

```
def basis(L,N):
    if L == 1 :
        yield [N, ]
    else :
        for j in range(N+1):
            for i in basis(L-1,N-j):
                yield [j,]+i
```

where L is the number of sites in a lattice and N the number of particles. Mark A. Valdez made me aware of this method, for which I am forever grateful, because it replaced a cumbersome and slow explicit algorithm that I wrote myself. Unfortunately I could not find the original author.

All operators and Hamiltonians whose representation in a given basis could not be simply derived by hand required a numerical evaluation of their matrix elements. To make these calculations efficient, a quick referencing of a basis state was required. This was accomplished with a very simple hashing scheme. In order to identify a basis vector

with a number, its Fock representation was complimented with a one at the beginning:

$$\begin{array}{lcl} & \vdots & \\ |0,1,2,0,0,3,0,2\rangle & \rightarrow & 101200302 \\ |0,1,2,0,0,3,1,1\rangle & \rightarrow & 101200311 \\ |0,1,1,1,0,3,1,1\rangle & \rightarrow & 101110311 \\ & \vdots & \end{array}$$

This scheme allowed for a quick lookup of the basis vectors and it did not require any binning, due to the small numbers involved.

Bibliography

[1] C. E. Creffield, G. Pieplow, F. Sols, and N. Goldman, New J. Phys. **18**, 093013 (2016).

[2] G. Pieplow, F. Sols, and C. E. Creffield, New J. Phys. **20**, 073045 (2018).

[3] G. Pieplow, C. Creffield, and F. Sols, arXiv:1905.13596 (2019).

[4] K. B. Davis, M. O. Mewes, M. R. Andrews, N. J. van Druten, D. S. Durfee, D. M. Kurn, and W. Ketterle, Phys. Rev. Lett. **75**, 3969 (1995).

[5] M. H. Anderson, J. R. Ensher, M. R. Matthews, C. E. Wieman, and E. A. Cornell, Science **269**, 198 (1995).

[6] A. Einstein, Preuss. Akad. Wiss. phys. math. (1924).

[7] P. A. Altin, M. T. Johnsson, V. Negnevitsky, G. R. Dennis, R. P. Anderson, J. E. Debs, S. S. Szigeti, K. S. Hardman, S. Bennetts, G. D. McDonald, L. D. Turner, J. D. Close, and N. P. Robins, New J. Phys. **15**, 023009 (2013).

[8] S. Abend, M. Gebbe, M. Gersemann, H. Ahlers, H. Müntinga, E. Giese, N. Gaaloul, C. Schubert, C. Lämmerzahl, W. Ertmer, W. Schleich, and E. Rasel, Phys. Rev. Lett. **117** (2016).

[9] K. Hardman, P. Everitt, G. McDonald, P. Manju, P. Wigley, M. Sooriyabandara, C. Kuhn, J. Debs, J. Close, and N. Robins, Phys. Rev. Lett. **117** (2016).

[10] P. Asenbaum, C. Overstreet, T. Kovachy, D. D. Brown, J. M. Hogan, and M. A. Kasevich, Phys. Rev. Lett. **118** (2017).

[11] D. Rätzel, R. Howl, J. Lindkvist, and I. Fuentes, New J. Phys. **20**, 073044 (2018).

[12] I. Bloch, Nat. Phys. **1**, 23 (2005).

[13] H. Price, O. Zilberberg, T. Ozawa, I. Carusotto, and N. Goldman, Phys. Rev. Lett. **115** (2015).

[14] C. Becker, P. Soltan-Panahi, J. Kronjäger, S. Dörscher, K. Bongs, and K. Sengstock, New J. Phys. **12**, 065025 (2010).

[15] B. Zimmermann, T. Müller, J. Meineke, T. Esslinger, and H. Moritz, New J. Phys. **13**, 043007 (2011).

[16] G.-B. Jo, J. Guzman, C. K. Thomas, P. Hosur, A. Vishwanath, and D. M. Stamper-Kurn, Phys. Rev. Lett. **108** (2012).

[17] M. Lewenstein, A. Sanpera, and V. Ahufinger, *Ultracold Atoms in Optical Lattices: Simulating quantum many-body systems* (Oxford University Press, 2012).

[18] S. Inouye, M. R. Andrews, J. Stenger, H.-J. Miesner, D. M. Stamper-Kurn, and W. Ketterle, Nature **392**, 151 (1998).

[19] M. Lewenstein, A. Sanpera, V. Ahufinger, B. Damski, A. Sen, and U. Sen, Adv. Phys. **56**, 243 (2007).

[20] J. Hubbard, Proc. Royal Soc. Lond. A **276**, 238 (1963).

[21] H. A. Gersch and G. C. Knollman, Phys. Rev. **129**, 959 (1963).

[22] D. Jaksch, C. Bruder, J. I. Cirac, C. W. Gardiner, and P. Zoller, Phys. Rev. Lett. **81**, 3108 (1998).

[23] M. Greiner, O. Mandel, T. Esslinger, T. W. Hänsch, and I. Bloch, Nature **415**, 39 (2002).

[24] R. P. Feynman, Int. Jour. Theor. Phys. **21**, 467 (1982).

[25] K. Madison, C. Bharucha, P. Morrow, S. Wilkinson, Q. Niu, B. Sundaram, and M. Raizen, Appl. Phys. B **65**, 693 (1997).

[26] J. R. Sanmartin, Am. J. Phys. **52**, 937 (1984).

[27] K. Y. Billah and R. H. Scanlan, Am. J. Phys. **59**, 118 (1991).

[28] G. W. Hill, Acta Math. **8**, 1 (1886).

[29] W. Magnus and S. Winkler, *Hill's equation* (Courier Corporation, 2013).

[30] W. D. Phillips, J. V. Prodan, and H. J. Metcalf, JOSA B **2**, 1751 (1985).

[31] A. Aspect, J. Dalibard, A. Heidmann, C. Salomon, and C. Cohen-Tannoudji, Phys. Rev. Lett. **57**, 1688 (1986).

[32] J. Dalibard and C. Cohen-Tannoudji, JOSA B **6**, 2023 (1989).

[33] W. S. Bakr, J. I. Gillen, A. Peng, S. Fölling, and M. Greiner, Nature **462**, 74 (2009).

[34] J. F. Sherson, C. Weitenberg, M. Endres, M. Cheneau, I. Bloch, and S. Kuhr, Nature **467**, 68 (2010).

[35] J. P. Dowling and G. J. Milburn, Philos. Trans. Royal Soc. A **361**, 1655 (2003).

[36] A. Eckardt, Rev. Mod. Phys. **89**, 011004 (2017).

[37] R. Blatt and C. F. Roos, Nat. Phys. **8**, 277 (2012).

[38] A. A. Houck, H. E. Türeci, and J. Koch, Nat. Phys. **8**, 292 (2012).

[39] A. Aspuru-Guzik and P. Walther, Nat. Phys. **8**, 285 (2012).

[40] I. Bloch, J. Dalibard, and W. Zwerger, Rev. Mod. Phys. **80**, 885 (2008).

[41] D. Jaksch and P. Zoller, New J. Phys. **5**, 56 (2003).

[42] N. Goldman, J. Budich, and P. Zoller, Nat. Phys. **12**, 639 (2016).

[43] D. Xiao, M.-C. Chang, and Q. Niu, Rev. Mod. Phys. **82**, 1959 (2010).

[44] E. Zohar, J. I. Cirac, and B. Reznik, Rep. Prog. Phys. **79**, 014401 (2015).

[45] G. Teschl, *Ordinary differential equations and dynamical systems*, Vol. 140 (American Mathematical Soc., 2012).

[46] G. Floquet, Ann. ENS **12**, 47 (1883).

[47] F. Bloch, Z. Phys. **52**, 555 (1929).

[48] E. Mathieu, *Traité de physique mathématique...*, Vol. 3 (Gauthier-Villars, 1885).

[49] W. H. Press, B. P. Flannery, S. A. Teukolsky, and T. V. William, *Numerical Recipes in FORTRAN 77* (Cambridge University Press, 1992).

[50] L. Ruby, Am. J. Phys. **64**, 39 (1996).

[51] P. Kapitza, J. Exp. Theor. Phys. **21**, 588 (1951).

[52] F. Phelps III and J. Hunter Jr, Am. J. Phys. **33**, 285 (1965).

[53] S. Humphries, *Principles of charged particle acceleration* (Courier Corporation, 2013).

[54] W. Paul, H. Reinhard, and U. Von Zahn, Z. Phys. **152**, 143 (1958).

[55] J. L. Massera and J. J. Schaffer, Ann. Math. **69**, 88 (1959).

[56] D. P. Williams, lecture notes (2008).

[57] N. Goldman and J. Dalibard, Phys. Rev. X **4**, 031027 (2014).

[58] S. Rahav, I. Gilary, and S. Fishman, Phys. Rev. A **68**, 013820 (2003).

[59] M. Bukov, L. D'Alessio, and A. Polkovnikov, Adv. Phys. **64**, 139 (2015).

[60] F. Grossmann, T. Dittrich, P. Jung, and P. Hänggi, Phys. Rev. Lett. **67**, 516 (1991).

[61] K. Drese and M. Holthaus, Chem. Phys. **217**, 201 (1997).

[62] M. Grifoni and P. Hänggi, Phys. Rep. **304**, 229 (1998).

[63] A. Eckardt, M. Holthaus, H. Lignier, A. Zenesini, D. Ciampini, O. Morsch, and E. Arimondo, Phys. Rev. A **79**, 013611 (2009).

[64] D. H. Dunlap and V. M. Kenkre, Phys. Rev. B **34**, 3625 (1986).

[65] H. Lignier, C. Sias, D. Ciampini, Y. Singh, A. Zenesini, O. Morsch, and E. Arimondo, Phys. Rev. Lett. **99**, 220403 (2007).

[66] C. Sias, H. Lignier, Y. P. Singh, A. Zenesini, D. Ciampini, O. Morsch, and E. Arimondo, Phys. Rev. Lett. **100**, 040404 (2008).

[67] A. Zenesini, H. Lignier, D. Ciampini, O. Morsch, and E. Arimondo, Phys. Rev. Lett. **102** (2009).

[68] A. Zenesini, H. Lignier, C. Sias, O. Morsch, D. Ciampini, and E. Arimondo, Laser Physics **20**, 1182 (2010).

[69] E. Michon, C. Cabrera-Gutiérrez, A. Fortun, M. Berger, M. Arnal, V. Brunaud, J. Billy, C. Petitjean, P. Schlagheck, and D. Guéry-Odelin, New J. Phys. **20**, 053035 (2018).

[70] A. Eckardt, C. Weiss, and M. Holthaus, Phys. Rev. Lett. **95**, 260404 (2005).

[71] C. E. Creffield and T. S. Monteiro, Phys. Rev. Lett. **96**, 210403 (2006).

[72] P. Zhang, N. K. Efremidis, A. Miller, Y. Hu, and Z. Chen, Opt. Lett. **35**, 3252 (2010).

[73] A. Eckardt and E. Anisimovas, New J. Phys. **17**, 093039 (2015).

[74] T. Giamarchi, *Quantum physics in one dimension*, Vol. 121 (Clarendon press, 2003).

[75] S. R. Wilkinson, C. F. Bharucha, K. W. Madison, Q. Niu, and M. G. Raizen, Phys. Rev. Lett. **76**, 4512 (1996).

[76] A. Eckardt and M. Holthaus, EPL **80**, 50004 (2007).

[77] V. V. Ivanov, A. Alberti, M. Schioppo, G. Ferrari, M. Artoni, M. L. Chiofalo, and G. M. Tino, Phys. Rev. Lett. **100**, 043602 (2008).

[78] H. Fukuyama, R. A. Bari, and H. C. Fogedby, Phys. Rev. B **8**, 5579 (1973).

[79] M. Abramowitz and I. A. Stegun, *Handbook of mathematical functions: with formulas, graphs, and mathematical tables*, Vol. 55 (Courier Corporation, 1965).

[80] E. E. Mendez and G. Bastard, Phys. Today **46**, 34 (1993).

[81] P. K. Tien and J. P. Gordon, Phys. Rev. **129**, 647 (1963).

[82] C. E. Creffield and F. Sols, Phys. Rev. Lett. **100**, 250402 (2008).

[83] A. R. Kolovsky and H. J. Korsch, arXiv:0912.2587 (2009).

[84] C. E. Creffield and F. Sols, Phys. Rev. A **84**, 023630 (2011).

[85] R. Peierls, Z. Phys. **80**, 763 (1933).

[86] E. Haller, R. Hart, M. J. Mark, J. G. Danzl, L. Reichsöllner, and H.-C. Nägerl, Phys. Rev. Lett. **104**, 200403 (2010).

[87] I. B. Spielman, Phys. Rev. A **79**, 063613 (2009).

[88] M. Aidelsburger, M. Atala, S. Nascimbène, S. Trotzky, Y.-A. Chen, and I. Bloch, Phys. Rev. Lett. **107**, 255301 (2011).

[89] M. Aidelsburger, M. Atala, M. Lohse, J. T. Barreiro, B. Paredes, and I. Bloch, Phys. Rev. Lett. **111**, 185301 (2013).

[90] M. Aidelsburger, M. Lohse, C. Schweizer, M. Atala, J. T. Barreiro, S. Nascimbene, N. Cooper, I. Bloch, and N. Goldman, Nat. Phys. **11**, 162 (2015).

[91] H. Miyake, G. A. Siviloglou, C. J. Kennedy, W. C. Burton, and W. Ketterle, Phys. Rev. Lett. **111**, 185302 (2013).

[92] A. Celi, P. Massignan, J. Ruseckas, N. Goldman, I. B. Spielman, G. Juzeliūnas, and M. Lewenstein, Phys. Rev. Lett. **112**, 043001 (2014).

[93] B. Stuhl, H.-I. Lu, L. Aycock, D. Genkina, and I. Spielman, Science **349**, 1514 (2015).

[94] C. E. Creffield and G. Sierra, Phys. Rev. A **91**, 063608 (2015).

[95] L. DAlessio and A. Polkovnikov, Ann. Phys. **333**, 19 (2013).

[96] L. D'Alessio and M. Rigol, Phys. Rev. X **4**, 041048 (2014).

[97] A. Lazarides, A. Das, and R. Moessner, Phys. Rev. E **90**, 012110 (2014).

[98] T. Mori, Phys. Rev. A **91**, 020101 (2015).

[99] P. Ponte, A. Chandran, Z. Papić, and D. A. Abanin, Ann. Phys. **353**, 196 (2015).

[100] A. Eckardt and M. Holthaus, Phys. Rev. Lett. **101**, 245302 (2008).

[101] W. Magnus, Commun. Pure Appl. Math. **7**, 649 (1954).

[102] S. Blanes, F. Casas, J. Oteo, and J. Ros, Phys. Rep. **470**, 151 (2009).

[103] E. Hairer, S. P. Nørsett, and G. Wanner, *Solving ordinary differential equations I: nonstiff problems*, Vol. 8 (Springer Science & Business Media, 2008).

[104] E. Jones, T. Oliphant, and P. Peterson, (2014).

[105] T. Haga, arXiv:1903.00195 (2019).

[106] D. W. Hone, R. Ketzmerick, and W. Kohn, Phys. Rev. A **56**, 4045 (1997).

[107] D. Poletti and C. Kollath, Phys. Rev. A **84**, 013615 (2011).

[108] D. A. Abanin, W. De Roeck, and F. Huveneers, Phys. Rev. Lett. **115**, 256803 (2015).

[109] T. Mori, T. Kuwahara, and K. Saito, Phys. Rev. Lett. **116**, 120401 (2016).

[110] D. A. Abanin, W. De Roeck, W. W. Ho, and F. Huveneers, Phys. Rev. B **95**, 014112 (2017).

[111] K. H. Baines, T. W. Momary, L. N. Fletcher, A. P. Showman, M. Roos-Serote, R. H. Brown, B. J. Buratti, R. N. Clark, and P. D. Nicholson, Planet. Space Sci. **57**, 1671 (2009).

[112] A. C. B. Aguiar, P. L. Read, R. D. Wordsworth, T. Salter, and Y. H. Yamazaki, Icarus **206**, 755 (2010).

[113] M. Weisberg, *Simulation and similarity: Using models to understand the world* (Oxford University Press, 2012).

[114] S. Huerta, Archit. Sci. Rev. **49**, 324 (2006).

[115] T. Häner and D. S. Steiger, in *Proc. Int. Conf. HPC* (ACM, 2017) p. 33.

[116] E. Pednault, J. A. Gunnels, G. Nannicini, L. Horesh, T. Magerlein, E. Solomonik, and R. Wisnieff, arXiv:1710.05867 (2017).

[117] C. V. Networking, (2016).

[118] S. Lloyd, Science **273**, 1073 (1996).

[119] I. Buluta and F. Nori, Science **326**, 108 (2009).

[120] J. I. Cirac and P. Zoller, Nat. Phys. **8**, 264 (2012).

[121] I. Georgescu, S. Ashhab, and F. Nori, Rev. Mod. Phys. **86**, 153 (2014).

[122] A. Daley, Int. School Phys. **198**, 55 (2018).

[123] R. Somma, G. Ortiz, J. E. Gubernatis, E. Knill, and R. Laflamme, Phys. Rev. A **65**, 042323 (2002).

[124] B. P. Lanyon, C. Hempel, D. Nigg, M. Müller, R. Gerritsma, F. Zähringer, P. Schindler, J. T. Barreiro, M. Rambach, G. Kirchmair, *et al.*, Science **334**, 57 (2011).

[125] L. M. Sieberer, T. Olsacher, A. Elben, M. Heyl, P. Hauke, F. Haake, and P. Zoller, arXiv:1812.05876 (2018).

[126] J. Benhelm, G. Kirchmair, C. F. Roos, and R. Blatt, Nat. Phys. **4**, 463 (2008).

[127] V. Schäfer, C. Ballance, K. Thirumalai, L. Stephenson, T. Ballance, A. Steane, and D. Lucas, Nature **555**, 75 (2018).

[128] I. Bloch, J. Dalibard, and S. Nascimbene, Nat. Phys. **8**, 267 (2012).

[129] C. Gross and I. Bloch, Science **357**, 995 (2017).

[130] D. G. Angelakis, Quantum Sci. Technol. (2017).

[131] P. Roushan, C. Neill, J. Tangpanitanon, V. Bastidas, A. Megrant, R. Barends, Y. Chen, Z. Chen, B. Chiaro, A. Dunsworth, *et al.*, Science **358**, 1175 (2017).

[132] D. R. Hofstadter, Phys. Rev. B **14**, 2239 (1976).

[133] D. Osadchy and J. E. Avron, J. Math. Phys. **42**, 5665 (2001).

[134] C. R. Dean, L. Wang, P. Maher, C. Forsythe, F. Ghahari, Y. Gao, J. Katoch, M. Ishigami, P. Moon, M. Koshino, T. Taniguchi, K. Watanabe, K. L. Shepard, J. Hone, and P. Kim, Nature **497**, 598 (2013).

[135] M. Nakahara, *Geometry, topology and physics* (CRC Press, 2003).

[136] M. V. Berry, Proc. Royal Soc. Lond. A **392**, 45 (1984).

[137] D. J. Thouless, M. Kohmoto, M. P. Nightingale, and M. den Nijs, Phys. Rev. Lett. **49**, 405 (1982).

[138] F. Gerbier and J. Dalibard, New J. Phys. **12**, 033007 (2010).

[139] A. R. Kolovsky, EPL **93**, 20003 (2011).

[140] J. Struck, C. Ölschläger, M. Weinberg, P. Hauke, J. Simonet, A. Eckardt, M. Lewenstein, K. Sengstock, and P. Windpassinger, Phys. Rev. Lett. **108** (2012).

[141] J. Struck, M. Weinberg, C. Ölschläger, P. Windpassinger, J. Simonet, K. Sengstock, R. Höppner, P. Hauke, A. Eckardt, M. Lewenstein, and L. Mathey, Nat. Phys. **9**, 738 (2013).

[142] P. Hauke, O. Tieleman, A. Celi, C. Ölschläger, J. Simonet, J. Struck, M. Weinberg, P. Windpassinger, K. Sengstock, M. Lewenstein, and A. Eckardt, Phys. Rev. Lett. **109** (2012).

[143] H. Miyake, G. A. Siviloglou, C. J. Kennedy, W. C. Burton, and W. Ketterle, Phys. Rev. Lett. **111** (2013).

[144] M. Aidelsburger, M. Atala, M. Lohse, J. T. Barreiro, B. Paredes, and I. Bloch, Phys. Rev. Lett. **111** (2013).

[145] G. Jotzu, M. Messer, R. Desbuquois, M. Lebrat, T. Uehlinger, D. Greif, and T. Esslinger, Nature **515**, 237 (2014).

[146] J. Dalibard, F. Gerbier, G. Juzeliūnas, and P. Öhberg, Rev. Mod. Phys. **83**, 1523 (2011).

[147] N. Goldman, G. Juzeliūnas, P. Öhberg, and I. B. Spielman, Rep. Prog. Phys. **77**, 126401 (2014).

[148] N. R. Cooper, J. Dalibard, and I. B. Spielman, Rev. Mod. Phys. **91**, 015005 (2019).

[149] K. Fang, Z. Yu, and S. Fan, Nat. Photonics **6**, 782 (2012).

[150] M. Hafezi, S. Mittal, J. Fan, A. Migdall, and J. M. Taylor, Nat. Photonics **7**, 1001 (2013).

[151] M. C. Rechtsman, J. M. Zeuner, Y. Plotnik, Y. Lumer, D. Podolsky, F. Dreisow, S. Nolte, M. Segev, and A. Szameit, Nature **496**, 196 (2013).

[152] L. Lu, J. D. Joannopoulos, and M. Soljačić, Nat. Photonics **8**, 821 (2014).

[153] T. Dubček, K. Lelas, D. Jukić, R. Pezer, M. Soljačić, and H. Buljan, New J. Phys. **17**, 125002 (2015).

[154] D. Yang, G. S. Giri, M. Johanning, C. Wunderlich, P. Zoller, and P. Hauke, Phys. Rev. A **94** (2016).

[155] A. Bermudez, T. Schaetz, and D. Porras, New J. Phys. **14**, 053049 (2012).

[156] W. Hu, J. C. Pillay, K. Wu, M. Pasek, P. P. Shum, and Y. Chong, Phys. Rev. X **5** (2015).

[157] V. Peano, C. Brendel, M. Schmidt, and F. Marquardt, Phys. Rev. X **5** (2015).

[158] R. Susstrunk and S. D. Huber, Science **349**, 47 (2015).

[159] G. Salerno, T. Ozawa, H. M. Price, and I. Carusotto, Phys. Rev. B **93** (2016).

[160] M. Aidelsburger, S. Nascimbene, and N. Goldman, C R Phys. **19**, 394 (2018).

[161] C. E. Creffield and F. Sols, Phys. Rev. A **90** (2014).

[162] S. Mukherjee, A. Spracklen, D. Choudhury, N. Goldman, P. Öhberg, E. Andersson, and R. R. Thomson, New J. Phys. **17**, 115002 (2015).

[163] S. Mukherjee, A. Spracklen, M. Valiente, E. Andersson, P. Öhberg, N. Goldman, and R. R. Thomson, Nat. Commun. **8**, 13918 (2017).

[164] N. Marzari, A. A. Mostofi, J. R. Yates, I. Souza, and D. Vanderbilt, Rev. Mod. Phys. **84**, 1419 (2012).

[165] B. MacGregor, A. McCoy, and S. Wickramasekara, Ann. Phys. **327**, 2310 (2012).

[166] W. Klink, Ann. Phys. **260**, 27 (1997).

[167] J. Dalibard, "Cours du collège de france, chapitre 4," (2013).

[168] W. H. Klink and S. Wickramasekara, Ann. Phys. **336**, 261 (2013).

[169] D. M. Greenberger, Phys. Rev. Lett. **87**, 100405 (2001).

[170] C. E. Creffield and F. Sols, EPL **101**, 40001 (2013).

[171] A. S. Sørensen, E. Demler, and M. D. Lukin, Phys. Rev. Lett. **94** (2005).

[172] Z.-F. Xu, L. You, and M. Ueda, Phys. Rev. A **87** (2013).

[173] B. M. Anderson, I. B. Spielman, and G. Juzeliūnas, Phys. Rev. Lett. **111** (2013).

[174] H. M. Price, O. Zilberberg, T. Ozawa, I. Carusotto, and N. Goldman, Phys. Rev. B **93**, 245113 (2016).

[175] Y. Hatsugai, T. Fukui, and H. Aoki, Phys. Rev. B **74** (2006).

[176] A. Górecka, B. Grémaud, and C. Miniatura, Phys. Rev. A **84** (2011).

[177] L. Tarruell, D. Greif, T. Uehlinger, G. Jotzu, and T. Esslinger, Nature **483**, 302 (2012).

[178] S. K. Baur, M. H. Schleier-Smith, and N. R. Cooper, Phys. Rev. A **89** (2014).

[179] P. A. M. Dirac, Proc. Royal Soc. Lond. A **133**, 60 (1931).

[180] K. A. Milton, Rep. Prog. Phys. **69**, 1637 (2006).

[181] Y. M. Shnir, *Magnetic Monopoles* (Springer Berlin Heidelberg, 2005).

[182] S. F. Edward Teller, Hans Mark, *Properties of matter under unusual conditions* (Interscience Publishers, 1969) p. 349.

[183] G. t Hooft, Nucl. Phys. B **79**, 276 (1974).

[184] T. W. B. Kibble, J. Phys. A **9**, 1387 (1976).

[185] Y. Zeldovich and M. Khlopov, Phys. Lett. B **79**, 239 (1978).

[186] J. P. Preskill, Phys. Rev. Lett. **43**, 1365 (1979).

[187] P. Langacker and S.-Y. Pi, Phys. Rev. Lett. **45**, 1 (1980).

[188] A. H. Guth and S. H. H. Tye, Phys. Rev. Lett. **44**, 631 (1980).

[189] M. S. Turner, E. N. Parker, and T. J. Bogdan, Phys. Rev. D **26**, 1296 (1982).

[190] T. W. Kephart and T. J. Weiler, Astropart. Phys. **4**, 271 (1996).

[191] Y. Cho, EPJ Web. Conf. **182**, 02030 (2018).

[192] R. D. Sorkin, Phys. Rev. Lett. **51**, 87 (1983).

[193] Y. Cho and D. Maison, Phys. Lett. B **391**, 360 (1997).

[194] X.-G. Wen, Rev. Mod. Phys. **89**, 041004 (2017).

[195] W. Zurek, Phys. Rep. **276**, 177 (1996).

[196] M. Hermele, M. P. A. Fisher, and L. Balents, Phys. Rev. B **69** (2004).

[197] C. Castelnovo, R. Moessner, and S. L. Sondhi, Nature **451**, 42 (2008).

[198] X.-L. Qi, R. Li, J. Zang, and S.-C. Zhang, Science **323**, 1184 (2009).

[199] S.-Z. Lin and A. Saxena, Phys. Rev. B **93**, 060401 (2016).

[200] C. Wang and T. Senthil, Phys. Rev. X **6** (2016).

[201] E. Yakaboylu, A. Deuchert, and M. Lemeshko, Phys. Rev. Lett. **119** (2017).

[202] Q. Meier, M. Fechner, T. Nozaki, M. Sahashi, Z. Salman, T. Prokscha, A. Suter, P. Schoenherr, M. Lilienblum, P. Borisov, I. Dzyaloshinskii, M. Fiebig, H. Luetkens, and N. Spaldin, Phys. Rev. X **9** (2019).

[203] C. Nisoli, R. Moessner, and P. Schiffer, Rev. Mod. Phys. **85**, 1473 (2013).

[204] D. J. P. Morris, D. A. Tennant, S. A. Grigera, B. Klemke, C. Castelnovo, R. Moessner, C. Czternasty, M. Meissner, K. C. Rule, J.-U. Hoffmann, K. Kiefer, S. Gerischer, D. Slobinsky, and R. S. Perry, Science **326**, 411 (2009).

[205] T. Fennell, P. P. Deen, A. R. Wildes, K. Schmalzl, D. Prabhakaran, A. T. Boothroyd, R. J. Aldus, D. F. McMorrow, and S. T. Bramwell, Science **326**, 415 (2009).

[206] S. Nakosai and S. Onoda, J. Phys. Soc. Jpn. **88**, 053701 (2019).

[207] L. A. Mól, R. L. Silva, R. C. Silva, A. R. Pereira, W. A. Moura-Melo, and B. V. Costa, J. Appl. Phys. **106**, 063913 (2009).

[208] R. V. Hügli, G. Duff, B. O'Conchuir, E. Mengotti, L. J. Heyderman, A. F. Rodríguez, F. Nolting, and H. B. Braun, J. Appl. Phys. **111**, 07E103 (2012).

[209] C. Phatak and A. Petford-Long, Nano Lett. **18**, 6989 (2018).

[210] A. Farhan, M. Saccone, C. F. Petersen, S. Dhuey, R. V. Chopdekar, Y.-L. Huang, N. Kent, Z. Chen, M. J. Alava, T. Lippert, A. Scholl, and S. van Dijken, Sci. Adv. **5**, 6380 (2019).

[211] A. Béché, R. V. Boxem, G. V. Tendeloo, and J. Verbeeck, Nat. Phys. **10**, 26 (2013).

[212] P. Milde, D. Kohler, J. Seidel, L. M. Eng, A. Bauer, A. Chacon, J. Kindervater, S. Muhlbauer, C. Pfleiderer, S. Buhrandt, C. Schutte, and A. Rosch, Science **340**, 1076 (2013).

[213] V. Pietilä and M. Möttönen, Phys. Rev. Lett. **103**, 030401 (2009).

[214] K. Tiurev, P. Kuopanportti, and M. Möttönen, Phys. Rev. A **99** (2019).

[215] X.-F. Zhou, C. Wu, G.-C. Guo, R. Wang, H. Pu, and Z.-W. Zhou, Phys. Rev. Lett. **120** (2018).

[216] M. W. Ray, E. Ruokokoski, S. Kandel, M. Möttönen, and D. S. Hall, Nature **505**, 657 (2014).

[217] K. Osterloh, M. Baig, L. Santos, P. Zoller, and M. Lewenstein, Phys. Rev. Lett. **95** (2005).

[218] J. Ruseckas, G. Juzeliūnas, P. Öhberg, and M. Fleischhauer, Phys. Rev. Lett. **95** (2005).

[219] N. Goldman, A. Kubasiak, P. Gaspard, and M. Lewenstein, Phys. Rev. A **79** (2009).

[220] V. Pietilä and M. Möttönen, Phys. Rev. Lett. **102** (2009).

[221] S. Sugawa, F. Salces-Carcoba, A. R. Perry, Y. Yue, and I. B. Spielman, Science **360**, 1429 (2018).

[222] J.-H. Jiang, Phys. Rev. A **85** (2012).

[223] T. Dubček, C. J. Kennedy, L. Lu, W. Ketterle, M. Soljačić, and H. Buljan, Phys. Rev. Lett. **114** (2015).

[224] D.-W. Zhang, S.-L. Zhu, and Z. D. Wang, Phys. Rev. A **92** (2015).

[225] X.-Y. Mai, D.-W. Zhang, Z. Li, and S.-L. Zhu, Phys. Rev. A **95** (2017).

[226] Y. Yan and Q. Zhou, Phys. Rev. Lett. **120** (2018).

[227] C. Shang, Y. Zheng, and B. A. Malomed, Phys. Rev. A **97** (2018).

[228] J. A. Heras and G. Báez, Eur. J. Phys. **30**, 23 (2008).

[229] P. Jordan, Ann. Phys. **424**, 66 (1938).

[230] I. S. Gradshteyn and I. M. Ryzhik, *Table of integrals, series, and products* (Academic press, 2014).

[231] F. D. M. Haldane, Phys. Rev. Lett. **51**, 605 (1983).

[232] M. Greiter, Phys. Rev. B **83**, 115129 (2011).

[233] Á. Rapp, X. Deng, and L. Santos, Phys. Rev. Lett. **109**, 203005 (2012).

[234] M. Di Liberto, C. E. Creffield, G. Japaridze, and C. M. Smith, Phys. Rev. A **89**, 013624 (2014).

[235] C. Gaul, E. Díaz, R. P. Lima, F. Domínguez-Adame, and C. A. Müller, Phys. Rev. A **84**, 053627 (2011).

[236] F. Meinert, M. J. Mark, K. Lauber, A. J. Daley, and H.-C. Nägerl, Phys. Rev. Lett. **116**, 205301 (2016).

[237] O. Dutta, M. Gajda, P. Hauke, M. Lewenstein, D.-S. Lühmann, B. A. Malomed, T. Sowiński, and J. Zakrzewski, Rep. Prog. Phys. **78**, 066001 (2015).

[238] C. Sträter, S. C. L. Srivastava, and A. Eckardt, Phys. Rev. Lett. **117**, 205303 (2016).

[239] F. Wilczek, *Fractional statistics and anyon superconductivity*, Vol. 5 (World scientific, 1990).

[240] T. Stöferle, H. Moritz, C. Schori, M. Köhl, and T. Esslinger, Phys. Rev. Lett. **92**, 130403 (2004).

[241] C. Kollath, A. Iucci, T. Giamarchi, W. Hofstetter, and U. Schollwöck, Phys. Rev. Lett. **97**, 050402 (2006).

[242] A. Dirks, K. Mikelsons, H. Krishnamurthy, and J. Freericks, Phys. Rev. A **89**, 021602 (2014).

[243] L. Cardarelli, S. Greschner, and L. Santos, Phys. Rev. A **94**, 023615 (2016).

[244] S. Van Der Walt, S. C. Colbert, and G. Varoquaux, Comput. Sci. Eng. **13**, 22 (2011).

[245] R. B. Lehoucq, D. C. Sorensen, and C. Yang, *ARPACK users' guide: solution of large-scale eigenvalue problems with implicitly restarted Arnoldi methods*, Vol. 6 (Siam, 1998).

[246] T. Sowiński, Phys. Rev. A **85**, 065601 (2012).

[247] V. A. Kashurnikov and B. V. Svistunov, Phys. Rev. B **53**, 11776 (1996).

[248] M. A. Cazalilla, R. Citro, T. Giamarchi, E. Orignac, and M. Rigol, Rev. Mod. Phys. **83**, 1405 (2011).

[249] S. Tomonaga, Prog. Theor. Phys. **5**, 544 (1950).

[250] J. M. Luttinger, J. Math. Phys. **4**, 1154 (1963).

[251] F. D. M. Haldane, Phys. Rev. Lett. **47**, 1840 (1981).

[252] L. Landau, Phys. Rev. **60**, 356 (1941).

[253] T. D. Kühner, S. R. White, and H. Monien, Phys. Rev. B **61**, 12474 (2000).

[254] S. Ejima, H. Fehske, and F. Gebhard, EPL **93**, 30002 (2011).

[255] P. Pippan, H. G. Evertz, and M. Hohenadler, Phys. Rev. A **80** (2009).

[256] V. Novičenko, E. Anisimovas, and G. Juzeliūnas, Phys. Rev. A **95**, 023615 (2017).

[257] J. Struck, C. Ölschläger, M. Weinberg, P. Hauke, J. Simonet, A. Eckardt, M. Lewenstein, K. Sengstock, and P. Windpassinger, Phys. Rev. Lett. **108**, 225304 (2012).

[258] M. Reitter, J. Näger, K. Wintersperger, C. Sträter, I. Bloch, A. Eckardt, and U. Schneider, Phys. Rev. Lett. **119**, 200402 (2017).

[259] M. Bukov, S. Gopalakrishnan, M. Knap, and E. Demler, Phys. Rev. Lett. **115**, 205301 (2015).

[260] E. Schrödinger, Sci. Nat. **23**, 823 (1935).

[261] J. Von Neumann, *Mathematische Grundlagen der Quantenmechanik*, Grundlehren der mathematischen Wissenschaften (Dover, 1932).

[262] W. H. Zurek, Phys. Rev. D **26**, 1862 (1982).

[263] E. Joos and H. D. Zeh, Z. Phys. B **59**, 223 (1985).

[264] W. Zurek, Phys. Today **44**, 36 (1991).

[265] M. O. Scully and K. Drühl, Phys. Rev. A **25**, 2208 (1982).

[266] T. J. Herzog, P. G. Kwiat, H. Weinfurter, and A. Zeilinger, Phys. Rev. Lett. **75**, 3034 (1995).

[267] D. V. Strekalov, A. V. Sergienko, D. N. Klyshko, and Y. H. Shih, Phys. Rev. Lett. **74**, 3600 (1995).

[268] R. I. Khakimov, B. M. Henson, D. K. Shin, S. S. Hodgman, R. G. Dall, K. G. H. Baldwin, and A. G. Truscott, Nature **540**, 100 (2016).

[269] P. Ryczkowski, M. Barbier, A. T. Friberg, J. M. Dudley, and G. Genty, Nat. Photonics **10**, 167 (2016).

[270] Y.-H. Kim, R. Yu, S. P. Kulik, Y. Shih, and M. O. Scully, Phys. Rev. Lett. **84**, 1 (2000).

[271] Y. Aharonov, Science **307**, 875 (2005).

[272] Y. Aharonov, E. Cohen, D. Grossman, and A. Elizutr, EPJ Web. Conf. **70**, 00038 (2014).

[273] X.-S. Ma, J. Kofler, and A. Zeilinger, Rev. Mod. Phys. **88**, 015005 (2016).

[274] S. J. Freedman and J. F. Clauser, Phys. Rev. Lett. **28**, 938 (1972).

[275] A. Aspect, P. Grangier, and G. Roger, Phys. Rev. Lett. **49**, 91 (1982).

[276] A. Aspect, J. Dalibard, and G. Roger, Phys. Rev. Lett. **49**, 1804 (1982).

[277] W. Tittel, J. Brendel, N. Gisin, and H. Zbinden, Phys. Rev. A **59**, 4150 (1999).

[278] A. J. Leggett, J. Phys. Condens. Matter **14**, R415 (2002).

[279] E. G. Cavalcanti and M. D. Reid, Phys. Rev. A **77**, 062108 (2008).

[280] B. Opanchuk, L. Rosales-Zárate, R. Teh, and M. Reid, Phys. Rev. A **94**, 062125 (2016).

[281] G. C. Knee, K. Kakuyanagi, M.-C. Yeh, Y. Matsuzaki, H. Toida, H. Yamaguchi, S. Saito, A. J. Leggett, and W. J. Munro, Nat. Commun. **7**, 13253 (2016).

[282] M. Reid, Phys. Rev. A **97**, 042113 (2018).

[283] J. Higbie and D. M. Stamper-Kurn, Phys. Rev. A **69**, 053605 (2004).

[284] J. J. . Bollinger, W. M. Itano, D. J. Wineland, and D. J. Heinzen, Phys. Rev. A **54**, R4649 (1996).

[285] D. Leibfried, E. Knill, S. Seidelin, J. Britton, R. B. Blakestad, J. Chiaverini, D. B. Hume, W. M. Itano, J. D. Jost, C. Langer, *et al.*, Nature **438**, 639 (2005).

[286] V. Giovannetti, S. Lloyd, and L. Maccone, Science **306**, 1330 (2004).

[287] J. A. Wheeler and W. H. Zurek, *Quantum theory and measurement* (Princeton University Press, 2014).

[288] M. Heimsoth, C. E. Creffield, L. D. Carr, and F. Sols, New J. Phys. **14**, 075023 (2012).

[289] R. Richardson, J. Math. Phys. **6**, 1034 (1965).

[290] J. Dukelsky, S. Pittel, and G. Sierra, Rev. Mod. Phys. **76**, 643 (2004).

[291] F. Sols, Physica B **194-196**, 1389 (1994).

[292] M. Greiner, O. Mandel, T. W. Hänsch, and I. Bloch, Nature **419**, 51 (2002).

[293] I. Zapata, F. Sols, and A. J. Leggett, Phys. Rev. A **67**, 021603 (2003).

[294] C. Monroe, D. Meekhof, B. King, and D. J. Wineland, Science **272**, 1131 (1996).

[295] M. Brune, E. Hagley, J. Dreyer, X. Maître, A. Maali, C. Wunderlich, J. M. Raimond, and S. Haroche, Phys. Rev. Lett. **77**, 4887 (1996).

[296] C. H. van der Wal, Science **290**, 773 (2000).

[297] J. R. Friedman, V. Patel, W. Chen, S. Tolpygo, and J. E. Lukens, Nature **406**, 43 (2000).

[298] D. Esteve, J. Martinis, C. Urbina, E. Turlot, M. Devoret, H. Grabert, and S. Linkwitz, Phys. Scr. **1989**, 121 (1989).

[299] R. Rouse, S. Han, and J. E. Lukens, Phys. Rev. Lett. **75**, 1614 (1995).

[300] P. Silvestrini, V. G. Palmieri, B. Ruggiero, and M. Russo, Phys. Rev. Lett. **79**, 3046 (1997).

[301] Y. Nakamura, Y. A. Pashkin, and J. Tsai, Nature **398**, 786 (1999).

[302] M. Arndt, O. Nairz, J. Vos-Andreae, C. Keller, G. Van der Zouw, and A. Zeilinger, Nature **401**, 680 (1999).

[303] O. Nairz, M. Arndt, and A. Zeilinger, Am. J. Phys. **71**, 319 (2003).

[304] S. Eibenberger, S. Gerlich, M. Arndt, M. Mayor, and J. Tüxen, Phys. Chem. Chem. Phys. **15**, 14696 (2013).

[305] S. Gerlich, S. Eibenberger, M. Tomandl, S. Nimmrichter, K. Hornberger, P. J. Fagan, J. Tüxen, M. Mayor, and M. Arndt, Nat. Commun. **2**, 263 (2011).

[306] D. D. Awschalom, J. F. Smyth, G. Grinstein, D. P. DiVincenzo, and D. Loss, Phys. Rev. Lett. **68**, 3092 (1992).

[307] E. M. Chudnovsky, J. Appl. Phys. **73**, 6697 (1993).

[308] J. R. Friedman, M. P. Sarachik, J. Tejada, and R. Ziolo, Phys. Rev. Lett. **76**, 3830 (1996).

[309] C. A. Sackett, D. Kielpinski, B. E. King, C. Langer, V. Meyer, C. J. Myatt, M. Rowe, Q. Turchette, W. M. Itano, D. J. Wineland, *et al.*, Nature **404**, 256 (2000).

[310] T. Monz, P. Schindler, J. T. Barreiro, M. Chwalla, D. Nigg, W. A. Coish, M. Harlander, W. Hänsel, M. Hennrich, and R. Blatt, Phys. Rev. Lett. **106**, 130506 (2011).

[311] A. Ourjoumtsev, R. Tualle-Brouri, J. Laurat, and P. Grangier, Science **312**, 83 (2006).

[312] A. Ourjoumtsev, H. Jeong, R. Tualle-Brouri, and P. Grangier, Nature **448**, 784 (2007).

[313] G. Kirchmair, B. Vlastakis, Z. Leghtas, S. E. Nigg, H. Paik, E. Ginossar, M. Mirrahimi, L. Frunzio, S. M. Girvin, and R. J. Schoelkopf, Nature **495**, 205 (2013).

[314] C. Wang, Y. Y. Gao, P. Reinhold, R. W. Heeres, N. Ofek, K. Chou, C. Axline, M. Reagor, J. Blumoff, K. Sliwa, *et al.*, Science **352**, 1087 (2016).

[315] N. Bruno, A. Martin, P. Sekatski, N. Sangouard, R. T. Thew, and N. Gisin, Nat. Phys. **9**, 545 (2013).

[316] A. Lvovsky, R. Ghobadi, A. Chandra, A. Prasad, and C. Simon, Nat. Phys. **9**, 541 (2013).

[317] B. Vlastakis, G. Kirchmair, Z. Leghtas, S. E. Nigg, L. Frunzio, S. M. Girvin, M. Mirrahimi, M. H. Devoret, and R. J. Schoelkopf, Science **342**, 607 (2013).

[318] A. D. OConnell, M. Hofheinz, M. Ansmann, R. C. Bialczak, M. Lenander, E. Lucero, M. Neeley, D. Sank, H. Wang, M. Weides, *et al.*, Nature **464**, 697 (2010).

[319] N. Kiesel, F. Blaser, U. Delić, D. Grass, R. Kaltenbaek, and M. Aspelmeyer, Proc. Natl. Acad. Sci. **110**, 14180 (2013).

[320] D. L. Haycock, P. M. Alsing, I. H. Deutsch, J. Grondalski, and P. S. Jessen, Phys. Rev. Lett. **85**, 3365 (2000).

[321] A. J. Leggett and A. Garg, Phys. Rev. Lett. **54**, 857 (1985).

[322] A. D. Armour, M. P. Blencowe, and K. C. Schwab, Phys. Rev. Lett. **88**, 148301 (2002).

[323] S. Bose, K. Jacobs, and P. L. Knight, Phys. Rev. A **59**, 3204 (1999).

[324] W. Marshall, C. Simon, R. Penrose, and D. Bouwmeester, Phys. Rev. Lett. **91**, 130401 (2003).

[325] Y. Shen, S. Assad, N. Grosse, X. Li, M. Reid, and P. Lam, Phys. Rev. Lett. **114**, 100403 (2015).

[326] J.-Q. Liao, J.-F. Huang, and L. Tian, Phys. Rev. A **93**, 033853 (2016).

[327] B. Yurke and D. Stoler, Phys. Rev. Lett. **57**, 13 (1986).

[328] S.-B. Zheng, Phys. Rev. Lett. **87**, 230404 (2001).

[329] J. I. Cirac, M. Lewenstein, K. Mølmer, and P. Zoller, Phys. Rev. A **57**, 1208 (1998).

[330] J. Ruostekoski, M. J. Collett, R. Graham, and D. F. Walls, Phys. Rev. A **57**, 511 (1998).

[331] D. A. R. Dalvit, J. Dziarmaga, and W. H. Zurek, Phys. Rev. A **62**, 013607 (2000).

[332] S. Kohler and F. Sols, Phys. Rev. A **63**, 053605 (2001).

[333] A. Polkovnikov, Phys. Rev. A **68**, 033609 (2003).

[334] P. Buonsante, V. Penna, and A. Vezzani, Phys. Rev. A **72**, 043620 (2005).

[335] J. A. Dunningham, K. Burnett, R. Roth, and W. D. Phillips, New J. Phys. **8**, 182 (2006).

[336] Y. P. Huang and M. G. Moore, Phys. Rev. A **73**, 023606 (2006).

[337] J. I. Korsbakken, K. B. Whaley, J. Dubois, and J. I. Cirac, Phys. Rev. A **75**, 042106 (2007).

[338] D. W. Hallwood, K. Burnett, and J. Dunningham, New J. Phys. **8**, 180 (2006).

[339] D. W. Hallwood, K. Burnett, and J. Dunningham, J. Mod. Opt. **54**, 2129 (2007).

[340] A. M. Rey, K. Burnett, I. I. Satija, and C. W. Clark, Phys. Rev. A **75**, 063616 (2007).

[341] A. Nunnenkamp, A. M. Rey, and K. Burnett, Phys. Rev. A **77**, 023622 (2008).

[342] L. D. Carr, D. Dounas-Frazer, and M. Garcia-March, EPL **90**, 10005 (2010).

[343] D. W. Hallwood, T. Ernst, and J. Brand, Phys. Rev. A **82**, 063623 (2010).

[344] T. Haigh, A. Ferris, and M. Olsen, Opt. Commun. **283**, 3540 (2010).

[345] P. Bader and U. R. Fischer, Phys. Rev. Lett. **103**, 060402 (2009).

[346] U. R. Fischer and M.-K. Kang, Phys. Rev. Lett. **115**, 260404 (2015).

[347] T.-L. Ho and S. K. Yip, Phys. Rev. Lett. **84**, 4031 (2000).

[348] B. Dakić and M. Radonjić, Phys. Rev. Lett. **119**, 090401 (2017).

[349] I. Mazets, G. Kurizki, M. Oberthaler, and J. Schmiedmayer, EPL **83**, 60004 (2008).

[350] S. Glancy and H. M. de Vasconcelos, J. Opt. Soc. Am. **25**, 712 (2008).

[351] U. R. Fischer and B. Xiong, Phys. Rev. A **88**, 053602 (2013).

[352] G. Sierra, J. Dukelsky, G. Dussel, J. von Delft, and F. Braun, Phys. Rev. B **61**, R11890 (2000).

[353] L. Amico, G. Falci, and R. Fazio, J. Phys. A **34**, 6425 (2001).

[354] A. L. Gaunt, T. F. Schmidutz, I. Gotlibovych, R. P. Smith, and Z. Hadzibabic, Phys. Rev. Lett. **110**, 200406 (2013).

[355] M. J. Everitt, T. P. Spiller, G. J. Milburn, R. D. Wilson, and A. M. Zagoskin, Front. ICT **1** (2014).

[356] H. Jeong, M. Kang, and H. Kwon, Opt. Commun. **337**, 12 (2015).

[357] F. Fröwis, N. Sangouard, and N. Gisin, Opt. Commun. **337**, 2 (2015).

[358] W. Dür, C. Simon, and J. I. Cirac, Phys. Rev. Lett. **89**, 210402 (2002).

[359] F. Marquardt, B. Abel, and J. von Delft, Phys. Rev. A **78** (2008).

[360] C.-W. Lee and H. Jeong, Phys. Rev. Lett. **106**, 220401 (2011).

[361] F. Fröwis and W. Dür, New J. Phys. **14**, 093039 (2012).

[362] T.-L. Ho and C. V. Ciobanu, J. Low Temp. Phys. **135**, 257 (2004).

[363] A. J. Leggett, Prog. Theor. Phys. Supp. **69**, 80 (1980).

[364] G. Mazzarella, L. Salasnich, A. Parola, and F. Toigo, Phys. Rev. A **83**, 053607 (2011).

[365] E. Cavalcanti and M. Reid, Phys. Rev. Lett. **97**, 170405 (2006).

[366] G. Björk and P. G. L. Mana, J. Opt. B **6**, 429 (2004).

[367] J. I. Korsbakken, F. K. Wilhelm, and K. B. Whaley, Phys. Scr. **2009**, 014022 (2009).

[368] F. Fröwis, M. Van den Nest, and W. Dür, New J. Phys. **15**, 113011 (2013).

[369] P. Sekatski, N. Sangouard, and N. Gisin, Phys. Rev. A **89**, 012116 (2014).

[370] C. A. Fuchs and J. Van De Graaf, IEEE Trans. Inf. Theory **45**, 1216 (1999).

[371] G. v. Rossum, CWI (1995).

[372] J. D. Hunter, Comput. Sci. Eng. **9**, 90 (2007).

[373] J. R. Johansson, P. D. Nation, and F. Nori, Comput. Phys. Commun. **184**, 1234 (2013).